Search for charginos in e^+e^- interactions with the DELPHI detector at LEP

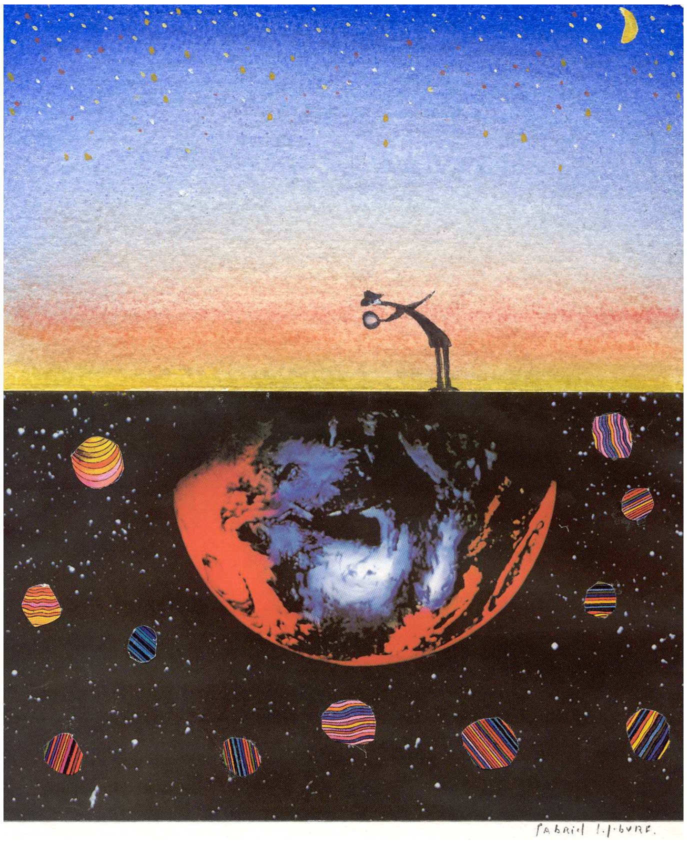

Thomas Alderweireld

Dissertation présentée en vue de
l'obtention du grade académique
de Docteur en Sciences

Promoteur: Pr Ph. Herquet

Septembre 2002

Dédié à Anne.

“Il a toujours fallu beaucoup plus d’imagination pour saisir la réalité que pour l’ignorer.”

J. Giraudoux

Cette thèse est l'aboutissement de plusieurs années de recherche au sein du service de physique des particules élémentaires de l'Université de Mons. Cette thèse, dont ce manuscrit ne constitue que la partie visible, est le reflet d'un travail de collaboration intense dans des domaines tels que la physique théorique et expérimentale, l'électronique et l'informatique. Elle est une preuve, s'il en est encore besoin, de la synergie que peut donner le travail en équipe dans la grande expérience internationale qu'est DELPHI. Elle n'aurait été possible sans l'intervention des personnes que je tiens à remercier aujourd'hui.

Je remercie sincèrement Philippe Herquet pour avoir choisi un "original créatif" au poste de recherche que j'ai eu la chance d'obtenir. Il a su encadrer cette thèse tout en me laissant un espace de liberté qui m'était indispensable. J'ai apprécié pendant ces dernières années les moyens qu'il a mis à ma disposition et je tiens encore une fois à le remercier ainsi que tous les autres membres du personnel de son service.

Mon estime à Fernand Grard. Bien que nous n'ayions pas énormément interagi, j'apprécie son esprit de rigueur, sa passion pour la physique et son enthousiasme. Je le remercie d'avoir accepté d'être membre de mon jury.

Je remercie par la même occasion tous les membres de mon Jury. Notamment Pierre Fayet et Luc Pape qui m'ont consacré du temps afin de rendre ce manuscrit plus lisible et compréhensible. Leur connaissance en la matière et leur patience m'ont été d'un grand secours et j'ai appris énormément sur la physique théorique et phénoménologique grâce à leur aide respective. Merci aussi à Tiziano Camporesi d'être dans mon jury et de m'avoir nommé il y a 3 ans coordinateur de l'équipe "$\gamma\gamma$ as background for searches" où Patrice Verdier et moi-même avons testé sans relâche les générateurs $\gamma\gamma$. Ce fut une expérience extrêmement enrichissante qui je pense a porté ses fruits. Merci à Myriam Deterck pour m'avoir formé à la finance, pour son aide précieuse à l'élaboration de mon travail de recherche de thèse annexe et ainsi que pour les connexions qu'elle a créées. Enfin, merci à Yves Brihaye et Claude Semay, en espérant que cette thèse leur plaira.

Certains ont joué un rôle important dans ma formation. Je tiens en particulier à remercier Pierpaolo Rebecchi pour m'avoir initié à la physique des charginos et m'avoir intégré dans son équipe. Je le remercie de m'avoir fait confiance et de m'avoir donné la responsabilité du groupe voici maintenant 3 ans. Aussi à Gustavo Wolf, Monsieur GMSB, pour son amitié et sa collaboration sur l'analyse GMSB. Je me souviens encore de mon premier shift de nuit, où suite à nos discussions, les prémices d'une nouvelle analyse chargino, basée sur la méthode des quotients de fonctions de vraisemblance, se sont imposées à mon esprit. Cette méthode, acceptée et mise en oeuvre par l'ancienne équipe chargino (Pierpaolo, Inès et moi-même), constitue la clef de voûte de l'analyse décrite dans ce manuscrit. Merci à Inès Gil Botella avec qui j'ai passé des heures à réfléchir, à coder, à optimiser et à espérer découvrir les charginos. Merci aussi pour sa joie de vivre et son amitié. Une mention spéciale pour Stefan Ask, la dernière recrue de l'équipe chargino, qui en quelques mois est devenu indispensable et expert en la recherche des particules supersymétriques. La magie de l'apprentissage, c'est lorsque l'élève dépasse le maître, et je pense que la situation s'est produite dans son cas. Je lui souhaite d'écrire une thèse à l'image de ses compétences et de faire la carrière qu'il mérite dans la physique des hautes énergies.

Merci à Maria Espirito Santo, Anna Lipniacka, Federica Mazzucato et Patrice Verdier, notre collaboration dans le cadre de l'uniformisation des recherches des particules supersymétriques SUGRA de DELPHI (the SUSANA project) fut une très bonne expérience.

J'ai beaucoup apprécié la partie On-Line de mon travail de recherche au CERN. Notamment la collaboration avec Nick Van Remortel (the "correlated" guy) et Jorgen D'Hondt (the "reconnected" guy) pour la responsabilité du fonctionnement des chambres à muons avant. Je leur souhaite du courage pour l'écriture de leur manuscrit de thèse. Merci à Catherine de Clercq, Ann Van Lysebetten, Jean-Paul Dewulf et Bob Goorens pour nous avoir appris à réparer ces chambres en toutes situations.

Les "shifts", nécessaires au bon fonctionnement d'une expérience de physique des hautes énergies, constituent une part non négligeable de la formation d'un jeune physicien. Je tiens à remercier en cette occasion Philippe Charpentier et Patrick Jarry pour leur encadrement durant mes shifts lors de la prise de données de DELPHI.

Merci à Donato Carrieri de m'avoir accueilli chez Fortis et de m'avoir donné une partie de son temps précieux pour définir le sujet de ma thèse annexe ainsi que les informations et explications nécessaires à la compréhension de la "réalité" du marché obligataire.

Je remercie Gabriel Lefebvre pour son illustration du "physicien à la loupe" en couverture de ce manuscrit.

Un clin d'oeil à André, Chantal, Greg, Hugor, JeanMichMuche, Jorge, Rafoul, Régis, Renaud, Samuël et tous mes autres amis, ainsi qu'à ma famille et celle de ma compagne.

Et finalement, à Anne, à qui cette thèse est dédiée, et Simon, merci de m'avoir supporté et accompagné durant l'écriture de ce manuscrit.

Thomas Alderweireld

Search for charginos in $\mathrm{e^+e^-}$ interactions with the DELPHI detector at LEP

by

T. Alderweireld
Faculté des Sciences, Université de Mons Hainaut, Mons, Belgium
email: thomas.alderweireld@cern.ch

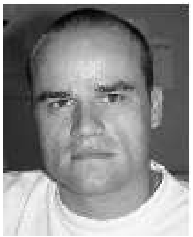

Abstract

DELPHI data collected at centre-of-mass energies up to 209 GeV have been analyzed in search for charginos in the framework of the constrained Minimal Supersymmetric extension of the Standard Model (cMSSM) with R-parity conservation. Supersymmetry breakings induced by the supergravity (SUGRA) or mediated by gauge interations (GMSB), giving rise to different experimental signatures, have been assumed. The likelihood ratio method was used to extract a possible signal from the real data. No evidence for a signal was found in any of the channels and the results of the searches were used to derive limits on chargino pair production cross-sections and masses. In the SUGRA scheme, the excluded regions in the theoretical parameter space of the constrained MSSM imply an indirect limit on the mass of the Lightest Supersymmetric Particle, here assumed to be the lightest neutralino, of 38.2 GeV/c^2. All limits are given at 95% confidence level.

Contents

Introduction

Theoretical physicists, like artists (we are tempted to say like *other* artists) are guided in their work by aesthetics as well as rational concerns. "Make any science, something else than pure logic is necessary," wrote Poincaré, who identified this additional element as intuition, involving "the feeling of mathematical beauty, of the harmony of numbers and forms and of geometric elegance". Aesthetics are notoriously subjective, and the statement that physicists seek beauty in their theories is meaningful only if we can define beauty. Fortunately this can be done for particle physics aesthetics which is related to the mathematical concept of *symmetry*.

A great achievement of our understanding of symmetries and their implications arose in 1918 when the German mathematician Emmy Noether demonstrated that every conservation law implied the existence of a symmetry and vice versa. Hence if natural laws arise from symmetries, then one ought to be able to search for previously unknown laws by looking for symmetrical relationship(invariance) in the nature. In the physicists' jargon, this may be obtained by building Lagrangian densities(theories) invariant under group transformations, perform experimental measurements and see if they match one of the theories.

(Un)fortunately, we live in an imperfect world, and many of the symmetries that show up in equations are found to be broken at low energies (e.g. 10^{-11} second after the big bang for the electroweak force). The remnants are (spontaneously) broken symmetries and physicists' tasks are to identify the deeper symmetries hidden beneath by performing experiments probing high energy scales.

This thesis is dedicated to the search(measurement) of a broken symmetry, the *supersymmetry* (SUSY), which relates fermions(matter) and bosons(forces). More precisely, this thesis consists of the search of new particles called charginos which are a manifestation of the broken supersymmetry. Among the various SUSY particles that might exist, the lightest chargino is of particular interest because it is expected to be light and to have a non-negligible production cross-section all over all the SUSY parameter space, and hence, might be observed if kinematically allowed by present experiments. The present search is performed using the data sample of the $\mathrm{e}^+\mathrm{e}^-$ collisions recorded by the DELPHI detector at the LEP collider at CERN during the years 1999 and 2000 at centre-of-mass energies up to 209 GeV.

The first chapter is dedicated to the supersymmetric theories, including a description of the so-called Standard Model (SM) which is a non-supersymmetric model based on (spontaneously broken) symmetries. The SM describes with a high precision the matter and its interactions until the energies reached by the present accelerators. Then, motivations for a minimal supersymmetric extension of this model (the MSSM) are given and followed by a description of the MSSM as well as several mechanisms responsible of its breaking. Namely the SUGRA, GMSB and AMSB mechanisms. Appendix A gives the notations and conventions used to derive the framework of the first chapter and appendix B describes how the electroweak symmetry breaking may be achieved in the MSSM.

In the second chapter, the chargino sector is described as well as the chargino pair production and decay mechanisms at LEP. All the theoretical and phenomenological assumptions made in this work are summarized at the end of the chapter. In appendix C, the contour distributions in the (μ, M_2)

plane of the most relevant variables used in the analysis are shown. Finally appendix D discusses the impact of the one-loop radiative corrections on the matching between the physical masses and MSSM theoretical parameters.

The third chapter describes the LEP accelerator and its great achievements in terms of the reached centre-of-mass energies, recorded luminosities and the precision of their measurements. The DELPHI detector is briefly described as well as its reconstruction and identification algorithms.

The fourth chapter is devoted to the investigated data samples and the chargino simulated signal. The data sample analyzed in this work are given and the characteristics of the chargino signal are analyzed. Depending on the experimental signatures, different decay channels are defined. The criteria followed in the choice of the generated chargino points are also described.

In the fifth chapter the SM processes with topological and kinematic characteristics similar to those of the chargino signal are given in details. This followed by a description of Monte Carlo generators and the cuts applied at the level of the generation are also mentioned. Finally the cross-sections at each investigated energies are given for all the relevant SM processes.

The sixth chapter describes the search for charginos carried out with the data collected in years 1999 and 2000. The event selection is performed using the likelihood ratio method. In the first part of the chapter, the likelihood ratio method is described. The definition of the four chargino topologies and the ΔM range division in more specific windows are given. The particle selections within each event are given followed by a description of the events *common* selections and preselections applied in each ΔM region and topology. The construction of likelihood ratio functions is detailed as well as the procedure used to determine the optimal set of discriminating variables and the likelihood ratio cut value in each investigated window. Finally a data MC comparison is performed at several levels, and possible problems are discussed. To illustrate the different steps of the event selection stream, appendices E, F and G contain respectively the distributions of the data and SM expectations at the *common* selection, preselection and likelihood ratio cut levels.

Results in terms of real data and SM expectations and detection efficiencies are discussed in chapter seven. In the same chapter, SM background compositions are described and some nice candidates are commented. Since the number of observed events is compatible with the expectations from the background simulation, exclusion limits are derived in the SUGRA and the GMSB scenarios. Chapter eight is devoted to the final results on the present chargino searches. The lightest chargino mass limits are derived in both scenarios. In the SUGRA scheme, a cross–section limit is computed at the highest centre–of–mass energy and an indirect neutralino mass limit is derived. These experimental results are then translated into exclusion regions for the parameter space of the MSSM. Appendix H is devoted to the techniques and approaches used to derive the obtained limits and appendix I gives the systematics computation and explains how those uncertainties have been propagated into the limits.

Finally, the most important conclusions extracted from this work are summarized.

Part I

Quantum Field Theory

Chapter 1

Theoretical framework

Before describing the supersymmetric theoretical framework, its motivations and its experimental signatures, we have to start from the so-called Standard Model which gives, at present time, the most accurate description of the phenomenological electromagnetic, weak and strong interactions. In what follows, it is assumed that the reader is familiar with the basic concepts of quantum field theory [1] and Yang-Mills prescriptions [2] to build invariant Lagrangian densities under local transformations.

1.1 The Standard Model

1.1.1 Historical overview

At the end of the fifties a severe problem was posed by the definition of quantum theories for the weak interactions. While these interactions were well described, at the classical level (i.e. low energy scale), by the Fermi theory involving local products of four fermion fields (times a coupling constant proportional to the Fermi constant, $G_F \simeq 10^{-5} GeV^{-2}$), it was not possible to compute higher quantum corrections to weak-interaction processes (non-negligible at high energy scale) which were found to be severely divergent[1].

The solution of this problem went through the understanding of (charged-current) weak interactions as due to exchanges of heavy charged intermediate bosons named W^+ and W^-, coupled proportionally to some dimensionless constant g and a linear combination of charged vector and axial-vector [2] with the following propagator:

$$\frac{\eta^{\mu\nu} + \frac{q^\mu q^\nu}{M_W^2}}{q^2 + M_W^2} \tag{1.1}$$

where $\eta^{\mu\nu}$ stands for the 4-dimensional Minkowski metric and q for the exchanged momentum between the interacting particles [3]. The Fermi constant G_F may then be expressed in terms of this coupling g and the mass of the intermediate bosons $W^{\pm}$. At low energy this relation is $G_F/\sqrt{2} = g^2/8M_W^2$.

[1]For instance, at high energy, the reaction $\bar{\nu} + p^+ \rightarrow e^+ + n^0$ has, using point interactions, a tree-level cross-section proportional to $G_F^2\ \ s$, where s is the Mandelstam variable defined as the square of the 4-momentum $p_{\bar{\nu}} + p_{p^+}$, and so diverges as s tends to infinity even at the tree-level.

[2]At this time,experimental measurements have shown that those currents were of the form V-A (i.e. involving $\gamma^\mu(1+\gamma_5)$) (The γ's are given in appendix A).

[3]The conventions chosen for the γ's and $\eta^{\mu\nu}$ are given in appendix A.

In 1957 [4], Schwinger [3] suggested the existence of an "isotopic" triplet of vector fields whose universal couplings would generate both the charged weak interactions and electromagnetism (e.m.). Four years later, his student, Glashow [4], following this direction, stated that if some symmetry was imposed on the lepton vector boson couplings then a coupling of a neutral boson to these leptons was required. Furthermore he mixed this neutral vector boson with the photon, involving the weak-mixing angle. He discovered that in this way parity violation in e.m. currents could be avoided while having parity violation in the weak current. Glashow justified his model by invoking the Lee-Yang article [6], where they showed that additional neutral intermediate bosons were required if one assumed the $|\Delta I| = \frac{1}{2}$ and $|\Delta S| \leq 1$ empirical rules [5]. But since there was no evidence of a coupling of a neutral vector boson to the leptons, Glashow assumed a heavy neutral boson which raised the question on how this could still explain the $|\Delta I| = \frac{1}{2}$ rule. Glashow's arguments to cure this problem were not clear and his results were forgotten by the physics community. Meanwhile important things with respect to the Standard Model foundation occurred. First there was the invention of $SU(3)$ for the meson and baryon classifications, followed by the Cabibbo theory of weak-interactions [6]. Next there was the introduction by Gell-Mann [7] and Zweig [8] of the quarks [7] which permits to construct charged weak currents satisfying the empirical $\Delta Q = \Delta S$ and $|\Delta S| \leq 1$ rules. In the paper of Gell-mann there was the idea that there should be a lepton-hadron symmetry. This led Hara [10] to the idea of a fourth quark [8] followed by a paper from Bjorken and Glashow [11] where they named it charm [9]. Nevertheless the quark idea was only gradually assimilated by the physics community. The very important contributions by Greenberg [12] and Nambu [13], essentially introducing colour, and finally the discovery of the proton structure in deep inelastic scattering experiments [14] were crucial for this.

In 1964 Salam and Ward [15] pursued the idea of a Yang-Mills theory for leptons. While the initial symmetry that they used was $SU(3)$ (they wanted something analogous to the strong interactions, where by then $SU(3)$ was the accepted symmetry) they later broke this to $SU(2) \otimes U(1)$ but still the boson masses were put by "hand" until 1967 when Weinberg [16] (following Kibble's work [17]) proposed a $SU(2) \otimes U(1)$ broken spontaneously by the Brout-Englert-Higgs mechanism [18]. Weinberg paper contains the Higgs sector as used today. He also generated fermions masses by mean of a non-vanishing vacuum expectation value (vev) [10]. This paper certainly contains a considerable part of the Standard Model as known today. But because nobody believed in all this it was not taken seriously by anybody including Weinberg himself! In 1970 the GIM paper [19] appeared, this paper was a synthesis of the Glashow papers and was showing that Yang-Mills theories might be less divergent and perhaps renormalizable by adding a fourth quark, moreover the addition of this fourth quark permitted to prevent first-order strangeness changing neutral currents. In addition they considered no interference between strong and electroweak interactions but the Higgs sector was absent. If somebody had synthesized Weinberg's paper and the GIM paper much of the Standard Model (excluding

[4] What follows is inspired from a review of the genesis of the Standard Model given by M. Veltman which can by found in [5].

[5] I and S are respectively the total isotopic spin and strangeness of the strongly interacting particles (i.e. baryons and the K and π mesons). In their paper, Lee and Yang showed that since this rule was favored by experimental measurements of the non-leptonic decay modes of strange particle, this was requiring the existence of neutral current due to at least one neutral vector boson (their conclusion was mainly due to the fact that the quarks did not yet exist.). So the neutral currents were believed in, for the wrong reason.

[6] Without using the quark theory.

[7] Even if Gell-Mann and Zweig considered in their paper non-integrally charged quarks (i.e. fractionally charged), they thought them as non real particles which permit to explain mathematically the strong interactions in its simplest way [9].

[8] The third lepton family was discovered only in 1975.

[9] Bjorken and Glashow (as Hara did) used integrally charged quarks and quote Hara's paper.

[10] Something that was actually done first by Schwinger [3] ten years before.

quantum chromodynamics) would have been written. And including the Han-Nambu paper [13] quantum chromodynamics would surely have been formulated as well. In fact this is of course precisely what happened later. Finally, in 1971 't Hooft's work [20] completed the proof of renormalizability of Yang-Mills theory. That proof led to an immediate acceptance of gauge theories by the theorists since the possibility to compute higher order corrections was there. Then it was shown by Bouchiat, Iliopoulos and Meyer [21] that to cure the non-renormalizability of Weinberg's model [16] , quarks with 3 colours had to be considered [11]. In 1973 the theoretically predicted neutral currents were discovered [22]. Those currents were preserving the strangeness which could at that time be explained only by theories including the GIM mechanism if the existence of a fourth quark was proven. This happened with the discovery of the charm quark [23] in 1974. Finally the asymptotic freedom of the quarks [24] through the running of $\alpha_S(Q^2)$, where Q^2 [12] is the energy scale of the interaction, was measured experimentally [25]

The Standard Model was born

In 1975, the discovery of the τ^- lepton [26] stated the existence of a third quark family (expected from the lepton-quark symmetry) which was discovered (the bottom (b) in 1977 [27] and the top (t) in 1995 [28]). In between, the production of on-shell W and Z was performed in 1983 [29]. It has to be emphasized that an accurate prediction of the top mass could be deduced using previous measurements (with an important LEP contribution) of the physical parameters of the electroweak interactions, namely $\alpha(M_Z)$, G_F and M_Z where $\alpha(M_Z)$ is the e.m. running coupling at the Z mass [13], only if radiative corrections were taken into account. This is a clear proof that to describe our world with a “Theory of Matter”, the classical description (i.e. the tree-level) is not sufficient and to be predictive we have to take into account quantum effects (i.e. higher order terms in the perturbation theory). This is a one of the great achievements of the LEP physics measurements (including the extremely precise M_Z, M_W and α_S determinations and a lot more...) and the Standard Model predictions [30].

1.1.2 The Standard Model field content

The Standard Model describes electromagnetic, weak and strong interactions between elementary particles. It is based on the gauge groups $SU(3)_C \otimes SU(2)_L \otimes U(1)_Y$. In this model the interactions are described by the exchanges of 12 spin-1 mediators, known as gauge bosons of the adjoint representations of $SU(3)_C \otimes SU(2)_L \otimes U(1)_Y$, between the "constituents of matter” as are often called the spin-$\frac{1}{2}$ leptons and quarks. The 12 gauge bosons consist of:

- 8 $SU(3)_C$ gluons G^a_μ with g_S as coupling constant,
- 3 $SU(2)_L$ non-Abelian bosons W^i_μ with g,
- 1 $U(1)_Y$ Abelian boson B_μ with g',

where the indices a and i stand for the boson label (with a = 1,...,8 and i = 1,2,3) and μ for the 4 dimensions of the Minkowski space. The matter fields are fermions belonging to the fundamental representations of the gauge groups. These are colour quark and lepton fields of at least 3 generations.

[11] Moreover this gave the right amplitude of the $\pi^0 \to 2\gamma$ decay.

[12] The energy scale of the interaction is given by $Q^2 = -q^2$ where q^2 is the four-momentum transfer squared of the interaction.

[13] This running behavior (i.e. the dependence of the energy scale) is deduced from renormalization [30].

Since the SM is left-right asymmetric, left-handed and right-handed fermions have different quantum numbers and left(right)-handed fermions transform as doublets(singlets) under $SU(2)_L$ transformations. Their electric charge is given by the electric charge operator Q defined as $Q = T^3 + Y/2$, where T^3 is the third generator [14] of $SU(2)_L$ (weak isospin) and Y is the $U(1)_Y$ generator (hypercharge), as shown in Table 1.1.

multiplets	particles	Y	T^3	Q
$doublets$ $left\ L_\alpha$	$\begin{pmatrix}\nu_e\\ e^-\end{pmatrix}_L \begin{pmatrix}\nu_\mu\\ \mu^-\end{pmatrix}_L \begin{pmatrix}\nu_\tau\\ \tau^-\end{pmatrix}_L$	-1	$\begin{pmatrix}1/2\\ -1/2\end{pmatrix}$	$\begin{pmatrix}0\\ -1\end{pmatrix}$
$singlets$ $right\ E_\alpha$	$(e^-)_R\ (\mu^-)_R\ (\tau^-)_R$	-2	0	-1
$doublets$ $left\ Q^i_\alpha$	$\begin{pmatrix}u\\ d\end{pmatrix}^i_L \begin{pmatrix}c\\ s\end{pmatrix}^i_L \begin{pmatrix}t\\ b\end{pmatrix}^i_L$	$1/3$	$\begin{pmatrix}1/2\\ -1/2\end{pmatrix}$	$\begin{pmatrix}2/3\\ -1/3\end{pmatrix}$
$singlets$ $right\ U^i_\alpha, D^i_\alpha$	$(u)^i_R\ (c)^i_R\ (t)^i_R$ $(d)^i_R\ (s)^i_R\ (b)^i_R$	$4/3$ $-2/3$	0 0	$2/3$ $-1/3$

Table 1.1: The three families of the leptons and quarks. Left-handed lepton and quark fields transform as members of $SU(2)_L$ electroweak doublets, while their right-handed counterparts are singlets. α is the index of the 3 leptonic and 3 hadronic families while the i index is the colour (Red,Green,Blue).

1.1.3 The Standard Model Lagrangian density

In the framework of Quantum Field Theory the Standard Model is described by the following Lagrangian density

$$\mathcal{L} = \mathcal{L}_{gauge} + \mathcal{L}_{Higgs} + \mathcal{L}_{Yukawa} \tag{1.2}$$

where

$$\begin{aligned}
\mathcal{L}_{gauge} \quad = \quad & -\tfrac{1}{4}\,G^{a\ \mu\nu}G^{a}{}_{\mu\nu} - \tfrac{1}{4}\,W^{i\ \mu\nu}W^{i}{}_{\mu\nu} - \tfrac{1}{4}\,B^{\ \mu\nu}B_{\ \mu\nu} \\
& -i\,\overline{L}_\alpha\gamma^\mu\,\mathcal{D}_\mu L_\alpha - i\,\overline{Q}_{\alpha\ i}\gamma^\mu\,(\mathcal{D}_\mu)^i_j Q^j_\alpha - i\,\overline{E}_\alpha\gamma^\mu\,\mathcal{D}_\mu E_\alpha \\
& -i\,\overline{U}_{\alpha\ i}\gamma^\mu\,(\mathcal{D}_\mu)^i_j U^j_\alpha - i\,\overline{D}_{\alpha\ i}\gamma^\mu\,(\mathcal{D}_\mu)^i_j D^j_\alpha
\end{aligned}$$

with

$$\begin{aligned}
G^{a}{}_{\mu\nu} &= \partial_\mu G^a_\nu - \partial_\nu G^a_\mu - g_S f^{abc} G^b_\mu G^c_\nu, \\
W^{i}{}_{\mu\nu} &= \partial_\mu W^i_\nu - \partial_\nu W^i_\mu - g\epsilon^{ijk} W^j_\mu W^k_\nu, \\
B_{\ \mu\nu} &= \partial_\mu B_\nu - \partial_\nu B_\mu, \\
\mathcal{D}_\mu L_\alpha &= (\partial_\mu \mathbb{1} + i\tfrac{g}{2}\tau^i W^i_\mu - i\tfrac{g'}{2} B_\mu \mathbb{1}) L_\alpha, \\
\mathcal{D}_\mu E_\alpha &= (\partial_\mu - ig' B_\mu) E_\alpha, \\
(\mathcal{D}_\mu)^i_j Q^j_\alpha &= (\delta^i_j \partial_\mu \mathbb{1} + \delta^i_j i\tfrac{g}{2}\tau^k W^k_\mu + \delta^i_j i\tfrac{g'}{6} B_\mu \mathbb{1} - i\tfrac{g_S}{2}(\lambda^a)^i_j G^a_\mu \mathbb{1}) Q^j_\alpha, \\
(\mathcal{D}_\mu)^i_j U^j_\alpha &= (\delta^i_j \partial_\mu + \delta^i_j i\tfrac{2}{3} g' B_\mu - i\tfrac{g_S}{2}(\lambda^a)^i_j G^a_\mu) U^j_\alpha, \\
(\mathcal{D}_\mu)^i_j D^j_\alpha &= (\delta^i_j \partial_\mu - \delta^i_j i\tfrac{1}{3} g' B_\mu - i\tfrac{g_S}{2}(\lambda^a)^i_j G^a_\mu) D^j_\alpha,
\end{aligned}$$

where the f^{abc} (ϵ^{ijk}) stand for the group $SU(3)(SU(2))$ structure constants, the τ^i are the three Pauli matrices and the $(\lambda^a)^i_j$ are the components of the 8 Gell-Mann matrices with a,b,c = 1,...,8 and

[14] The 3 $SU(2)_L$ generators are here related to the three Pauli matrices by the relation $T^i = \frac{(1+\gamma_5)}{2}\frac{\tau^i}{2}$ when acting on left-handed fermionic doublets.

$i,j,k = 1,2,3$ (the $\frac{\lambda^a}{2}$'s are one of the representations of the generators of the $SU(3)$ Lie algebra).

$\mathcal{L}_{gauge}$ is invariant under Lorentz and local $SU(3)_C \otimes SU(2)_L \otimes U(1)_Y$ transformation since it has been built using Yang-Mills prescriptions. If we expand the covariant derivatives ($\mathcal{D}_\mu$) in the Lagrangian density, terms will appear with different powers of the gauge and matter fields, their physical meanings are

- terms $\propto A^2$ are related to the free-bosonic field A (A stands for W, G, B),
- terms $\propto \overline{\psi}\psi$ are related to the free-fermionic field ψ (ψ stands for E, L, Q, U, D),
- terms $\propto \overline{\psi}\psi A$ are the interactions terms (i.e. vertex) between the gauge boson and the matter,
- terms $\propto A^3$ and A^4 are the self-interaction terms which are determined by the structure of the related gauge group (e.g. a vertex built only with gluons).

We see that the $\mathcal{L}_{gauge}$ Lagrangian density contains all the propagation and interaction information of its gauge and matter field contents. Nevertheless, explicit mass terms in the Lagrangian density are forbidden because they are not $SU(2)_L$ symmetric, hence a new Lagrangian density ($\mathcal{L}_{Higgs}$) which performs a spontaneous symmetry breaking of $SU(3)_C \otimes SU(2)_L \otimes U(1)_Y$ to $SU(3)_C \otimes U(1)_{ElectroMagnetism}$ must be added.

1.1.4 The electroweak symmetry breaking

Since adding the mass terms "by hand" would destroy the renormalizability of the Standard Model, an alternative way, referred as spontaneous symmetry breaking, must be implemented. The idea of spontaneous symmetry breaking mechanism is to have a theory where the Lagrangian density is still exactly symmetric under the group transformations, but is giving rise, for dynamical reasons, to a ground state which is not invariant (i.e. a non-vanishing vev) under those group transformations.

1.1.4.1 Spontaneously broken global symmetries

Let us consider a theory of self-interacting scalar isodoublet field Φ with an interaction invariant under global isospin transformations, defined as :

$$\Phi = \begin{pmatrix} \phi^+ \\ \phi^o \end{pmatrix} \quad \begin{cases} \phi^+ = \frac{\phi_1 + i\phi_2}{\sqrt{2}} \\ \\ \phi^o = \frac{\phi_3 + i\phi_4}{\sqrt{2}} \end{cases} \tag{1.3}$$

$$\begin{cases} \mathcal{L}_{Higgs} &= -(\partial_\mu \Phi)^\dagger (\partial^\mu \Phi) - V(\Phi) \\ V(\Phi) &= \mu^2 \Phi^\dagger \Phi + \lambda (\Phi^\dagger \Phi)^2 \end{cases} \tag{1.4}$$

where the ϕ_i are real fields, λ and μ^2 are real constants. Usually one assumes that the lowest energy state correspond to the field configuration $\Phi = 0$ but for scalar fields it may happen that the lowest energy configuration corresponds to $\Phi = \text{cst}$ [15] $= \Phi_0 \neq 0$, if it is so, particles should be associated to the oscillations of Φ around Φ_0. Hence to study the mass spectrum of the particles associated to

[15] The constancy of Φ_0 is required for the vacuum to be translation invariant.

the field Φ, the Lagrangian density must be expanded around the non-vanishing vacuum value of Φ as follows:

$$\begin{cases} \Phi(\mathbf{x}) = \Phi_0 + \chi(\mathbf{x}) \\ \mathcal{L} = "\chi^{2}" + "\chi^{3}" + "\chi^{4}" + ... \end{cases} \tag{1.5}$$

The true particle spectrum is then determined by the equation of motion obtained from the $"\chi^{2}"$ terms. In order to have a consistent theory with $\Phi_0 \neq 0$, the ground state (Φ_0) must be the absolute minimum of the energy density, this corresponds to the situation where $\lambda > 0$ and $\mu^2 < 0$, implying $\Phi_0^\dagger \Phi_0$ to be equal to $\frac{-\mu^2}{2\lambda}$.

The isospin frame can always be chosen so that the constant Φ_0 isospinor is a down isospinor

$$\langle\Phi\rangle_0 \equiv \Phi_0 = \begin{pmatrix} 0 \\ \frac{\eta}{\sqrt{2}} \end{pmatrix} \text{ with } \eta = \sqrt{\frac{-\mu^2}{\lambda}} \tag{1.6}$$

In this frame, any deviation from the ground state (i.e. vacuum) can be expressed as

$$\Phi(\mathbf{x}) = \mathcal{U}(\mathbf{x}) \begin{pmatrix} 0 \\ \frac{\eta}{\sqrt{2}} + \frac{\sigma(\mathbf{x})}{\sqrt{2}} \end{pmatrix} \tag{1.7}$$

where $\sigma(\mathbf{x})$ is a real function of the space-time coordinates and $\mathcal{U}(\mathbf{x})$ is the local $SU(2)$ transformation, which brings the frame where $\Phi(\mathbf{x})$ is down to the frame where Φ_0 is down, defined as

$$\mathcal{U}(\mathbf{x}) = e^{i\tau_a\theta^a(\mathbf{x})} \tag{1.8}$$

where the τ_i (i=1,2,3) are the three Pauli matrices and the $\theta^i(\mathbf{x})$ (i=1,2,3) are real functions of the space-time coordinates. For small perturbations this reduces to

$$\chi(\mathbf{x}) \approx \begin{pmatrix} \frac{\eta}{\sqrt{2}} \; (\theta^2 + i\theta^1) \\ \frac{\sigma(\mathbf{x})}{\sqrt{2}} - i\,\frac{\eta}{\sqrt{2}}\,\theta^3 \end{pmatrix} \tag{1.9}$$

If we inject $\Phi(\mathbf{x})$ (= $\chi(\mathbf{x}) + \Phi_0$) into the Lagrangian density defined in Eq.(1.4), the $"\chi^{2}"$ terms correspond to

$$-\frac{1}{2}\partial_\mu\sigma\partial^\mu\sigma - \frac{1}{2}m^2\sigma^2 - \frac{1}{2}\partial_\mu\tilde{\theta}^a\partial^\mu\tilde{\theta}^a \tag{1.10}$$

where $m = \sqrt{-2\mu^2}$ and $\tilde{\theta}^a = \eta\theta^a$

So we see that just by requiring a non-vanishing vev in the $SU(2)$ isospin space (i.e. $\Phi_0 \neq 0$) we end up with 4 types of particles, as in the $\Phi_0 = 0$ case but with different mass spectrum, we have

- one massive scalar boson with mass $m = \sqrt{-2\mu^2}$ associated to the field σ,
- three massless scalar (Nambu-Goldstone) bosons associated to the fields $\tilde{\theta}^a$.

This mechanism called global spontaneous symmetry breaking, when applied to local gauge invariance is the key foundation of the Brout-Englert-Higgs mechanism which provides the mass to the gauge bosons and the matter fields of the Standard Model.

1.1.4.2 The Englert-Brout-Higgs mechanism

The $SU(3)_C \otimes SU(2)_L \otimes U(1)_Y$ locally gauge invariant form of the Lagrangian density defined in Eq.(1.4) is

$$\left\{ \begin{array}{lcl} \mathcal{L}_{Higgs} & = & -(\mathcal{D}_\mu \Phi)^\dagger (\mathcal{D}^\mu \Phi) - V(\Phi) \\ V(\Phi) & = & \mu^2 \Phi^\dagger \Phi + \lambda (\Phi^\dagger \Phi)^2 \end{array} \right. \tag{1.11}$$

with

$$\mathcal{D}_\mu \Phi = (\partial_\mu + i\frac{g}{2}\tau^i W^i_\mu + i\frac{g'}{2} B_\mu)\Phi \tag{1.12}$$

Since this Lagrangian density is invariant under local $SU(3)_C \otimes SU(2)_L \otimes U(1)_Y$ transformations, any deviation from the ground state (i.e. vacuum) can be expressed as

$$\chi(\mathbf{x}) = \Phi(\mathbf{x}) - \Phi_0 = \begin{pmatrix} 0 \\ \frac{\eta}{\sqrt{2}} + \frac{\sigma(\mathbf{x})}{\sqrt{2}} \end{pmatrix} - \begin{pmatrix} 0 \\ \frac{\eta}{\sqrt{2}} \end{pmatrix} \tag{1.13}$$

Due to local gauge invariance [16], the $\mathcal{U}(\mathbf{x})$ matrix has disappeared, and so are the 3 degrees of freedom (the θ^i's). If we build a new Lagrangian density as $\mathcal{L}_{gauge} + \mathcal{L}_{Higgs}$ and expand the covariant derivative defined in Eq.(1.12), the mass terms appear as:

$$\left\{ \begin{array}{lll} M_{W^\pm} = & \frac{1}{2}\eta g & \\ M_{Z^0} = & \frac{1}{2}\eta \frac{g}{\cos\theta_W} & \text{with} \quad \tan\theta_W = \frac{g'}{g} \end{array} \right. \tag{1.14}$$

where the physical weak massive intermediate bosons, $W^\pm$ and Z^0, are linear combinations of the gauge ones

$$W^\pm_\mu = \frac{W^1_\mu \mp i W^2_\mu}{\sqrt{2}} \quad , \; Z_\mu = -\sin\theta_W B_\mu + \cos\theta_W W^3_\mu \tag{1.15}$$

while the photon field, A_μ, defined as orthogonal to Z_μ, is given by

$$A_\mu = \cos\theta_W B_\mu + \sin\theta_W W^3_\mu \tag{1.16}$$

remains massless (as the gluons do). Its corresponding generator which remains conserved is $T^3 + \frac{Y}{2} = Q$ [17] and the coupling constant is $g \sin\theta_W = e$ where e is the electric charge.

A massive vector field has one more degree of freedom, with respect to the massless case, namely that associated with the longitudinal waves. There are, therefore, three more degrees of freedom for the vector fields $W^\pm$ and Z^0 in the spontaneously broken theory. This exactly compensates the three degrees of freedom we have lost due to the the local gauge invariance. These have been simply transferred from the scalar Nambu-Goldstone bosons to the longitudinal mode of the intermediate weak bosons.

We see that this mechanism associates massive particles to some of the gauge fields (those corresponding to the broken generators) without having to introduce mass terms "by hand" in the Lagrangian. Moreover this mechanism predicts the existence of an additional neutral scalar massive

[16] Because of the local gauge invariance, in every point of the space-time, we can define a local transformation which transforms $\Phi(\mathbf{x})$ in a down isospinor.

[17] Q is the generator of the non-broken $U(1)_{EM}$ group.

boson, which is usually called the Higgs boson (H), with a mass equals to $m_H = \sqrt{-2\mu^2} = \sqrt{2\lambda}\eta$. This mass depends on λ and η. η is related to the intermediate weak bosons masses (as does $\sin\theta_W$) by the relations given in Eq.(1.14). LEP measurements give $\eta \simeq 246$ GeV and $\sin^2\theta_W = 0.23184 \pm 0.00023$. Since the λ parameter is unknown, the mass of the Higgs boson, at this point, is completely undetermined.

To generate the mass of the matter fields, some new gauge invariant terms generating Yukawa couplings must be added to the previous Lagrangian density

$$\mathcal{L}_{Yukawa} = -y^L_{\alpha\beta}\overline{L}_\alpha E_\beta \Phi - y^D_{\alpha\beta}\overline{Q}_\alpha D_\beta \Phi - y^U_{\alpha\beta}\overline{Q}_\alpha U_\beta\ \tilde{\Phi} +\ h.c. \tag{1.17}$$

where the $y^{L,U,D}_{\alpha\beta}$ are the Yukawa matrices and $\tilde{\Phi}$ is defined as $i\tau^2\Phi^\dagger$. When we expand this Lagrangian density after the spontaneous symmetry breaking, the mass term of the fermions appear ($\propto \eta y^i_{\alpha\beta}$) due to the non-vanishing vacuum expectation value η .

The complete Lagrangian density of the Standard Model can now be written

$$\mathcal{L}_{SM} = \quad \mathcal{L}_{gauge} + \quad \mathcal{L}_{Higgs} + \mathcal{L}_{Yukawa} \tag{1.18}$$

The relevance of this Brout-Englert-Higgs mechanism is greatly enhanced by the fact that this non-Abelian spontaneously broken theory is renormalizable and so physical amplitudes can be computed to any given order in the coupling constants, in terms of only a finite number of parameters, namely those contained in the $\mathcal{L}_{SM}$ Lagrangian density.

1.1.5 The Standard Model predictions

The Standard Model has been constructed as a result of numerous efforts both theoretical and experimental. At present, the SM is extraordinary successful, the experimental data agree with its predictions within a precision from 10^{-2} to 10^{-4} [31] [32]. To illustrate this, the combined results of the Global SM fit are shown in Fig. 1.1 [32]. All the particles, except the Higgs boson, have been discovered experimentally (see section 1.1.1). And the Higgs mass is severely constrained from precision electroweak data (see Fig. 1.2 [32]). However the Standard Model has its drawbacks and unsolved problems that we will describe in the next section.

1.1.6 The weaknesses of the Standard Model

Although the Standard Model is extremely predictive, it suffers from the following weak points and unsolved problems. Among them are:

- It does not include the gravity.
- The large number of free parameters. This number can be reduced by embedding $SU(3)_C \otimes SU(2)_L \otimes U(1)_Y$ into a Grand Unification group, e.g. $SU(5)$ or $SO(10)$ (see section 1.2.3).
- The hierarchy problem and the quadratic divergence of the Higgs potential. This can be solved by introducing a cut-off, due to the existence of new particles, at a scale around 1 TeV (see section 1.2.2).
- The formal unification of strong and electroweak unification, i.e. the 3 running coupling constants do not converge at high energy, and Grand Unification, which is commonly believed, is not achieved.

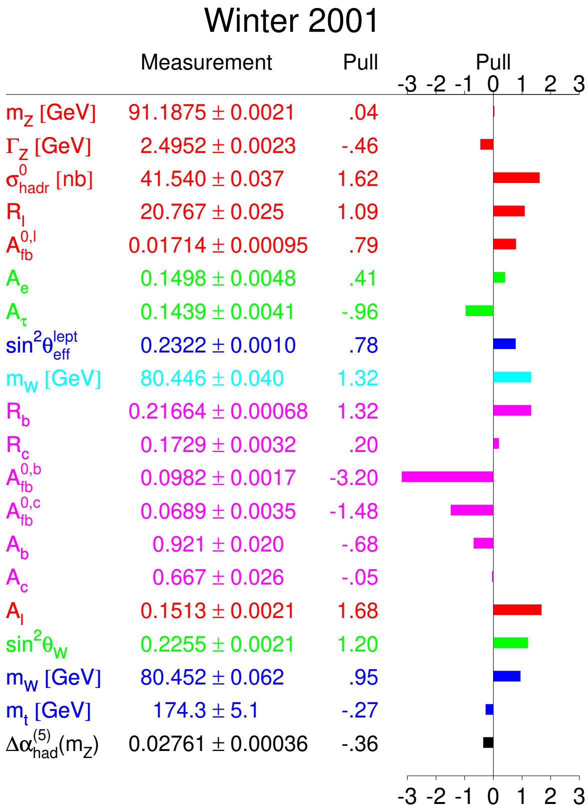

Figure 1.1: Global Fit of the Standard Model. The *pull* is the difference between the measurement and the fitted value, divided by the experimental error.

As already indicated, the answer to these problems lies beyond the SM, and at the present time there are two possible ways to go beyond the SM :

1. To consider fundamental fields with **new** symmetries. This way leads us to supersymmetry, grand unification, string theories, etc.

2. To consider fundamental fields with **new** interactions. This way leads us to compositeness, fermion-antifermions condensates, technicolor, etc.

In what follows we go along the lines of the first possibility and describe supersymmetry as the nearest option for the new physics at the TeV scale.

1.2 Why a Supersymmetric extension of the Standard Model ?

As for the Standard Model, several scientists played an important role in building the model which is called today the Minimal Supersymmetric extension of the Standard Model (MSSM). A review of the origin of the MSSM is given in [34].

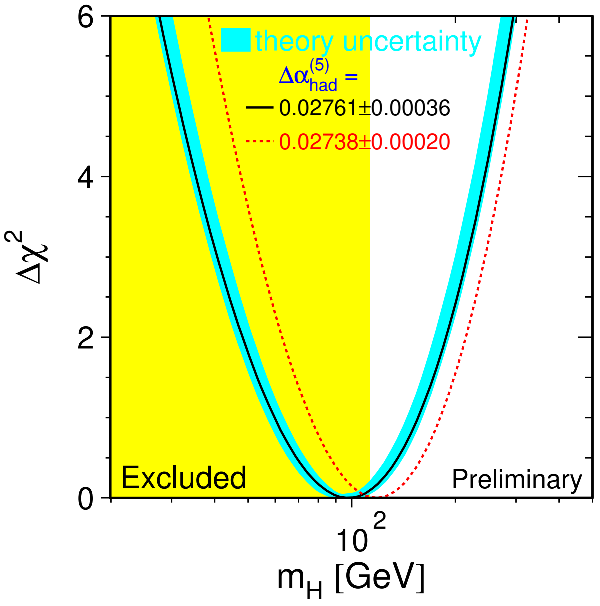

Figure 1.2: $\Delta\chi^2 - \chi^2_{min}$ versus the m_H curve. The line is the result of the fit using all data recorded by LEP; the band represents an estimate of the theoretical error due to missing higher order corrections. The vertical band shows the 95% CL exclusion limit on m_H curve from the direct search at LEP2. The dashed curve is the result obtained using the evaluation of $\Delta\alpha^{(5)}_{had}(m_Z^2)$ from Reference [33].

The supersymmetric (SUSY) theories (i.e. fermion-boson symmetries) were introduced in the years 1971-1973, by three different groups, with quite different motivations. Gol'fand and Likhtman first introduced it in connection with parity-violation in weak interactions. Volkov and Akulov hoped to explain the masslessness of the neutrino from a possible interpretation of the neutrino as a spin-$\frac{1}{2}$ Goldstone particle (responsible of the SUSY breaking) while Wess and Zumino wrote the SUSY algebra by extending to four dimensions the “supergauge” (i.e. supersymmetry) transformations and algebra acting on the two-dimensional string worldsheet. Supersymmetry has not yet been observed in Nature. This is a purely theoretical invention [35]. For Reviews see, e.g. Refs. [36]- [42]. The generic algebraic structure of supersymmetry in four dimensions involves a Majorana[18] spin-$\frac{1}{2}$ fermionic supersymmetry generator Q_M satisfying the (anti)commutation relations [19]:

$$\begin{cases} \{Q_M, \bar{Q}_M\} = 2\gamma^\mu P_\mu \\ [Q_M, P_\mu] = 0 \end{cases} \tag{1.19}$$

This Majorana spin-$\frac{1}{2}$ generator Q_M (and its adjoint $\bar{Q}_M \equiv Q_M^\dagger \gamma^0$) relates fermionic to bosonic fields as

$$Q_M|Boson> \; = \; |Fermion> \quad \text{and} \quad Q_M|Fermion> \; = \; |Boson>$$

[18]Majorana fermions are described in appendix A.

[19]If only one set of supersymmetry generators $(Q_M, \bar{Q}_M)$ is assumed, which is the case in the MSSM.

The presence of the generators of spacetime translations P_μ in the right-handside of the anticommutation relations 1.19 is at the origin of the relation of supersymmetry with general relativity. For completeness, each supermultiplet [20] must contains an equal number of fermionic and bosonic degrees of freedom [42].

In the seventies, physicists attempted to relate known fermions with known bosons (in particular the photon with a neutrino and the $W^\pm$'s with charged leptons [34]). Nevertheless, for several reasons[21], in the MSSM all known particles are associated with new superpartners [43]. In addition, in the MSSM, the electroweak symmetry breaking is induced by a pair of Higgs doublets which implies the existence of charged Higgs bosons and of several neutral ones [43] (see appendix B).

The following sections give some of the key-properties which make the MSSM the best candidate to go beyond the SM.

1.2.1 The MSSM is elegant

First of all, the MSSM is elegant. By definition it connects the bosonic to the fermionic representation and vice versa. As will be seen in section 1.3, the number of categories of fundamental objects (without gravity) is decreased from 3 in ordinary gauge theories (spin-1 gauge bosons interacting with spin-$\frac{1}{2}$ fermions and spin-0 Higgs fields) to 2 in the MSSM gauge theory: (spin-1/spin-$\frac{1}{2}$) supermultiplets of "gauge particles" interacting with (spin-$\frac{1}{2}$/spin-0) "chiral" supermultiplets describing Higgs, lepton and quark superfields. Moreover, in the MSSM, the number of categories of coupling constants gets reduced to 2, namely the gauge and Yukawa couplings.

1.2.2 Solution of the hierarchy problem

The hierarchy problem [44] is present at both classical and quantum levels. At the tree-level, there is a huge difference between the scales associated with the electroweak and the gravitational [22] interactions, $M_W/M_{\rm P} \sim 10^{-17}$. Although this hierarchy is softened when GUTs are considered, it persists since $M_W/M_{GUT} \sim 10^{-13}$. If quantum corrections were not to significantly alter the value of the Higgs (mass)^2, m_H^2, computed classically, one could consider the above mentioned hierarchy at the tree-level as one of the many extreme ratios existing in Nature. However, there are huge quadratic corrections to m_H^2 at the quantum level due to the fact that the Higgs particle is described by a fundamental scalar field. The corrections change the classical value of m_H^2 by many orders of magnitude, and adjusting the value back to its classical one requires a fine-tuning of order 10^{-34} in the case of a gravitational cutoff or of order 10^{-26} in GUTs.

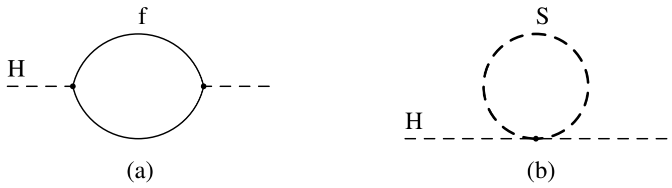

Figure 1.3: Quantum corrections to m_H^2.

More quantitatively, one-loop corrections (Fig. 1.3a) in the SM involve fermions coupling to

[20] A supermultiplet contains the fermionic and bosonic degrees of freedom related by the supersymmetric tranformations.

[21] For instance, in the SM, the number of degrees of freedom is larger for the fermions (90) than for the bosons (27, ignoring the graviton and the not-yet-discovered Higgs boson) and they have different gauge symmetry properties.

[22] $M_{\rm P} = (8\pi G_{\rm Newton})^{-1/2} = 2.4 \times 10^{18}$ GeV is the reduced Planck mass.

the Higgs via the Yukawa interaction term $-\lambda_f H\overline{f}f$. Each Dirac fermion type contributes with a correction which dominant terms are [23]

$$\Delta m_H^2|_f = \frac{|\lambda_f|^2}{8\pi^2}\left[-\Lambda_{\rm UV}^2 + 6m_f^2\ln(\Lambda_{\rm UV}/m_f) + \ldots\right]. \tag{1.20}$$

where $\Lambda_{\rm UV}$ is an ultraviolet momentum cutoff used to regulate the loop integral; it should be interpreted as the energy scale at which new physics enters to alter the high-energy behavior of the SM theory [24]. The leading term in Eq.(1.20) diverges quadratically. This correction is very different from the one obtained, for instance, on the electron mass. For the latter, the divergence is only logarithmic and is proportional to the electron mass itself. Hence it goes to zero in the limit of zero electron mass, which reflects the existence of a symmetry (chiral symmetry) which "protects" the electron mass from acquiring large radiative corrections. The Higgs radiative corrections are not proportional to the mass, which shows that the symmetry of the Lagrangian density is not increased when the Higgs mass goes to zero. If no physical meaning is attached to the scale $\Lambda_{\rm UV}$, the quadratic divergence can be removed by dimensional regularization. But even so, if new (spin-$\frac{1}{2}$) particles exist at some scale below the Planck mass, they will induce large corrections through the second term in 1.20. Altogether, the Higgs mass is extremely sensitive to the heaviest particle to which the H couples and its most "natural" value is close to the largest mass scale in the theory.

If there exists a scalar which couples to the Higgs by a quartic interaction of the form $-\lambda_S|H|^2|S|^2$ (Fig. 1.3b), the corresponding loop correction contributes to the Higgs mass by

$$\Delta m_H^2|_S = \frac{\lambda_S}{16\pi^2}\left[\Lambda_{\rm UV}^2 - 2m_S^2\ln(\Lambda_{\rm UV}/m_S) + \ldots\right]. \tag{1.21}$$

It also generates a quadratic divergence but its sign is opposite to the one of the fermions. It is seen that if every fermion is accompanied by two scalars, with coupling $\lambda_S = \lambda_f^2$, the quadratic divergences cancel exactly. This relation between the coupling and hence the cancellation is provided by the MSSM [46].

The contribution remaining after the cancellation can also be evaluated. This yields a contribution without quadratic divergence and with a leading term in $m_f^2\ln(\Lambda_{\rm UV}/m_S)$. If the two scalars are assumed to have the same mass, and in the approximation where the mass difference between the fermion and the scalars is small, the total correction is reduced to

$$\Delta m_H^2|_{tot} \simeq \frac{\lambda_f^2}{4\pi^2}(m_S^2 - m_f^2)\ln(\Lambda_{\rm UV}/m_S) \tag{1.22}$$

The resulting radiative correction is logarithmic and proportional to the mass-squared difference, reflecting the additional symmetry imposed on the couplings. The particles running in the loop can now be really heavy. Moreover, if one requires that the radiative corrections be not much larger than the masses themselves, one obtains a constraint on $m_S \equiv M_{SUSY}$

$$M_{SUSY} \leq 10^3 \mathrm{GeV}/c^2 \tag{1.23}$$

1.2.3 Unification of the gauge couplings.

The philosophy of Grand Unification is based on a *hypothesis*: Gauge symmetry increases with energy. Having in mind unification of all forces of Nature and neglecting gravity for the time being due

[23]The proof of the following digression can be found in [45].

[24]In other terms, the ∞ in the one-loop integral is replaced by the cutoff $\Lambda_{\rm UV}$, namely $M_{\rm P}$ or M_{GUT}.

to its weakness, the idea of GUTs is the following: All known interactions are different branches of a unique interaction associated with a single gauge group. The unification occurs at high energy.

$$\begin{array}{cccccc} & \text{Low energy} & & \Rightarrow & \text{High energy } (\Lambda) \\ SU(3)_C \otimes & SU(2)_L \otimes & U(1)_Y & \Rightarrow & G_{GUT} \\ \text{gluons} & W, Z & \text{photon} & \Rightarrow & \text{gauge bosons} \\ \text{quarks} & \text{leptons} & & \Rightarrow & \text{fermions} \\ g_S & g & g' & \Rightarrow & g_{GUT} \end{array}$$

At first sight this is impossible due to the big difference in the values of the coupling of strong, weak and electromagnetic interactions. However, this is not so. The crucial point here is the running coupling constant. It is a generic property of Quantum Field Theory (QFT) which has an analogy in classical physics. Indeed consider electric and magnetic phenomena. Let us take some dielectric medium and put a simple charge in it. What happens is that the medium is polarized. It contains electric dipoles which are arranged in such way as to screen the charge (see Fig. 1.4). It is a consequence of the Coulomb law: attraction of the opposite charges and repulsion of the same ones. This is the origin of the electric screening. The opposite situation occurs in magnetic medium. According to the Biot-Savart law, electric currents of the same direction are attracted to each other, while those of the opposite one are repulsed (see Fig. 1.4). This lead to anti-screening of electric currents in magnetic fields.

In QFT the role of the medium is played by the vacuum. Vacuum is polarized due to the presence of virtual pairs of particles in it. The matter fields and transverse quanta of the vector fields, in this case, behave like dipoles, while the longitudinal quanta of the vector fields behave like currents and these two effects compete with each other [47].

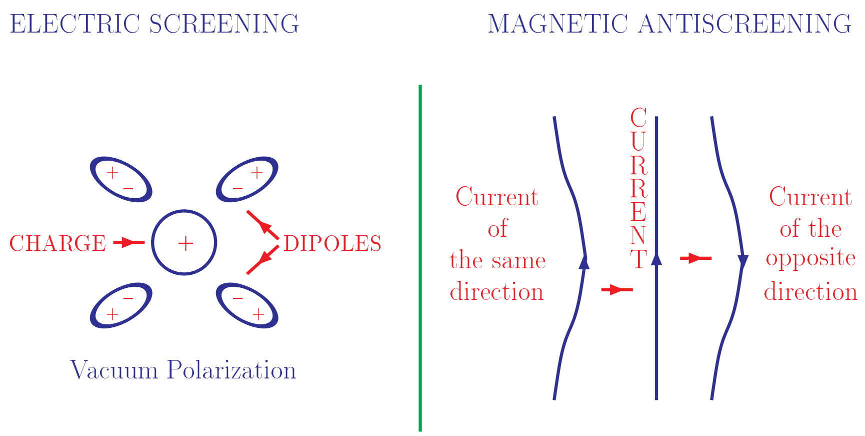

Figure 1.4: Electric screening and magnetic anti-screening.

Thus the couplings become functions of a distance or an energy scale

$$\alpha_i = \alpha_i(\frac{Q^2}{\mu^2}) = \alpha_i(distance) \tag{1.24}$$

with

$$\left\{ \begin{array}{lllll} \alpha_1 & = & (5/3)g'^2/4\pi & = & 5\alpha/(3cos^2\theta_W) \\ \alpha_2 & = & g^2/4\pi & = & \alpha/sin^2\theta_W \\ \alpha_3 & = & g_S^2/4\pi & & \end{array} \right. \tag{1.25}$$

where α is the fine structure constant, θ_W the electroweak mixing angle, Q is the energy scale of the interaction and μ is the input parameter (energy scale) at which renormalization was performed. The factor 5/3 in the definition of α_1 is included for proper normalization (to obtain a common electric charge for all fermions at the GUT scale).

This dependence is described by the Renormalization Group Equations (RGE) [20] and is confirmed experimentally (see Fig. 1.5 for the running of α_S and section 1.1).

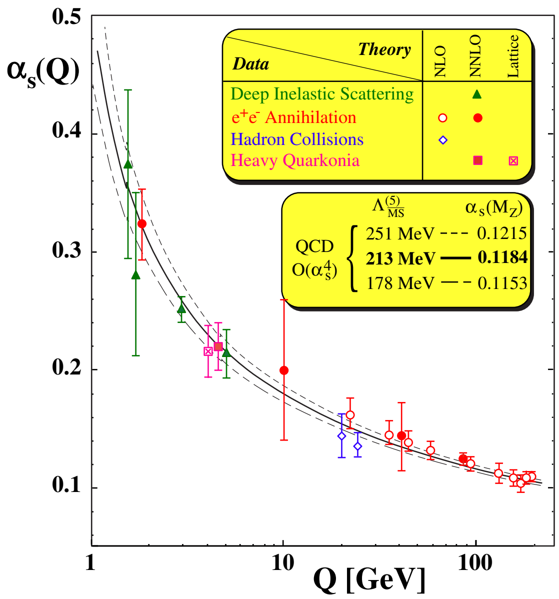

Figure 1.5: Summary of the running of the strong coupling α_S [48].

Assuming that there is a desert above the E.W. scale until the Planck scale, one can use the RGEs for the three couplings. At first order they are the following:

$$\frac{d\alpha_i}{dt} = b_i {\alpha_i}^2 \text{ with } t = \log\left(\frac{Q^2}{\mu^2}\right) \tag{1.26}$$

where the SM b_i coefficients are (41/10, -19/6, -7). The solution of Eq.(1.26) is :

$$\frac{1}{\alpha_i(Q^2)} = \frac{1}{\alpha_i(\mu^2)} - b_i \log\left(\frac{Q^2}{\mu^2}\right) \tag{1.27}$$

Fig. 1.6 Shows the evolution of the inverse of the three coupling constants as a function of the logarithm of the energy. In this presentation, the evolution becomes a straight line in the first order. The second order corrections are small and do not cause any visible deviation from a straight line. Fig. 1.6 clearly demonstrates that within the SM no unification is achieved (unification is excluded by 8 standard deviations). This result means that unification can only be achieved if new physics enters between the electroweak and the Planck scale.

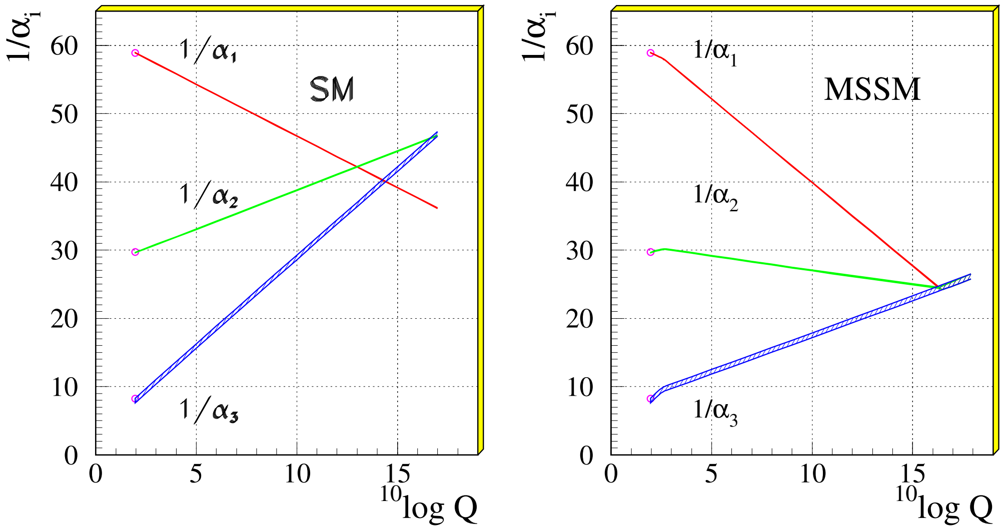

Figure 1.6: Evolution of the inverse of the three coupling constants in the Standard Model (left) and in the supersymmetric extension of the SM (MSSM) (right). Only in the latter case unification is achieved. The SUSY particles are assumed to contribute only above the effective SUSY scale M_{SUSY} of about 1 TeV, which causes a change in the slope in the evolution of couplings. The thickness of the lines represents the error in the coupling constants [49].

In the MSSM the b_i's are equal to (33/5,1, -3). It has to be emphasized that the b_i's depend on the number of generations of matter multiplets, the number of Higgs doublets and the gauge field content of the Theory but not on assumptions about the unification group. This is why their values change in the MSSM scheme where we introduce superpartners and two Higgs doublets.

It turns out that within the SUSY model a perfect unification can be obtained if the SUSY masses are of order of 1 TeV. This is shown in Fig. 1.6(right) where the SUSY particles are assumed to effectively contribute to the running of the couplings only for energies above the typical SUSY mass scale, which causes the changes in the slope of the lines near 1 TeV. From the fit requiring unification one finds for the break point M_{SUSY} and the unification point M_{GUT} [49] (updated results can be found in [50] [51])

$$\left\{ \begin{array}{ccc} M_{SUSY} & = & 10^{3.4\pm0,9\pm0.4}\mathrm{GeV} \\ M_{GUT} & = & 10^{15.8\pm0.3\pm0.1}\mathrm{GeV} \\ \alpha_{GUT}^{-1} & = & 26.3\pm1.9\pm1.0 \end{array} \right. \tag{1.28}$$

where $\alpha_{GUT} = g_5^2/4\pi$. The first error originates from the uncertainty in the coupling constants while the second one is due to the uncertainty in the mass splittings between the SUSY particles. The χ^2 distributions of M_{SUSY} and M_{GUT} are shown in Fig. 1.7 [49], where

$$\chi^2 = \sum_{i=1}^{3} \frac{(\alpha_i^{-1} - \alpha_{GUT}^{-1})^2}{\sigma_i^2} \tag{1.29}$$

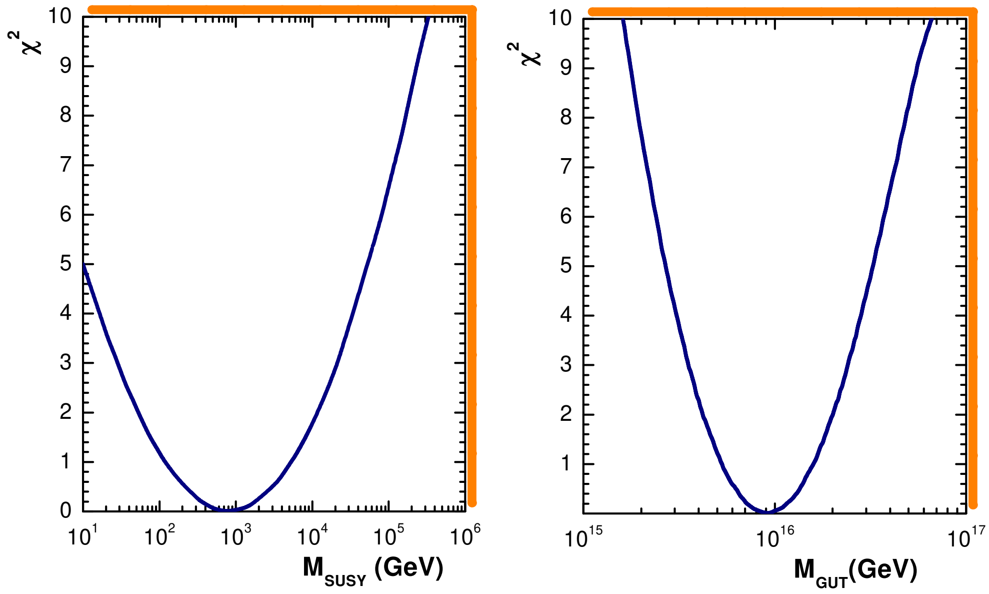

Figure 1.7: The χ^2 distribution of M_{SUSY} and M_{GUT}

As we see, according to this fit:

- unification occurs below the Planck scale. This is important since above the Planck scale gravitational interactions could no longer be neglected,
- the unified coupling amounts to $\alpha_{GUT} \simeq 1/26$, well inside the perturbative regime.

For many physicists this fit was the first indirect evidence for supersymmetry since M_{SUSY} was found in the range where the fine-tuning problem does not reappear (see Eq.(1.23)). It should be noted that the unification of the three curves at a single point is not as trivial as it may seem from the existence of three parameters (M_{SUSY}, M_{GUT} and α_{GUT}). Out of several models tried only a handful yielded unification. The reason is simple: introducing new particles one influences all three curves simultaneously, thus giving rise to strong correlations between the slopes of the three lines. For example, in the MSSM, if we use four doublets instead of two [25], we never achieve unification. Nevertheless unification does not prove supersymmetry. The real proof would be the observation of the sparticles.

1.2.4 Unification with gravity

The graviton has spin 2 while the other gauge bosons have spin 1. Therefore, they correspond to different representations of the Poincaré algebra. Attempts to unify all four forces within the same

[25] An even number of Higgs doublets is mandatory to generate the chargino mass eigenstates.

algebra face a problem. Due to the no-go theorems [52], unification of spin 2 and spin 1 gauge fields within the same unique algebra is forbidden. The only evasions from this theorem are, for the time being, the supersymmetry algebras. Since the SUSY models use anti-commutating generators, they are not forbidden by the no-go theorems which were proven assuming only commutation relations between internal symmetry generators. Using the relation (in four dimensions)

$$\{Q_M, \bar{Q}_M\} = 2\gamma^\mu P_\mu$$

and taking infinitesimal transformations $\delta_{\bar{\epsilon}} = \bar{\epsilon}^\alpha (Q_M)_\alpha$, $\bar{\delta}_\epsilon = (\bar{Q}_M)_\alpha \epsilon^\alpha$ with $\alpha = 1..4$, one gets

$$\{\delta_{\bar{\epsilon}}, \bar{\delta}_\epsilon\} = 2\bar{\epsilon}\gamma^\mu \epsilon P_\mu \tag{1.30}$$

where ϵ is a 4-dimensional transformation parameter ($\bar{\epsilon} = \epsilon^T \gamma_0$). Choosing ϵ to be local, i.e. function of the space-time, one finds from Eq.(1.30) that an anticommutator of two SUSY transformations is a local coordinate translation. Thus, making SUSY local, one may obtain General Relativity, or a theory of gravity [53].

1.3 MSSM particle content

The following section relies mainly on and follows the same conventions of the primer of S. Martin [42] and the summer school lecture of L. Pape [54]. For the interested readers, Appendix A describes Dirac, Weyl and Majorana fermions in more details and gives the conventions chosen for the present work.

Supersymmetry is a symmetry which relates fermions and bosons. A bosonic state is transformed into a fermionic state and vice versa by an anticommuting Majorana spinorial operator Q_M (The MSSM is based on a SUSY N=1 model, i.e. one generation of $(Q_M, \bar{Q}_M)$)

$$Q_M|B>=|F>; \quad Q_M|F>=|B> \tag{1.31}$$

where the boson B and the fermion F differ by one half in spin. The fermionic operators Q_M and $\bar{Q}_M$ carry spin angular momentum $\frac{1}{2}$. They satisfy an algebra of anticommutation and commutation equations:

$$\begin{aligned} &\{Q_M, \bar{Q}_M\} = 2\gamma^\mu P_\mu \\ &\{Q_M, Q_M\} = \{\bar{Q}_M, \bar{Q}_M\} = 0 \\ &[P^\mu, Q_M] = [P^\mu, \bar{Q}_M] = [P^2, Q_M] = [P^2, \bar{Q}_M] = 0 \end{aligned} \tag{1.32}$$

In supersymmetry, the single particle states fall into irreductible representations of the supersymmetric algebra called *supermultiplets*. Hence, a supermultiplet consists of both fermions and bosons differing by 1/2 unit of spin. All members of a supermultiplet have the same momentum and hence the same mass. The supersymmetry generators commute with the generator of gauge transformations. Therefore all members of a supermultiplet are in the same representation of the gauge groups and have identical charge and colour. Furthermore, the number of bosonic degrees of freedom, n_B, and the number of fermionic degrees of freedom, n_F, in a supermultiplet are equal ($n_B = n_F$) and all the particles/bosons and their superpartners can be classified into 2 kinds of supermultiplets:

Chiral supermultiplet

An on-shell (i.e. satisfying its equation of motion) Standard Model [26] fermion corresponds to a Weyl fermion with one degree of freedom [27] (e.g. the left-handed electron). It is via supersymmetry accompanied by one scalar particle (i.e. spin 0). To obtain a Lorentz invariant theory it is necessary to include also the charge conjugate representation which has a Weyl anti-fermion with opposite helicity (e.g, the right-handed anti-electron) and another scalar. Together these two representations constitute a complex Weyl fermion and a complex scalar field (e.g. $(e_L, \tilde{e}_L)$) which is called **chiral or matter supermultiplet**. The left(right)- and right(left)-handed (anti-)fermions have different gauge and Lorentz transformation properties and so belong to separate chiral supermultiplets. Therefore, each has its own complex scalar partner, with the same name preceded by "s" (e.g. selectron). In the notation they are referred to by the subscripts "L" and "R", like their fermionic partners, although they have spin 0 , e.g. (e_L, $\tilde{e}_L \equiv$ selectron-left).

Higgs bosons are defined as complex spin 0 fields and also reside in chiral supermultiplets. Their fermionic partners are called "higgsinos" [28]. In supersymmetric models one needs (at least) two Higgs doublets, $H_u(H_u^+, H_u^0)$ and $H_d(H_d^0, H_d^-)$ (so 8 degrees of freedom) in order to provide masses to up- and down-type particles, but they are also required in order to cancel triangle gauge anomalies [42] and provide enough fermionic degrees of freedom to generate the chargino and neutralino mass eigenstates.

All the chiral supermultiplets of the MSSM are summarized in Table 1.2 where all chiral supermultiplets are defined in terms of left-handed Weyl spinors, so that the *conjugates* of the right-handed quarks and leptons (and their superpartners) appear in the Table (see Appendix A). Indices on colour and lepton/quark families have been omitted in the Table.

Names		spin 0	spin 1/2	$SU(3)_C$, $SU(2)_L$, $U(1)_Y$
squarks, quarks	Q	$(\widetilde{u}_L\ \ \widetilde{d}_L)$	$(u_L\ \ d_L)$	$(\,\mathbf{3},\ \mathbf{2}\,,\ \frac{1}{3})$
(×3 families)	$\overline{u}$	$\widetilde{u}_R^*$	$u_R^\dagger$	$(\,\overline{\mathbf{3}},\ \mathbf{1},\ -\frac{4}{3})$
	$\overline{d}$	$\widetilde{d}_R^*$	$d_R^\dagger$	$(\,\overline{\mathbf{3}},\ \mathbf{1},\ \frac{2}{3})$
sleptons, leptons	L	$(\widetilde{\nu}\ \widetilde{e}_L)$	$(\nu\ \ e_L)$	$(\,\mathbf{1},\ \mathbf{2}\,,\ -1)$
(×3 families)	$\overline{e}$	$\widetilde{e}_R^*$	$e_R^\dagger$	$(\,\mathbf{1},\ \mathbf{1},\ 2)$
Higgs, higgsinos	H_u	$(H_u^+\ \ H_u^0)$	$(\widetilde{H}_u^+\ \ \widetilde{H}_u^0)$	$(\,\mathbf{1},\ \mathbf{2}\,,\ +1)$
	H_d	$(H_d^0\ \ H_d^-)$	$(\widetilde{H}_d^0\ \ \widetilde{H}_d^-)$	$(\,\mathbf{1},\ \mathbf{2}\,,\ -1)$

Table 1.2: Chiral supermultiplets in the Minimal Supersymmetric Standard Model.

Vector supermultiplet

A SM gauge boson corresponds to a vector field. If the gauge symmetry is unbroken, this spin-1

[26] The following digression assumes massless fermions.

[27] The Weyl representation permits to separate a Dirac spinor into Left and Right Weyl spinors, so to have a Dirac spinor one needs two Weyl spinors.

[28] The –ino suffix was invented by Pierre Fayet.

boson is massless and has only two helicity states. Gauge bosons transform as the adjoint representation of their gauge group and their fermionic partners must be in the same representation. Since the adjoint representation is its own conjugate, the left– and right–handed components of these fermions must have the same gauge transformation properties, hence not allowing for chiral fermions. Secondly the gauge bosons are neutral (before applying transformation defined in Eq.(1.15)) so the superpartners are described by a Majorana spinor with two degrees of freedom (here, the helicities). This is called **vector or gauge supermultiplet** and the superpartners are called **gauginos** which include the 8 gluinos $\tilde{g}^a$, from $SU(3)_C$, the 3 winos, $\tilde{W}^i$, from $SU(2)_L$ and the bino, $\tilde{B}$, from $U(1)_Y$. The complete list of the MSSM vector supermultiplets is given in Table 1.3.

Names	spin 1/2	spin 1	$SU(3)_C,\ SU(2)_L,\ U(1)_Y$
gluino, gluon	$\widetilde{g}^a$	g^a	$(\,\mathbf{8},\ \mathbf{1}\,,\ 0)$
winos, W bosons	$\widetilde{W}^i$	W^i	$(\,\mathbf{1},\ \mathbf{3}\,,\ 0)$
bino, B boson	$\widetilde{B}$	B	$(\,\mathbf{1},\ \mathbf{1}\,,\ 0)$

Table 1.3: Gauge supermultiplets in the Minimal Supersymmetric Standard Model.

After the spontaneous symmetry breaking of $SU(2)_L \otimes U(1)_Y$ to $U(1)_{EM}$, W^3 and B mix to form the Z^0 and the γ. The corresponding mixtures of their superpartners $\tilde{W}^3$ and $\tilde{B}$ are called the zino ($\tilde{Z}^0$) and the photino ($\tilde{\gamma}$). Moreover, the gauginos will mix with the higgsinos and give rise to mass eigenstates which are called:

- charginos from mixing of $\tilde{W}^{1-2}$ and $\tilde{H}^{\pm}$, leading to two states $\tilde{\chi}^{\pm}_{1-2}$ (Dirac fermions);
- neutralinos from mixing of $\tilde{W}^3$, $\tilde{B}$, $\tilde{H}^0_d$ and $\tilde{H}^0_u$, leading to four states $\tilde{\chi}^0_{1-4}$ (Majorana fermions)

1.4 From SM to MSSM interactions

The trilinear gauge interactions in the MSSM can be derived from the SM ones in the following way. The SM particles and their superpartners have the same gauge properties and hence should couple with the same strength. The MSSM interaction terms can be inferred from the SM ones by replacing the SM particles by their superpartners. However, as they differ by 1/2 unit in spin, the resulting interaction term can only remain scalar in spin space if the replacement is done in pairs. The convention used for the fields is that: chiral supermultiplets consist of field (ψ,ϕ) where ψ is the fermion and ϕ is the complex scalar; vector supermultiplets contains (A,λ), where A stands for the gauge boson and λ for the gaugino. The interactions vertices will be labeled by the fields only, ignoring their space-time structure as it will not be needed in the following. The SM gauge coupling between a boson and a fermion pair is written as ($A\psi\psi$) and using the above replacement rule, is completed in the MSSM by couplings ($A\phi\phi$) and ($\lambda\phi\psi$) with the same coupling constant (within a factor $\sqrt{2}$). For example, the ($W^{\pm}\mathrm{e}_L\nu$) vertex in the SM is accompanied in the MSSM by the ($W^{\pm}\tilde{\mathrm{e}}_L\tilde{\nu}$),($\tilde{W}^{\pm}\tilde{\mathrm{e}}_L\nu$) and ($\tilde{W}^{\pm}\mathrm{e}_L\tilde{\nu}$) vertices. Similarly, the SM vertex (AAA) gives rise to a ($A\lambda\lambda$) coupling. It has to be emphasized that to preserve the invariance of the Lagrangian density under supersymmetric transformations, additional quadrilinear terms are necessary. For instance, the vertex photino-electron-selectron implies a quadrilinear vertex with 4 selectrons.The complete set of trilinear gauge couplings is illustrated in Fig. 1.8

For the electroweak interactions, the couplings strengths are summarized as:

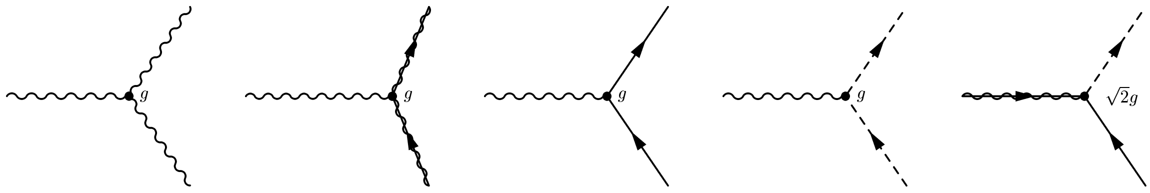

(AAA) $(A\lambda\lambda)$ $(A\psi\psi)$ $(A\phi\phi)$ $(\lambda\phi\psi)$

Figure 1.8: MSSM trilinear gauge interactions. Full lines represent fermions, dashed lines scalars, wiggly lines vector bosons and wiggly+full lines gauginos.

$$W^{\pm}(\tilde{W}^{\pm}) \propto gT^{\pm} \text{ where } T^{\pm} = \frac{T^1 \mp iT^2}{2} \tag{1.33}$$

$$\gamma(\tilde{\gamma}) \propto eQ = g \ \ sin\theta_W Q \tag{1.34}$$

$$Z^0(\tilde{Z}^0) \propto g(T^3 - Qsin^2\theta_W) \tag{1.35}$$

The charged wino, like the $W^{\pm}$, couples to the third component of the weak isospin; the photino, like the photon, couples to the electric charge; the zino couples to the same combination of isospin and charge as the Z^0. The same replacement rule can be applied to SM Yukawa interactions. For example, the $(h_e \mathrm{e}_R^{\dagger} \mathrm{e}_L H_d^0)$ coupling which induces a mass for the electron in the SM, leads to couplings $(h_e \mathrm{e}_R^{\dagger} \tilde{\mathrm{e}}_L \tilde{H}_d^0)$ and $(h_e \tilde{\mathrm{e}}_R^{*} \mathrm{e}_L \tilde{H}_d^0)$ in the MSSM defined by the same Yukawa coupling. It could be naively expected to also give a vertex like $(h_e \tilde{\mathrm{e}}_L \tilde{\mathrm{e}}_R^{*} H_d^0)$. This however, does not exist as it has the wrong dimensionality. It is easily seen from the kinetic terms that the dimensionality of fermions is $(E)^{3/2}$ and that for scalar and vector bosons is $(E)^1$. Such a term could enter the Lagrangian density provided it is multiplied by a constant with dimension of a mass, which is actually the case in the MSSM (see later). Weak isospin invariance implies the existence of a $(-h_e \mathrm{e}_R^{\dagger} \nu H_d^-)$ term. Supersymmetry then requires the terms $(-h_e \mathrm{e}_R^{\dagger} \tilde{\nu} \tilde{H}_d^-)$ and $(-h_e \tilde{\mathrm{e}}_R^{*} \nu \tilde{H}_d^-)$.

After the electroweak symmetry breaking, both Higgs fields H_d and H_u acquire vacuum expectation values (vev), respectively v_d and v_u. The mass of the up– and down–type fermions are obtained from the Yukawa terms $(h_d v_d d_R^{\dagger} d_L)$ and $(h_u v_u u_R^{\dagger} u_L)$. The vev $\eta = \sqrt{v_d^2 + v_u^2}$, which plays the same role as the SM Higgs vev, is determined by the vector boson mass, $\eta = 2\frac{M_{W^{\pm}}}{g} \simeq 246\mathrm{GeV}$. The remaining free parameter is defined as $\tan\beta = v_u/v_d$, the ratio of Higgs expectation values. The Yukawa couplings are then given in terms of the particle masses by

$$h_u = \frac{m_u}{\eta \sin\beta}, h_d = \frac{m_d}{\eta \cos\beta} \tag{1.36}$$

where u and d stand for the up–type and down–type particles. Unlike in the SM, the Yukawa couplings of the MSSM are not uniquely determined by the fermion masses, but depend also on the parameter $\tan\beta$.

1.5 The MSSM Lagrangian density

Once the supermultiplets and their gauge transformation properties are defined, the gauge interactions in the Lagrangian density are fully determined (as $\mathcal{L}_{gauge}$ is). Some freedom remains only in the specification of the potential and the Yukawa couplings. In this section, the basic formulas will be stated without justification. The reader may be interested to look at the more rigorous derivation in [42].

1.5.1 Kinetic terms and gauge interactions

The part of the Lagrangian density (invariant under supersymmetric transformations) describing the kinetic terms and the interactions of matter fields with gauge and gaugino fields is given by

$$\begin{aligned}\mathcal{L}_{gauge} = & - \mathcal{D}^{\mu}\phi^{*i}\mathcal{D}_{\mu}\phi_i - i\psi^{\dagger i}\bar{\sigma}^{\mu}\mathcal{D}_{\mu}\psi_i \\ & - \frac{1}{4}F^{a}_{\mu\nu}F^{\mu\nu a} - i\lambda^{\dagger a}\bar{\sigma}^{\mu}\mathcal{D}_{\mu}\lambda^{a} \\ & - \sqrt{2}g[(\phi^{*i}T^{a}\psi_i)\lambda^{a} + \lambda^{\dagger a}(\psi^{\dagger i}T^{a}\phi_i)]\end{aligned} \tag{1.37}$$

The first line, with covariant derivatives defined by

$$\begin{aligned}\mathcal{D}_{\mu}\phi_i = \partial_{\mu}\phi_i + igA^{a}_{\mu}(T^{a}\phi)_i \\ \mathcal{D}_{\mu}\psi_i = \partial_{\mu}\psi_i + igA^{a}_{\mu}(T^{a}\psi)_i\end{aligned} \tag{1.38}$$

contains the kinetic terms for the complex scalar and the two-component fermionic matter fields, as well as their interactions with the gauge bosons. The latter include the trilinear couplings called ($A\psi\psi$) and ($A\phi\phi$) in section 1.4, together with a quartic interaction between the scalars and gauge bosons. The second line contains the usual Yang-Mills field strength

$$F^{a}_{\mu\nu} = \partial_{\mu}A^{a}_{\nu} - \partial_{\nu}A^{a}_{\mu} - gf^{abc}A^{b}_{\mu}A^{c}_{\nu} \tag{1.39}$$

which leads to the kinetic terms of the gauge fields, the trilinear interactions called (AAA) in section 1.4 and a quartic interaction of the gauge bosons. The second term, with covariant derivative

$$\mathcal{D}_{\mu}\lambda^{a} = \partial_{\mu}\lambda^{a} - gf^{abc}A^{b}_{\mu}\lambda^{c} \tag{1.40}$$

yields the kinetic term for the gauginos and their trilinear interactions called ($A\lambda\lambda$) in section 1.4. The third line corresponds to the trilinear interactions called ($\lambda\phi\psi$) in section 1.4 which ensure $\mathcal{L}_{gauge}$ to be invariant under supersymmetric transformations [42]. We remark that this supersymmetric $\mathcal{L}_{gauge}$ contains the SM $\mathcal{L}_{gauge}$ defined in Eq.(1.2) plus the kinetic and gauge interaction terms of the Higgs sector which were previously included in $\mathcal{L}_{Higgs}$ defined in Eq.(1.11).

1.5.2 The MSSM superpotential

The potential and Yukawa interactions of the MSSM Lagrangian density can be derived from a function called *superpotential*. Its form is constrained by the requirement of invariance under supersymmetric transformation, gauge invariance and conservation of the R-parity :

$$W = \sum_{ij}\epsilon_{ij}(-\tilde{e}^{*}_{R}\ \mathbf{h_L}\tilde{L}^{i}H^{j}_{d} - \tilde{d}^{*}_{R}\ \mathbf{h_D}\tilde{Q}^{i}H^{j}_{d} + \tilde{u}^{*}_{R}\ \mathbf{h_U}\tilde{Q}^{i}H^{j}_{u} + \mu H^{i}_{u}H^{j}_{d}) \tag{1.41}$$

with i, j being isospin indices, $\epsilon_{ij} = -\epsilon_{ji}$ ($\epsilon_{12} = 1$). The objects H_u, H_d, $\tilde{L}$, $\tilde{Q}$ are the $SU(2)_L$ doublets defined in Table 1.2. $\mathbf{h_{U,D,L}}$ are the dimensionless Yukawa coupling parameters. They are 3 $\times$ 3 matrices in the family space which determine the masses and CKM mixing angles of the ordinary quarks and leptons. In the superpotential definition, the $SU(3)_C$ color indices are implicitly supposed to be summed. The minus signs in the superpotential were chosen to produce positive contributions to the mass terms of down–type particles. This is the most general form consistent with gauge invariance and conserving R–parity (R_p). R–parity is a multiplicative quantum number defined as

$$R_p = (-1)^{2S+3B+L} \tag{1.42}$$

where L and B are the lepton and baryon numbers and S is the spin quantum number. Particles within the same supermultiplet do not have the same R–parity. The R–parity is +1 for the ordinary particles (fermions, gauge bosons and Higgs bosons) and –1 for their supersymmetric partners. In this framework, conservation of R–parity implies the conservation of lepton and baryon numbers.

The most obvious experimental constraint to the possible existence of terms violating the lepton and baryon numbers, hence violating R–parity, comes from the non–observation of fast proton decay. In the case of SUSY models with R–parity violation [29], the lifetime of the proton would be measured in a fraction of second. For example, the proton could decay into e$^+$ π^0 or e$^+$ K^0, etc.

The conservation of R–parity has important phenomenological consequences:

- The SUSY particles are always produced in pairs.
- In the decay products of the SUSY particles there is always an odd number of SUSY particles.
- The lightest supersymmetric particle (LSP) is stable since its decay into ordinary particles would change R–parity. If the LSP is electrically neutral, it interacts only weakly with ordinary matter, and is therefore an appealing candidate for the non–baryonic dark matter.

Once the superpotential is specified, it is possible to derive the contribution to the potential in the MSSM Lagrangian density.

1.5.3 The MSSM Lagrangian density for chiral fields

Apart from the kinetic and gauge interaction terms present in $\mathcal{L}_{gauge}$, the contribution to the Lagrangian density for chiral fermions is

$$\mathcal{L}_{chiral} = -\frac{1}{2}\frac{\partial^2 W}{\partial\phi_i \partial\phi_j}\psi_i\psi_j + h.c. \tag{1.43}$$

with ϕ_i the spin–0 partner of the ψ_i fermionic field. It generates Yukawa interactions and fermion mass terms. For example, this yields for the first leptonic family (ignoring the off-diagonal elements of the Yukawa matrices) the following interaction terms:

$$\begin{aligned}\mathcal{L}_{chiral,e} = -\frac{h_e}{2}[&(\mathrm{e}_L\mathrm{e}_R^\dagger)H_d^0 + (\mathrm{e}_R^\dagger\tilde{H}_d^0)\tilde{\mathrm{e}}_L + (\mathrm{e}_L\tilde{H}_d^0)\tilde{\mathrm{e}}_R^* \\ &-(\nu\mathrm{e}_R^\dagger)H_d^- - (\mathrm{e}_R^\dagger\tilde{H}_d^-)\tilde{\nu} - (\tilde{\nu}\tilde{H}_d^-)\tilde{\mathrm{e}}_R^*] + h.c.\end{aligned} \tag{1.44}$$

[29] Some R–parity violating models assume only one violating term at once, avoiding fast proton decay.

It contains the trilinear Yukawa interactions between fermions, scalar and a Higgs or Higgsino. The first term reproduces the familiar SM Yukawa interaction and will generate a mass for the fermions after electroweak symmetry breaking. The others correspond to new interactions, but do not introduce new parameters. In addition, there is a contribution from the μ–term in the superpotential:

$$\mu(\tilde{H}_d^0 \tilde{H}_u^0 - \tilde{H}_d^- \tilde{H}_u^+) + c.c. \tag{1.45}$$

providing off-diagonal elements in the mass matrices for the higgsino fermions. In consequence, the physical states will be mixtures of the higgsino fields $\tilde{H}_u$ and $\tilde{H}_d$.

1.5.4 The MSSM scalar potential

It is also possible to derive the *scalar potential*. This includes two contributions

$$\begin{cases} F^i &= \dfrac{\partial W}{\partial \phi_i} \\ D^a &= -g\phi^{*i} T^a_{ij} \phi^j \end{cases} \tag{1.46}$$

The first term is called the chiral contribution, called *F-term*, the second one is the gauge contribution called *D-term*, with T^a_{ij} being the generators of the gauge groups. The full scalar potential is then (summation implied) :

$$V(\phi_i, \phi_i^*) = F^i F_i^* + \frac{1}{2} D^a D_a \tag{1.47}$$

The fields F_i and D^a are called *auxiliary fields*. They originate from the fact that the matching of degrees of freedom discussed in section 1.3 holds only when the particles are on–shell, whereas the theory should be able to cope with the off–shell case as well. In the chiral supermultiplet, the Weyl spinor is a complex two–component, so off-shell it acquires two more degrees of freedom than on–shell. The matching of the degrees of freedom is achieved by the introduction of another two scalar degrees of freedom, a complex scalar field called F_i. In the gauge supermultiplet, the fermion also acquires two more degrees of freedom while the vector field acquires only an additional one (the longitudinal component). The matching is obtained by introducing a real scalar field D^a. These auxiliary fields should not affect the physics on-shell. This is achieved by not giving them a kinetic term in the Lagrangian density. After working out the classical equation of motion, the auxiliary field F_i and D^a can be expressed in terms of the scalar fields (Eq.(1.46)). Actually, Eq.(1.47) is not the most general form of the MSSM scalar potential. In fact, when considering an Abelian gauge symmetry, the hypercharge in the MSSM, one can introduce in the Lagrangian density a term linear in the corresponding auxiliary field of the gauge supermultiplet. Fayet and Iliopoulos considered this hypothesis in order to generate a spontaneous supersymmetry breaking mechanism [55]. The contribution to the Lagrangian was

$$\mathcal{L}_{Fayet-Iliopoulos} = \kappa D \tag{1.48}$$

where κ is a constant parameter with dimension of (mass)^2. This term is gauge-invariant and supersymmetric by itself. Under certain conditions, D may get a non-zero vev proportional to κ, depending on the other interactions of the scalar fields that are charged under this Abelian group. Nevertheless, the scenario where one assumed that this term was related to the hypercharge led for some sparticles to a negative (mass)^2 splitting since it was proportional to the electric charge [43], hence not satisfying the goal of generating positive mass contributions. In order to cure this, Fayet [43] used an extra $U(1)$ gauge symmetry but this did not cure the problem of generating masses in the gaugino sector [30] owing the continuous R-invariance [31]. Moreover, this new local symmetry induced new the triangle gauge anomalies. R-parity, the Z_2 remnant of the continuous R-symmetry (Eq.(1.42)), had to be postulated instead, and more complex models generating the masses by means of the supergravity or radiative corrections in connection with a hidden sector had to be considered (see section 1.6).

The F-term contribution from the Yukawa interactions to the scalar potential leads to quartic terms, for example

$$V_e = |h_e \tilde{e}^*_R H^0_d|^2 + |h_e \tilde{e}_L H^0_d|^2 + |h_e \tilde{e}_L \tilde{e}^*_R|^2 + |h_e \tilde{e}^*_R H^-_d|^2 + |h_e \tilde{\nu} H^-_d|^2 + |h_e \tilde{\nu} \tilde{e}^*_R|^2 \tag{1.49}$$

which do not have their equivalent in the Standard Model. The first two contribute to (mass)^2 terms for the left and right scalars. The third one introduces quartic interactions between the left and right scalars. By comparing Eq.(1.44) and Eq.(1.49), it is also observed that the scalars and the fermions are mass degenerate.

The F-term contribution from only the μ-term in the superpotential yields:

$$|\mu|^2(|H^0_d|^2 + |H^0_u|^2 + |H^-_d|^2 + |H^+_u|^2) \tag{1.50}$$

giving rise to a quadratic term in the Higgs fields. As this expression is positive definite, it is clear that in an unbroken supersymmetric theory, the electroweak symmetry breaking does not occur (at least at the tree level). The minimum of the Higgs potential is located at $v_d = v_u = 0$, so that quarks, leptons and gauge bosons remain massless.

In addition, the $\partial W/\partial H_i$ also contributes with a product of the μ and Yukawa terms, leading to trilinear interactions of scalars:

$$\begin{aligned}
&\frac{1}{2}\mu^*(h_e \tilde{e}_L \tilde{e}^*_R H^{0*}_u + h_d \tilde{d}_L \tilde{d}^*_R H^{0*}_u + \tilde{u}_L \tilde{u}^*_R H^{0*}_d) \\
&+h_e \tilde{\nu} \tilde{e}^*_R H^{-*}_u + \tilde{u}_L \tilde{d}^*_R H^{-*}_u + \tilde{d}_L \tilde{u}^*_R H^{+*}_d) + c.c.
\end{aligned} \tag{1.51}$$

with coupling strength (μh). They connect the right to left scalars and play an important role in determining the mixing between left and right sfermions.

The D-term contribution (without the Fayet-Iliopoulos term) is entirely determined by supersymmetry and gauge invariance. In particular, it does not depend on the assumptions underlying the specification of the superpotential (nor on supersymmetry breaking). It introduces in the scalar potential quartic interactions with coupling strength g^2 of sfermions and Higgses, for example, the piece containing the Higgs fields reads:

$$\frac{1}{2}g^2(H^*_d \frac{\tau^a}{2} H_d + H^*_u \frac{\tau^a}{2} H_u)^2 + \frac{1}{8}g'^2(|H_u|^2 - |H_d|^2)^2 \tag{1.52}$$

where g' and g refer to the gauge group $U(1)$ and $SU(2)$ and the τ^a are the Pauli matrices. They generate quartic terms in the neutral Higgses potential with strength fixed by the gauge couplings. This is a fundamental difference with respect to the SM where this coupling remains a free parameter (the λ in Eq.(1.4)).

[30] This model implied a chargino lighter than the W and a massless gluino, which turned out to be in contradiction with the experimental measurements.

[31] To preserve the conservation of the "fermion numbers", it was firstly considered the existence of a new additive quantum number (R) carried by the supersymmetric generator [56]. This quantum number was associated with a continuous global symmetry called the R-symmetry.

1.5.5 Soft supersymmetry breaking

As mentioned in the introduction, particles in the same supermultiplet must have the same mass if the symmetry is respected. If supersymmetries were unbroken, then there would be, for example, selectrons with masses exactly equal to the electron mass and there would also be massless gluinos and photinos. All these particles would have been detected long ago. However, no supersymmetric particle has been observed with the same mass as its standard partner. Therefore, supersymmetry is a broken symmetry hidden at low energies in a manner analogous to the one of the electroweak symmetry in the ordinary Standard Model.

Many models of spontaneous symmetry breaking have indeed been proposed. These always involve extending the MSSM to include new particles and interactions at very high mass scales. There is no consensus on exactly how this should be done. The easiest way to parametrize the ignorance of the actual mechanism of supersymmetry breaking is to introduce breaking parameters to the Lagrangian density.

To avoid that radiative corrections generate quadratic divergences in the Higgs sector, Supersymmetry has to be softly broken [57]. The effective Lagrangian density of the MSSM can be written as

$$\mathcal{L}_{MSSM} = \underbrace{\mathcal{L}_{gauge} + \mathcal{L}_{chiral} - V(\phi,\phi^*)}_{\mathcal{L}_{SUSY}} + \mathcal{L}_{soft} \tag{1.53, 1.54}$$

where $\mathcal{L}_{SUSY}$ preserves supersymmetry invariance and $\mathcal{L}_{soft}$ violates Supersymmetry and contains only mass terms and couplings with (positive) mass dimensions.

The supersymmetry breaking terms which are added to the Lagrangian density without reintroducing the quadratic divergences are [42]:

$$\begin{aligned}\mathcal{L}_{soft} = & -\sum_i M_{0,i}^2|\phi_i|^2 - \sum_a \frac{1}{2}M_{1/2,a}\overline{\lambda_M^a}\lambda_M^a - \{\epsilon_{kl}B_0 H_u^k H_d^l + c.c.\} \\ & -\{\epsilon_{kl}[\tilde{u}_R^*\mathbf{a_u}\tilde{Q}^k H_u^l + \tilde{d}_R^*\mathbf{a_d}\tilde{Q}^k H_d^l + \tilde{\mathrm{e}}_R^*\mathbf{a_e}\tilde{L}^k H_d^l] + h.c.\}\end{aligned} \tag{1.55}$$

with k, l being isospin indices, $\epsilon_{kl} = -\epsilon_{lk}$ ($\epsilon_{12} = 1$). $M_{0,i}$ are the ϕ_i mass terms (including Higgses), $M_{1/2,a}$ the gaugino masses for each gauge group, λ^a the gaugino fields (in the 4-component Majorana form), B_0 the mixing (mass)^2 term for the two Higgs doublets, $H_{u,d}$ the corresponding $SU(2)_L$ doublet Higgs fields, $\mathbf{a_u}$, $\mathbf{a_d}$ and $\mathbf{a_e}$ are the 3×3 matrices containing the trilinear couplings with dimensions of mass between sfermions and Higgs bosons, $\tilde{Q}$, $\tilde{L}$ are the $SU(2)_L$ doublets fields described in Table 1.2.

Up to now, no constraint is applied to this Lagrangian density. This MSSM model is called the "unconstrained MSSM". However, this $\mathcal{L}_{soft}$ introduces a huge number of free parameters: 105 parameters in addition to the 19 parameters of the Standard Model. Moreover, most parameters involve flavor changing neutral currents (FCNC) or CP violating phases at an unacceptable level. More restrictive models satisfying these requirements and relying on fewer parameters have been developed and will be considered later.

1.6 SUSY breaking mechanisms

Although the effective theory, defined by the soft supersymmetry breaking contribution to the potential (with some additional conditions to define the LSP), is sufficient to develop the phenomenology, it is nevertheless interesting to discuss the question of the origin of SUSY breaking. This will allow, by means of simple arguments, to understand better the very distinctive properties of the SuperGravity Supersymmetry breaking (SUGRA), Gauge Mediated Supersymmetry Breaking (GMSB) and Anomaly Mediated Supersymmetry Breaking (AMSB) that will be developed later.

It is shown in the primer of S. Martin [42] that the soft supersymmetry breaking masses cannot be generated by tree level interactions with SUSY particles. It is expected instead that there is a "hidden" sector of particles with no (or very weak) direct couplings to the MSSM supermultiplets of the "observable" sector. The breaking of supersymmetry, which is supposed to occur in the hidden sector, is transmitted via a "messenger" sector to the "observable" sector, resulting in the soft terms of Eq.(1.55). Models have been proposed where this transmission is either induced by gravitational interactions (SUGRA) or is mediated by gauge interactions (GMSB) [32]. Therefore, the SUSY breaking mechanism can be separated in three levels: the hidden sector, the messenger sector and the visible sector.

The hidden sector

The spontaneous breaking of global supersymmetry requires the existence of a massless spin-$\frac{1}{2}$ fermion, the *goldstino* ($\tilde{G}$) which is a part of a chiral supermultiplet. If the auxiliary [33] field, F_S, associated to the goldstino and the scalar field S, acquires a vev $< F_S >$, of dimension of (mass)^2, the interaction of the goldstino with the other supermultiplets is defined by the following effective Lagrangian density [58]

$$\mathcal{L}_{goldstino} \propto -\frac{1}{< F_S >} j^{\mu\alpha} \partial_\mu \tilde{G}_\alpha + \cdots \tag{1.56}$$

where the supercurrent $j^{\mu\alpha}$ involves fermion-scalar and gaugino-gauge boson products, leading to interactions pictured in Fig. 1.9

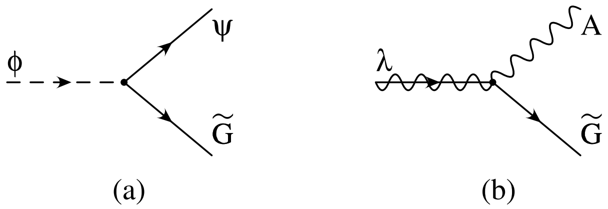

Figure 1.9: Goldstino interactions with superpartner pairs (ϕ, ψ) and (λ^a, A^a).

If gravity is taken into account, supersymmetry must be a local symmetry. The resulting locally supersymmetric theory is called supergravity. In supergravity, the spin–2 graviton has a spin–3/2 fermion superpartner called the *gravitino*.

As long as supersymmetry is unbroken, the graviton and the gravitino, each with two spin helicity states, are both massless. Once supersymmetry is spontaneously broken, the gravitino acquires a mass by absorbing the goldstino, which becomes its longitudinal component (polarization $\pm$1/2). This is called the super–Higgs mechanism. It is analogous to the ordinary Higgs mechanism for gauge theories, by which the $W^\pm$ and Z^0 gauge bosons in the Standard Model gain mass by absorbing the Nambu–Goldstone bosons associated with the spontaneously broken electroweak gauge invariance.

[32] The AMSB mechanism is described at the end of this chapter.

[33] Any chiral superfield can be split up in three components: scalar, fermionic and auxiliary. The last one can be expressed in terms of the first component using the equation of motion.

If one requires the invariance under supersymmetric transformations and a vanishing cosmological constant, the gravitino mass called $m_{3/2}$ is related to the scale of spontaneous supersymmetry breaking as:

$$m_{3/2} = \frac{< F_S >}{\sqrt{3} M_P} = 2.37 \times 10^{-2} \left(\frac{\sqrt{< F_S >}}{10 \ \mathrm{TeV}} \right)^2 \mathrm{eV} \tag{1.57}$$

where $< F_S >$ is the square of the SUSY breaking scale (the vev) and M_P is the Planck mass. As seen from Eq.(1.56) and Eq.(1.57), an increase of the vev $< F_S >$ leads to an increase of the gravitino mass, but to a decrease of the effective coupling strength related to the $\pm$1/2 degrees of freedom. Moreover, the SUSY breaking generates mass splittings (Δm), by an effective coupling λ to the goldstino

$$\Delta m^2 \sim \lambda < F_S > \tag{1.58}$$

The messenger sector

Two different approaches can be considered in the messenger sector depending on the type of interactions/fields which communicate the hidden sector vev with the visible sector: the supergravity–induced supersymmetry breaking models (SUGRA) and the gauge–mediated supersymmetry breaking scenarios (GMSB).

- *Supergravity–induced supersymmetry breaking models*

  In the SUGRA models, the breaking of the of hidden sector ($< F_S >$) is communicated to the observable sector (the MSSM) only through supergravity itself. Hence the coupling must be small, roughly of order $\lambda \simeq < F_S > /M_P^2$, yielding soft mass terms (or mass splittings)

  $$m_{soft}^2 = \Delta m^2 \sim < F_S >^2 /M_P^2 \simeq m_{3/2}^2 \tag{1.59}$$

  We see that this expression yields the expected assymptotical behavior: m_{soft} vanishes in the limit $m_{3/2} \propto < F_S > \rightarrow 0$ where supersymmetry is unbroken. In order for supersymmetry to solve the naturalness problem, it is customary to require that the mass splitting among the MSSM states is $\Delta m^2 \sim G_F^{-1} \sim M_W^2 \sim$ few hundred GeV. Hence, the scale associated with the origin of supersymmetry breaking in the hidden sector should be roughly $m_{3/2} \sim 10^2$ or 10^3 GeV. This implies that in the SUGRA models, the gravitino is heavy, of the same order of m_{soft}, and its interaction is extremely weak so that it plays no role in the phenomenology of particle physics.

- *Gauge–mediated supersymmetry breaking scenarios*

  In the gauge–mediated SUSY breaking scenarios(GMSB) the supersymmetry breaking is communicated by gauge interactions. In these scenarios, the MSSM soft terms arise from loop diagrams involving some messenger particles consisting of chiral supermultiplets with quantum numbers of q, $\bar{q}$, l, $\bar{l}$. A similar approach was used, at the end of the seventies, to generate a mass for the gluinos by the radiative corrections involving quark messengers [59]. Nowadays, they are used to generate masses for all the new sparticles [60][61][62]. If we want to ensure gauge coupling unification, the messenger families must appear in complete representations of the GUT group. In a $SU(5)$ model, they belong for instance, to a $5 + \bar{5}$ and/or a $10 + \bar{10}$ representation. Masses are generated for the messengers through their coupling to the goldstino superfield S. At the other extreme, compared to the supergravity–induced case, it is assumed that the coupling is strong, $\lambda \simeq 1$, providing mass splittings in the messenger sectors of order

$$\Delta m^2 \sim < F_S > \simeq M_P m_{3/2} \tag{1.60}$$

The messengers have $SU(3)_C \times SU(2)_L \times U(1)_Y$ interactions in the visible sector which provide a link to the MSSM and generate the soft mass terms as shown for the gaugino mass terms in Fig. 1.10 and scalar mass terms in Fig. 1.11.

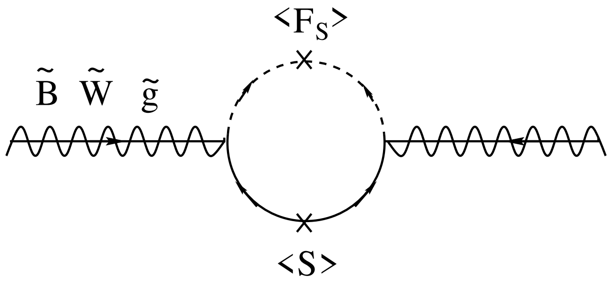

Figure 1.10: Contributions to the MSSM gaugino masses in gauge-mediated supersymmetry breaking scenarios arise from one-loop graphs involving messenger particles. The interaction vertices are of gauge interaction strength.

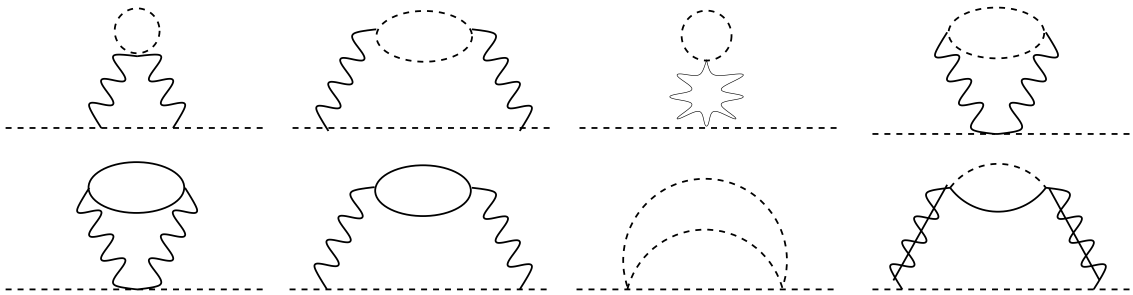

Figure 1.11: Contributions to the MSSM scalar squared masses in gauge-mediated supersymmetry breaking models arise in leading order from these two-loop Feynman graphs. The messenger fermions are represented by the heavy solid lines, the messenger scalars by the heavy dashed lines, the ordinary gauge bosons by the squiggly line and the gauginos by the solid line superimposed on a squiggly line. The straight dashed line at the bottom represent the scalar that is getting the mass.

These diagrams introduce typically a loop factor $\alpha/4\pi$, so that the gaugino masses M_i are of order

$$M_i \sim \frac{\alpha_i}{4\pi} \frac{\sqrt{< F_S >}}{< S >} \sqrt{< F_S >} \tag{1.61}$$

where $< S >$ is the vev of the S scalar component. On the other hand, the universal scalar (masses)^2 are generated at two loops and have the form

$$m_0^2 \sim (\frac{\alpha_i}{4\pi})^2 \frac{< F_S >}{< S >^2} < F_S > \tag{1.62}$$

In one assumes $< S >$ to be of the same order of $\sqrt{< F_S >}$. To yield masses of the order of the weak scale, the scale of supersymmetry breaking should be as low as $\sqrt{< F_S >} \sim$

$10^4 - 10^5$ GeV. This implies a small gravitino mass, of order $m_{3/2} \sim 1 \;\; eV$ and a non-negligible interaction strength.

The visible sector
The Standard Model particles and their superpartners are all in the visible sector.

- In the SUGRA models, the gravitino mass is comparable to the masses of the MSSM sparticles. $m_{3/2}$ is expected to be at least 100 GeV. Its interactions will be of gravitational strength, thus the gravitino will not play any role in collider physics, but it can be a very important consideration in cosmology. In these models the lightest neutralino ($\tilde{\chi}_1^0$) is generally the LSP, and is a perfect candidate for the non baryonic dark matter.

- In GMSB scenarios, the gravitino is much lighter than the MSSM sparticles. It will be the LSP and all the MSSM sparticles will eventually decay into final states that include it. The decay rate of any sparticle $\tilde{X}$ into its Standard Model partner X plus a gravitino $\tilde{G}$ is given by

$$\Gamma(\tilde{X} \to X\tilde{G}) = \frac{m_{\tilde{X}}^5}{16\pi < F_S >^2} \left(1 - \frac{m_X^2}{m_{\tilde{X}}^2}\right)^4 \tag{1.63}$$

This corresponds to either Fig. 1.9.a or 1.9.b with ($\tilde{X}$,X) = (ϕ, ψ) or (λ, A) respectively. Taking into account the expression 1.57, Eq.(1.63) can be rewritten as:

$$\Gamma(\tilde{X} \to X\tilde{G}) = \frac{m_{\tilde{X}}^5}{48\pi M_P^2 m_{3/2}^2} \left(1 - \frac{m_X^2}{m_{\tilde{X}}^2}\right)^4 \tag{1.64}$$

The decay is larger for smaller $< F_S >$ or equivalently for smaller $m_{3/2}$, if the other masses are fixed. If $\tilde{X}$ is a mixture of superpartners of different Standard Model particles X, then Eq.(1.63) should be multiplied by a suppression factor equal to the square of the cosine of the appropriate mixing angle. If $m_{\tilde{X}}$ is of order 100 GeV$/c^2$ or more, and $\sqrt{F_S} \leq$ few $\times$ 10^6 GeV (corresponding to $m_{3/2}$ less than roughly 1 KeV), then the decay $\tilde{X} \to$ X $\tilde{G}$ can be fast enough to be observed in a collider detector.

1.6.1 minimal SUGRA

All phenomenological problems of the MSSM (mainly the introduction of FCNC's) are solved if one assumes that the MSSM parameters obey a set of boundary conditions at the Unification scale. These assumptions are usually assumed in the SUGRA models.

The basic universality assumptions are:

- Gauge coupling unification:

$$\alpha_1(M_{GUT}) = \alpha_2(M_{GUT}) = \alpha_3(M_{GUT}) \equiv \alpha_{GUT} \tag{1.65}$$

This relation fixes the Grand Unification scale M_{GUT}.

- Unification of gaugino masses:

$$M_{1/2,1}(M_{GUT}) = M_{1/2,2}(M_{GUT}) = M_{1/2,3}(M_{GUT}) \equiv m_{1/2} \tag{1.66}$$

There is a common gaugino mass: $m_{1/2}$. Since the gaugino masses and the gauge couplings are governed by the same renormalization group equations (at one loop), at the electroweak scale the previous relations give:

$$M_{1/2,i} \equiv M_i(M_Z) = \frac{\alpha_i(M_Z)}{\alpha_{GUT}} m_{1/2} \rightarrow M_3 = \frac{\alpha_3(M_Z)}{\alpha_2(M_Z)} M_2 = \frac{\alpha_3(M_Z)}{\alpha_1(M_Z)} M_1 \tag{1.67}$$

From the last equation, the relation between the $U(1)_Y$ and $SU(2)_L$ gaugino masses can be derived:

$$M_1 = \frac{5}{3} tan^2\theta_W M_2 \sim \frac{1}{2} M_2 \tag{1.68}$$

where θ_W is the electroweak mixing angle.

- Universal scalar mass, including the additional assumption of connecting the Higgs sector to the "matter" sector:

$$M_{0,i} \equiv M_{\tilde{Q}} = M_{\tilde{L}} = M_{\tilde{e}_R} = M_{\tilde{u}_R} = M_{\tilde{d}_R} = M_{H_u} = M_{H_d} \equiv m_0 \tag{1.69}$$

  There is a common scalar mass: m_0.

- Universal trilinear couplings:

  One can make the further assumption that the (scalar)^3 couplings are each proportional to the corresponding Yukawa coupling matrix

$$\mathbf{a_u} = A_u \mathbf{h_u}, \quad \mathbf{a_d} = A_d \mathbf{h_d}, \quad \mathbf{a_e} = A_e \mathbf{h_e} \tag{1.70}$$

  and assume a universal trilinear coupling at M_{GUT}

$$A_u(M_{GUT}) = A_d(M_{GUT}) = A_e(M_{GUT}) \equiv A_0 \tag{1.71}$$

- Finally one can avoid disastrously large CP-violating effects with the assumption that the soft parameters do not introduce new complex phases. If one assumes that

$$arg(M_1), arg(M_2), arg(M_3), arg(A_u), arg(A_d), arg(A_e) = 0 \quad \text{or} \quad \pi \tag{1.72}$$

  then the only CP–violating phase in the theory will be the ordinary CKM phase found in the ordinary Yukawa couplings.

Therefore, the only free parameters at high energy are

$$m_0, m_{1/2}, A_0, \mu, B_0 \tag{1.73}$$

With these parameters and the initial conditions at the GUT scale the masses of all SUSY particles can be calculated at low energy via the renormalization group equations (RGEs). This is called the constrained MSSM (cMSSM SUGRA). An example is given in Fig. 1.12, from Wim de Boer *et al.* [51].
The following qualitative features emerges

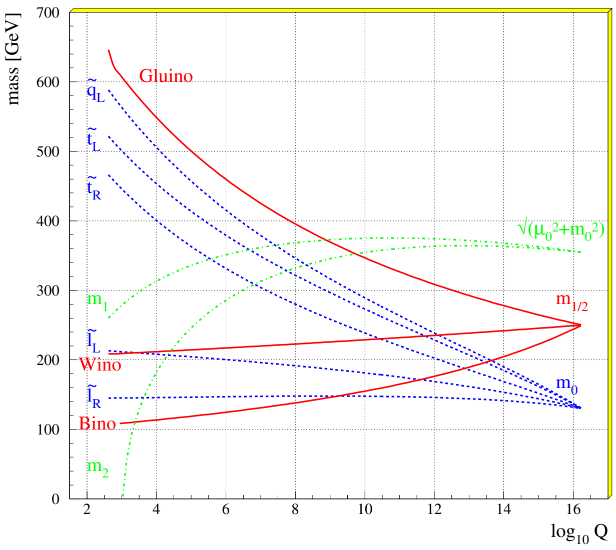

Figure 1.12: Evolution of the mass parameters in SUGRA[51].

- the sfermion masses start from the common value m_0 at the GUT scale. The squark masses increase fast, due to the contributions proportional to α_3 in the RGEs. The slepton masses increase slowly, as the only contribution in the RGEs are from the couplings $\alpha_{1,2}$. For a given type, the left scalar is heavier than the right scalar, since there is not contribution from α_2 in the RGEs,
- the gaugino masses start from the common value $m_{1/2}$. The gluino mass increases fast while the $\tilde{B}$ and $\tilde{W}$ masses remain low.

It is thus expected that the strongly interacting particles, the squarks and gluinos, will generally be heavy compared to the sleptons, winos and binos.

The Higgs (mass)^2 parameters [34] start from the value $(m_0^2 + \mu^2)$, determined by the soft breaking mass for scalars and the μ-term in the superpotential (Eq.(1.50)). The large Yukawa coupling of H_u to the top quark drives the (mass)^2 parameter of H_u negative. In consequence, the coefficient of the quadratic term in the Higgs potential becomes **negative**, which allows with some additional conditions the breaking of the electroweak symmetry. All of this is discussed in more detail in Appendix B. The MSSM therefore incorporates a quite natural/elegant mechanism for breaking the electroweak symmetry. It is customary to replace the high scale parameter B_0 in $\mathcal{L}_{soft}$ (Eq.(1.55)) by the low energy parameter $\tan\beta = v_u/v_d$, the ratio of vacuum expectation values of the Higgs fields H_u H_d, leaving as free parameters

$$m_0, m_{1/2}, A_0, \mu, \tan\beta \tag{1.74}$$

Moreover one may require that electroweak symmetry be broken "correctly", i.e. reproduces the Z^0 mass. With this additional constraint, it is possible to eliminate the μ and B_0 parameters as a consequence of the radiative electroweak symmetry breaking. Thus, in this model, four continuous and one discrete parameters are free:

[34] Not to be confused with the physical masses which require the knowledge of the B_0 parameter.

$$m_0, m_{1/2}, A_0, \tan\beta, sign(\mu) \tag{1.75}$$

This constrained model is called the minimal SUGRA model (cMSSM mSUGRA) [63].

1.6.2 Gauge mediated supersymmetry breaking (GMSB)

The parameters which will govern the phenomenology related to the GMSB scenarios are [35]:

- The scale Λ, related to the mass splitting of the scalar components ($\sqrt{<F_S>}$) of the messenger supermultiplets. This parameter sets the scale of the entire superpartner spectrum.
- The messenger scale, M, which represents the average mass of the messengers. This scale determines the amount of RGE evolution and, therefore, enters only logarithmically in the values of the masses.
- The existence of the messengers modifies the RGEs of the gauge couplings and increase the value of the unified gauge coupling constant α_{GUT}. These extra contributions depend on a parameter called messenger index N, which is the sum $N = \sum n_i$ of constants determined by the group representations with n_i = 1 for $5+\bar{5}$ and n_i = 3 for $10+\bar{10}$. The requirement that the gauge couplings remain perturbative up to the GUT scale limits the messengers index to values $N \leq 5-10$ for messenger scales $M = 10^5 - 10^{10}$ GeV respectively.
- The parameters A_0 and B_0 are taken to be zero at the messenger scale but yield non zero values at E.W. thanks to the RGEs. Under the assumption of correct breaking of the electroweak symmetry the absolute of μ and the value of B_0 can be obtained from the gauge boson masses and the parameter $\tan\beta$.

In summary, the scenarios are parametrized using

$$\Lambda, N, M, \tan\beta, sign(\mu) \tag{1.76}$$

with the condition that $\Lambda < M$ to avoid that scalar messengers get a negative squared mass and break gauge symmetry at the messenger scale [62].

In the GMSB scenarios, the gaugino mass terms present in $\mathcal{L}_{soft}$ take the simple form

$$m_{\lambda_i}(t) = \frac{\alpha_i(t)}{4\pi} N\Lambda \tag{1.77}$$

The scale at which they are defined is given by $t = \ln(M^2/Q^2)$, hence we have the same evolution as encountered in the SUGRA framework. The masses of the scalar particles at the messenger scale are proportional to

$$\tilde{m}^2 \propto 2N\Lambda^2 \sum (\frac{\alpha_i}{4\pi})^2 \tag{1.78}$$

These values have to be RGE-evolved down to the electroweak scale and the effect of mixing and the D-term contribution have to be included. The exact formulae can be found in [62]. As an example, the dependence of the scalar and gaugino masses as function of the $U(1)$ mass parameter M_1 is given in Fig. 1.13 from [62]. We see that, for $N = 1$ the neutralino(bino) is the Next-to-LSP(NLSP), whereas for larger N values, the NLSP becomes the $\tilde{l}_R$ over most of the parameter space. The relative increase of the gaugino masses with N is due to the linear dependence on N in the mass expression given in Eq.(1.77), while this dependence is $\sqrt{N}$ for the scalars (Eq.(1.78)).

[35] The parameters will be given without any justification. A didactic introduction to GMSB scenarios is given in [42]. A complete presentation can be found in the review article by Giudice and Rattazzi [62]

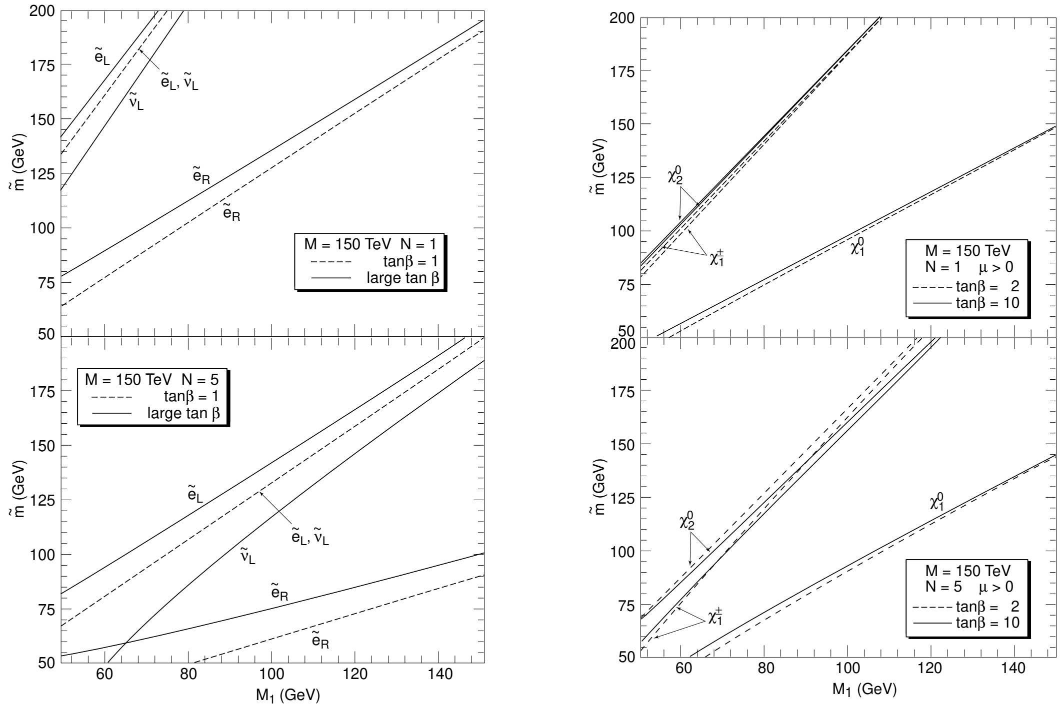

Figure 1.13: SUSY masses in GMSB [62].

1.6.3 Anomaly mediated supersymmetry breaking (AMSB)

Recently, new scenarios where the SUSY breaking is not directly communicated from the hidden to the visible sector have been built. This is the case in the so-called anomaly mediated SUSY breaking models (AMSB), where gauginos masses are generated at one loop and scalar masses at two loops as a consequence of the 'super–Weyl (superconformal) anomaly' [64]. The gaugino masses are no more universal, but are given by

$$M_i = \frac{\beta_i}{g_i} m_{3/2} \, , \tag{1.79}$$

where β_i are the one–loop beta functions arising from dimensional regularization. In the simplest form, however, the squared masses of the sleptons turn out to be negative (tachyonic). To avoid this, it suffices phenomenologically to introduce a universal scalar mass m_0^2 at the GUT scale. The parameters of the model are then m_0, $m_{3/2}$, $\tan\beta$ and $sign(\mu)$.

The most characteristic feature is the relation $M_1 \sim 3\,M_2$ in contrast to SUGRA scenarios, where $M_1 \simeq 0.5\,M_2$. Therefore, one has near degeneracy of the lighter chargino $\chi_1^\pm$ and the wino–like neutralino χ_1^0 masses, which has important phenomenological implications.

Recently, a search for charginos in the context of AMSB assuming a sneutrino LSP have been performed by a reinterpretation of the chargino SUGRA analysis described in this thesis. Nevertheless, the results have been finalized only recently and are not described here. DELPHI experimental results covering several possible AMSB signatures can be found in [65].

Chapter 2

The gaugino–higgsino sector

The solutions of the renormalization group equations for the gaugino masses are in the SUGRA scheme [1]

$$M_i(t) = \frac{\alpha_i(t)}{\alpha_{GUT}} m_{1/2}, \ \ i = 1, 2, 3 \tag{2.1}$$

Numerically, at the electroweak scale the relations give:

$$\begin{aligned} \mathrm{B}ino\, U(1)_Y : & \quad M_1(M_Z) \simeq 0.4\, m_{1/2} \\ \mathrm{W}ino\, SU(2)_L : & \quad M_2(M_Z) \simeq 0.8\, m_{1/2} \\ \mathrm{G}luino\, SU(3)_C : & \quad M_3(M_Z) \simeq 2.7\, m_{1/2} \end{aligned} \tag{2.2}$$

In the present thesis, M_2 is used to parametrize the gaugino masses instead of $m_{1/2}$. Higgsinos and gauginos are spin 1/2 particles, their mass eigenstates are in general mixtures of the weak interaction eigenstates. The higgsinos and electroweak gauginos mix with each other because of the electroweak symmetry breaking. The neutral higgsinos ($\tilde{H}_u^0$ and $\tilde{H}_d^0$) and the neutral gauginos ($\tilde{B}$, $\tilde{W}^0$) combine to form four neutral mass eigenstates called *neutralinos* ($\tilde{\chi}_i^0$, i=1,2,3,4). The charged higgsinos ($\tilde{H}_u^+$ and $\tilde{H}_d^-$) and winos ($\tilde{W}^+$ and $\tilde{W}^-$) mix to form two mass eigenstates with charge ± 1 called *charginos* ($\tilde{\chi}_i^\pm$, i=1,2). By convention, these are labeled in ascending order of mass so that $M_{\tilde{\chi}_1^0} < M_{\tilde{\chi}_2^0} < M_{\tilde{\chi}_3^0} < M_{\tilde{\chi}_4^0}$ and $M_{\tilde{\chi}_1^\pm} < M_{\tilde{\chi}_2^\pm}$. The lightest neutralino, $\tilde{\chi}_1^0$, is usually assumed to be the LSP, unless there is a lighter gravitino or unless R–parity is not conserved.

2.1 Chargino mass spectrum

Contributions to the masses of winos and higgsinos arise respectively from the soft SUSY breaking terms ($M\lambda\lambda$) (Eq.(1.55)) and from the chiral contributions of the superpotential in the form ($\mu\tilde{H}_d^-\tilde{H}_u^+$) (Eq.(1.45)). In addition, there are mixing terms generated by the ($\lambda\phi\psi$) vertex in $\mathcal{L}_{gauge}$ leading to ($\tilde{W}^\pm H_{d,u}^0 \tilde{H}_{d,u}^\mp$). The electroweak symmetry breaking provides off-diagonal elements $v_{d,u}\tilde{W}^\pm\tilde{H}_{d,u}^\mp$ in the mass matrix and mixes the charged wino and higgsino states. The chargino mass terms in the Lagrangian density are given by [37][66]

[1] In the GMSB scheme the relation still holds but $m_{1/2}$ is equal to $\alpha_{GUT}M\Lambda$ with M as input scale of the renormalization.

$$\mathcal{L} = -\frac{1}{2}(\psi^{\pm})^T \mathbf{M}_{\tilde{\chi}^{\pm}} \psi^{\pm} + c.c. \tag{2.3}$$

where $\psi^{\pm}$ = (-i$\tilde{W}^{+}$,$\tilde{H}_u^{+}$,-i$\tilde{W}^{-}$,$\tilde{H}_d^{-}$) is the interaction–eigenstate basis and

$$\mathbf{M}_{\tilde{\chi}^{\pm}} = \begin{pmatrix} 0 & X^T \\ X & 0 \end{pmatrix} \text{with} \quad \mathbf{X} = \begin{pmatrix} M_2 & \sqrt{2} M_W sin\beta \\ \sqrt{2} M_W cos\beta & \mu \end{pmatrix} \tag{2.4}$$

The chargino mass matrix depends on the parameters M_2, μ and $\tan\beta$. The mass eigenstates are related to the gauge eigenstates by two unitary 2×2 matrices **U** and **V** according to

$$\begin{pmatrix} \tilde{\chi}_1^{+} \\ \tilde{\chi}_2^{+} \end{pmatrix} = \mathbf{V} \begin{pmatrix} \tilde{W}^{+} \\ \tilde{H}_u^{+} \end{pmatrix}; \quad \begin{pmatrix} \tilde{\chi}_1^{-} \\ \tilde{\chi}_2^{-} \end{pmatrix} = \mathbf{U} \begin{pmatrix} \tilde{W}^{-} \\ \tilde{H}_d^{-} \end{pmatrix} \tag{2.5}$$

There are different mixing matrices for the positively charged states and for the negatively charged states since the two higgsino states belong to different multiplets. **U** and **V** are chosen to diagonalize the chargino mass matrix:

$$\tilde{M}_i^{\pm}\, \delta_{ij} \quad = \quad U_{im}^{*}\, V_{jn}\, X_{mn} \tag{2.6}$$

These unitary matrices define the composition of the charginos. The corresponding chargino mass eigenvalues are

$$\begin{aligned} (\tilde{M}_{1,2}^{\pm})^2 = \; & \tfrac{1}{2} \Big[M_2^2 \, + \, \mu^2 \, + \, 2M_W^2 \\ & \mp \sqrt{(M_2^2 + \mu^2 + \, 2M_W^2)^2 - \, 4(M_2\mu - M_W^2 \sin 2\beta)^2} \Big] \end{aligned} \tag{2.7}$$

with $M_{\tilde{\chi}_i^{\pm}}$ = $|\tilde{M}_{1,2}^{\pm}|$. Therefore, the chargino masses can be written as a function of three parameters: M_2, μ and $\tan\beta$. Fig. C.1 and C.2 show the $\tilde{\chi}_1^{\pm}$ and $\tilde{\chi}_2^{\pm}$ mass isocurves [2], in the (μ, M_2) plane for different $\tan\beta$ values: 1.0, 1.5 and 35. As can be seen, the curves are not symmetric except for large $\tan\beta$.

A useful approximation is obtained in the limit where the electroweak symmetry breaking effects can be viewed as small perturbations, namely $|\mu \pm M_2| \gg M_Z$, the masses of the two charginos reduce to ($\epsilon \equiv$ sign(μ)):

$$M_{\tilde{\chi}_1^{\pm}} \quad \simeq \quad M_2 - \frac{M_W^2 (M_2 + \mu \sin 2\beta)}{\mu^2 - M_2^2} \tag{2.8}$$

$$M_{\tilde{\chi}_2^{\pm}} \quad \simeq \quad |\mu| + \frac{M_W^2 (|\mu| + \epsilon M_2 \sin 2\beta)}{\mu^2 - M_2^2} \tag{2.9}$$

[2] All the equations and plots given in this chapter and in the appendix C were computed assuming tree-level relations. Effects of the one-loop radiative corrections are discussed in appendix D.

For $|\mu| \gg M_2$, the lightest chargino corresponds to a pure wino state with $M_{\tilde{\chi}_1^\pm} \simeq M_2$, while the heavier chargino corresponds to a pure higgsino state with $M_{\tilde{\chi}_2^\pm} \simeq |\mu|$. For $M_2 \gg |\mu|$, then the situation is reversed.

Another interesting case occurs when $\mu \simeq -M_2$, then the chargino masses are:

$$M^2_{\tilde{\chi}^\pm_{1,2}} = (M_2^2 + M_W^2) \mp [(M_2^2 + M_W^2)^2 - (M_2^2 + M_W^2 sin2\beta)^2]^{1/2} \tag{2.10}$$

and for $\tan\beta \simeq 1$ both charginos become degenerate with masses $M^2_{\tilde{\chi}_2^\pm} \simeq M^2_{\tilde{\chi}_1^\pm} \simeq M_2^2 + M_W^2$ and nearly degenerate with the $W^\pm$ if M_2 is small.

2.2 Neutralino mass spectrum

Due to the same reasons as seen for the charginos, mixing between the neutral gaugino and higgsino states occurs when the $SU(2) \otimes U(1)$ symmetry is broken. In the neutralino case, the mass terms in the Lagrangian density can be written as [67]

$$\mathcal{L} = -\frac{1}{2}(\psi^0)^T \mathbf{Y}_{\tilde{\chi}^0} \psi^0 + c.c. \tag{2.11}$$

in the basis $\psi^0 = (-i\tilde{\gamma}, -i\tilde{Z}^0, \tilde{H}_a^0, \tilde{H}_b^0)$ where $\tilde{H}_a^0 = \tilde{H}_d^0 \cos\beta - \tilde{H}_u^0 \sin\beta$ and $\tilde{H}_a^0 = \tilde{H}_d^0 \sin\beta - \tilde{H}_u^0 \cos\beta$. The mass matrix takes the form

$$\mathbf{Y}_{\tilde{\chi}^0} = \begin{pmatrix} M_1 c_W^2 + M_2 s_W^2 & (M_2 - M_1) s_W c_W & 0 & 0 \\ (M_2 - M_1) s_W c_W & M_1 s_W^2 + M_2 c_W^2 & M_Z & 0 \\ 0 & M_Z & \mu \sin 2\beta & -\mu \cos 2\beta \\ 0 & 0 & -\mu \cos 2\beta & -\mu \sin 2\beta \end{pmatrix} \tag{2.12}$$

with $s_W = sin\theta_W$ and $c_W = cos\theta_W$. The mass matrix $\mathbf{Y}_{\tilde{\chi}^0}$ can be diagonalized by a real unitary matrix $\mathbf{N}$ with $\tilde{\chi}_i^0 = \mathbf{N}_{ij}\, \psi_j^0$, so that:

$$\tilde{M}_k^0\, \delta_{kl} \quad = \quad N_{km}\, N_{ln}\, Y_{mn} \tag{2.13}$$

The corresponding neutralino mass eigenvalues depend on the parameters: M_1, M_2, μ and $\tan\beta$ and it is easier to compute them numerically. If universality of gaugino masses is assumed ($M_1 \simeq 0.5$ M_2), the neutralino mass isocurves can be plotted. Fig. C.3 and C.4 show these curves for the two first neutralinos in the (μ, M_2) plane for different $\tan\beta$ values: 1.0, 1.5 and 35.

In the same approximation as charginos ($|\mu \pm M_2| \gg M_Z$), approximate values for the neutralino masses are:

$$M_{\tilde{\chi}_1^0} \simeq M_1 - \frac{M_Z^2 s_W^2 (M_1 + \mu \sin 2\beta)}{\mu^2 - M_1^2} \tag{2.14}$$

$$M_{\tilde{\chi}_2^0} \simeq M_2 - \frac{M_Z^2 c_W^2 (M_2 + \mu \sin 2\beta)}{\mu^2 - M_2^2} \tag{2.15}$$

$$M_{\tilde{\chi}_3^0} \simeq |\mu| + \frac{M_Z^2 (1 - \epsilon \sin 2\beta)(|\mu| + M_1 c_W^2 + M_2 s_W^2)}{2(|\mu| + M_2)(|\mu| + M_1)} \tag{2.16}$$

$$M_{\tilde{\chi}_4^0} \simeq |\mu| + \frac{M_Z^2 (1 + \epsilon \sin 2\beta)(|\mu| - M_1 c_W^2 - M_2 s_W^2)}{2(|\mu| - M_2)(|\mu| - M_1)} \tag{2.17}$$

where ϵ is the sign of μ. In this approximation, the neutralino mass eigenstates are nearly $\tilde{\chi}_1^0 \simeq \tilde{B}$, $\tilde{\chi}_2^0 \simeq \tilde{W}^0$ and $\tilde{\chi}_3^0$,$\tilde{\chi}_4^0 \simeq (\tilde{H}_u^0 \pm \tilde{H}_d^0)/\sqrt{2}$. For $|\mu| \gg M_2$, two neutralinos are pure gaugino states with masses $M_{\tilde{\chi}_1^0} \simeq M_1$, $M_{\tilde{\chi}_2^0} = M_2$, while the two others are pure higgsino states with masses $M_{\tilde{\chi}_3^0} \simeq M_{\tilde{\chi}_4^0} \simeq |\mu|$. If $M_2 \gg |\mu|$, the LSP is higgsino-like and nearly degenerate with the lightest chargino.

2.3 The gaugino contents

It is also convenient to further divide the (μ,M_2) plane into regions based on the gaugino contents of the light gauginos. The field composition of the first chargino and the first neutralino can be expressed by the gaugino content as:

$$\rho_{\tilde{\chi}_1^\pm} = |V_{11}|^2 \tag{2.18}$$

$$\rho_{\tilde{\chi}_1^0} = |N_{11}|^2 + |N_{12}|^2 \tag{2.19}$$

The variables $\rho_{\tilde{\chi}_1^\pm}$ and $\rho_{\tilde{\chi}_1^0}$ lie in the range $0 \leq \rho_{\tilde{\chi}_1^\pm}, \rho_{\tilde{\chi}_1^0} \leq 1$. $\rho_{\tilde{\chi}_1^\pm}$ ($\rho_{\tilde{\chi}_1^0}$) is zero when $\tilde{\chi}_1^\pm$ ($\tilde{\chi}_1^0$) is pure higgsino and is one when $\tilde{\chi}_1^\pm$ ($\tilde{\chi}_1^0$) is pure gaugino. Although they may differ substantially in certain regions of parameter space, these parameters are correlated: when M_2, $M_1 << |\mu|$, both $\tilde{\chi}_1^\pm$ and $\tilde{\chi}_1^0$ are essentially gaugino states, while in the opposite limit, M_2, $M_1 \gg |\mu|$, they are both dominated by their higgsino components.

Although the specific boundaries are not particularly important, the different regions can be considered as (the same definitions apply for the neutralino case):

$$\begin{array}{lcl} 0 \leq \rho^{(\tilde{\chi}_1^\pm)} \leq 0.2 & \equiv & \text{Higgsino} \\ 0.2 < \rho^{(\tilde{\chi}_1^\pm)} < 0.9 & \equiv & \text{Mixed region} \\ 0.9 \leq \rho^{(\tilde{\chi}_1^\pm)} \leq 1 & \equiv & \text{Gaugino} \end{array} \tag{2.20}$$

One may illustrate the gaugino-higgsino content of the charginos and neutralinos with Fig. 2.1, were the slopes of the lines reflect the particle composition. Horizontal lines correspond to gaugino-like regions (determined by M_2, independent of μ), lines along the diagonals to the higgsino-like regions (given by μ). The kinks of the mass solutions 1 for neutralino and chargino are due to the sign change of their corresponding eigenvalues. The gaugino composition of neutralinos and charginos is important since it determines the coupling to the $SU(2)_L$ gauge bosons and the sfermions and thus the cross–section and branching ratios.

2.4 Chargino production

In e^+e^- collisions, charginos are pair produced via Z^0/γ annihilation in the s–channel and via sneutrino interchange in the t–channel. The first order Feynman diagrams contributing to process $e^+e^- \to \tilde{\chi}_i^+ \tilde{\chi}_i^-$ are shown in Fig. 2.2.

The gauge interactions mediated by the s–channel Z^0 and γ exchange gives rise to gaugino and to higgsino final states. The gauginos are produced via the $(A\lambda\lambda)$ vertex, the supersymmetric analog of the SM $(W^0W^+W^-)$ vertex. The higgsinos originate from a $(A\psi\psi)$ vertex, the same as the $(Af\bar{f})$ of the SM. The photon couples to the charge eQ and hence to the mass eigenstates. The Z^0 couples proportionally to $(T^3 - Qsin^2\theta_W)$ where ($T^3 = 1$,$Q = +1$) for the winos and ($T^3 = 1/2$,$Q = +1$)

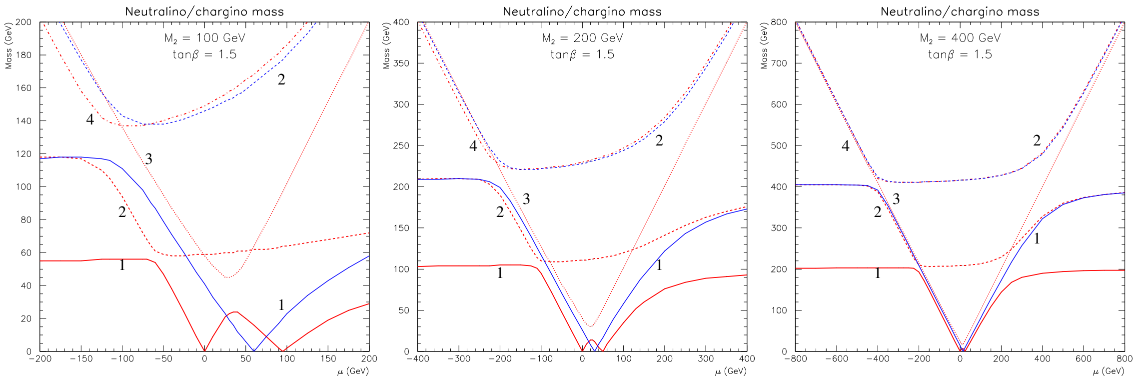

Figure 2.1: Chargino and neutralino mass solutions as function of μ for $M_2 = 100,\ 200$ and $400\ GeV$ and $tan\beta = 1.5$. The neutralino mass solutions are labeled from 1 to 4 on the left and the chargino solutions 1 and 2 on the right.

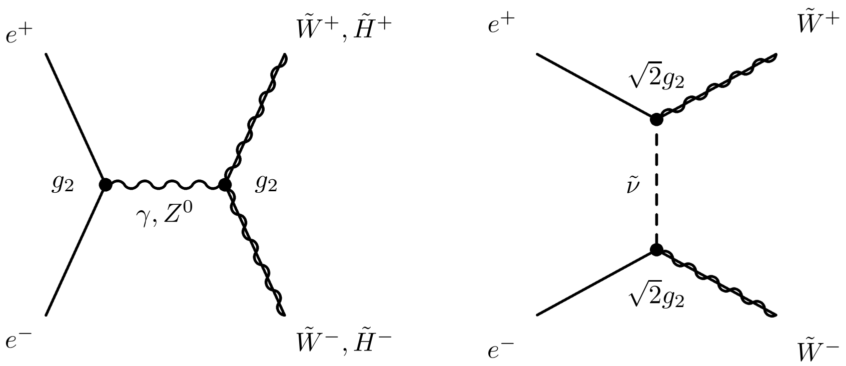

Figure 2.2: Feynman diagrams for chargino production in $\mathrm{e}^+\mathrm{e}^-$ collisions.

for the higgsinos. Therefore the production of higgsinos through the Z^0 exchange is suppressed compared to the winos.

The t–channel production occurs through $\tilde{\nu}$ exchange via a $(\lambda\phi\psi)$ and can (almost) only lead to winos in the final state since the vertex $(\psi\psi\phi)$ has a magnitude determined by a Yukawa coupling which is negligible for the electrons.

The expressions of the differential and total chargino production cross–section corresponding to the Feynman diagrams shown in Fig. 2.2 can be found in reference [68].

At LEP2, the typical chargino pair production cross–section are of the order of a few picobarns when considering high sneutrino masses. This makes the chargino signal one of the first to be discovered if kinematically allowed. Fig. C.6 shows the contours of constant σ_{tot} in the $(\mu,\ M_2)$ plane for three values of $\tan\beta$ (1, 1.5 and 35). A heavy sneutrino ($m_{\tilde{\nu}}$ = 1 TeV/c^2) has been assumed. The cross–section decreases globally when the chargino mass increases due to the β dependence of the cross–section. As can be seen, the cross–section dependence on $\tan\beta$ is weak except in the $M_2 \simeq |\mu|$, $\mu < 0$ region. Using

$$\xi \equiv \frac{\xi_0}{1\ +\ (1+\beta^2)\xi_0/4} \tag{2.21}$$

with $\xi_0\ \equiv\ s/m^2_{\tilde{\nu}}$ and β the chargino velocity, for small ξ the cross–section in the gaugino region is approximately [69]

$$\sigma_{total} \simeq f(\beta)\left[1 + \left(\frac{s}{s - M_Z^2}\right)^2 \left(\frac{1}{4\sin^2\theta_W}\right)^2 - \frac{|V_{11}|}{4\sin^2\theta_W}\left(1 + \frac{s}{s - M_Z^2}\,\frac{1}{4\sin^2\theta_W}\right)\xi\right] \quad (2.22)$$

where $f(\beta) = \frac{1}{2}\beta(3 - \beta^2)$. In the higgsino region

$$\sigma_{total} \simeq f(\beta)\left[1 + \left(\frac{s}{s - M_Z^2}\right)^2 \left(\frac{\frac{1}{2} - sin^2\theta_W}{1 - sin^2\theta_W}\right)^2\right] \quad (2.23)$$

As shown in Eq.(2.22), a strong sensitivity to $m_{\tilde{\nu}}$ is found in the gaugino region but disappears altogether in the higgsino region. The effect of the possible destructive interference between the chargino production channels can be observed in Fig. 2.3. The total chargino production cross–section for $\sqrt{s}$ = 208 GeV is plotted for three representative (μ, M_2, $\tan\beta$=1.5) points as a function of $m_{\tilde{\nu}}$. The chosen points are (μ, M_2) = (–400, 67.5) in the gaugino region (red line), (–50, 87.5) in the mixed region (green line) and (–74.5, 1000) in the far–higgsino region (blue line).

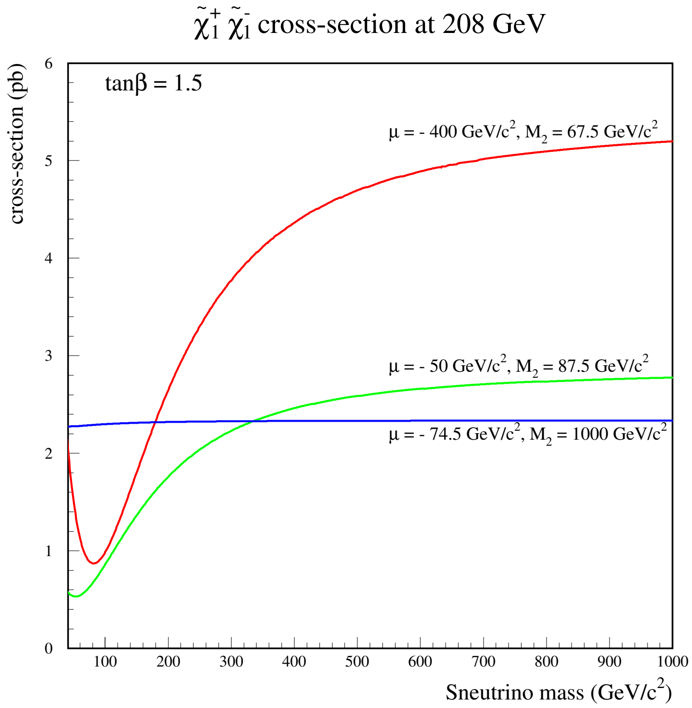

Figure 2.3: Chargino production cross–sections as a function of $m_{\tilde{\nu}}$ are plotted for $\tan\beta$ = 1.5 and the three representative (μ, M_2) points indicated in the figure. The red line corresponds to a chargino in the gaugino region, the blue line to the higgsino region and the green line to a chargino in a mixed region.

The $\tilde{\nu}$ diagram gives a large and destructive contribution for the gaugino (high $|\mu|$) and mixed gaugino–higgsino points when the $m_{\tilde{\nu}}$ is small. The minimum of the cross–section is found for a sneutrino mass around 80 GeV/c^2 in the pure gaugino case. In the mixed region it moves to a sneutrino mass around 60 GeV/c^2. As the higgsino component increases (high M_2), the dependence of the cross–section on $m_{\tilde{\nu}}$ decreases.

Another effect visible in the figure is that for high values of $m_{\tilde{\nu}}$ the cross–section is smaller for higher higgsino–like chargino field composition. As mentioned before, the coupling of the chargino to the Z^0 is stronger in the gaugino region.

2.4.1 Cross-section dependence on Initial State Radiation (ISR)

Before the production of the charginos, the incoming electron and positron may radiate a photon, modifying their momentum hence modifying the production cross-section for a given $\sqrt{s}$. This effect on the cross-section can be estimated by convoluting the cross-section with the probability of emission of a photon. This probability, for the radiation of one photon by the electron, is approximatively given by the formula [70]

$$P_\gamma(u_\gamma) = \frac{b}{u_\gamma^{1-b}}(\frac{1}{2}u_\gamma^2 - u_\gamma + 1) \tag{2.24}$$

where

$$u_\gamma = \frac{2k_\gamma}{\sqrt{s}} \text{ with } k_\gamma \equiv \text{photon momentum} \tag{2.25}$$

$$b = \frac{2\alpha}{\pi}(\ln\frac{s}{m_e^2} - 1) \tag{2.26}$$

b is obtained by integrating P_γ on all the solid angle. This effect is taken into account in this thesis.

2.5 Chargino signature in the SUGRA scheme

2.5.1 Chargino decays

Decays with SM vector boson emission

A gaugino-like chargino may decay through a $(A\lambda\lambda)$ gauge coupling to a vector boson and a gaugino. A higgsino-like chargino has a $(A\psi\psi)$ vertex leading to a vector boson and a higgsino. Both have electroweak strength

$$\left\{ \begin{array}{l} \tilde{\chi}_i^\pm \to \tilde{\chi}_j^0 + W^{\pm(*)} \\ \tilde{\chi}_2^\pm \to \tilde{\chi}_1^\pm + Z^{0(*)} \end{array} \right. \tag{2.27}$$

where the $*$ stands for the off-shell states. The decays occur through a transition between gaugino-like charginos and neutralinos and between higgsino-like charginos and neutralinos. The transitions from gaugino(higgsino)-like charginos to higgsino(gaugino) neutralinos are suppressed. In most of the parameter space, the lightest chargino and neutralino are of the same kind as can be seen in Fig. 2.1. If the gaugino mass unification condition is assumed, the decay of the lightest chargino leads, in most of the SUSY parameter space, directly to $\tilde{\chi}_1^0$ by the emission of a W. This behavior may be understood because the heavier neutralino states may not be kinematically accessible. Even if they are, the fact that when the lightest chargino is dominantly gaugino(higgsino)-like, the lightest neutralino will also be dominantly gaugino(higgsino)-like implies that the transition to $\tilde{\chi}_1^0$ is not suppressed and the decay will proceed preferentially into states providing the largest phase space, i.e. into the lightest neutralino. In the region approximatively defined by $-M_2 \leq \mu \leq -M_1$ where $M_{\tilde{\chi}_2^0}$ $< M_{\tilde{\chi}_1^\pm}$ (see Fig. 2.1). , the $\tilde{\chi}_1^\pm$ and the $\tilde{\chi}_2^0$ are higgsino-like and the $\tilde{\chi}_1^0$ is gaugino-like. In this region, the $\tilde{\chi}_1^\pm$ can first decay into $\tilde{\chi}_2^0$ which in turn will decay into $\tilde{\chi}_1^0$ with the emission of a Z^0, those decays are called cascade decays. When M_2 is not too large, i.e. $M_2 < 200\mathrm{GeV}/c^2$, these cascade decays can reach 30 % of branching ratios. For small $\tan\beta$, the $\tilde{\chi}_2^0$ can decay, via loops, into $\tilde{\chi}_1^0$ + γ (see Fig 2.4), giving instead topologies with isolated photon. Fig. C.7 shows the contours of constant value of the radiative branching fraction in the (μ, M_2) plane for three values of $\tan\beta$. As can be seen, the radiative decays are only significant in the region where $\mu \simeq -M_2$ and for small values of $\tan\beta$.

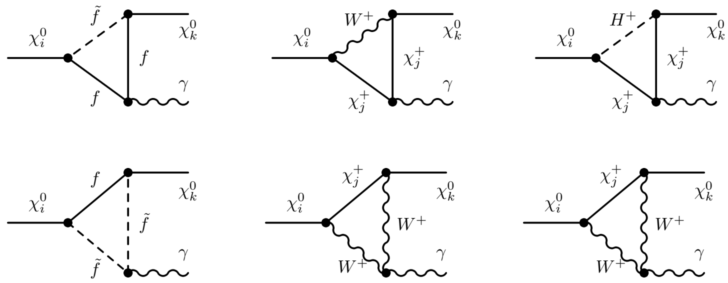

Figure 2.4: Radiative decays of the neutralinos.

Decays into sleptons

Provided the chargino contains at least a small wino component it may decay, similarly to the $W^\pm$, into a fermion-scalar pair with coupling ($\lambda\phi\psi$) of weak interaction strength. Since the squarks are probably heavier than the sleptons (due to the squark mass dependence on α_S [42]) the most likely decay will be into a lepton-slepton pair:

$$\tilde{\chi}_i^\pm \rightarrow \tilde{\nu} + \ell^\pm \ , \ \tilde{\ell}^\pm + \nu \tag{2.28}$$

assuming a slepton lighter than the chargino. As the coupling in the decay (Eq.(2.28)) is exclusively to winos, only left sleptons and leptons are obtained. The sleptons will further decay into their partner and a neutralino. This reaction could therefore significantly increase the leptonic branching fraction above the value of 1/3 expected for the $W^\pm$. Conversely, a lower branching fraction would be obtained in case of light squarks. These effects can still contribute if the sfermions are not allowed kinematically but are nevertheless light (i.e. a mass under 200 GeV/c^2). When the chargino is pure higgsino, it can still decay into sfermions, but only via the ($\tilde{H}\phi\psi$) Yukawa coupling. It would almost exclusively lead to states containing scalars from the third leptonic or hadronic families.

Decays into Higgses

Charginos can decay via ($\lambda\phi\psi$) gauge coupling into Higgses. Such vertices induce transition from gaugino to higgsino states and vice versa. This decay might dominate over the decay via vector bosons provided h^0 to be sufficiently light. Nevertheless, given the actual excluded mass range of the h^0, this would require the chargino to be rather heavy and unobservable at LEP.

In summary, assuming that there are no cascade decays and that the LSP is the first neutralino, then the two only possible decay modes of the lightest chargino are $\tilde{\chi}_1^{\pm} \rightarrow \tilde{\chi}_1^0\, l^{\pm}\, \nu$ and $\tilde{\chi}_1^{\pm} \rightarrow \tilde{\chi}_1^0\, q\, \bar{q}$ which take place through the Feynman diagrams depicted in Fig. 2.5.a-d.

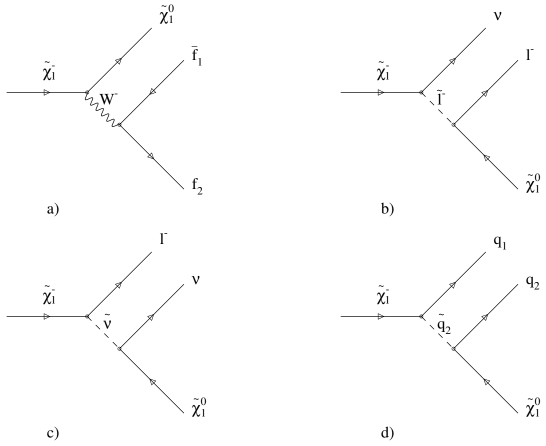

Figure 2.5: Feynman diagrams at tree-level for the lightest chargino decay

2.5.2 Leptonic branching fraction

The leptonic branching fraction B_ℓ of the chargino decay is an important parameter which will define the strategy of our search analyses. From what have been said above one may summarize the following dependence of B_ℓ:

- $B_\ell \sim$ 33 % when the sfermions are heavy.
- $B_\ell \sim$ 100 % when $m_{\tilde{\nu}} \leq M_{\tilde{\chi}_1^{\pm}}$ and the chargino is not purely higgsino.
- $B_\ell \sim$ 0 % when $\mathrm{m}_{\tilde{q}} \leq M_{\tilde{\chi}_1^{\pm}}$, if the chargino is not purely higgsino.
- B_ℓ variable when the gaugino component of the chargino is not negligible and there is at least one light sfermion (with mass smaller than 200 GeV/c^2). The growth of B_ℓ is much faster in the large $\tan\beta$ case than in the small $\tan\beta$ case. The B_ℓ will be variable as well in the case of cascade decay through $\tilde{\chi}_2^0$.

2.5.3 Mass difference $\Delta M = M_{\tilde{\chi}_1^{\pm}} - M_{\tilde{\chi}_1^0}$

The difference between the chargino and neutralino (LSP) masses ($\Delta M \equiv M_{\tilde{\chi}_1^{\pm}} - M_{\tilde{\chi}_1^0}$) has a high influence on the amount of missing momentum, visible energy and other variables characterizing the signal events (due to the 2 non-detected LSPs). Depending on the ΔM value of the chargino signal, the SM background types and the efficiency of the signal detection will change.

In Fig. C.5 the isocurves of ΔM in the (μ, M_2) plane are shown for three different values of $\tan\beta$. The degeneracy between the first chargino and the lightest neutralino (low ΔM) starts when the higgsino component of the chargino is dominant. In that case, both masses are determined by $|\mu|$.

The mass degeneracy is asymmetric in μ for low $\tan\beta$ values and is symmetric for high $\tan\beta$. For low $\tan\beta$, ΔM is lower for $\mu > 0$ than for $\mu < 0$.

2.6 Chargino signature in the GMSB scheme

In the GMSB scenarios the LSP is the gravitino[61]. It can be relevant for collider phenomenology because it contains as its longitudinal component the goldstino, which has a non–gravitational coupling to all sparticle–particle pairs ($\tilde{X}$,X). The decay rate found in Eq.(1.63) for $\tilde{X} \to X\tilde{G}$ is usually not fast enough to compete with other decays of sparticles $\tilde{X}$ except in the case where $\tilde{X}$ is the next–to–lightest supersymmetric particle (NLSP). It should always decay into its SM partner and the LSP gravitino. Hence if the NNLSP is produced, its dominant decay will proceed through the NLSP and the emission of a SM particle.

Any of the MSSM superpartners could be the NLSP. Nevertheless, since $\alpha_1 < \alpha_2$, α_3, those superpartners which have only $U(1)_Y$ interactions will tend to acquire the smallest masses. This means for instance that $\tilde{l}_R$ will be lighter than $\tilde{l}_L$ and the lightest neutralino(bino) will be lighter than the lightest chargino(wino).

Following the discussion in the last section, a likely NLSP candidate for a messenger index $N = 1$ is a neutralino(bino). Nevertheless, in the GMSB parameter space where the neutralino is the NLSP, the chargino is always much heavier than 100 GeV$/c^2$ when considering experimental results from the two TeVatron collaborations [90] and hence is not kinematically allowed in LEP2.

For $N > 1$, a likely candidate for the NLSP is a charged slepton $\tilde{\ell}$. Due to fact that the scalar masses evolution is enterely determined by their gauge couplings (as in SUGRA models), the sparticles of the first two generations are almost degenerate [3] (i.e. $m_{\tilde{\mu}_R} = m_{\tilde{e}_R} < m_{\tilde{\mu}_L} = m_{\tilde{e}_L}$). In contrast, $\tilde{\tau}_R$ may have a quite significant mixing with $\tilde{\tau}_L$. Therefore, the lightest stau mass eigenstate, $\tilde{\tau}_1$, is pushed to lower masses than $\tilde{e}_R$ or $\tilde{\mu}_R$, by an amount that depends very strongly on $\tan\beta$ and $|\mu|$. If $\tan\beta$ is not too large, the lightest stau eigenstate, $\tilde{\tau}_1$, is predominantly the right–handed partner and is nearly degenerate in mass with the other right–handed sleptons. Thus, they act as co–NLSPs. The only allowed decays for the three lightest leptons are $\tilde{e}_R \to e\tilde{\mathrm{G}}$, $\tilde{\mu}_R \to \mu\tilde{\mathrm{G}}$ and $\tilde{\tau}_1 \to \tau\tilde{\mathrm{G}}$. For larger values of $\tan\beta$, the lightest stau eigenstate is lighter than $\tilde{e}_R$, $\tilde{\mu}_R$ and decays of all other MSSM supersymmetric particles into it are kinematically allowed.

In the case of a $\tilde{\tau}_1$ NLSP, there are regions in parameter space where the chargino is light enough to be pair produced at LEP2. Fig. 2.6 from [71] shows the region in the Λ-$\tan\beta$ plane where the chargino mass is less than the beam energy (here 91.5 GeV) for $N = 2$ and 4.

For $N = 2$ and $M/\Lambda = 1.1$, there is a triangular region around $\Lambda \simeq 20\,TeV$ and $\tan\beta \simeq 13-22$ as shown in Fig. 2.6(left). For $N = 4$ the region expands somewhat around $\Lambda \simeq 13\ TeV$ and $\tan\beta \simeq 5 - 20$. The mass hierarchy in these regions is

$$m_{\tilde{\chi}^0_2} \geq m_{\tilde{\chi}^\pm_1} > m_{\tilde{e}_1,\tilde{\mu}_1} > m_{\tilde{\chi}^0_1} > m_{\tilde{\tau}_1} \ . \tag{2.29}$$

The scalars $\tilde{e}_1$ and $\tilde{\mu}_1$ are essentially the right-handed selectron and smuon and have equal masses. The only allowed decay mode for the chargino is: $\tilde{\chi}^+_1 \to \nu_\tau\tilde{\tau}_1$ (since the lighter $\tilde{e}_1$ and $\tilde{\mu}_1$ are essentially right handed the branching ratios of the two kinematically allowed decay modes, $\nu_e\tilde{e}_1$ and $\nu_\mu\tilde{\mu}_1$ are essentially zero. Moreover, the chargino is wino- and the neutralino is bino-like so the decay

[3] Almost no mixing occurs due to the tiny electron and muon Yukawa couplings.

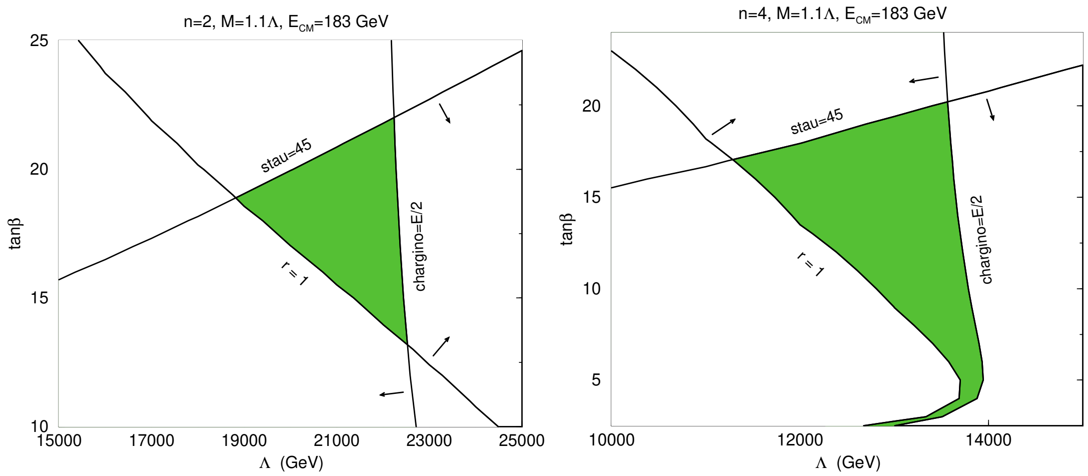

Figure 2.6: Allowed regions for chargino-pair production at LEPII with $\sqrt{s}$ = 183 GeV for (left) $N = 2,\ M = 1.1\Lambda$ and (right) $N = 4,\ M = 1.1\Lambda$. The constraints shown are: $m_{\tilde{\tau}_1} > 45$ GeV, $r \equiv m_{\tilde{\tau}_1}/m_{\tilde{\chi}_1^0} < 1$, and $m_{\tilde{\chi}_1^+} < 91.5\mathrm{GeV}/c^2$ [71].

of the chargino to the neutralino is suppressed [71].). The $\tilde{\tau}_1$ then decays to a τ-lepton and a gravitino with a 100% branching ratio.

In the present thesis chargino pair production will be considered with the $\tilde{\tau}_1$ NLSP. This channel is of outmost importance and could be the discovery channel since, if kinematically allowed, the chargino pair production reaches a very large cross-section with respect to the $\tilde{\tau}_1$ one. In this hypothesis, the chargino decays through the following chain

$$\tilde{\chi}_1^{\pm} \rightarrow \tilde{\tau}_1^{\pm}\nu \rightarrow \nu\tau^{\pm}\tilde{G} \tag{2.30}$$

Moreover, only extremely light gravitino masses will be investigated ($m_{\tilde{G}} \leq 1eV/c^2$) and so the stau decays promptly to a tau and a gravitino. Within this assumptions the chargino signature is almost identical to the chargino SUGRA one with $M_{\tilde{\chi}_1^0}$ = 0 GeV$/c^2$ and a light stau mass.

2.7 Theoretical assumptions

The searches described in this thesis have been carried out within the following assumptions

- *cMSSM*: The constrained Minimal Supersymmetric extension of the Standard Model has been assumed. Two different hypotheses have been considered on the SUSY breaking mechanism: the supergravity induced supersymmetry breaking (SUGRA) and the gauge–mediated supersymmetry breaking (GMSB). The search for charginos in the Anomalous Mediated Supersymmetry Breaking model (AMSB) is not described here. The AMSB theoretical framework is described in [64] and the DELPHI experimental results are given in [65].

- *R–parity conservation*: The implications of this conservation are that charginos are produced in pairs and the lightest supersymmetric particle is stable. It must be among the decay products of any sparticle.

- *Lightest supersymmetric particle: neutralino and gravitino*: Concerning the LSP the present analysis treats two cases. Firstly, it has been assumed that the lightest neutralino is the LSP, which is the most natural hypothesis in the cMSSM. In the GMSB scenarios, the LSP is the gravitino and the second lightest supersymmetric particle is, here, the lightest stau. It decays into a gravitino and a tau.

- *High m_0 value*: The value of the common scalar mass at the unification scale, m_0, has been fixed to 1 TeV/c^2 and consequently sleptons, squarks and sneutrinos have masses beyond the kinematic limit of LEP2. This assumption has important consequences in the possible chargino production and decay channels. Searches for charginos assuming low m_0 parameter values have been performed by the DELPHI Collaboration [72] by combining the analysis described in the present thesis and the slepton and neutralino analyses. The obtained results are not described in the present thesis.

- *Mass difference*: The mass difference $\Delta M = M_{\tilde{\chi}^\pm} - M_{\tilde{\chi}_1^0}$ plays an important role in the analysis of chargino events. In the SUGRA scheme charginos and neutralinos with mass differences ranging from 3 GeV/c^2 to 70 GeV/c^2 have been searched for. In the case of higher mass degeneracy between the chargino and the neutralino, dedicated analyses may be found in [72][73]. In the GMSB scheme ΔM (here defined as $M_{\tilde{\chi}^\pm} - M_{\tilde{\tau}_1}$) was required to be greater than 0.3 GeV/c^2 in order to suppress the decay of the chargino to the gravitino with emission of a $W^\pm$.

2.8 Thesis content

In this thesis, the SUGRA analysis is fully described. On the other hand, the GMSB analysis is described only in terms of the obtained mass limits (see section 8.2). In the GMSB scheme, in the hypothesis of low gravitino masses, the GMSB signatures are almost equivalent to the SUGRA ones assuming a massless neutralino. Hence, the GMSB analysis was set by means of the use of the SUGRA $\ell\ell$ selection functions of the highest ΔM region (fully described in chapter 6) where the efficiencies were recomputed using GMSB chargino samples.

Part II

Experimental Setup

Chapter 3

Experimental setup

3.1 The LEP collider

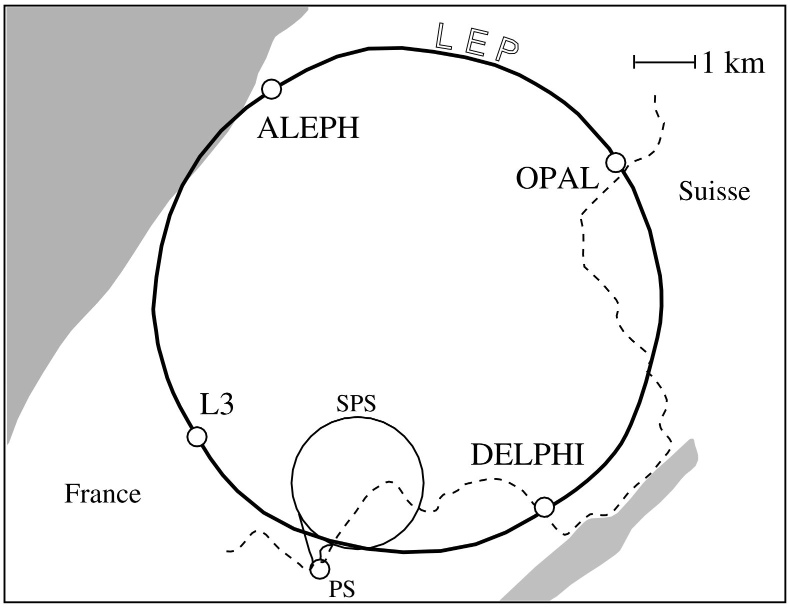

Figure 3.1: Schematic view of the CERN site at the border between Switzerland and France, situated between the Jura mountains and the Geneva airport (shaded in grey).

The Large Electron Positron (LEP) collider was built and operated by the European Organization for Nuclear Research (CERN) in Geneva; its geographical location is shown in Fig. 3.1. The electrons and positrons were produced and accelerated in a chain of accelerators before being injected into the LEP main ring, illustrated in Fig. 3.2. First of all the LEP Injector Linacs (LIL) produced electrons and positrons and accelerated them to 600 MeV. The Electron Positron Accumulator collected the electrons and positrons in bunches which were accelerated to 3.5 GeV in the Proton Synchrotron (PS). Before injecting the bunches into the LEP main ring, the Super Proton Synchrotron (SPS) accelerated them to 22 GeV. The electrons and positrons were collected in four bunches inside LEP, increasing their number until the maximum beam current was reached. Then the LEP RF voltages were increased, accelerating the electrons and positrons to physics energies. When the beam reached stable conditions at the correct energy, the super-conducting quadrupole magnets a few meters away

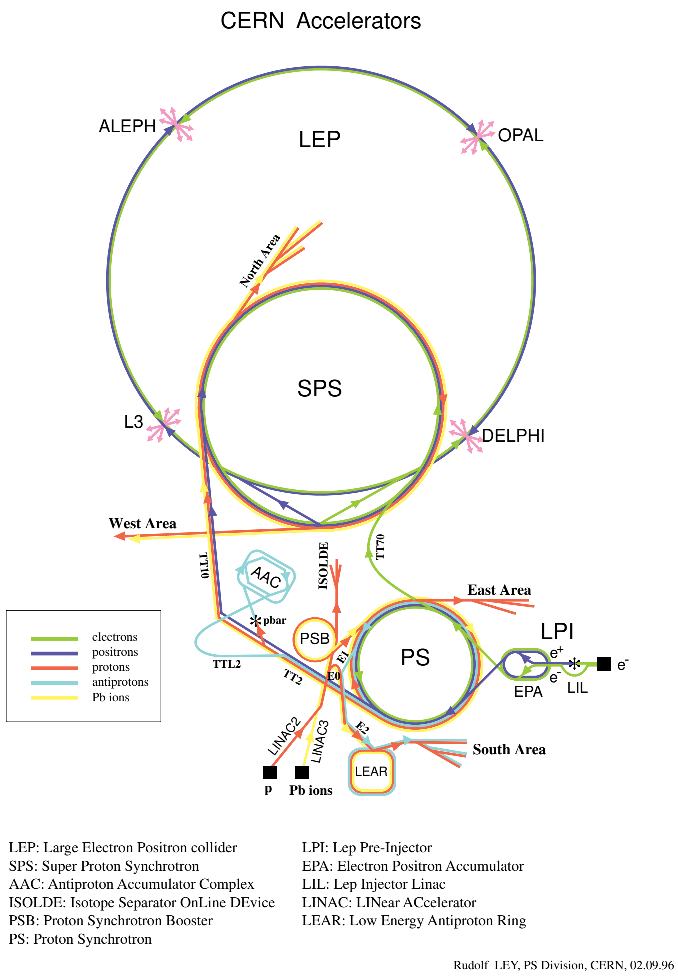

Figure 3.2: Schematic drawing of the LEP e^+e^- injection and accelerator set-up.

from the interaction points focused the beams in the interaction region. As soon as "colliding beams" settings were declared, the collaborations ramped up the voltages of their detectors and started recording data of the physics processes that occurred each time an e^- and e^+ collided. A "fill" of electrons and positrons could typically be kept inside LEP for several hours until the beam was dumped and the whole procedure was repeated from the beginning.

The LEP ring was located in an almost circular tunnel, on average 100 m below the surface. In eight regions the tunnel was straight over a distance of a few hundred meters. In four of these straight sections, large underground halls housed the detectors that were operated by the 4 LEP collaborations: ALEPH, DELPHI, L3 and OPAL. The particles traveled inside a vacuum pipe, surrounded by magnets to keep them in their orbit and radio frequency (RF) cavities to accelerate them. During the first years (LEP1) copper cavities were used, allowing centre-of-mass energies around the Z^0 peak, while during the LEP2 phase super-conducting cavities were installed every year, reaching centre-of-mass energies up to 209 GeV in 2000 — the final year of LEP running. Table 3.1 shows the different delivered energies between 1995 and 2000. The physical motivations to increase the energy of LEP2 were first, to test the validity of the Standard Model at these energies, in particular the study of the production of the Z^0Z^0 and WW pairs and, secondly, the search for new particles, especially the Higgs boson and supersymmetric particles.

YEAR	1995	1996	1997	1998	1999	2000
$\sqrt{s}$ (GeV)	130, 136	161, 172	183, 130, 136	189	192,196,200,202	204 $\rightarrow$ 209

Table 3.1: Delivered energies (GeV) between 1995 and 2000.

LEP operation during 2000 had two significant differences with respect to previous years, both of which were motivated by the aim of delivering luminosity (defined in page 59) at the highest possible collision energies [74].

- **Miniramps**
  Fills were started at a given beam energy safely within the capabilities of the RF system. When the beam currents had decayed significantly, typically after an hour, the dipoles were ramped and luminosity delivered at a higher energy. This procedure was repeated until the energy was at the limit of the RF, and data taken until the beam was lost through a klystron trip. These *miniramps* lasted less than a minute, and varied in step size with a mean value of 600 MeV. Hardware signals were used to flag the start and end of miniramps to the experiments, and this information was recorded with the logged triggers. The starting energy of fills, and the precise strategy of miniramping varied throughout the year, depending on the status of the RF system.

- **Bending Field Spreading (BFS)**
  Given a fixed RF acceleration voltage the synchrotron radiation power depends on how the bending field is distributed. During the 2000 run $\sim$ 100 previously unconnected corrector magnets were powered, in order to exploit this dependence to boost the beam energies by 0.18 GeV with respect to what would otherwise be possible. The BFS scheme was first enabled soon after the start of run, and increased in power for the final three months of operation.

To illustrate the continuous energy distribution due to this *miniramp* technique, the luminosity collected in a single experiment as a function of $\sqrt{s}$ is shown in Fig. 3.3 (left plot), excluding the Z^0 calibration fills. The mean energy was 205.9 GeV, with some running up to almost 209 GeV. The distribution of $\sqrt{s}$ with time into the run is shown in Fig. 3.3 (right plot).

3.1.0.1 LEP beam energy loss and variation

The RF cavities were needed not only for acceleration, but also to continuously replenish the energy that was lost "in orbit" due to the synchrotron radiation emitted by the electrons and positrons moving through the LEP magnetic field. The radiated power for a relativistic particle is given by

$$P_{\mathrm{radiated}} = \frac{q^2 c}{6\pi\epsilon_0}\frac{\gamma^4\beta^4}{\rho^2} \tag{3.1}$$

where $\gamma = E_{\mathrm{beam}}/m_e$, q denotes the charge of the particle and ρ is the local bending radius. The velocity of the electrons and positrons in the LEP beam was very close to the speed of light, $\beta \equiv v/c \approx 1$, and assuming that the local bending radius inside all magnets was constant the energy loss was equal to:

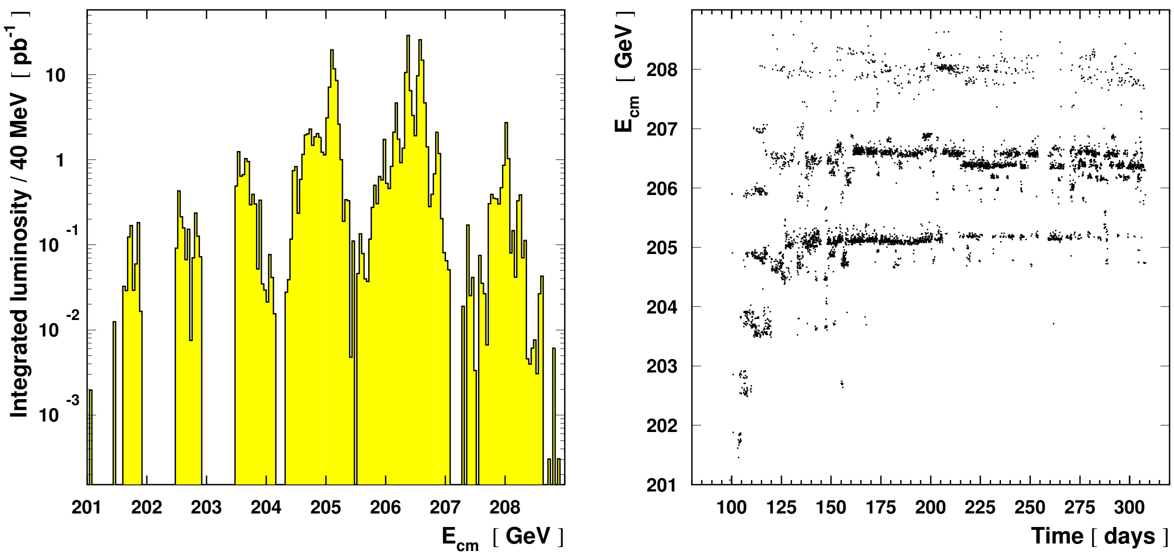

Figure 3.3: Left plot shows the integrated luminosity in bins of $\sqrt{s}$ for a single LEP experiment in 2000. Right plot shows the variation of $\sqrt{s}$ against day of year; each entry corresponds to the mean energy for a data file of maximum length $\sim$ 30 minutes.

$$E_{\text{loss}} = 8.85 \times 10^{-5} \frac{E_{\text{beam}}^4}{\rho} \text{ MeV (per turn)} \tag{3.2}$$

where E_{beam} is given in GeV and ρ in km. This corresponded to ≈ 2.5 GeV per turn at $\sqrt{s} = 209$ GeV. The accelerating RF cavities were located in the straight sections while the bending field was concentrated in the arc sections, so the energy of the particles was not constant along the circumference of LEP, but showed a saw-tooth like dependence with variations in energy of about $E_{\text{loss}} \sim 600$ MeV.

Such variations in energy could be monitored and had been accurately modeled. The results of a simulation are shown in Fig. 3.4.

3.1.0.2 LEP beam energy model

The LEP Beam Energy Model describes all relative variations in energy taking into account the precise RF and magnet configuration at all times. Additionally it includes small corrections in order to reach a systematic precision better than 2 MeV at the Z^0 peak [75]. An example of the kind of effects which needed to be taken into account is the gravitational pull of the Moon and Sun distorting the Earth's crust and thereby periodically changing the circumference of the LEP ring by approximately ± 0.5 mm. In Fig. 3.5 the measured effect on the LEP beam energy is compared to the prediction from a geological model.

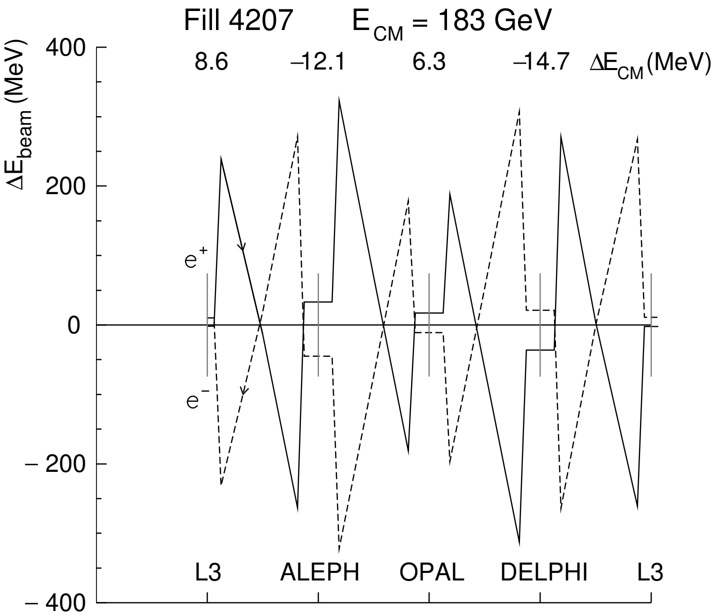

Figure 3.4: The energy "saw-tooth" (see text) for a typical RF configuration at a centre-of-mass energy of 183 GeV. The variations in energy are shown separately for the electron beam (dotted line) and positron beam (solid line). $\Delta E = 0$ corresponds to the average LEP energy [74] for this fill.

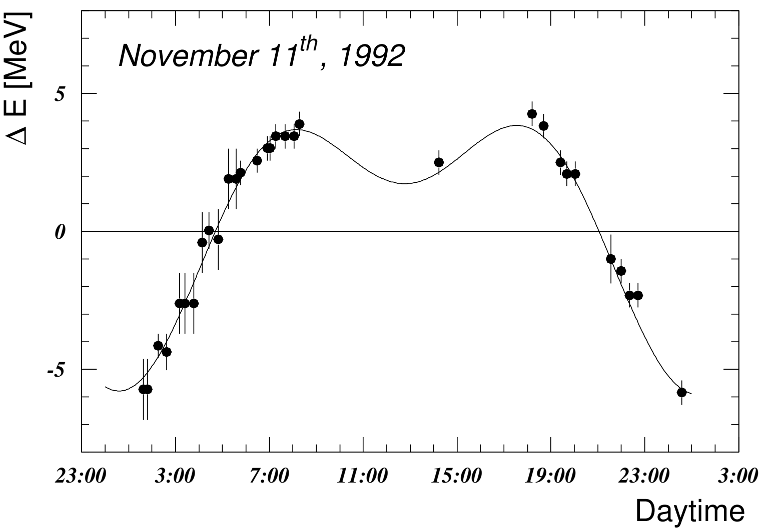

Figure 3.5: The shift of the LEP beam energy during a full Moon tide. The measured energy is compared to the prediction from a geological model [76].

3.1.0.3 Resonant De-Polarization

The calibration of the absolute energy scale was based on the method of Resonant De-Polarization (RDP). The emission of synchrotron radiation leads to the build-up of transverse beam polarization [1] in e^+e^- storage rings. Application of a small RF magnetic field perpendicular to the LEP bending field rotated the spins of the electrons in the beam, and destroyed the polarization, provided the applied RF frequency matched the natural spin precession frequency which was proportional to the beam energy:

$$\nu = \frac{g_e - 2}{2} \frac{E_{\mathrm{beam}}}{m_e c^2} \tag{3.3}$$

where $(g_e - 2)/2$ is the electron anomalous magnetic moment and m_e is its mass. Using this method a precision better than 1 MeV had been achieved.

3.1.0.4 Energy calibration at LEP2

Unfortunately, for beam energies at LEP2 a direct calibration using the RDP technique was not possible, because at energies above 60 GeV transverse polarization does not build up (due to the increased beam energy spread). Instead, one had to rely on magnetic extrapolation. In 1997 sixteen Nuclear Magnetic Resonance (NMR) probes were installed in the arc sections of LEP to continuously monitor the local magnetic bending fields. These probes were calibrated with RDP energy measurements in the region between 41 and 61 GeV, and were then used to determine the beam energy during physics conditions by means of a linear extrapolation. A similar magnetic extrapolation could be done using the flux loop system that was installed in the LEP dipole magnets, covering 96.5% of the total bending field. This measured the change of the bending field through magnetic induction during magnet cycling. A comparison of these two methods showed a difference of about 10-15 MeV for a beam energy of 94.5 GeV. This extrapolation uncertainty constituted the largest contribution to the systematic error quoted by the LEP energy working group. Numerous other possible sources of systematics have been studied and were taken into account. For illustrative purposes the complete list of error contributions is shown in Table 3.2. A precise description can be found in [74].

3.1.0.5 Energy Spread

The energy calibration described above determined the average energy of the beam. From event to event, however, the actual e^+e^- centre-of-mass energy $\sqrt{s} = 2 \cdot E_{\mathrm{beam}}$ showed a statistical random variation due to the natural energy spread σ_E of electrons and positrons in the beam. This spread could be predicted for certain settings of the beam optics, energy and RF frequency shift, or derived from the longitudinal size of the interaction region σ_z^{IP} that was measured by the experiments, via the relation

$$\frac{\sigma_E}{E_{\mathrm{beam}}} \propto \omega_{\mathrm{rev}} Q_s \sigma_z^{\mathrm{IP}} \tag{3.4}$$

This corresponds to a typical spread in $\sqrt{s}$ of the order of 200 MeV.

[1] This effect was first described by Sokolov and Ternov [77].

Source	uncertainty [MeV]			
	1997	1998	1999	2000
Extrapolation from NMR–polarization:				
NMR rms/$\sqrt{N}$ at physics energy	10	8	11	13
Variations from calibration procedure	5	4	3	3
Flux-loop test of extrapolation:				
NMR flux-loop difference at physics energy	20	15	15	15
Field not measured by flux loop	5	5	5	5
Polarization systematic	1	1	1	1
e^+e^- energy difference	2	2	2	2
Optics difference	4	6	4	4
Corrector effects	3	4	2	13
Tide	1	1	1	1
Initial dipole energy	2	1	1	2
Dipole rise modeling	1	1	1	1
IP specific corrections ($\delta E_{\rm CM}/2$):				
RF model	4	4	5	5
Dispersion	1	1	1	1
Total	25	20	21	25

Table 3.2: List of contributions to the uncertainty on the LEP beam energy calibration [74].

3.1.0.6 Luminosity

Another important collider parameter is the luminosity. The instantaneous luminosity is related to the number of particles that cross the collision region per unit of (transverse) area per second. In the case of an e^+e^- collider, the luminosity can be written as:

$$\mathcal{L} = \frac{N_e N_p n_b f}{4\pi\sigma_x\sigma_y} \tag{3.5}$$

where N_e and N_p are the number of electrons and positrons per bunch, n_b the number of bunches per beam in the ring, f the rotation frequency and σ_x and σ_y the transverse sections of the beams. The event rate $\dot{N}$ of a physical process with a cross-section $\sigma_{\rm proc}$ is proportional to the luminosity $\mathcal{L}$:

$$\dot{N} = \mathcal{L} \cdot \sigma_{\rm proc} \tag{3.6}$$

The number of events available for physics analysis is therefore determined by the luminosity, integrated over the period of data taking:

$$\int_{\Delta t} \mathcal{L}\mathrm{d}t = \frac{N}{\sigma_{\mathrm{proc}}} \tag{3.7}$$

As the cross-sections for typical processes studied at LEP are usually expressed in pb (where 10^{12} pb $=$ 1 b $\equiv 10^{-28}$ m^2), the integrated luminosity is often quoted in units of inverse cross-section such as pb^{-1}. A high integrated luminosity is desirable to obtain the best statistical precision on a measurement or increase the reach of a particle search. LEP has surpassed all expectations by delivering $\approx$ 1000 pb^{-1} of integrated luminosity to each of the LEP experiments during the LEP program, where the original aim was 800 pb^{-1} per experiment. The integrated luminosity day by day provided by LEP to each one of the four experiments since 1989 is shown in Fig. 3.6. As can be seen, 1998 was the first year of data taking at high luminosity.
The most precise determination of the luminosity at LEP was obtained by measuring the rate of small angle Bhabha scattering ($e^+e^- \rightarrow e^+e^-$ ($n\gamma$)) events [2]. The choice of Bhabha scattering as the reference process is due to the following reasons:

1. it is mainly a QED process and therefore the cross-section can be calculated with high precision (its relative uncertainty is about 0.15 %),

2. it has a large cross–section, which ensures the statistical accuracy of the measurement and allows to study the systematics without any statistical limitation,

3. it has a simple signature, allowing for a selection of the events with high efficiency, no background contamination and a well known acceptance, which guarantees an accurate control of the systematics.

The DELPHI sub-detector used for the Bhabha selection was the STIC (see page 63), a second generation luminometer, installed inside DELPHI at the beginning of 1994. In order to take advantage of the $1/\theta^3$ dependence [3] of the Bhabha cross–section, the STIC luminometer sat at very low angle with respect to the LEP beam-pipe and thus had provided a measurement of the luminosity using very high statistics. This permitted to achieve a relative uncertainty on the integrated luminosity measured by DELPHI, below 2 per mill during LEP1 operation [78] and below 6 per mill during LEP2 operation [79]. Those uncertainties are dominated by systematics [78] [79] which consist mainly of :

Source	$\Delta\mathcal{L}/\mathcal{L}$	
	LEP1	LEP2
uncertainty on the inner edge size	0.04%	0.4%
uncertainties from the beams (IP,energy)	0.06%	0.05%
Bhabha cross-section theoretical uncertainty	0.15%	0.15%

Table 3.3: Main contributions to the total uncertainty on the integrated luminosity measurement by DELPHI.

[2] knowing the rate, the cross-section and the DELPHI measurement efficiency of the Bhabha process, the integrated luminosity can be computed using Eq.(3.7).

[3] see Fig. 3.8 for the DELPHI coordinate system definition.

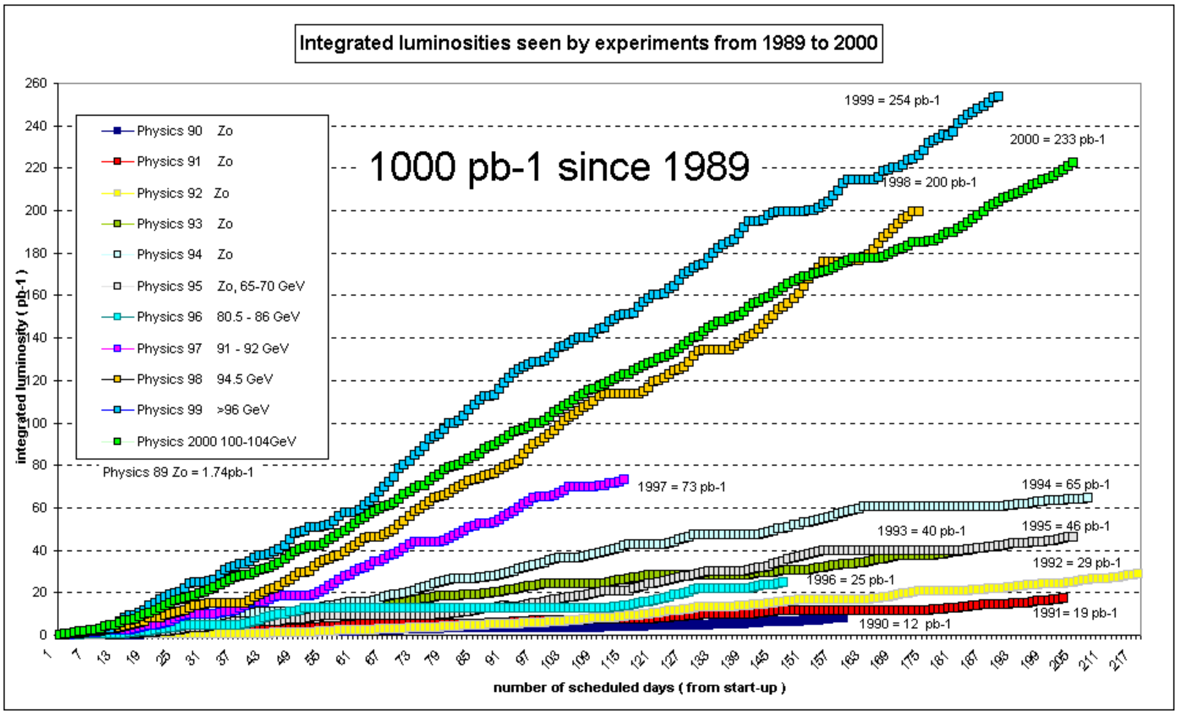

Figure 3.6: Integrated luminosity provided by LEP during 1989-2000.

3.2 The DELPHI detector

The DELPHI detector (DEtector with Lepton, Photon and Hadron Identification) was one of the four detectors operating at LEP since 1989. It was designed as a general purpose detector to cover all physics channels at LEP1 and LEP2. It was characterized by powerful particle identification, three–dimensional information, high granularity over a 4π solid angle and precise vertex determination.

DELPHI consisted of two parts: a central cylindrical section ("barrel") which covered 70 % of the solid angle and two end–caps ("forward" regions). Both sections were divided radially from the interaction point in different sub-detector layers. The end–caps could be moved to allow access to the sub-detectors. Fig. 3.7 shows a general scheme of the detector. The overall length and diameter of DELPHI were over 10 m and the total weight was 3500 tons,

In the standard DELPHI coordinate system, the z axis is along the electron beam direction, the x axis points toward the center of LEP and the y axis points upwards. The polar angle to the z axis is called θ and the azimuthal angle around the z axis is called ϕ; the radial coordinate is $R = \sqrt{x^2 + y^2}$. The "barrel" region covered $40° \leq \theta \leq 140°$.

In the design of DELPHI special emphasis was put on charged particle identification. In particular the Ring Imaging CHerenkov (RICH) detectors provided particle identification capabilities unique among the 4 LEP experiments. Also the high precision silicon Vertex Detector provided excellent identification of b-quark jets through secondary vertex reconstruction. However, the analysis presented here did not exploit DELPHI's extended particle identification capabilities. The information from the RICH detectors was not used at all in this analysis.

The experimental physics measurement relies mainly on the reconstruction of jets and identification of isolated leptons and photons. These functions all rely on tracking (for the detection of charged particles) and calorimetry (for the detection of both charged and neutral particles). Moreover, in

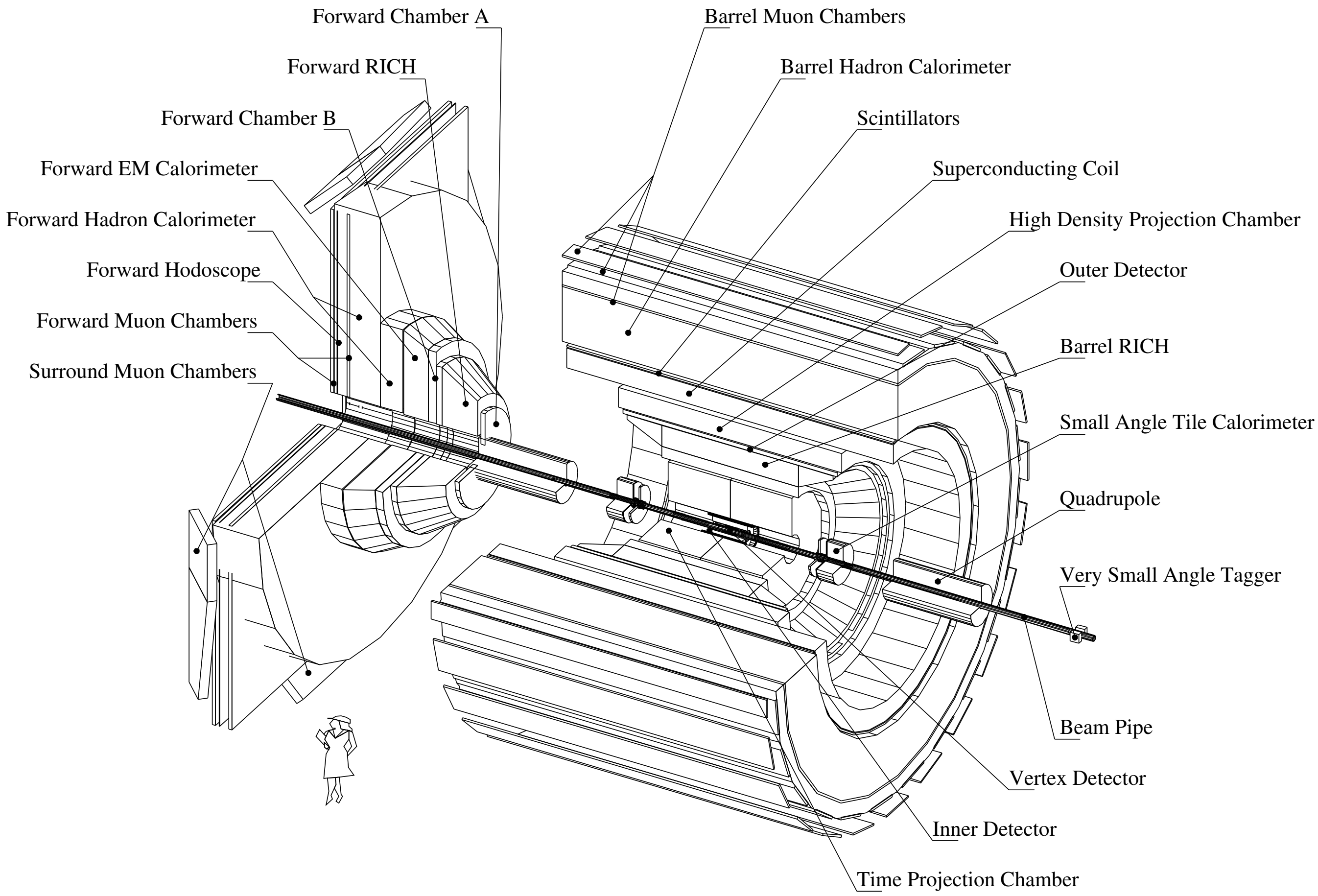

Figure 3.7: Overview of the DELPHI detector. .

order to be sensitive to possible new physics whose experimental signatures are based on missing energy and momentum in the event (see in next chapter), a hermetic detector is needed. Hence, the sub-detectors relevant for the present analysis are:

Tracking: The DELPHI tracking system in the barrel region consisted of four detectors at different radii centered at the beam axis. They were surrounded by a super-conducting solenoidal coil with an inner diameter of 5.2 m and a length of 7.5 m providing a homogeneous magnetic field of 1.23 Tesla aligned along the z axis. The bending radius of charged particle tracks in the magnetic field as recorded by the DELPHI tracking detectors was used to measure the momentum/charge ratio of the corresponding particle. The system consisted of the Vertex Detector (VD), Inner Detector (ID), Time Projection Chamber (TPC) and the Outer Detector (OD). Out of these detectors the main tracking device was the TPC, which was able to reconstruct 3D tracks with good resolution over a large volume.

The inclusion of the RICH system inside the tracking volume limited the volume available for other tracking systems, in particular the TPC. Hence, in order to have precise tracking with adequate lever arm for the precise reconstruction of high momentum tracks, an additional layer of tracking (i.e. the Outer Detector) was included outside the RICH but still inside the solenoid magnetic field.

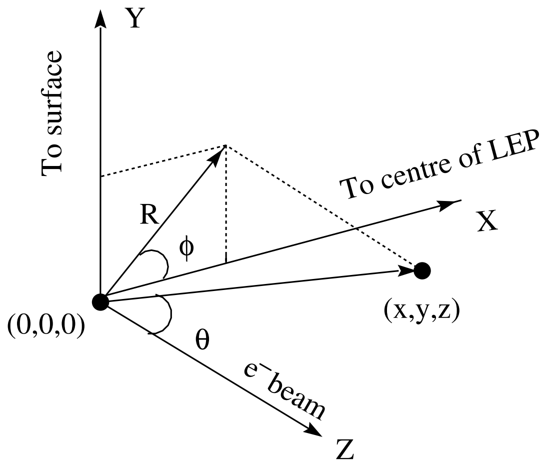

Figure 3.8: In the standard DELPHI coordinate system, the origin is the nominal interaction point, which coincides with the geometrical center of the detector. The z axis points along the flight direction of the beam electrons, the x axis in the horizontal plane toward the centre of LEP, and the y axis points upwards. Cylindrical coordinates (R,ϕ,θ) are defined with respect to the Cartesian system in the usual way.

Also in the forward regions ($11° \leq \theta \leq 33°$ and $147° \leq \theta \leq 169°$) a tracking detector was placed before (Forward Chambers A, FCA) and just after (Forward Chambers B, FCB) the Forward RICH. The outer layer of DELPHI consisted of the Barrel, Forward and Surround muon chambers (MUB, MUF and SMC).

Calorimetry: The DELPHI electromagnetic calorimeters were the High density Projection Chamber (HPC) located in the barrel on the inside of the solenoid, and the lead-glass Forward Electro-Magnetic Calorimeter (FEMC) in the end-caps. The Hadron Calorimeter (HAC) was an iron-gas sampling calorimeter integrated in the iron return yoke of the solenoid, covering the whole polar angle between 10° and 170°. On both sides of the interaction region, about 2 m away, the Small angle Tile Calorimeter (STIC) enclosed the beam-pipe, covering the polar angle regions between about $1.7°$ and $10°$. This electromagnetic calorimeter was also used for the luminosity measurements based on small angle Bhabha scattering.

Hermeticity taggers: The barrel electromagnetic calorimeter (HPC) consisted of 144 modules, arranged in six rings with 24 sectors. Gaps between modules were about 1 cm in ϕ and z. At θ = 90° there was a 7.5 cm gap to accommodate a stiffening ring for the cryostat. This central z gap and all the ϕ cracks pointed straight back to the interaction region making possible for particles to escape undetected. In addition, a gap of 5° was located between the HPC and FEMC at $\theta \approx 40°$. Therefore, in order to achieve complete hermeticity for high energy photon detection, three supplementary photon taggers were installed in the cable duct regions:

- 40°–taggers: Three concentric rings of lead–scintillator counters were mounted to cover the holes of the complicated geometry between the HPC and the FEMC. They were installed between the barrel and the forward RICHes. Each counter consisted of a 2 cm thick lead absorber and 1 cm thick scintillator. The light collection was done via wavelength–shifting fibers glued to the scintillator side. They connected the scintillator to fine–mesh photo-multipliers tubes, which could operate in the magnetic field.

- 90°–taggers: A gap of $\sim 2^\circ$ was located in the HPC at θ = 90°. A system of 24 counters was installed at 2.1 meters from the interaction point. They consists of 2 cm thick scintillator preceded with 2 cm thick lead absorber. They were read–out via wavelength–shifting fibers to photo-multipliers mounted outside the magnetic field.
- ϕ–taggers were installed to cover the cracks between the HPC modules. The read–out system was the same as in the 90°–taggers.

More details about the DELPHI sub-detectors can be found in [80]. After a brief overview of some further points concerning the DELPHI data processing in the next paragraph, section 3.4 concentrates on the reconstruction of muons, electrons, photons and jets.

3.3 Trigger, data stream and simulation

The DELPHI trigger system consisted of four levels. The first two levels were fully electronic and synchronized with the beam crossing (every 22 μs), making their trigger decision within 3.5 μs and 40 μs respectively. The third and fourth levels were slower (software based) and asynchronous with the beam. The trigger efficiency for chargino-like events selected by the analysis is practically 100% with respect to the efficiency for the Bhabha events used to define the integrated luminosity.

Online system For all events passing the trigger, the DELPHI data acquisition system collected the raw digitized data from the event buffers from each of the sub-detector systems. The data were written to disk and then stored on magnetic tape for later analysis. Information about the status of the sub-detectors and LEP, calibration constants relevant for data reconstruction, or other specific conditions at a given moment were kept in a database.

Offline system The DELPHI reconstruction program DELANA [81] reconstructed particles by applying pattern recognition and track fitting to combine information from different sub-detectors. It also used the information stored in the database. Some particle identification was done already at this stage and a basic event classification was performed. The output from DELANA was stored on magnetic Data Summary Tapes (DST), from where it is available for physics analysis.

The analysis presented here relied on the standard DELPHI software packages PHDST [82] for reading data from the DST, SKELANA [83] providing a convenient analysis framework and SUSANA for its routines aimed at the discovery of supersymmetric signal.

Alternatively, the working of the DELPHI detector can be simulated using the DELphi SIMulation program DELSIM [84]. Applied to simulated particles produced by a Monte Carlo generator this package simulates the detailed response of the DELPHI detector to the particles crossing the detector, taking granularity, resolution and efficiencies of the detector into account. The output of DELSIM is in raw data format, to be analysed further by DELANA in an manner identical to the real data.

3.4 Reconstruction of leptons, photons and jets

In this section a short description is given of the standard tools used for the identification of leptons, photons and jets used in the present work.

electrons and photons are identified and distinguished using the REMCLU (Reconstruction of ElectroMagnetic CLUsters) software package [85]: electrons are identified as a track in the central tracking chamber whose extrapolation points to a shower in the electromagnetic calorimeter, without associated activity in the hadron calorimeter. The ratio of the shower energy E and the measured track momentum p is expected to be close to 1 (compared to $E/p < 0.05$ for muons), and the REMCLU package makes an empirical combination of the two to obtain a best estimate of the electron energy, with a resolution between $\approx 5\%$ and $\approx 15\%$, depending on the electron energy and the polar angle. Both the identification and the energy resolution are hampered by interactions that electrons can have before reaching the calorimeters, especially in the forward region.

Photons are also treated by REMCLU, being identified as electromagnetic clusters without an associated track. Complications arise from photon conversion into e^+e^- pairs before the calorimeter. About 40% of all photons convert before reaching the HPC, including about 7% even before reaching the TPC, thus creating visible tracks.

muons can be identified with excellent efficiency by their minimum ionizing signature in the calorimeters, complemented with at least one hit in the muon chambers. Their momentum can be measured with a good resolution of about 3% in the momentum range of interest (5 - 70 GeV/c).

jets can be identified/built using several different clusterization algorithms [86] [87]. Their main goal is to reverse the fragmentation and hadronization steps in order to access initial parton informations. In all cases, first, all particles are considered as jets/clusters, then a separation distance in the 4-momentum space [4] is defined and the first two particles found with the lowest separation in terms of the defined distance are associated to form a new jet (i.e. their four-momenta are added vectorially to give the energy and momentum of the new cluster/jet.) This last procedure is repeated until the required number of jet(s) is found (`DURHAM` [86]) or when the remaining jet(s) have a separation greater than a minimal required distance (`LUCLUS` [87]). In this work, the `LUCLUS` algorithm has been chosen for the jets clusterization/building requiring the separation distance to be greater than 10 GeV/c. The separation distance d_{ij} is given by Eq.(3.8).

$$d_{ij}^2 = \frac{1}{2}\left(|\mathbf{p}_i|\,|\mathbf{p}_j| - \mathbf{p}_i \cdot \mathbf{p}_j\right) \frac{4\,|\mathbf{p}_i|\,|\mathbf{p}_j|}{(|\mathbf{p}_i| + |\mathbf{p}_j|)^2} = \frac{4\,|\mathbf{p}_i|^2\,|\mathbf{p}_j|^2\,\sin^2(\theta_{ij}/2)}{(|\mathbf{p}_i| + |\mathbf{p}_j|)^2}\,. \tag{3.8}$$

where $\mathbf{p}_{i,j}$ are the four-momenta of clusters i and j, and θ_{ij} is their separation angle.

[4] The definition of this distance depends on the chosen algorithm.

Part III

Chargino Search

Chapter 4

Data samples and chargino signal

This chapter describes the data samples that have been analyzed. In this work, the 451 pb^{-1} recorded by DELPHI from 192 to 209 GeV during the years 1999 and 2000 have been investigated. Previous chargino searches performed by the DELPHI collaboration may be found in the following papers [88]. Then, the investigated decay modes of the chargino and the signal simulation characteristics are given.

4.1 Data samples

An analysis of the data collected in the years 1999 and 2000 was performed. More emphasis will be put on the analysis of data recorded in the year 2000 since, as will be seen in chapter 8, this is the sample which has the highest statistical significance on the mass and cross-section limits.

In 1999, the DELPHI detector collected about 227 pb^{-1} around four different $\sqrt{s}$. Namely, 25.9 pb^{-1} around 192 GeV, 76.4 pb^{-1} around 196 GeV, 83.4 pb^{-1} around 200 GeV and 40.6 pb^{-1} around 202 GeV. During year 2000 DELPHI collected data in the centre-of-mass energies ranging from 201.5 to its historical maximum value of 208.8 GeV(thanks to the miniramp technique). The average centre-of-mass energy was $<\sqrt{s}>= 206$ GeV and the total integrated luminosity amounted to about 224 pb^{-1}.

Unfortunately, on September 1$^{\mathrm{st}}$ 2000, sector 6 of the TPC (corresponding to 1/12 of the TPC acceptance) failed beyond repair due to a loose wire that melted to another wire inside the chamber triggering continuous shortcuts, hence preventing the increase of the current in the chamber. This makes this sector unusable.

In order to recover from this situation, a software reshuffling was performed requiring modifications of the pattern recognition. This permitted to recover part of the track information in this sector acceptance but still affected the quality of charged track reconstruction.

The accumulated integrated luminosities with and without a working sector 6 were respectively 164 pb^{-1} and 60 pb^{-1} at average centre-of-mass energies around 206 GeV. The reprocessing (the software and pattern recognition version) of the data with TPC sector 6 on(off) is called reprocessing C1(S1).

Fig 4.1 shows the integrated luminosity versus $\sqrt{s}$ for the data recorded in year 2000 with and without sector 6.

In order to increase the sensitivity for a discovery, the data collected in 2000 were divided into 4 regions of centre-of-mass energy as given in Table 4.1 [1].

[1]The three energy bins for the period in which the detector was fully operational will be referred to in the text by the centre-of-mass energy of the background simulation with which they are compared. Namely, 205, 206 and 208 GeV (see Table 4.2)

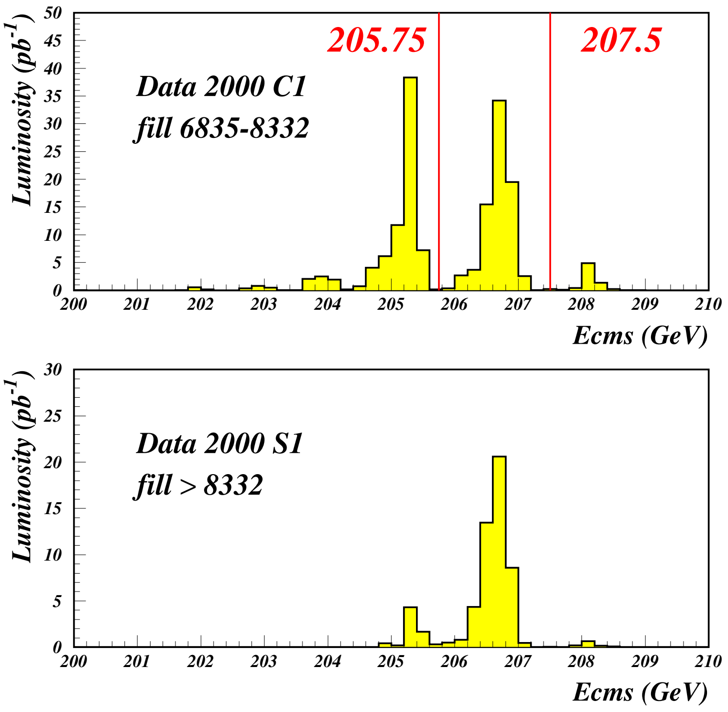

Figure 4.1: Integrated luminosity versus the $\sqrt{s}$ for the data recorded in year 2000 with and without sector 6.

$\sqrt{s}$ region of analysis			$\mathcal{L}$ (pb^{-1})	$<\sqrt{s}>$ (GeV)
1	Sector 6 On	$\sqrt{s}\leq$ 205.75 GeV	77.7 $\pm$ 0.2	204.8
2	Sector 6 On	205.75 $<\sqrt{s}\leq$ 207.5 GeV	79.4 $\pm$ 0.2	206.5
3	Sector 6 On	207.5 GeV$<\sqrt{s}$	7.1 $\pm$ 0.1	208.0
4	Sector 6 Off	all $\sqrt{s}$	60.1 $\pm$ 0.1	206.3

Table 4.1: Definition of the $\sqrt{s}$ regions used to analyze the data collected in 2000.

Finally, Table 4.2 gives the $\sqrt{s}$ and integrated luminosities of the real data and background simulations for the eight windows of analysis.

4.2 Investigated decay modes

All the possible decays of a pair of lightest charginos, in terms of the fermions/boson(s) present in the final states, were considered in this analysis. The possible decays can lead to the following final states (including cascade decays):

Year	$<\sqrt{s}>$ (GeV) real data	$\sqrt{s}$ (GeV) simulation	integrated luminosity (pb^{-1})
1999 C1	191.6	192	25.9 $\pm$ 0.1
	195.6	196	76.4 $\pm$ 0.2
	199.6	200	83.4 $\pm$ 0.2
	201.6	202	40.6 $\pm$ 0.1
2000 C1	204.8	204	77.7 $\pm$ 0.2
	206.5	206	79.4 $\pm$ 0.2
	208.0	208	7.1 $\pm$ 0.1
2000 S1	206.3	206,7	60.1 $\pm$ 0.1

Table 4.2: Integrated luminosity and its uncertainty versus $\sqrt{s}$ for the data collected during years 1999 and 2000. The third column gives the $\sqrt{s}$ at which the background samples have been generated.

- $\mathrm{e^+e^-} \rightarrow \tilde{\chi}_1^+ \tilde{\chi}_1^- \rightarrow \tilde{\chi}_1^0 \tilde{\chi}_1^0 \; \mathrm{f\,\bar{f}\,f'\,\bar{f}'}$
- $\mathrm{e^+e^-} \rightarrow \tilde{\chi}_1^+ \tilde{\chi}_1^- \rightarrow \tilde{\chi}_2^0 \tilde{\chi}_1^0 \; \mathrm{f\,\bar{f}\,f'\,\bar{f}'} \rightarrow \tilde{\chi}_1^0 \tilde{\chi}_1^0 \; \mathrm{f\,\bar{f}f'\,\bar{f}'}\,\gamma$
- $\mathrm{e^+e^-} \rightarrow \tilde{\chi}_1^+ \tilde{\chi}_1^- \rightarrow \tilde{\chi}_2^0 \tilde{\chi}_1^0 \; \mathrm{f\,\bar{f}\,f'\,\bar{f}'} \rightarrow \tilde{\chi}_1^0 \tilde{\chi}_1^0 \; \mathrm{f\,\bar{f}\,f'\,\bar{f}'\,f''\,\bar{f}''}$
- $\mathrm{e^+e^-} \rightarrow \tilde{\chi}_1^+ \tilde{\chi}_1^- \rightarrow \tilde{\chi}_2^0 \tilde{\chi}_2^0 \; \mathrm{f\,\bar{f}\,f'\,\bar{f}'} \rightarrow \tilde{\chi}_1^0 \tilde{\chi}_1^0 \; \mathrm{f\,\bar{f}\,f'\,\bar{f}'}\,\gamma\,\gamma$
- $\mathrm{e^+e^-} \rightarrow \tilde{\chi}_1^+ \tilde{\chi}_1^- \rightarrow \tilde{\chi}_2^0 \tilde{\chi}_2^0 \; \mathrm{f\,\bar{f}\,f'\,\bar{f}'} \rightarrow \tilde{\chi}_1^0 \tilde{\chi}_1^0 \; \mathrm{f\,\bar{f}\,f'\,\bar{f}'\,f''\,\bar{f}''}\,\gamma$
- $\mathrm{e^+e^-} \rightarrow \tilde{\chi}_1^+ \tilde{\chi}_1^- \rightarrow \tilde{\chi}_2^0 \tilde{\chi}_2^0 \; \mathrm{f\,\bar{f}\,f'\,\bar{f}'} \rightarrow \tilde{\chi}_1^0 \tilde{\chi}_1^0 \; \mathrm{f\,\bar{f}\,f'\,\bar{f}'\,f''\,\bar{f}''\,f'''\,\bar{f}'''}$

where $\mathrm{f\,\bar{f}}$ can be a pair of leptons ($l^\pm\,\nu$) or quarks ($q\,\bar{q}$).

Moreover, as said before, above the WW production threshold, for low $\tan\beta$ values, $\tilde{\chi}_1^\pm \tilde{\chi}_2^\pm$ and $\tilde{\chi}_2^\pm \tilde{\chi}_2^\pm$ production processes may be allowed. Nevertheless, in order to simplify the analysis, only the process $\tilde{\chi}_2^\pm \tilde{\chi}_2^\pm$ was investigated and only if $\tilde{\chi}_1^\pm$ and $\tilde{\chi}_2^\pm$ were degenerate. Hence, the decay of the $\tilde{\chi}_2^\pm$ into $\tilde{\chi}_1^\pm$ is suppressed due to their degeneracy and the final states arising from their production and decay are the same that the ones of $\tilde{\chi}_1^\pm \tilde{\chi}_1^\pm$. All these different signatures can be classified in four different decay channels as follows:

- *leptonic* channel ("$\ell\ell_c$"): the decay products are only leptons and the LSP's. Both charginos decay into fully leptonic final states plus missing energy.
- *hadronic* channel ("$jets_c$"): the decay products are only quarks and the LSP's. Both charginos decay into fully hadronic final states. The experimental signature is multi–jet events with missing energy.
- *semi–leptonic* channel ("$jj\ell_c$"): the decay products are quarks, leptons and the LSP's. At least one charged lepton, originating from a $\tilde{\chi}$ decay, is required in the final state.
- *radiative channel* ("*rad*$_c$"): there is at least one photon in the final state coming from the $\tilde{\chi}_2^0$ decay.

The branching ratio (BR) of each decay channel depends on the sfermion masses and on the chargino field components. Since in this work, all sfermions are supposed to be much heavier than $\tilde{\chi}_1^{\pm}$, the chargino decay to the neutralino proceeds by the emission of a W boson and, therefore, if no cascade occurs, the $\tilde{\chi}_1^{\pm}$ decay branching ratios are those of the W boson ($\sim$ 33 % to $l^{\pm}\,\nu$).

4.2.1 Constraint on the minimal chargino mass and ΔM value.

In the present work, the minimum chargino mass searched for was set to 45 GeV/c^2. This corresponds to the chargino mass limit, set independently of the chargino composition and sneutrino mass, by the measurement of the Z^0 width at LEP1 [89] [90]. Moreover, this search covered scenarios in which the mass difference ΔM was above 3 GeV/c^2. In the case of higher mass degeneracy between the chargino and the neutralino, dedicated analyses may be found in [72][73].

4.2.2 Signal simulation

In order to estimate the detection efficiency of the chargino signal and optimize the analysis procedure, different chargino-neutralino sets in the MSSM parameter space were generated by Monte Carlo simulation using the SUSYGEN [91] program. All chargino events were then processed through the DELPHI full chain of simulation and reconstruction programs [81, 84]. Different samples of chargino points, i.e. ($M_{\tilde{\chi}_1^{\pm}}$,$M_{\tilde{\chi}_1^0}$) sets, were generated at center–of–mass energies up to 207 GeV. The computation of the masses, chargino production cross–section and branching ratios as a function of the MSSM parameters were based on the predictions from the MSSM model. The cascade decays of the supersymmetric particles were also considered.

The criteria followed in the choice of the chargino points are based on the dependence of the chargino signal characteristics on their field composition and mass difference between the chargino and the lightest neutralino. Different combinations of ($\tilde{\chi}_1^{\pm}$,$\tilde{\chi}_1^0$) were chosen for a given chargino mass to cover all the allowed mass regions.

These mass values were determined by using three MSSM parameters : M_2(the mass of the $SU(2)$ gaugino sector), the Higgs mass parameter μ and the ratio $\tan\beta$ of the vacuum expectation values of the two Higgs doublets. The GUT relation between the M_1 mass of the $U(1)$ gaugino and M_2 ($M_1 = \frac{5}{3}\tan^2\theta_W\, M_2 \approx 0.5\ M_2$) was assumed. The sneutrino mass value was fixed to $m_{\tilde{\nu}}$ = 1000 GeV/c^2 for all generated points (high m_0 scenario).

All chargino points were generated at energies ranging from E_{cm} = 192 GeV to 207 GeV and processed through the DELPHI chain of simulation and reconstruction. A maximum of 132 different combinations of chargino and neutralino masses were chosen to be representative of the MSSM parameter space. A total of about 3000 events were generated for every chargino point. The main characteristics of all simulated points are summarized in tables 4.3 (all points) and 4.4 (radiative points, i.e. samples containing cascades with $\tilde{\chi}_2^0$ decaying radiatively).

The SUSY parameters (M_2, μ,$\tan\beta$), the corresponding masses of the first and second chargino and neutralino, the ΔM value as well as the probability of having at least one radiative photon in the final state are shown. The arrows (→) next to some $\tilde{\chi}_2^0$ mass values, indicate that cascade decays are allowed. The generated samples in the ($M_{\tilde{\chi}_1^{\pm}}$, $M_{\tilde{\chi}_1^0}$) plane are shown in Fig 4.2 (upper plot). The lower plot shows the regions of the ($M_{\tilde{\chi}_1^{\pm}}$, $M_{\tilde{\chi}_2^0}$) plane where radiative chargino events are found. The small (yellow) points displayed in the two figures were obtained varying M_2, μ and $\tan\beta$. The empty lower-right regions in the two plots are not allowed due to the assumed relation between M_1 and M_2.

Hence, with this choice, the parametrization of the detection efficiency (section 7.1) as a function of $M_{\tilde{\chi}_1^{\pm}}$ and $M_{\tilde{\chi}_1^0}$ ($M_{\tilde{\chi}_2^0}$, in the radiative case) will be determined with ($M_{\tilde{\chi}_1^{\pm}}$, $M_{\tilde{\chi}_1^0}$) and ($M_{\tilde{\chi}_1^{\pm}}$, $M_{\tilde{\chi}_2^0}$)

sets covering properly the allowed mass regions. The computation of the efficiencies at 208 GeVwill be discussed in section 7.1.

M_2 (GeV/c^2)	μ (GeV/c^2)	$\tan\beta$	ΔM (GeV/c^2)	$M_{\tilde{\chi}_2^\pm}$ (GeV/c^2)	$M_{\tilde{\chi}_1^\pm}$ (GeV/c^2)	$M_{\tilde{\chi}_2^0}$ (GeV/c^2)	$M_{\tilde{\chi}_1^0}$ (GeV/c^2)
2036.9	-100.2	1.0	3.0	2039.9	103.3	105.0	100.2
1185.1	-98.3	1.0	4.9	1190.1	103.3	106.0	98.3
733.9	113.4	1.0	7.0	744.1	103.3	113.4	96.2
606.4	116.0	1.0	9.0	619.2	103.3	116.0	94.3
418.4	123.7	1.0	15.0	438.8	103.3	123.7	88.3
218.3	-83.3	1.0	19.9	238.3	103.3	111.5	83.3
89.5	-364.8	1.0	55.0	378.5	103.3	104.2	48.3
2038.4	-98.7	1.0	3.0	2041.4	101.8	103.5	98.7
958.3	109.3	1.0	4.9	965.8	101.8	109.3	96.8
541.1	-91.7	1.0	10.0	551.1	101.8	106.8	91.7
415.4	122.3	1.0	14.9	435.9	101.8	122.3	86.8
337.4	129.0	1.0	20.0	364.7	101.8	129.0	81.7
285.4	136.8	1.0	24.9	320.4	101.8	136.8	76.8
211.8	160.2	1.0	35.0	270.2	101.8	137.0	66.7
145.6	248.4	1.0	44.9	292.2	101.8	111.3	56.8
85.8	-300.6	1.0	55.0	316.5	101.8	103.1	46.7
2482.6	-97.3	1.0	2.4	2485.1	99.8	101.2	97.3
2047.8	-96.8	1.0	2.9	2050.8	99.8	101.5	96.8
955.2	107.3	1.0	4.9	962.7	99.8	107.3	94.8
489.9	116.2	1.0	11.7	506.4	99.8	116.2	88.0
411.1	120.4	1.0	14.9	431.8	99.8	120.4	84.8
157.4	-74.8	1.0	25.0	182.4	99.8	86.6 $\rightarrow$	74.8
2469.5	-95.4	1.0	2.5	2472.0	97.9	99.3	95.4
2048.2	-94.9	1.0	2.9	2051.2	97.8	99.6	94.9
1189.2	-92.9	1.0	4.9	1194.2	97.8	100.6	92.9
545.3	-87.9	1.0	9.9	555.3	97.8	102.9	87.9
330.8	-82.9	1.0	15.0	345.8	97.9	104.8	82.9
159.3	-72.9	1.0	25.0	184.3	97.9	87.6 $\rightarrow$	72.9
2049.0	-91.3	1.0	3.0	2052.0	94.3	96.0	91.3
1192.0	-89.3	1.0	5.0	1197.0	94.3	97.0	89.3
548.9	-84.3	1.0	10.0	558.9	94.3	99.3	84.3
334.5	-79.3	1.0	15.0	349.5	94.3	101.2	79.3
162.9	-69.3	1.0	25.0	187.9	94.3	89.5 $\rightarrow$	69.3
192.0	160.1	1.0	34.9	257.8	94.3	126.3	59.3
155.9	198.7	1.0	39.9	260.3	94.3	111.5	54.3
71.5	-188.0	1.0	53.9	210.7	94.3	96.9	40.3
59.8	-92.4	1.0	59.2	126.8	94.3	92.4 $\rightarrow$	35.0

M_2 (GeV/c^2)	μ (GeV/c^2)	$\tan\beta$	ΔM (GeV/c^2)	$M_{\tilde{\chi}_2^\pm}$ (GeV/c^2)	$M_{\tilde{\chi}_1^\pm}$ (GeV/c^2)	$M_{\tilde{\chi}_2^0}$ (GeV/c^2)	$M_{\tilde{\chi}_1^0}$ (GeV/c^2)
2480.7	-82.4	1.0	2.5	2483.2	84.9	86.4	82.4
1472.0	89.3	1.5	2.9	1476.6	85.0	89.5	82.0
900.0	93.0	1.5	5.1	907.8	85.6	93.4	80.4
570.0	98.0	1.5	8.9	583.1	85.6	98.6	76.6
350.0	108.0	1.5	16.3	373.8	85.2	108.8	68.8
200.0	138.0	1.5	29.8	254.2	85.1	126.1	55.3
140.0	196.0	1.5	37.1	252.2	85.2	100.7	48.1
65.0	-190.0	1.5	48.7	214.2	85.3	87.3	36.6
61.6	-190.0	1.0	49.9	213.3	84.9	87.9	35.0
54.1	-89.2	1.0	58.1	125.0	89.9	89.2	31.8
51.0	-104.6	1.0	54.9	138.5	85.0	90.1	30.0
46.0	-80.0	1.0	57.6	118.9	85.0	80.0 $\rightarrow$	27.3
42.3	-80.0	1.0	56.7	119.7	82.0	80.0 $\rightarrow$	25.2
1671.9	74.0	1.0	2.5	1675.9	70.0	74.0	67.5
2073.9	-67.0	1.0	3.0	2076.9	70.0	71.7	67.0
1216.0	-65.0	1.0	5.0	1221.0	70.0	72.8	65.0
573.2	-60.0	1.0	10.0	583.2	70.0	75.2	60.0
358.8	-55.0	1.0	15.0	373.8	70.0	77.2	55.0
187.3	-45.0	1.0	24.9	212.2	69.9	80.1	45.0
113.8	-35.0	1.0	34.9	148.7	69.9	65.3 $\rightarrow$	35.0
85.7	-28.7	1.0	41.3	127.0	70.0	50.3 $\rightarrow$	28.7
42.8	-166.9	1.0	45.0	194.1	70.0	74.2	24.9
33.5	-106.2	1.0	49.9	142.7	70.0	76.3	20.0
24.7	-72.2	1.0	54.9	117.4	70.0	72.2	15.0
34.2	-192.0	1.0	39.7	217.5	59.7	64.1	20.0
63.5	0.0	1.0	54.5	118.0	54.5	38.4	0.0
2520.0	-47.5	1.0	2.5	2522.5	50.0	51.4	47.5
2094.0	-47.0	1.0	3.0	2097.0	50.0	51.7	47.0
1236.3	-45.0	1.0	5.0	1241.3	50.0	52.8	45.0
593.2	-40.0	1.0	10.0	603.2	50.0	55.4	40.0
378.8	-35.0	1.0	15.0	393.8	50.0	57.5	35.0
57.2	10.0	1.0	40.0	117.2	50.0	34.8 $\rightarrow$	10.0
110.8	-10.0	1.0	40.0	150.8	50.0	63.2	10.0
66.9	5.0	1.0	45.0	121.9	50.0	40.5 $\rightarrow$	5.0
92.9	-5.0	1.0	45.0	137.9	50.0	54.9	5.0
78.6	0.0	1.0	50.0	128.6	50.0	47.1 $\rightarrow$	0.0
207.3	-25.0	1.0	24.9	232.2	49.9	60.7	25.0
133.8	-15.0	1.0	34.9	168.7	49.9	62.6	15.0

M_2 (GeV/c^2)	μ (GeV/c^2)	$\tan\beta$	ΔM (GeV/c^2)	$M_{\tilde{\chi}_2^\pm}$ (GeV/c^2)	$M_{\tilde{\chi}_1^\pm}$ (GeV/c^2)	$M_{\tilde{\chi}_2^0}$ (GeV/c^2)	$M_{\tilde{\chi}_1^0}$ (GeV/c^2)
1623.9	49.0	1.0	2.5	1628.0	44.9	49.0	42.4
2098.0	-42.0	1.0	3.0	2101.0	45.0	46.7	42.0
1241.0	-40.0	1.0	5.0	1246.0	45.0	47.8	40.0
598.0	-35.0	1.0	10.0	608.0	45.0	50.4	35.0
383.8	-30.0	1.0	15.0	398.8	45.0	52.6	30.0
212.2	-20.0	1.0	25.0	237.2	45.0	55.9	20.0
138.7	-10.0	1.0	35.0	173.7	45.0	57.8	10.0
74.1	9.0	1.0	36.0	128.1	45.0	44.7	9.0
115.8	-5.0	1.0	40.0	155.8	45.0	58.5	5.0
97.9	0.0	1.0	45.0	142.9	45.0	57.9	0.0

Table 4.3: Selected non–radiative sets for Monte Carlo simulation up to E_{cm} = 207 GeV. The values of the SUSY parameters (M_2, μ, $\tan\beta$), the corresponding masses of the first and second chargino and neutralino as well as the mass difference between the lightest chargino and neutralino (ΔM) are shown.

M_2 (GeV/c^2)	μ (GeV/c^2)	$\tan\beta$	ΔM (GeV/c^2)	$M_{\tilde{\chi}_2^\pm}$ (GeV/c^2)	$M_{\tilde{\chi}_1^\pm}$ (GeV/c^2)	$M_{\tilde{\chi}_2^0}$ (GeV/c^2)	$M_{\tilde{\chi}_1^0}$ (GeV/c^2)	$P(\rightarrow n\,\gamma)$ (%)
154.0	-78.3	1.0	24.9	179.0	103.3	84.7 →	78.3	7.2
139.9	-82.3	1.5	29.9	169.0	103.3	83.6 →	73.3	18.7
121.5	-74.7	1.0	35.0	150.1	103.3	74.7 →	68.2	62.8
108.0	-72.8	1.0	41.9	138.5	103.3	72.8 →	61.3	33.0
96.6	-71.1	1.0	48.0	128.7	103.3	71.1 →	55.2	19.3
65.1	-65.1	1.0	65.0	103.3	103.3	65.1 →	38.3	7.0
128.3	-73.8	1.0	29.9	156.2	101.8	73.8 →	71.8	88.6
118.6	-72.6	1.0	34.9	147.7	101.8	72.6 →	66.8	66.9
108.9	-71.2	1.0	40.0	139.4	101.8	71.2 →	61.8	43.9
89.9	-68.2	1.0	49.9	123.4	101.8	68.2 →	51.8	18.9
71.4	-64.6	1.0	59.9	108.5	101.8	64.6 →	41.8	9.9
62.7	-62.7	1.0	64.7	101.8	101.8	62.7 →	37.0	8.7
114.6	-69.8	1.0	35.0	144.6	99.8	69.8 →	64.7	71.8
95.5	-66.8	1.0	45.0	128.4	99.8	66.8 →	54.8	33.0
86.1	-65.2	1.0	49.9	120.7	99.7	65.2 →	49.7	22.6
59.5	-59.4	1.0	64.5	99.9	99.7	59.4 →	35.2	11.6
110.8	-67.0	1.0	35.0	141.6	97.9	67.0 →	62.8	76.2
91.8	-64.0	1.0	44.9	125.7	97.8	64.0 →	52.9	38.0
82.5	-62.2	1.0	50.0	118.1	97.9	62.2 →	47.9	26.8
56.4	-56.2	1.0	64.4	98.0	97.9	56.2 →	33.5	15.1

M_2 (GeV/c^2)	μ (GeV/c^2)	$\tan\beta$	ΔM (GeV/c^2)	$M_{\tilde{\chi}_2^\pm}$ (GeV/c^2)	$M_{\tilde{\chi}_1^\pm}$ (GeV/c^2)	$M_{\tilde{\chi}_2^0}$ (GeV/c^2)	$M_{\tilde{\chi}_1^0}$ (GeV/c^2)	$P(\rightarrow n\,\gamma)$ (%)
65.5	-56.1	1.0	57.3	105.3	95.9	56.1 →	38.6	21.2
98.9	-62.2	1.0	38.6	132.0	95.3	62.2 →	56.7	67.6
103.7	-61.8	1.0	34.9	136.2	94.3	61.8 →	59.3	82.8
84.8	-58.4	1.0	45.0	120.7	94.3	58.4 →	49.2	48.2
75.7	-56.4	1.0	50.0	113.5	94.3	56.4 →	44.2	35.9
49.6	-49.7	1.0	64.6	94.3	94.3	49.7 →	29.6	23.4
40.9	-40.9	1.0	65.3	90.0	90.0	40.9 →	24.6	43.0
87.9	-47.8	1.0	37.2	125.1	85.0	51.1 →	47.8	47.4
67.5	-42.8	1.0	44.9	109.7	85.0	42.8 →	40.0	72.2
58.6	-40.2	1.0	50.0	103.3	84.9	40.2 →	34.9	62.6
50.0	-37.4	1.0	55.0	97.6	85.0	37.4 →	30.0	61.7
41.6	-34.4	1.0	59.9	92.3	85.1	34.4 →	25.1	57.8
28.0	-28.0	1.0	67.8	84.9	84.9	28.0 →	17.0	54.7
17.2	-17.2	1.0	71.4	82.0	82.0	17.2 →	10.5	65.1
1.6	-0.4	1.0	79.1	80.7	79.6	1.0 →	0.4	71.9
72.9	-25.0	1.0	45.0	117.9	70.0	43.3 →	25.0	9.0
58.6	-20.0	1.0	50.0	108.6	70.0	35.2 →	20.0	25.8
28.9	-5.0	1.0	65.0	93.9	70.0	17.7 →	5.0	39.1
21.9	0.0	1.0	69.9	91.8	69.9	13.4 →	0.0	43.4
37.2	-10.0	1.0	60.0	97.2	70.0	22.7 →	10.0	36.4
25.3	13.4	1.0	47.5	99.8	60.9	15.6 →	13.4	67.1
28.8	16.1	1.0	41.9	102.9	58.0	17.7 →	16.1	68.7
38.1	23.0	1.0	27.0	111.1	50.0	23.4 →	23.0	71.1
48.9	15.0	1.0	35.0	113.9	50.0	29.9 →	15.0	14.5
43.4	27.7	1.0	18.1	116.1	45.0	27.7 →	26.8	71.0
47.0	24.9	1.0	20.0	116.9	45.0	28.9 →	24.9	44.1
53.9	20.0	1.0	25.0	118.9	45.0	33.0 →	20.0	6.0

Table 4.4: Selected radiative set for Monte Carlo simulation up to E_{cm} = 207 GeV. The values of the SUSY parameters (M_2, μ, $\tan\beta$), the corresponding masses of the first and second chargino and neutralino as well as the mass difference between the lightest chargino and neutralino (ΔM) are shown. The probability of having at least one photon in the final state coming from the neutralino decay $\tilde{\chi}_2^0 \rightarrow \tilde{\chi}_1^0\,\gamma$ is also given.

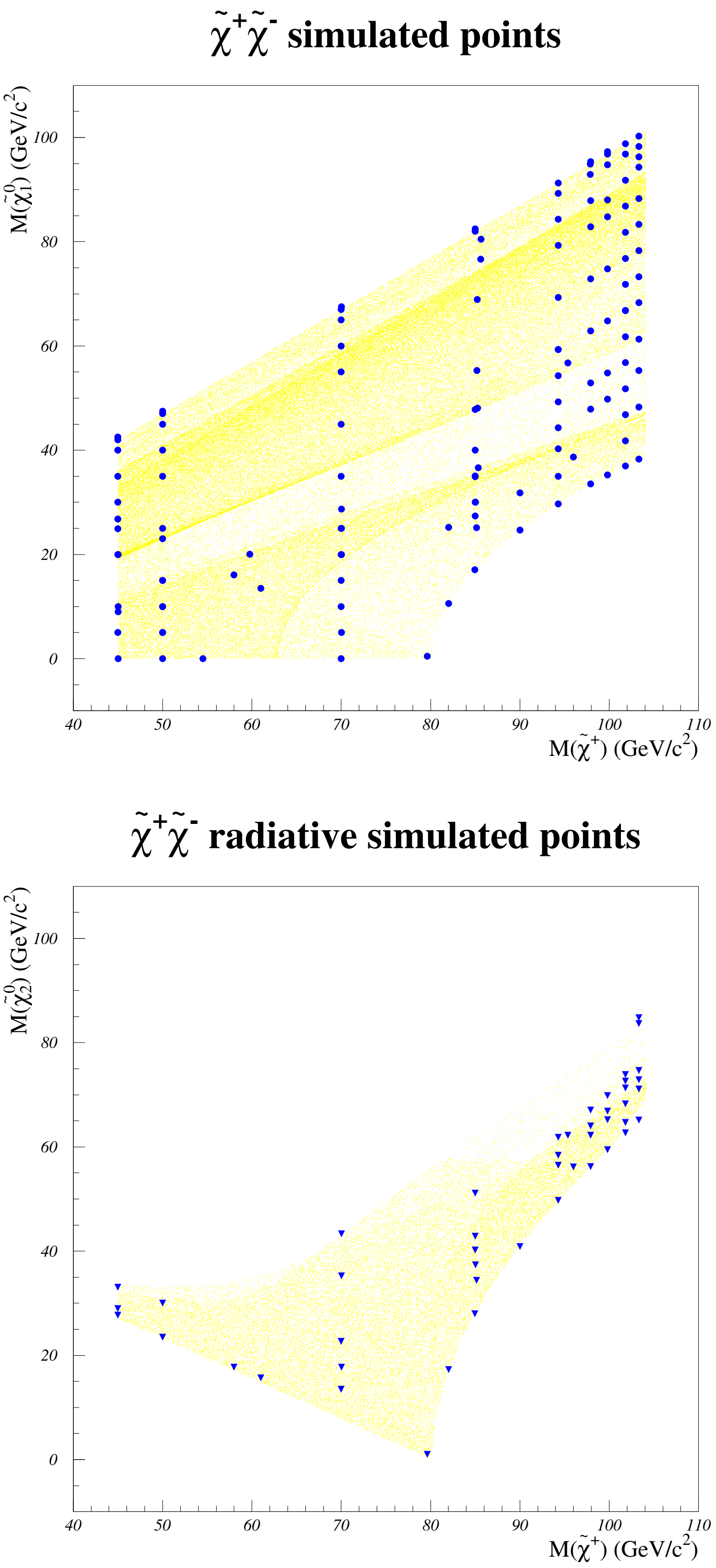

Figure 4.2: Diagrams showing the position of each generated (radiative) chargino-neutralino sets in the ($M_{\tilde{\chi}^\pm}$, $M_{\tilde{\chi}_1^0}$ ($M_{\tilde{\chi}_2^0}$)) plane. The small (yellow) points displayed in the figure correspond to the uniform scan over M_2, μ and $\tan\beta$ for all (top) and radiative (bottom) final states.

Chapter 5

Characteristics of SM backgrounds

Several Standard Model processes mimic the supersymmetric signal and hence are a potential background in the present search. This implies that the discovery of a supersymmetric signal will be stated as an excess with respect to the SM predictions. The SM processes at LEP2 which generate a background in the chargino search are described in this chapter.

Fig. 5.1 shows the cross–sections of the main Standard Model processes at LEP2 versus the center–of–mass energy. As can be seen, the cross–section of some SM processes can change strongly with the increase in the center–of–mass energy.
For instance, $\sigma(\mathrm{e^+e^-} \rightarrow WW)$ and $\sigma(\mathrm{e^+e^-} \rightarrow ZZ)$ increase when the production of real W and Z^0 particles is allowed. On the contrary, the cross–section of processes such as $\mathrm{e^+e^-} \rightarrow q\,\bar{q}\,(\gamma)$ decreases with $\sqrt{s}$.

At typical LEP2 centre–of-mass energies, the most dangerous background processes for the chargino search are four/two–fermion productions and the two–photon interaction ($\gamma\gamma$) processes due to their high production cross–section.

5.1 Two–fermion processes

The $\mathrm{e^+e^-} \rightarrow Z^0/\gamma \rightarrow \mathrm{f\,\bar{f}}\,(\gamma)$ process proceeds in the s–channel via an off-shell photon or a Z^0 boson, as shown in figure 5.2.

At energies above the Z^0 resonance peak, the $\mathrm{f\,\bar{f}}\,(\gamma)$ events can arise in two different configurations. The first possibility is that no high energy photons are radiated. This kind of events is characterized by a high visible energy and visible mass, which are about the center–of–mass energy. Moreover, the collinearity (coplanarity), the angle between the two fermions/jets in space (transverse plane), is close to 180° (or the acollinearity (acoplanarity) is close to 0°). On the other hand, the chargino events are typically characterized by non negligible values of missing transverse momentum, missing mass, missing energy, acollinearity and acoplanarity due to the presence of the $\tilde{\chi}^0_1$'s. Using these variables $\mathrm{f\,\bar{f}}$ events can be rejected.

The second configuration is the radiative return to the Z^0 boson resonance. One or more photons are emitted as initial state radiation (ISR) with an energy such that the effective center–of–mass energy of the $\mathrm{f\,\bar{f}}$ pair "returns" to the Z^0 boson resonance energy. In this case the invariant mass of the $\mathrm{f\,\bar{f}}$ pair ($m_{\mathrm{f\,\bar{f}}}$) is close to the Z^0 boson mass (m_Z). Since the Z^0 boson is produced on-shell, the cross-section of this process becomes important compensating the low probability to have an emitted photon ($P_\gamma \simeq 7\%$). If a single photon is radiated, its energy will be equal to:

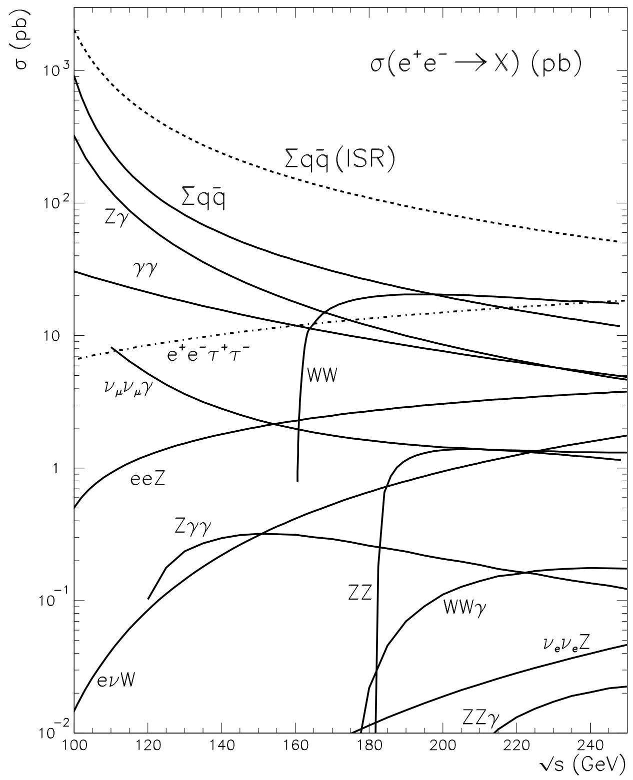

Figure 5.1: Cross–sections of the Standard Model processes at LEP2 as a function of the center–of–mass energy. For $\mathrm{e^+e^-} \to Z^0e^+e^-$, $We\,\nu_e$ and $Z\nu_e\overline{\nu}_e$ only the t-channel contribution is shown. The photons in $Z\gamma$ and $\gamma\gamma$ are such that $|cos_{e\gamma}| < 0.9$. For $\gamma\nu_\mu\overline{\nu}_\mu$ there is a cut in the photon energy of $E_\gamma > 10$ GeV. In $Z\gamma\gamma$, $WW\gamma$ and $ZZ\gamma$, the transverse momentum cut for the photon is $\mathrm{P}_T^\gamma > 10$ GeV.

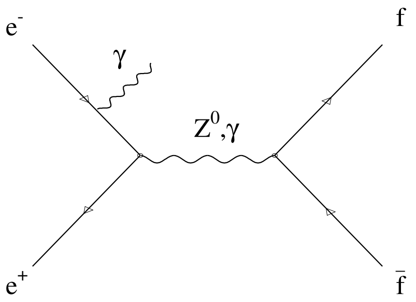

Figure 5.2: Two–fermion production diagram with an ISR photon.

$$E_\gamma = \frac{s - m^2_{\mathrm{f\,\bar{f}}}}{2\sqrt{s}} \approx \frac{s - m_Z^2}{2\sqrt{s}} \tag{5.1}$$

giving e.g. $E_\gamma \sim 83$ GeV for $\sqrt{s} = 206$ GeV. Radiative events can be further subdivided in two different groups depending on whether the photon(s) is(are) detected or not. Typically, the initial state radiation is emitted in the longitudinal direction with little transverse momentum since $< \theta_\gamma > \propto \frac{m_e^2}{E_e^2} \simeq 0°$.

The energetic photon will escape undetected in the beam pipe below the acceptance of the STIC luminometer. Thus, ISR will be a source of missing energy in the two–fermion events. Such events are characterized by large visible mass ($\sim M_Z$) and a missing momentum pointing to the beam direction. The $\mathrm{f\,\bar{f}}$ system recoils against the photon and is therefore boosted in the direction of the beam axis. The angle between the two fermions in the transverse plane, the coplanarity, ignores the boost in the z direction and thus is close to 180° in order to balance the total momentum. Therefore these events can be reduced by requiring significant missing transverse momentum ($\not{P}_t$) or acoplanarity. This kind of events can be selected as chargino candidates if additional $\not{P}_t$ is generated by a wrong measurement of the momentum of one of the fermions or by the neutrinos present in b decays.

If the initial state radiation is present as a photon emitted at larger polar angles with a large transverse momentum, the photon will be detected. In this case no missing energy is present and these background events can be reduced by vetoing events with energetic isolated photons in the detector. However, if the energetic photon is emitted in a region of the detector with weak calorimetry and escapes detection, then both the acoplanarity and the $\not{P}_t$ of the $\mathrm{f\,\bar{f}}$ system can be large, hence resembling a chargino event. This effect can be reduced by rejecting events if the hermeticity detectors give an isolated signal matching the missing momentum azimuthal direction.

5.1.1 $\mathrm{e^+e^-}$ scattering: Bhabha events

A special case of two–fermion background is the electron pair production (Bhabha). In this case, a second production diagram is present, the t–channel photon exchange, which is the dominant contribution to the total cross–section at low angles. These events are characterized by high electromagnetic energy deposited in the forward and backward regions, a visible energy around twice the beam energy and small $\not{P}_t$. Electron pairs are produced with small acollinearity and acoplanarity. Usually, this kind of background is easily rejected. The main problem comes from the $\mathrm{e^+e^-}$ radiative events. In this case, if reconstruction problems are present, the acoplanarity can increase. If no reconstruction problems are present, the radiative Bhabha $\mathrm{e^+e^-}$ events can be rejected by requiring significant $\not{P}_t$.

5.2 Four–fermion processes

In this section, single and pair production of W and Z^0 bosons processes are studied. Although $\gamma\gamma$ events are also four–fermion processes, they are separately described in section 5.3, since their kinematics are very different.

5.2.1 W single and pair production

WW events are produced in the s–channel through photon or Z^0 boson exchange or via neutrino interchange in the t–channel, as shown in Fig. 5.3. The decay of the $W^\pm$ boson can give a pair of quarks ($W^\pm \to q\,\bar{q}$) or a lepton–(anti)neutrino pair ($W^\pm \to \ell^\pm\nu$). Therefore, the final states are very similar to those of chargino events for small neutralino masses. In the WW production process, the missing energy is carried by the neutrino in the leptonic decays. This background is one of the most dangerous for chargino searches due to its high cross–section at the LEP2 typical center–of–mass energies. However, some variables can be used to distinguish these events from the chargino signal. The hadronic decays of WW events are characterized by high visible mass while, in a large part of the ($M_{\tilde{\chi}_1^\pm}$,$M_{\tilde{\chi}_1^0}$) plane, $\tilde{\chi}^+\tilde{\chi}^-$ events present lower visible mass values due to the undetected neutralinos. Moreover, the leptonic decays of the W give typically high momentum tracks while the momenta of the leptons produced in the chargino final states are concentrated at low values. Applying cuts on these variables and on the invariant mass of the hadronic system (M_{jj}) and the invariant mass of the lepton and neutrino system ($M_{\ell\nu}$) , the contamination of this background can be reduced.

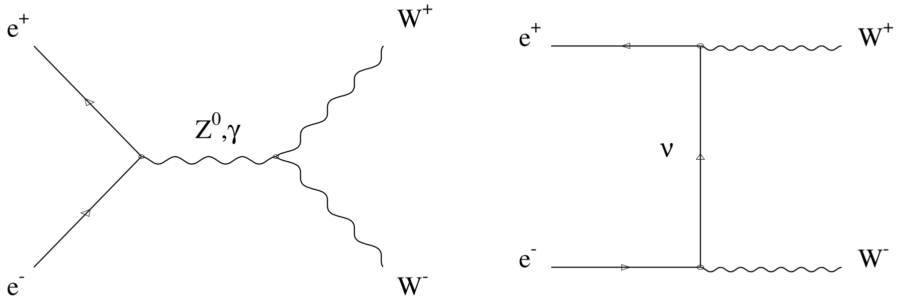

Figure 5.3: WW pair production diagrams.

If the $\tilde{\chi}_1^0$ is light, the mass difference between $\tilde{\chi}_1^+$ and $\tilde{\chi}_1^0$ (ΔM) will be high and the visible energy and mass distributions of the chargino events will shift to the WW regions, making it more difficult to separate both processes. When $\Delta M \sim m_W$, WW events constitute an irreducible background to the $\tilde{\chi}^+\tilde{\chi}^-$ topologies. In this region, however, charginos tend to decay radiatively, so the WW background can be reduced by requiring the presence of photons.

In Fig. 5.4 the diagram corresponding to the $\mathrm{e^+e^-} \rightarrow We\nu_e$ process is shown. $We\nu_e$ events have high visible mass ($\sim$ 80 GeV/c^2), $\not{P}_t$ and missing mass, since an energetic neutrino at large angles and an energetic electron ($E \sim E_{beam}$) at low angles escape detection. Such events can be rejected when the reconstructed hadronic mass is close to m_{W}.

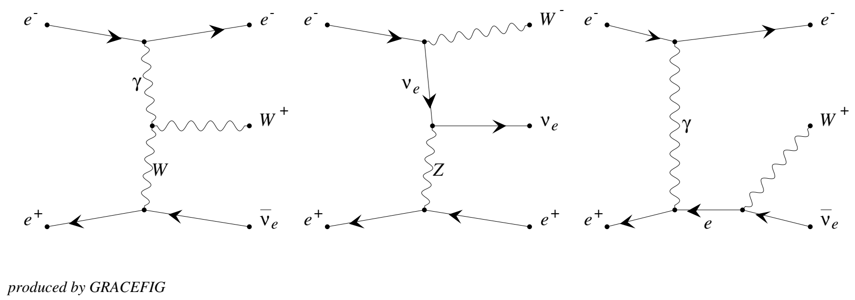

Figure 5.4: $\mathrm{e^+e^-} \rightarrow We\nu_e$ process.

Fig. 5.5 shows the distribution of the visible mass for $We\nu_e$ simulated events before and after detector simulation/reconstruction. Before the reconstruction, the distribution is peaked at $\sim$ 80 GeV/c^2 with a tail of a few off–shell events with lower visible mass. After reconstruction the distribution is broader and shifted to lower visible mass values due to the detector modeling. This takes place when one or both visible jets contain neutrinos or are in weak regions of the detector. The distribution after the hadronic selection (i.e. cuts which are mainly based on high multiplicity and sufficient $\not{P}_t$ requirements) shows that $We\nu_e$ events contribute to the background mainly when the W is on–shell and part of its energy is not measured. Therefore, the $We\nu_e$ events constitute a dangerous and irreducible background for the chargino searches.

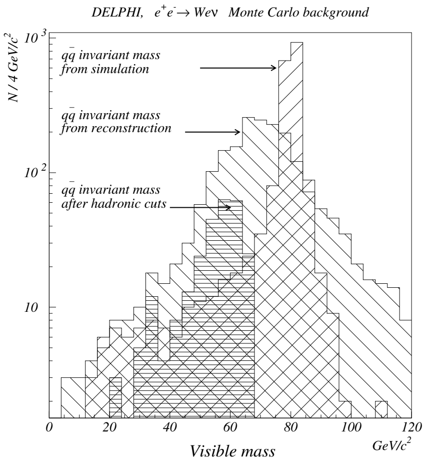

Figure 5.5: $We\nu_e$ visible mass distributions: visible mass from simulation, from reconstruction and from reconstruction after the hadronic selection.

5.2.2 Z^0 single and pair production

Tree–level diagrams of the $(Z^0/\gamma^*)(Z^0/\gamma^*)$ production processes are shown in Fig. 5.6. The sum of the 3 diagrams defines the so-called conversion diagram. Fig. 5.7 show the $Z^0e^+e^-$ production processes.

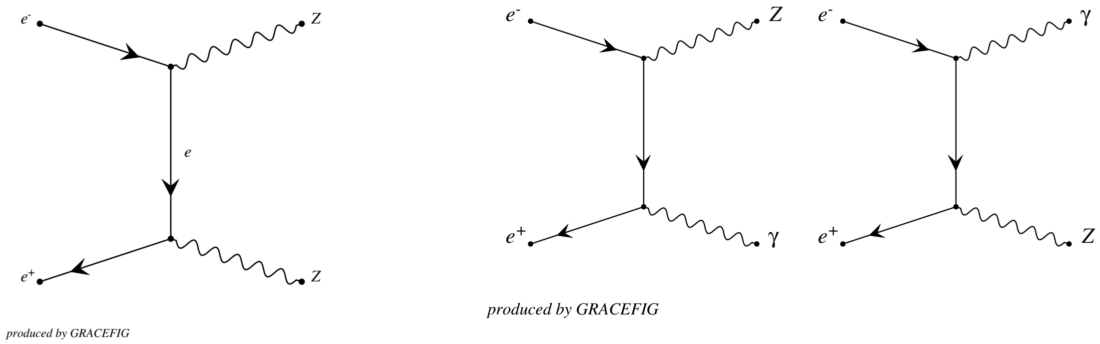

Figure 5.6: Z^0Z^0 and $Z^0\gamma^*$ processes.

$(Z^0/\gamma^*)(Z^0/\gamma^*)$ events have a cross–section an order of magnitude smaller than WW events. For center–of–mass energies greater than about $2m_Z$, two on–shell Z^0 bosons are produced. Above the production threshold for two on–shell Z^0 bosons around 182 GeV, the cross–section grows slowly. The main source of missing energy is the decay of one of the Z^0 bosons to neutrinos. The $Z^0e^+e^-$ process resembles the $We\nu_e$ process. One energetic electron ($E \sim E_{beam}$) is emitted at low angles with small transverse momentum. The electron usually escapes undetected or is sometimes detected

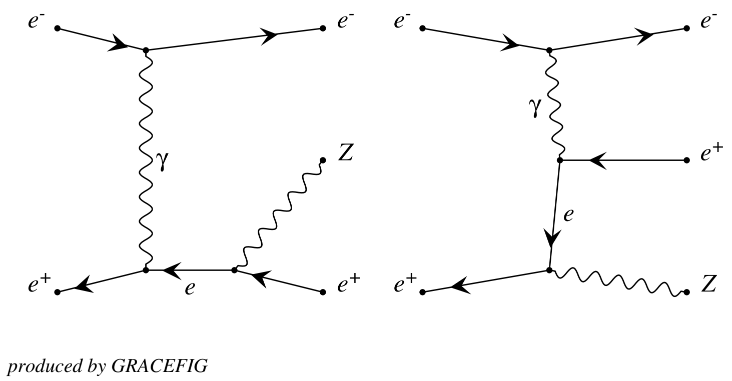

Figure 5.7: $Z^0e^+e^-$ processes.

by the STIC. The second electron recoils against the Z^0 boson and will therefore have a large angle and be seen as a track. The missing energy in this process can be due to the undetected electron. The hadronic mass of the process is close to m_{Z}.

5.3 Two–photon interactions ($\gamma\gamma$)

$\gamma\gamma$ events correspond to the interaction of two virtual photons emitted by the colliding electrons and positrons. The interaction gives a final system consisting of leptons or hadrons that recoil against the initial electron and/or positron. The total cross–section of $\gamma\gamma$ interactions can be described by a sum of three components: a soft non-perturbative interaction part described by the Vector meson Dominance Model (VDM), a perturbative term with a direct quark exchange using the Quark Parton Model (QPM) and the perturbative hard scattering of the partonic constituents of the photon (QCD model). Fig. 5.8 shows the corresponding $\gamma\gamma$ diagrams. It has to be emphasized that for leptonic production only the QPM contribution needs to be taken into account.

The cross–section of these events is very high ($\sigma \approx 10^4$ pb), but decreases when the detection of some of the electrons or a non–negligible $\not{P}_t$ or visible mass are required. This kind of process is a dangerous background for chargino events with a low visible energy (low mass difference between the chargino and the lightest neutralino). In most of the events, both the electron and the positron escape undetected below the detector acceptance. In this case the visible energy and the $\not{P}_t$ of the event will be small due to the electron emission at low angles.

If one or both electrons are visible, they will be detected at low angles as a large energy deposit in the STIC calorimeter. The visible energy will be high and located in the forward region of the detector. The missing transverse momentum of the events will always be small because of the absence of missing particles at large angles.

Therefore, $\gamma\gamma$ events are characterized by large missing energy and low visible mass or large visible electromagnetic energy in the forward region of the detector. The final system $\mathrm{f\bar{f}}$ has the same invariant mass as the $\gamma\gamma$ system. The energy spectrum of the radiated photons follows the law $\frac{1}{E_\gamma}$. Thus, the energy and invariant mass of the $\mathrm{f\bar{f}}$ system is low. The number of charged particles at low invariant mass and the $\not{P}_t$ are also small. Then, the jet or lepton system tends to be coplanar with the beam direction. These events can thus be rejected by requiring substantial transverse momentum and acoplanarity and a small jet activity in the forward–backward region. Due to the fact that the $\gamma\gamma$

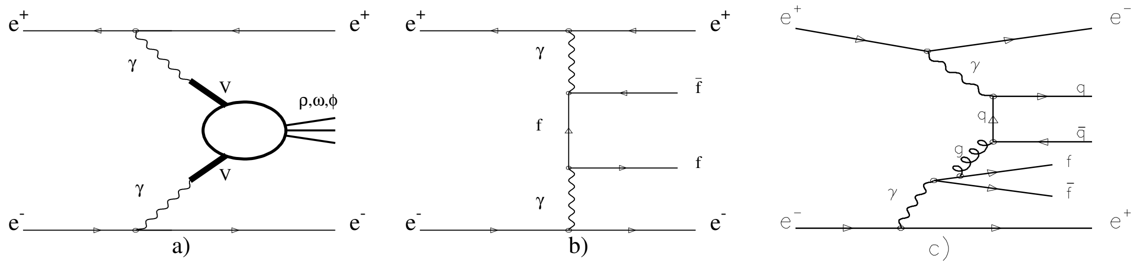

Figure 5.8: Diagrams corresponding to the a) $\gamma\gamma_{VDM}$, b) $\gamma\gamma_{QPM}$ and c) $\gamma\gamma_{QCD}$ (single-resolved) processes.

events are soft, it is difficult to reconstruct them and they are very sensitive to the value of the cut on the missing transverse momentum. The visible production cross–section of these events decreases strongly with the increase of the cut on $\not{P}_t$. Therefore, a variation of the $\not{P}_t$ cut leads to a high variation of the contribution of this process in the chargino search. Thus, in the degenerate region of ΔM, where this background is dominant, the chargino analysis is very sensitive to the $\not{P}_t$ cut. Tails from these events can be present after selection cuts due to a bad reconstruction of the jets in the forward regions or due to missing energetic neutrinos generating missing transverse momentum.

5.4 SM background composition and ΔM value

Fig 5.9 shows a schematic view of the background composition in the ($M_{\tilde{\chi}_1^\pm}$,$M_{\tilde{\chi}_1^0}$) plane. At the level of the mass parameters, only a dependence on ΔM is observed since the present search was divided in ΔM dependent analyses (see section 6.3). The Low ΔM region is dominated by the $\gamma\gamma$ processes while high ΔM region is dominated by 2- and 4-fermions processes. The intermediate region consists of all the SM processes.

5.5 Cross-sections and generators

The list of the cross-sections of the generated SM background processes is summarized in Table 5.1. For all the entries in Table 5.1, generated events were passed through the detailed simulation of the DELPHI detector and then processed with the same reconstruction and analysis programs as the real data. For the two/four-fermion processes, the number of generated events (N_{gen}), for a given process, is at least fifty times its corresponding expected number in the real data, i.e. for a given $\sqrt{s}$ and $\mathcal{L}$, $N_{gen}(s) > 50\sigma(s)\mathcal{L}(s)$. For the $\gamma\gamma$ background, the extremely high cross–section makes it difficult to generate a statistical significant sample of Monte Carlo events. In fact, it is not useful, since most of the $\gamma\gamma$ events may be cut away by appropriate selection criteria. What is crucial in this case is to have a good control of the tails, i.e. of those events which are more likely to pass the selection criteria. Therefore, biased samples were used, i.e. events with features more similar to the signal but with manageable cross–sections. For the leptonic $\gamma\gamma$, the biased events were required to have a transverse energy, E_t (at generator level), above 4 GeV while the "unbiased" sample have this cut lowered to 2 GeV. The case of hadronic $\gamma\gamma$ will be discussed in more details at the end of this section. The numbers of the $\gamma\gamma$ generated events are at least ten times their corresponding expected number in the real data.

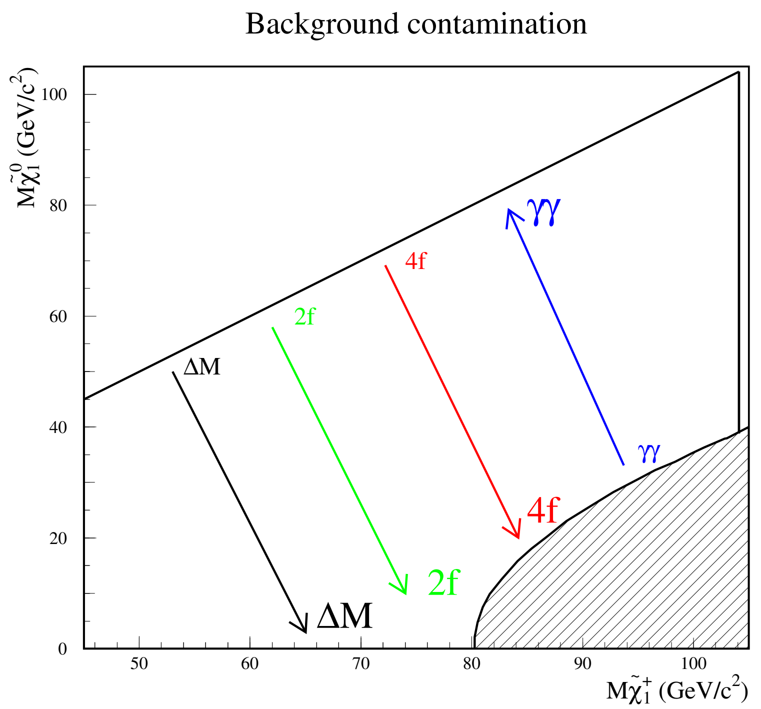

Figure 5.9: Schematic description of the SM background composition in the ($M_{\tilde{\chi}_1^\pm}$,$M_{\tilde{\chi}_1^0}$) plane.

All the generation programs rely on `JETSET 7.4`[87], tuned to LEP1 data[92], for quark fragmentation. The background process $e^+e^- \to q\,\bar{q}\ (n\gamma)$ was generated with `PYTHIA 6.125`[93], while `KORALZ`[94] was used for $\tau^+\tau^-(\gamma)$ and `DYMU3`[95] for $\mu^+\mu^-(\gamma)$. The generator `BHWIDE` [96] was used for $e^+e^- \to e^+e^-(\gamma)$ events.

Other radiative processes like Compton events and the QED process $e^+e^- \to \gamma\gamma(\gamma)$ were generated using `RADCOR` and $e^+e^- \to \nu\bar{\nu}(\gamma)$ using `KORALZ`. Compton events were simulated by requiring $\theta_e > 10°$, $\theta_\gamma > 10°$ and photon and electron energies greater than 1 GeV. In the case of $e^+e^- \to \nu\bar{\nu}(\gamma)$, the angle of the photon emission was required to be $40° < \theta_\gamma < 140°$ and a photon energy above 4 GeV.

For the simulation of four–fermion samples, the program `EXCALIBUR`[97] was used. The $W^+W^-\,(\gamma)$ –like process includes $Z^0\,Z^0\,(\gamma)$, $W^+\,W^-$, $W e\,\nu_e$ and $Z^0 e^+e^-$ backgrounds. The `EXCALIBUR` version used in the analysis uses the ISR program `QEDPS`[98] from `GRACE` [99], τ decays via `TAUOLA` and final state radiation (FSR) via `JETSET`. It takes into account all amplitudes leading to a given four–fermion final state. `EXCALIBUR` does not, however, include the transverse momentum of initial state radiation in the case where electrons are present in the final state. The `GRC4F` generator[100] was used for the single W channel where the electron escapes through the beam pipe in the region cos $\theta_e > 0.9999$, which is not covered by `EXCALIBUR`.

Two–photon interactions leading to leptonic final states (QPM process only) were generated using `BDKRC`[101] for both biased and unbiased samples.

In DELPHI, Two–photon interactions leading to hadronic final states were generated using two generators, namely `TWOGAM` [102] and `PYTHIA 6.143` [103]. This process is hard to simulate since it involves, for instance, hadronic interactions between gluons and quarks originating from resolved photon(s) as illustrated in Fig. 5.10. Moreover, the modeling has to take into account perturbative and non-perturbative contributions whose properties depend on the transverse momentum of the 2-photon system ($P_t^{\gamma\gamma}$) and other kinematic variables (e.g. quark transverse momenta from resolved photons). For low $P_t^{\gamma\gamma}$, the QCD contribution diverges, and cuts must be applied. Each generator has its peculiar way to modelize hadronic $\gamma\gamma$ interactions and to deal with the diverging contributions. Intensive studies have been performed in collaboration with P. Verdier and phenomenologists involved in the generator design [104]. The conclusion of the studies led to the choice of the `PYTHIA 6.143` generator as the official DELPHI generator, keeping samples generated with `TWOGAM` for cross-checks. In summary, the available samples and their corresponding cuts at the generator level are (.OR. stands for logical or):

- PYTHIA1: $E_t > 3\ GeV$ with at least three charged particles with momentum greater than 0,1 GeV$/c$ .OR. one particle ($\theta > 2^o$) with energy greater than $0.2\sqrt{s}$.
- PYTHIA2: $E_t > 3\ GeV$ .OR. one particle ($\theta > 2^o$) with associated energy greater than $0.2\sqrt{s}$.
- TWOGAM: $E_t > 3\ GeV$ .OR. one particle ($\theta > 2^o$) with associated energy greater than $0.2\sqrt{s}$.

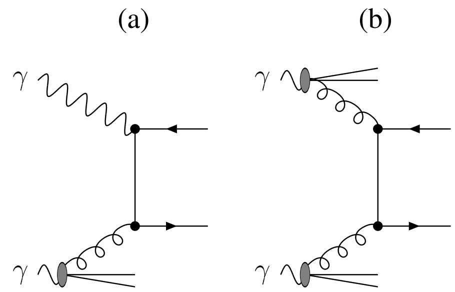

Figure 5.10: Schematic diagrams involving one resolved photon (a) and two resolved photons (b) in hadronic $\gamma\gamma$ processes.

$\sqrt{s}$ (GeV)	192	196	200	202	204	206	206.7	208
two–fermion processes								
$Z/\gamma^* \rightarrow q\bar{q}(\gamma)$	96.0400	90.0400	86.1100	83.2700	81.8500	80.1400	79.2900	78.3200
$Z/\gamma^* \rightarrow \tau\bar{\tau}(\gamma)$	7.8500	7.5500	7.1970	7.0200	6.9400	6.7500	6.6740	6.6000
$Z/\gamma^* \rightarrow \mu\bar{\mu}(\gamma)$	8.0400	7.6300	7.3000	7.2000	6.9600	6.7900	6.7890	6.6500
$Z/\gamma^* \rightarrow \nu\bar{\nu}(\gamma)$	10.8500	10.4800	10.0660	9.9400	9.6500	9.6500	9.5400	9.6200
$\mathrm{e^+e^-} \rightarrow \mathrm{e^+e^-}(\gamma)$ (Bhabha)	-	1123.0000	1081.0000	-	1033.0000	1010.0000	1000.7000	-
QED processes								
$\mathrm{e^+e^-} \rightarrow \mathrm{e^+e^-}$ (Compton)	51.8000	49.6000	47.6600	46.9000	46.0700	44.9000	44.9700	44.6900
$\mathrm{e^+e^-} \rightarrow \gamma\gamma$	-	9.7200	9.4200	9.2900	9.0000	-	8.7800	-
four-fermion processes								
$\mathrm{e^+e^-} \rightarrow WW\ like$	18.2700	18.4820	18.7200	18.7940	18.8680	18.9120	18.9400	18.9570
$\mathrm{e^+e^-} \rightarrow ee\mu\mu$	-	0.3637	0.3520	0.3474	0.3425	0.3378	0.3352	0.3324
$\mathrm{e^+e^-} \rightarrow eett$	-	0.0749	0.0730	0.0723	0.0711	0.0705	0.0703	0.0696
$\mathrm{e^+e^-} \rightarrow llll$	-	0.0432	0.0422	0.0418	0.0413	0.0406	0.0404	0.0400
$\mathrm{e^+e^-} \rightarrow qqee$	0.4247	0.4184	0.4112	0.4076	0.4040	0.3998	0.3970	0.3961
$\mathrm{e^+e^-} \rightarrow qq\mu\mu$	0.2614	0.2578	0.2530	0.2504	0.2476	0.2448	0.2427	0.2418
$\mathrm{e^+e^-} \rightarrow qqtt$	0.1095	0.1125	0.1140	0.1142	0.1143	0.1134	0.1133	0.1131
$\mathrm{e^+e^-} \rightarrow qq\nu\nu$	0.2969	0.3282	0.3509	0.3587	0.3657	0.3709	0.3735	0.3751
$\mathrm{e^+e^-} \rightarrow e\nu qq$ (GRACE)	-	0.3900	0.4200	0.4260	0.4500	-	-	0.4600
$\mathrm{e^+e^-} \rightarrow eeqq$(1) (GRACE)	-	-	6.7000	-	-	-	-	6.6910
$\mathrm{e^+e^-} \rightarrow eeqq$(2) (GRACE)	-	-	6.7000	-	-	-	-	6.7040
$\mathrm{e^+e^-} \rightarrow eeqq$(4) (GRACE)	-	-	13.0000	-	-	-	-	12.9000
$\mathrm{e^+e^-} \rightarrow eeqq$(5) (GRACE)	-	-	13.0000	-	-	-	-	12.9960
$\gamma\gamma$ processes								
$\gamma\gamma \rightarrow had.$ (PYTHIA1)	7533.2000	7655.2000	7741.6000	7828.6000	7870.5000	7935.5000	-	7982.0000
$\gamma\gamma \rightarrow had.$ (PYTHIA2)	8606.2000	8765.8000	8911.8000	8983.4000				
$\gamma\gamma \rightarrow had.$ (TWOGAM)	-	-	-	-	9881.0000	-	-	-
$\gamma\gamma \rightarrow ee$ (unbiased)	-	2168.0000	2185.0000	-	2175.0000	-	2194.0000	-
$\gamma\gamma \rightarrow ee$ (biased)	-	657.5000	659.2000	-	650.4000	-	643.6000	-
$\gamma\gamma \rightarrow \mu\mu$ (unbiased)	-	1900.0000	1940.0000	1931.0000	1956.5000	-	1985.0000	-
$\gamma\gamma \rightarrow \mu\mu$ (biased)	-	523.0000	514.0000	-	520.0000	-	524.0000	-
$\gamma\gamma \rightarrow \tau\tau$	-	441.0000	444.0000	-	451.2000	-	454.1000	-

Table 5.1: Standard model process cross-sections (pb) in function of the investigated centre-of-mass energies.

Chapter 6

Event selection stream

The analysis performed on the data collected in the years 1999 and 2000 is described in this chapter. The data collected by DELPHI since 1998 were analyzed using the likelihood ratio (LR) method (section 6.1). This method permits to select events by means of only one discriminating variable (the likelihood ratio value) instead of several ones. This is a powerful statistical method which allows to adapt the analysis to the desired luminosity more easily than a sequential analysis where all cuts have to be retuned. For instance, Fig. 6.1(left) and Fig. 6.1(right) show the dependence of the optimum expected excluded cross-section at 95% confidence level (defined in appendix H and [90]), σ^{95}_{excl}, and the likelihood ratio cut on the luminosity [1]. It is seen that for higher luminosity the likelihood ratio cut becomes tighter.

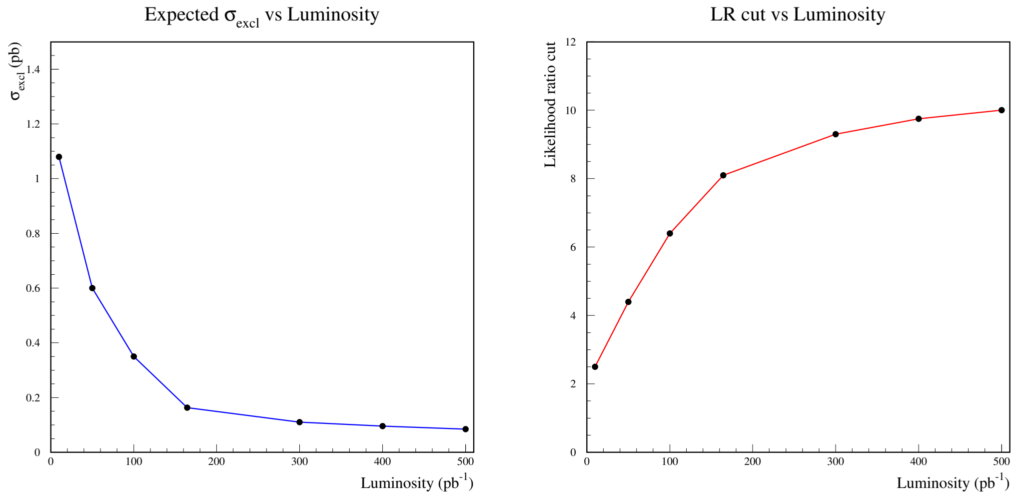

Figure 6.1: The expected excluded cross-section (left) and its corresponding LR cut (right) found for the fourth ΔM region of the $\ell\ell$ topology as a function of the luminosity at $\sqrt{s}$ = 206 GeV (C1).

[1]In the present analysis, the optimization was performed in terms of the expected excluded cross-section instead of the expected excluded number of signal events. This permitted to take into account the signal efficiency and the integrated luminosity ($\sigma_{excl} = N_{excl}/\mathcal{L}\varepsilon$). Moreover, the fact that the analysis scheme was performed by optimizing the exclusion power instead of the discovery power does not reflect any kind of "a priori" skepticism about a possible SUSY signal discovery. During the data taking, no significant deviations from the SM expectations were observed using the selection functions of the previous year. Hence the results were recomputed in terms of excluded masses and cross-sections. It has to be emphasized that an optimization for a discovery just implies a tighter cut on the LR function value, and as can be seen in appendix G, no deviations are observed in the tail of the LR function distributions.

The construction of the likelihood ratio functions and the event selection using a single cut on this variable are explained in section 6.4.4.

Different selections of chargino topologies were chosen and specific ΔM regions were defined in order to have sets of signal events with similar characteristics. Six different ΔM regions were considered from 3 GeV/c^2 up to 70 GeV/c^2(see section 6.3).

The event selection chain is shown in Fig. 6.2. All selection criteria were chosen using only simulated signal and background events. Apart from the particle selection performed within each event, they can be grouped in three steps plus a step "zero", the latter defining four topologies reflecting the 4 physical decay channels given in section 4.2. They are defined in such a way that every event from the simulation and the real data belongs to only one topology, hence generating 4 independent data/MC samples. The first step concerns the *common* selection cuts which are identical for each ΔM region inside a given topology. They reject events not coming from the e^+e^- collisions (cosmics, beam–gas, detector noise, etc.) and reduce the very high cross–section backgrounds. The second step consists of *preselection* cuts which are different for each (ΔM region,topology) window. They were built by an automatic procedure within the likelihood ratio function generation (see section 6.4.4.3), and permit to focus only on the variable ranges where the chargino signal related to this window is present. Finally, for each (ΔM region,topology) window, a likelihood ratio function was built and the optimal set of variables and the corresponding optimal likelihood ratio cut were found so as to have the minimal expected excluded chargino cross–section at 95 % confidence level. With only one cut on the likelihood ratio function, events were selected from each specific window.

EVENTS

$\mathcal{L}$	=	25.9	76.4	83.4	40.6	164.4	60.2(S1) pb^{-1}
$< E_{cm} >$	=	192	196	200	202	206	206.3(S1) GeV

$\Downarrow$

for a given topology

Common selection cuts

(the same for all ΔM)

$\Downarrow$

Preselection cuts

(different for each ΔM)

$\Downarrow$

Likelihood cut

(different for each ΔM)

Figure 6.2: Event selection chain with the likelihood ratio method.

6.1 The likelihood ratio method

The likelihood ratio method is a powerful method to classify events in two different categories. It consists of combining different discriminating variables into a single variable. If the variables are not correlated, this method provides the best possible background suppression for a given efficiency of the signal detection and the best efficiency for a given background contribution (with respect to the variables chosen to define the function).

A set of discriminating variables $\{x_1, \ldots, x_n\}$ which have different distributions for signal and background are considered. The probability density functions (pdf) of these variables are denoted as $\mathrm{f}_i^S(x_i)$ for signal events and $\mathrm{f}_i^B(x_i)$ for background events for the variable i. In the case of independent discriminating variables, the likelihood ratio function is defined as:

$$\mathcal{L}_R(x_1, x_2, \cdots, x_n) = \frac{f_1^S(x_1)\cdots f_n^S(x_n)}{f_1^B(x_1)\cdots f_n^B(x_n)} \tag{6.1}$$

In this way, a single function, $\mathcal{L}_R(x_1, x_2, \cdots, x_n)$, contains the dependence of n different variables. A maximal $\mathcal{L}_R(x_1, x_2, \cdots, x_n)$ corresponds to regions of the phase-space in $\{x_1, \ldots, x_n\}$ with the best signal to background ratio.

If Ω is the region where $\mathcal{L}_R(x_1, x_2, \cdots, x_n) > \mathcal{L}_R^{cut}$, the signal efficiency (ϵ_S) and the number of background events (N_B) are defined as:

$$\begin{aligned} \epsilon_S(\mathcal{L}_R^{cut}) &= \epsilon_S(0) \times \frac{\int_\Omega f_1^S(x_1)\cdots f_n^S(x_n)\; dx_1\cdots dx_n}{\int f_1^S(x_1)\cdots f_n^S(x_n)\; dx_1\cdots dx_n} \\ N_B(\mathcal{L}_R^{cut}) &= N_B(0) \times \frac{\int_\Omega f_1^B(x_1)\cdots f_n^B(x_n)\; dx_1\cdots dx_n}{\int f_1^B(x_1)\cdots f_n^B(x_n)\; dx_1\cdots dx_n} \end{aligned} \tag{6.2}$$

where ϵ_S is maximal for a given N_B and N_B is minimal for a given ϵ_S. Events with $\mathcal{L}_R(x_1, x_2, \cdots, x_n)$ $> \mathcal{L}_R^{cut}$ are tagged as signal-like events. The value $\mathcal{L}_R^{cut}$ can be varied to select the best expected σ_{excl} using the distributions $\epsilon_S(\mathcal{L}_R^{cut})$ and $N_B(\mathcal{L}_R^{cut})$. Therefore, optimal results are obtained by a simple cut on the $\mathcal{L}_R$ variable.

The procedure defined in this way is simple and allows any number of discriminating variables to be included. In practical applications, if the variables are not independent, a n–dimensional definition of the likelihood Ratio function should be used:

$$\mathcal{L}_R(x_1, x_2, \cdots, x_n) = \frac{f^S(x_1, \cdots, x_n)}{f^B(x_1, \cdots, x_n)} \tag{6.3}$$

Although it gives optimal results, in practice it is difficult to define and use n–dimensional functions for $n > 2$. Another possibility is to select discriminating variables with a small correlation and to apply the method as if the variables were independent. If the correlations between the discriminating variables are sufficiently small, results will be very close to optimal.

6.2 Topology definition (Topological cuts)

The simulated signal and background events and all the data collected by DELPHI in the years 1999 and 2000, were analyzed through the event selection chain given in Fig. 6.2. At the first level, events were divided into four mutually exclusive topologies which reflect the physical decay channels (section 4.2):

- *radiative topology*: requires the presence of at least one isolated photon of more than 5 GeV of energy, pointing to the region $15° < \theta_\gamma < 165°$ and with an isolation angle with respect to any other well reconstructed neutral or charged particle greater than 15°.
- $\ell\ell$ *topology*: requires no more than 5 charged particles and no isolated photon. The definition is based on the event multiplicity and no flavor identification is required.
- $jj\ell$ *topology*: is characterized by more than 5 charged particles, at least one isolated identified lepton and no isolated photon. Leptons with momentum of at least 3 GeV$/c$ and emitted at an angle of at least 20° from the jets, built without the lepton, are considered as isolated.
- $jets$ *topology*: asks for more than 5 charged particles and no isolated photon or lepton.

With these definitions there is no overlap between the topologies: each event belongs to only one topology. This division does not correspond exactly to the chargino decay–channel definition made in section 4.2. Events classified in a given topology can belong to another decay channel. For instance, events with low visible energy and, therefore, low mass difference between the chargino and the LSP, coming from hadronic decays can be selected by the leptonic topology due to the low multiplicity of these events. Some $jj\ell$ events with an unidentified isolated lepton are classified in the $jets$ topology. This migration effect tends to disappear as ΔM increases. In the final efficiency and limit computation all these effects were taken into account.

6.3 Choice of ΔM regions

In 1998 a study was done to determine a splitting of the chargino search into several analyses in the allowed ($M_{\tilde{\chi}_1^\pm}$,ΔM) plane [88]. The main goal of this study was to optimize the search to the characteristics of the chargino signal in each allowed mass region and therefore obtain a better efficiency as well as better background suppression. The ideal technique would have been to subdivide the searches in several "squares" in the ($M_{\tilde{\chi}_1^\pm}$,ΔM) plane for a given topology (decay channel), since it would permit to take into account the chargino boost as well as the difference of masses. The study led to the choice of a splitting in ΔM only. This comes from the fact that until 1998, LEP had increased its energy every year, and after each energy upgrade, a chargino mass was excluded almost up to the kinematic limit. Hence the need, at each energy upgrade, to be more focused on the new accessible range, making the signature (since the chargino searched for was expected already to have a high mass) sensitive almost only to ΔM and the topology (decay channel). Details of this study can be found in [88]. Basically, this was done analyzing chargino/neutralino simulated samples, with a chargino mass near the kinematic limit. For each generated chargino point, the mean value of the distribution of some event variables were analyzed, and a splitting was chosen in order to keep a regular behavior in the event variable distributions. To illustrate this dependence on the ΔM value, the mean values of the distribution of the missing transverse momentum and visible energy as a function of ΔM for hadronic chargino events with $M_{\tilde{\chi}_1^\pm}$ = 103.3 GeV$/c^2$ and $\sqrt{s}$ = 207 GeV is given in Fig. 6.3 The study led to the choice of six ΔM regions given in Table. 6.1. For the radiative topology where ΔM is defined as $M_{\tilde{\chi}_1^\pm}$-$M_{\tilde{\chi}_2^0}$, the study showed that the event properties were varying monotonously (in term of the mean values) with the ΔM value, hence, the same ΔM region splitting was kept to simplify the analysis.

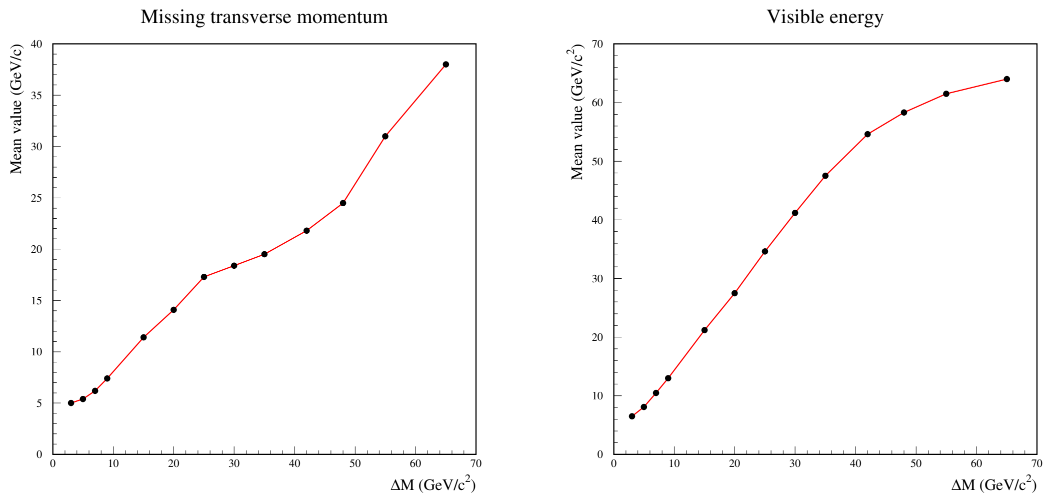

Figure 6.3: Mean values of the distribution of the missing transverse momentum (left) and visible energy (right) as a function of ΔM for hadronic chargino events with $M_{\tilde{\chi}_1^\pm}$ = 103.3 GeV$/c^2$ and $\sqrt{s}$ = 207 GeV.

ΔM regions	
1	$3 \leq \Delta M < 5$ GeV$/c^2$
2	$5 \leq \Delta M < 10$ GeV$/c^2$
3	$10 \leq \Delta M < 25$ GeV$/c^2$
4	$25 \leq \Delta M < 35$ GeV$/c^2$
5	$35 \leq \Delta M < 50$ GeV$/c^2$
6	50 GeV$/c^2 \leq \Delta M$

Table 6.1: Definition of the ΔM regions

This splitting was kept in all the $\sqrt{s}$ investigated in this work, since

- using only splitting in term of ΔM regions and topologies was enough,
- this permitted to merge the results of several $\sqrt{s}$ in an easier way than redefining the splitting at every $\sqrt{s}$.

The ΔM (and the topological) splitting must be seen more like an intuitive procedure to divide the analysis into several ones instead of being seen as an optimal procedure to do so. The properties of the distributions of the variables change with ΔM (see for instance Fig. 6.3) and even the choice of the regions was not made in an optimal manner, it makes sense to use a ΔM splitting. Hence, the definition given in Table. 6.1 was kept.

6.4 Event selection stream

This section describes in more details, all the sequential selections applied inside all windows and the generation of the likelihood ratio functions. These selections were applied in the same way to simulated chargino signal, background and real data events.

6.4.1 Particle selections

In order to reconstruct the event-shape variables, which are computed from the particle informations (kinematic informations, energy deposits), a particle selection was first performed. This permits mainly to reject particles not coming from e^+e^- collisions and detector reconstruction problems. The following quality requirements were applied to the charged and neutral particles observed in the detector.

- Charged particles were required to have momentum p above 100 MeV/c and below $1.5\sqrt{s}/2$, a relative momentum error less than 100 %, and to extrapolate back to within 5 cm of the main vertex in the transverse ($r\phi$) plane and 10 cm/$\sin\theta$ in the longitudinal (z) direction.
- VD–ID and OD–ID tracks with no signal in the TPC detector but with θ and ϕ angles inside the TPC acceptance were rejected. More stringent quality cuts on the relative momentum error, maximal momentum and impact parameter of such tracks with respect to the nominal beam interaction point were applied to discard badly measured tracks from the events. A summary of the quality cuts on these tracks is shown in table 6.2. The resulting distribution of the transverse momentum of the VD–ID only tracks over the missing transverse momentum of the event after the quality cuts can be seen in Fig. 6.5. The excess around 1 (see Fig. 6.4) due to the badly measured VD–ID only tracks has disappeared.
- Energy clusters in the calorimeters were taken as neutral particles if not associated to a charged particle and if above an energy threshold ranging from 300 to 500 MeV for deposits in the electromagnetic calorimeters (depending on the region of the detector) and 900 MeV for deposits in the hadron calorimeters. Cuts removing clusters created by radioactivity in the lead of the HPC or by cosmics were also applied.

VD–ID only tracks	**OD–ID only tracks**
θ and ϕ outside the TPC acceptance	θ and ϕ outside the TPC acceptance
ΔP/P < 1.5	ΔP/P < 0.05
P$_{track}$ < 10 GeV$/c$	
z impact parameter < 4 cm	z impact parameter < 0.005 cm
$r\phi$ impact parameter < 1.02 cm	$r\phi$ impact parameter < 0.2 cm

Table 6.2: Quality preselection cuts applied on VD–ID only and OD–ID only tracks.

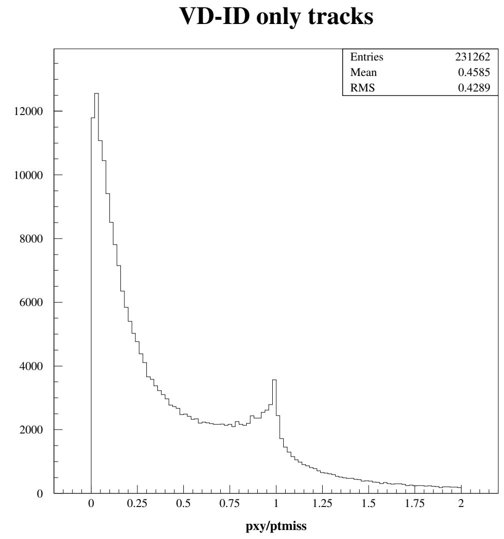

Figure 6.4: Distribution of the ratio between the transverse momentum of the VD–ID only tracks and the missing transverse momentum of the real data selected by the first ΔM region of the $jets$ topology at 189 GeV [88] before applying track quality cuts.

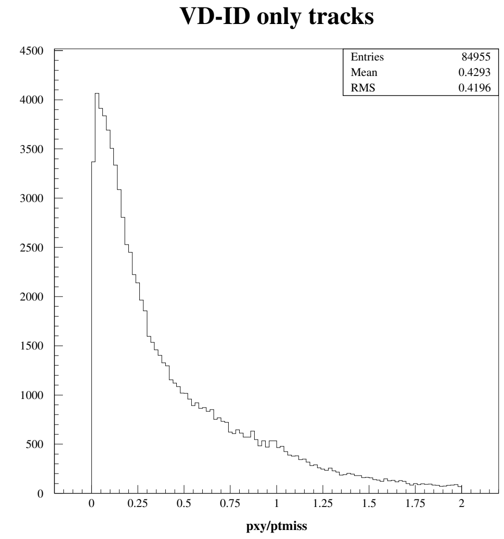

Figure 6.5: Distribution of the ratio between the transverse momentum of the VD–ID only tracks and the missing transverse momentum of the real data selected by the first ΔM region of the $jets$ topology at 189 GeV [88] after applying track quality cuts.

6.4.2 Topological selections

Are defined in section 6.2

6.4.3 *Common* selections

After classifying the events in different topologies, the next step consisted to apply a set of *common* selection cuts which were identical for all ΔM regions within a given topology. They permitted to solve some disagreements (at a very loose level of selection) between the data and the Monte Carlo events due to weaknesses of the simulation or to detector noise and to reduce high cross–section backgrounds in order to have the cleanest possible sample before starting the likelihood ratio function generation. Although the topological separation has already been performed at this level, it is nevertheless interesting to inspect the cuts which are common to the 4 topologies and observe their impact on the general agreement between the data and the SM simulation. Those cuts consisted of the following requirements:

- There had to be at least one charged particle with a transverse momentum above 1.5 GeV/c and the transverse energy of the event [2] must exceed 4 GeV/c. This is extremely close to the DELANA filter [3] when considering topologies containing charged particles. In the following, the word DELANA will be associated to the DELANA filter as well as these two cuts.
- The presence of at least 2 charged particles.
- At least one track had to be reconstructed by the TPC.

[2]The transverse energy is defined as the sum of the absolute values of the transverse momenta of all particles in the event.

[3]The DELANA filter consists of several loose selections applied on variables reconstructed at the level of DELANA. Those loose selection criteria permit to decrease the contribution of events not coming from e^+e^- interactions.

- The percentage of rejected particles per event had to be less than 75 %.
- The sum of the energy of the VD-ID only tracks was not exceeding 40% of the total visible energy.
- The relative error on the neutral energy was not exceeding 40% of the total visible energy.

Those cuts permitted mainly to eliminate noise and badly reconstructed events and the main background processes rejected by this level were two-photon interactions (for which most of the energy is deposited in the forward regions of the detector), neutral or single track final states (like $e^+e^- \to \gamma\gamma$, $e\gamma \to e\gamma$) and beam-related backgrounds.

Then cuts dedicated to focus on the SUSY typical signatures were applied, those common to the 4 topologies were:

- The requirement of a $\not{p}_t$ larger than 2 GeV/c (which will be extended to 4 GeV/c in all the windows but the first leptonic one) to reject $\gamma\gamma$-like events.
- The STIC luminometer had to contain less than 40 % of the visible energy (against $\gamma\gamma$ and 2-fermion process with ISR).
- The thrust value had to be lower than 0.98 to prevent cigar-like events typical of the 2-fermion process.
- A positive missing mass squared ($\not{M}^2$) typical of SUSY signatures with R-parity conservation was required.
- In case of active taggers not associated to reconstructed jets/particles, the event was rejected if the tagger location was correlated in azimuth (the ϕ angle in the DELPHI coordinate system) with the direction of the missing momentum. This procedure permits to reject events faking chargino signal due to the loss of particles in the DELPHI insensitive region at polar angles around 40° and 140°.

Tables 6.3 and 6.4 show the data-SM simulation agreement after each cut for the data recorded in year 2000 with and without TPC sector 6 respectively. After the first level of cuts, almost a perfect agreement is achieved between the real data and the SM expectation even when the TPC sector 6 was off. Then discrepancies occur as soon as a cut on the missing transverse momentum is performed. Nevertheless, at the end of this selection, common to all windows of investigation, only a disagreement of about 4% is observed which is quite satisfactory for this phase-space region (dominated by the tails of the distribution of several SM processes). The numbers shown in the table were computed using the "unbiased" leptonic $\gamma\gamma$ samples to account for the smearing effect due to the cut on the transverse energy performed at the generator level (see section 5.5). The smearing effect can be illustrated by the following example. Events (not generated) with a transverse energy under 4 GeV (the cut applied in the leptonic $\gamma\gamma$ simulation) may give a reconstructed transverse energy greater than 4 GeV and sufficient $\not{p}_t$, hence passing the selection described previously. But since those events are not simulated due to the cut at the simulation level, it may give rise to discrepancies. This is illustrated in Fig. E.3 which contains several distributions at the level of the $\ell\ell$ *common* selection for the data collected in year 2000 with TPC sector 6 (C1 reprocessing). Those plots have been generated with the biased leptonic $\gamma\gamma$ samples since they reproduce better the tail of the distributions due to their higher statistics compared to the "unbiased" samples. Nevertheless near the verge of the generation cut one observes discrepancies. If one uses the "unbiased" samples instead, the low momentum and low energy regions are well described but the tails suffer from some discrepancies due only to the statistics since the "unbiased" and biased samples were generated with exactly the same generator. This is why in the following, all the likelihood ratio functions were generated with "unbiased" samples but the optimal likelihood ratio cuts and final numbers were computed with the biased samples. All the plots given in the appendices were generated using the biased samples in order to reproduce correctly the tail of the distributions. Another study of this smearing effect in the case of the maximum transverse momentum may be found in [105]. It has to be emphasized that only the $\ell\ell$ topology is sensitive to this choice and that as soon as a cut on the likelihood ratio function is performed both samples give compatible results (within their statistical uncertainty).

Table 6.5 shows the impact of the cuts common to the 4 topologies on 3 different chargino simulated samples with $M_{\tilde{\chi}_1^\pm}$ = 103 GeV$/c^2$ and ΔM = 65, 30 and 3 GeV$/c^2$. The first 2 samples are almost insensitive to the cuts, the situation is quite different when considering the low ΔM region where the DELANA cut already lowers the efficiency by a factor 6. This is due to the softness and the low visible energy of the events arising from such mass configurations. This is why in the leptonic topology (the low multiplicity channel) the cut on the $\not{P}_t$ for the first ΔM region was not increased to 4 GeV$/c$ but kept at 2 GeV$/c$ in order to still have a non-vanishing efficiency in this region.

Cuts	**Data**	**MC (total)**	**Relative difference**	$\gamma\gamma$	**2-fermion**	**4-fermion**
DELANA	271292	225395	16.9%	141088	80900	3407
$N_{charged}$	258578	219678	15.0%	137595	78724	3359
N_{TPC}	172775	169373	2.0%	129081	36961	3331
% rejected tracks	169364	166226	1.9 %	128439	34463	3324
$\%E_{VD-ID}$	162053	161117	0.6%	123927	33924	3266
$\Delta E_{neu.}/E_{neu.}$	156953	156734	0.1 %	120534	32954	3246
$P_t^{mis.}$	65595	60107	8.3%	30747	26178	3182
$E_{STIC}/E_{vis.}$	38118	36248	4.9%	10687	22567	2994
$Thrust$	23631	22450	5.0%	9629	9914	2907
$\not{M}^2$	20607	19753	4.1%	9492	7828	2433
Hermeticity	20162	19342	4.0%	9369	7617	2356

Table 6.3: Real data and SM expectations after each cut common to all topologies for the 2000 data C1. The 2-fermion background rates contain the QED and Compton processes contributions.

To illustrate this selection graphically, Fig 6.15 and Fig 6.16 located at the end of this chapter, show the evolution of the data-MC agreement when considering the data recorded in year 2000 with the TPC sector 6 (reprocessing C1). The arrows on the figures show the cut values which have been applied. The last figure shows the hermeticity tag value, a value greater than zero corresponds to the situation where an active tagger is correlated in azimuth with the transverse missing momentum. Hence, events with non-zero values have been discarded.

After these requirements common to the 4 topologies, other cuts have been applied within each topology:

- To reject $\gamma\gamma$ and 2-fermion events, a missing transverse momentum greater than 4 GeV$/c$ was required except in the first $\ell\ell$ window,

Cuts	**Data**	**MC (total)**	**Relative difference**	$\gamma\gamma$	**2-fermion**	**4-fermion**
DELANA	104534	86275	17.0%	56409	28644	1222
$N_{charged}$	100519	83992	16.0%	54959	27831	1202
N_{TPC}	57830	56557	2.2%	42590	12778	1189
% rejected tracks	56081	55020	1.8%	42216	11620	1184
$\%E_{VD-ID}$	53242	52897	0.7%	40369	11368	1160
$\Delta E_{neu.}/E_{neu.}$	51572	51653	-0.2%	39464	11035	1154
$P_t^{mis.}$	22096	20471	7.4%	10477	8862	1132
$E_{STIC}/E_{vis.}$	12596	12078	4.2%	3411	7602	1065
$Thrust$	7957	7546	5.2%	3092	3417	1037
$\not{M}^2$	6912	6619	4.2%	3043	2700	876
Hermeticity	6744	6465	4.1%	3006	2625	834

Table 6.4: Real data and SM expectations after each cut common to all topologies for the 2000 data S1. The 2-fermion background rates contain the QED and Compton processes.

	Chargino efficiency (%)					
Cuts	($M_{\tilde{\chi}_1^\pm}$,ΔM) (103,65)		($M_{\tilde{\chi}_1^\pm}$,ΔM) (103,30)		($M_{\tilde{\chi}_1^\pm}$,ΔM) (103,3)	
	C1	S1	C1	S1	C1	S1
DELANA	99.8	99.6	98.9	98.9	14.7	13.6
$N_{charged}$	99.4	98.8	98.2	98.2	14.7	13.6
N_{TPC}	99.3	98.7	98.1	98.0	14.6	13.5
% rejected tracks	99.1	98.3	97.9	97.2	14.6	13.5
$\%E_{VD-ID}$	97.5	96.5	96.0	95.0	14.4	13.4
$\Delta E_{neu.}/E_{neu.}$	97.2	96.0	95.8	93.2	14.2	13.0
$P_t^{mis.}$	96.4	95.1	93.5	91.4	9.3	8.6
$E_{STIC}/E_{vis.}$	93.7	92.9	90.1	89.9	9.3	8.3
$Thrust$	92.7	92.0	89.8	88.6	9.0	8.3
$\not{M}^2$	92.4	91.8	89.8	88.5	9.0	8.3
Hermeticity	90.5	89.3	88.6	87.5	9.0	8.3

Table 6.5: Impact of the cuts common to the 4 topologies on the detection efficiency of 3 chargino points generated with reprocessing C1 and S1.

- To reject Bhabha events, the percentage of electromagnetic energy had to be smaller than 95 % in the $jets$ and $jj\ell$ topologies. In the $\ell\ell$ topology, an acoplanarity greater than 10°was required.

- Cosmics clusters and noises in the hadronic calorimeter superimposed to $\gamma\gamma$ events can be an important source of background. These events are characterized by a low visible mass, low energy deposit in the HCAL (E_{HCAL}) and low but sufficient $\not{P}_t$ due essentially to one reconstructed neutral particle in the HCAL. To eliminate this kind of background, in the low visible mass region ($M_{\mathrm{vis}} \leq$ 40 GeV$/c^2$ and $E_{\mathrm{HCAL}} \leq$ 20 GeV), a ratio between the transverse momentum of the most energetic HCAL neutral particle in the event and the $\not{P}_t$ lower than 0.4 was required. The anode information from the HCAL clusters was also used , as explained in [88]. In the leptonic case, this cut was not applied.

- An additional cut was applied in the low visible energy region of the *radiative* topology requiring the photon to have reached one of the electromagnetic calorimeters to reject photon conversion.

- Finally, the non–degenerate ΔM regions of the $jets$ topology are dominated by the 4-fermion and 2-fermion backgrounds. To reduce their contribution, events with a visible mass larger than 65 GeV$/c^2$ were rejected.

6.4.4 Likelihood ratio function generation

Different *common* selections, depending on the considered topology, were applied to reject the most basic background events. 24 different windows were defined (4 topologies and 6 ΔM regions). The next step consisted in building a likelihood ratio function in each window.

The variables $\{x_i\}$ used to build the $\mathcal{L}_R$ functions in the present analysis were : the visible energy (E_{vis}), transverse energy (E_t), charged transverse energy (E_t^{ch}) , visible mass (M_{vis}), effective centre-of-mass energy ($\sqrt{s'}$), squared sum of the transverse momenta with respect to the thrust axis ($\tilde{P}^2$), missing transverse momentum ($\not{P}_t$), polar angle of the missing momentum ($\theta_{\not{p}}$), missing mass ($\not{M}$), number of charged particles, total number of particles, number of identified leptons, acoplanarity, acollinearity, ratio of the electromagnetic energy to the total energy ($\%\ E_{EM}$), percentage of total energy within 30° of the beam axis ($\%\ E_{30^\circ}^{cone}$), invariant mass of the hadronic system (M_{jj}), invariant mass of lepton and neutrino system ($M_{\ell\nu}$), kinematic information concerning the isolated photons and leptons and two most energetic charged particles, and finally the jet characteristics including the separation distance (y_2^{cut}) to switch from a 3-jet to a 2-jet event using the DURHAM [86] algorithm.

From the distributions of these variables for signal and background events, the corresponding probability density functions were generated (section 6.4.4.1). To reduce statistical fluctuations in the pdf's a filter was applied (section 6.4.4.2) and automatic *preselection* cuts were generated (section 6.4.4.3). Then, using a sub–set of these filtered pdf's, the likelihood ratio function was built (section 6.4.4.4).

6.4.4.1 Probability density functions

More than 40 variables were chosen to discriminate chargino signal events from background events. The signal and background distributions of each variable were generated with the respective signal and background events passing the topological and *common* selection cuts corresponding to each particular topology. Normalizing to 1 these distributions, the probability density functions were obtained. The signal distributions of all the variables $\{x_i\}$ were built with signal events generated with parameter sets giving rise to charginos and neutralinos with masses in the corresponding ΔM region.

An example of the pdf distribution of the ratio of E_{vis} and the centre-of-mass energy ($E_{cm} \equiv \sqrt{s}$) for signal, $\mathrm{f}^S(E_{\mathrm{vis}}\ /E_{cm})$, and background, $\mathrm{f}^B(E_{\mathrm{vis}}\ /E_{cm})$ events passing the 4^{th} ΔM region cuts of the $\ell\ell$ topology at E_{cm} = 206 GeV is shown in Fig. 6.6. The ratio between both probability density functions corresponds to the likelihood ratio function of this single variable $\frac{f^S(E_{vis}/E_{cm})}{f^B(E_{vis}/E_{cm})}$ (Fig. 6.7). The likelihood ratio function indicates the range of the variable in which it is more likely to distinguish the signal from the background.

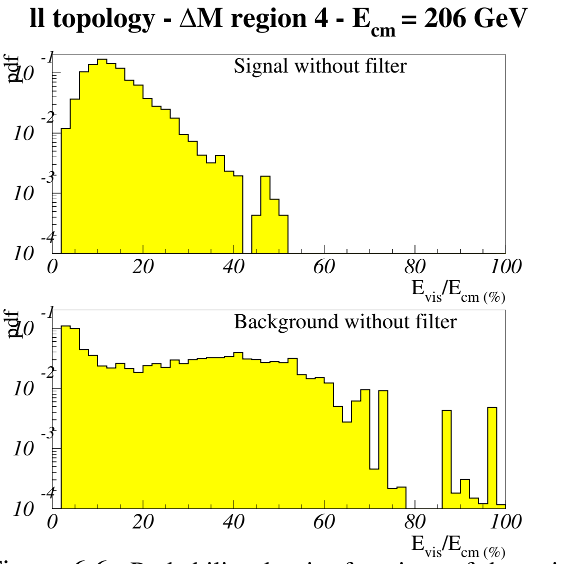

Figure 6.6: Probability density functions of the ratio between the visible energy and $\sqrt{s}$ for signal (top) and background (bottom) events of the 4^{th} ΔM region of the $\ell\ell$ topology before filtering.

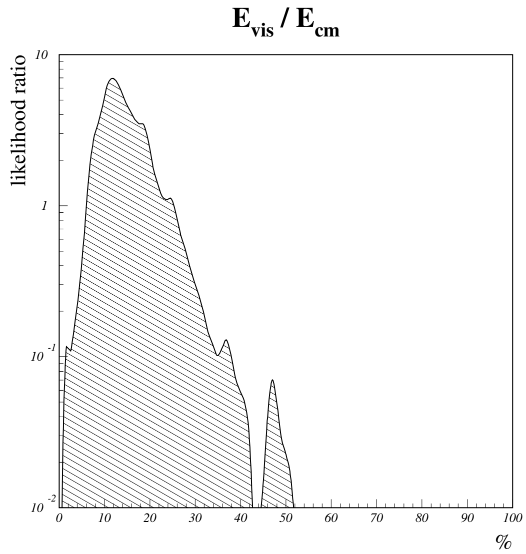

Figure 6.7: Likelihood ratio function of the ratio between the visible energy and $\sqrt{s}$ of the 4^{th} ΔM region of the $\ell\ell$ topology before filtering.

6.4.4.2 Filtering of signals

The probability density functions obtained for all variables and ΔM regions show statistical fluctuations, as seen in Fig. 6.6. To reduce them a smoothing of the signal and background pdf's was performed using a triangular filter and a linear interpolation between bins. After this operation, to further reduce the fluctuations, disconnected areas with low probability (i.e. less than 1% of the total probability) were eliminated.

A triangular filter is a low pass filter which rejects the high frequency components of a signal. Its impulse response to a δ function is a triangular function. The output signal will be the convolution of the input signal and the filter response function.

The result of applying this kind of filter to the pdf distributions of the ratio of $E_{\rm vis}$ and the centre-of-mass energy (E_{cm}) in the 4^{th} ΔM region cuts of the $\ell\ell$ topology is plotted in Fig. 6.8. Smoothing was performed and the right disconnected part of the background pdf was eliminated due to its low probability. The likelihood ratio function corresponding to the filtered signal and background functions is shown in Fig. 6.9.

6.4.4.3 generation of the *preselection* cuts

Finally, an automatic procedure scanned all the signal pdf's, generating a new set of cuts to constrain the allowed variable ranges in the regions where the chargino signal of the corresponding window was present. This procedure is important since the variables used in the present search are all correlated, and a cut in a variable changes the shape of the others. Those cuts do not affect the signal pdf's but the background pdf's only. After those cuts were determined, the pdf's were regenerated requiring the events to satisfy those new *preselection* cuts. In the distribution given in Fig 6.6, this procedure triggered a cut at 52%.

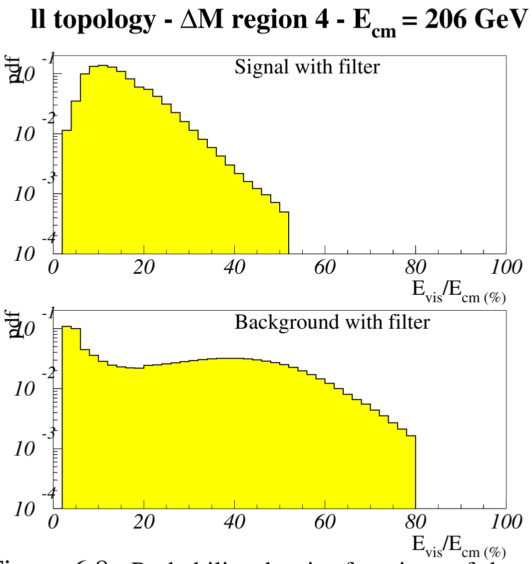

Figure 6.8: Probability density functions of the ratio between the visible energy and $\sqrt{s}$ for signal (top) and background (bottom) events of the 4^{th} ΔM region of the $\ell\ell$ topology after filtering.

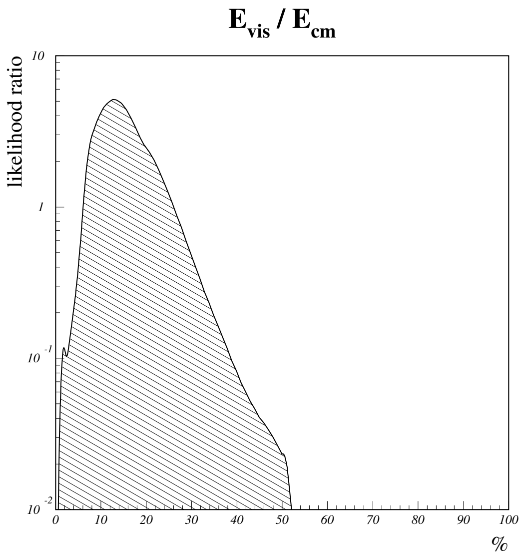

Figure 6.9: Likelihood ratio function of the ratio between the visible energy and $\sqrt{s}$ of the 4^{th} ΔM region of the $\ell\ell$ topology after filtering.

6.4.4.4 The likelihood ratio function

After having generated and smoothed the probability density functions of the variables $\{x_i\}$ for signal $\mathrm{f}_i^S(x_i)$ and background $\mathrm{f}_i^B(x_i)$ events in all ΔM regions and topologies, the likelihood ratio function can be defined. A sub–set of n discriminating variables to be combined can be chosen for each (ΔM topology) window. From the product of the corresponding pdf's, the likelihood ratio function $\mathcal{L}_R(x_1, x_2, \cdots, x_n)$ can be obtained, as shown in Eq.(6.1). The dependence of n variables is contained in a single variable: the likelihood ratio function.

The likelihood ratio function built with simulated events passing the 4^{th} ΔM region preselection cuts of the $\ell\ell$ topology at $\sqrt{s}$ = 206 GeV can be seen in Fig. 6.10. This $\mathcal{L}_R$ function was built with 7 discriminating variables: the total and the charged multiplicity per event, the acoplanarity, $\not{P}_t$, $\theta_{\not{p}}$, % $E^{cone}_{30^\circ}$ and the momentum of the leading charged particle (P^{max}_{track}).

Background events are essentially concentrated at low $\mathcal{L}_R$ values, while signal events extend over the whole range. Thus, this variable $\mathcal{L}_R$, which takes into account 7 variables in this example, can be used to discriminate chargino signal events from the SM background ones.

6.4.4.5 Minimal expected excluded cross–section (likelihood ratio cut)

Using the chargino simulation and the SM background samples, the distributions of the mean [4] efficiency and the number of expected background events can be plotted as a function of $\mathcal{L}^{cut}_R$. This is shown in Fig. 6.11.

The efficiency (ϵ_S) and the number of background events (N_B) decrease when $\mathcal{L}^{cut}_R$ increases. In this example, for $\mathcal{L}^{cut}_R$ = 9.3, a 30 % efficiency and $\approx$ 11.8 background events are found. As can be

[4] Corresponding to the averaged efficiency of the chargino samples belonging to the investigated window.

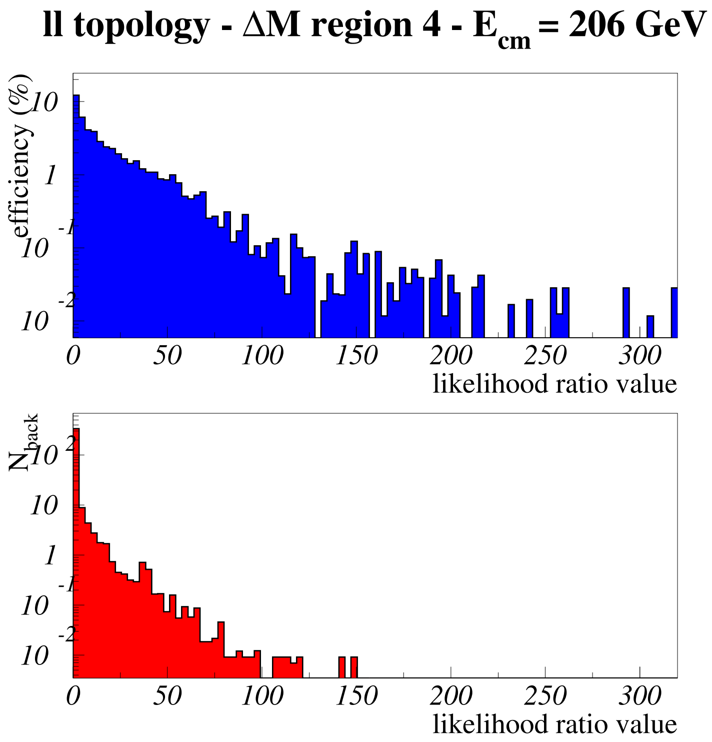

Figure 6.10: Likelihood ratio distribution $\mathcal{L}_R(\#Part, \#Tracks, \not{P}_t, \theta_{\not{p}}, \%\ E^{cone}_{30^\circ}, P^{max}_{track})$ for signal (top) and background (bottom) events passing the 4^{th} ΔM region preselection cuts of the $\ell\ell$ topology.

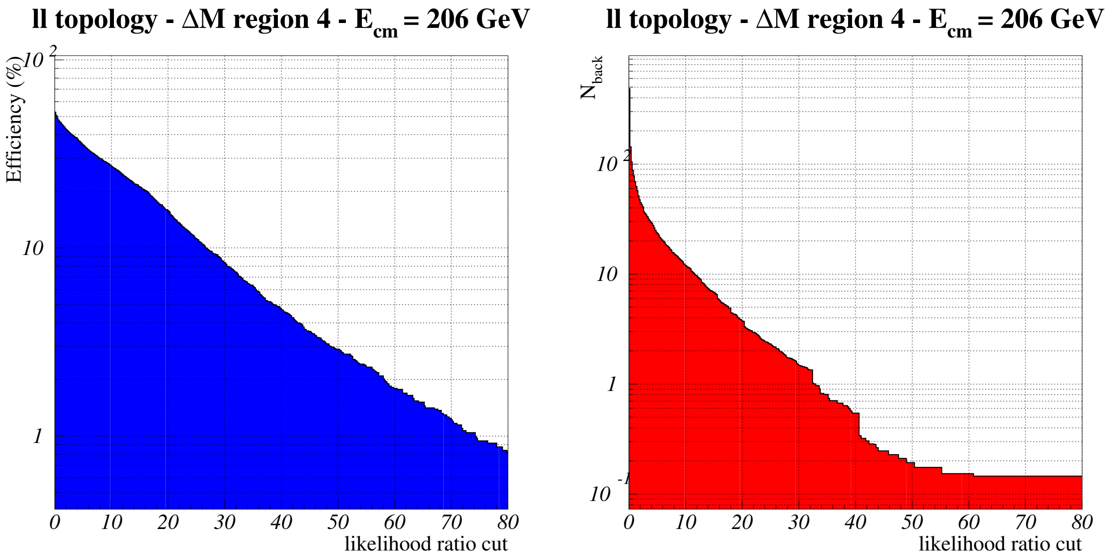

Figure 6.11: Distributions of efficiency (left) and expected number of background events (right) as a function of the likelihood ratio cut for events passing the 4^{th} ΔM region cuts of the $\ell\ell$ topology.

seen in Fig. 6.12, a minimum on $\sigma_{exclusion}$ can be extracted for a certain $\mathcal{L}_R^{cut}$ value.

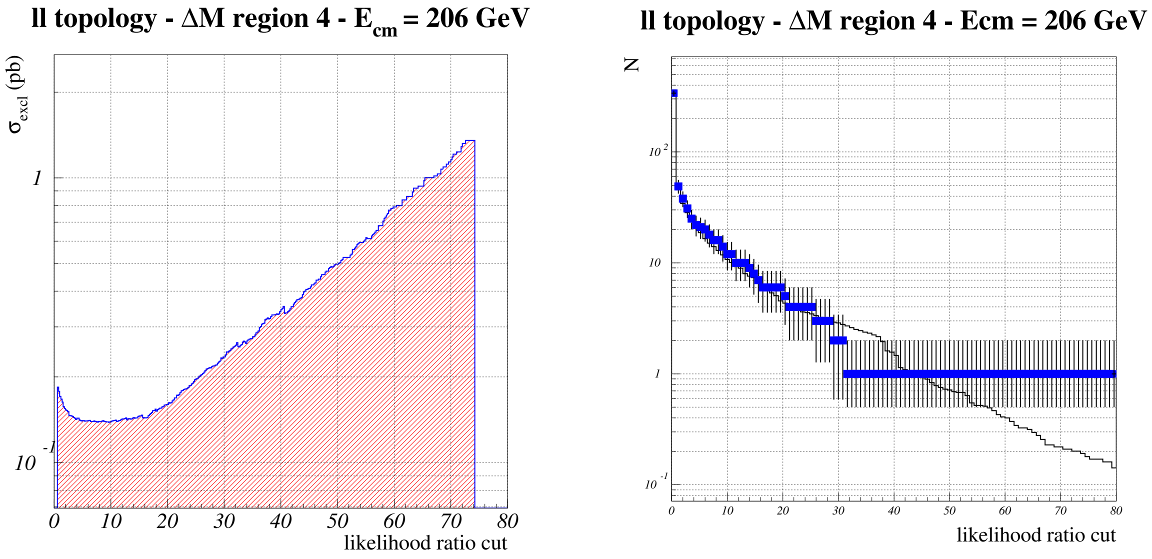

Figure 6.12: Expected excluded cross–section distribution (left) and data-MC agreement (right) as a function of the likelihood ratio cut for events passing the 4^{th} ΔM region cuts of the $\ell\ell$ topology at $\sqrt{s}$ = 206 GeV with DELPHI TPC sector 6 (164 pb^{-1}).

In each window all the combinations of the pdf's were tested, starting from a minimal set of four variables. Every combination defined a $\mathcal{L}_R$ function and a $\mathcal{L}_{R_{CUT}}$ that minimized the expected excluded cross-section at 95% C.L. using the monochannel formula given in appendix H. The parameters entering this computation were the number of expected background events and the window efficiency of the chargino selection, defined as the mean efficiency of the chargino-neutralino mass sets belonging to the investigated window [5]. The combination of variables corresponding to the lowest excluded cross-section defined the $\mathcal{L}_R$ function and the $\mathcal{L}_{R_{CUT}}$ of this window.

This procedure was performed in every window with two exceptions. The first two degenerate ΔM regions were merged with the third one in the $jj\ell$ topology, since the efficiency to identify the isolated lepton is very low due to its low momentum, hence the construction of likelihood ratio function suffers from high statistical fluctuations in those first two windows. In addition, the multiplicity of the events in these regions is also low. However, these $jj\ell$ events are not lost, since they are selected by the merged $jj\ell$ window (which nevertheless focus mainly of the third ΔM range since the statistics are higher there). Moreover, from the study on the ΔM splitting performed in 1998 [88], it has been shown that radiative event properties varied monotonously with ΔM(here defined as $M_{\tilde{\chi}_1^\pm}$ - $M_{\tilde{\chi}_2^0}$). In order to simplify the analysis the first four and the last two ΔM regions were merged.

Tables 6.6 to 6.9 summarize the optimal set of variables which define the likelihood ratio function for each (ΔM,topology) window for the analysis of the 2000 C1 and S1 data.

[5]The efficiency of one chargino-neutralino mass set is defined as the number of events satisfying $\mathcal{L}_R > \mathcal{L}_{R_{CUT}}$ divided by the total number of chargino events satisfying the topological cuts.

Topology	Variables	ΔM regions (GeV$/c^2$)					
		$3 \leq \Delta M < 5$	$5 \leq \Delta M < 10$	$10 \leq \Delta M < 25$	$25 \leq \Delta M < 35$	$35 \leq \Delta M < 50$	$50 \leq \Delta M$
$jets$	# Part	X		X	X	X	
	# Tracks	X	X		X	X	X
	Acoplanarity	X	X	X	X	X	X
	$\not{P}_t$		X	X			
	$\theta_{\not{p}}$	X	X	X	X	X	X
	$\%\ E_{30^\circ}^{cone}$		X	X			
	$M_{\rm vis}$				X	X	X
	$E_{\rm vis}$			X	X	X	X
	P_{track}^{max}					X	
	$\sqrt{s'}$	X					
	θ_{jets}	X	X	X	X	X	X
	$\theta_{neutral}^{max}$			X			
	y_2^{cut}	X		X	X	X	X

Table 6.6: The optimal set of variables defining the likelihood ratio for each ΔM region in the $jets$ topology for the analyses of 2000 C1 and S1 data.

Topology	Variables	ΔM regions (GeV$/c^2$)					
		$3 \leq \Delta M < 5$	$5 \leq \Delta M < 10$	$10 \leq \Delta M < 25$	$25 \leq \Delta M < 35$	$35 \leq \Delta M < 50$	$50 \leq \Delta M$
$jj\ell$	Acoplanarity	X			X	X	X
	$\not{P}_t$	X			X	X	
	$\theta_{\not{p}}$	X			X	X	X
	$\%\ E_{EM}$						X
	$\not{M}$						X
	θ_{jets}				X		X
	$M_{\ell\nu}$	X			X	X	X
	M_{jj}				X	X	X
	P_ℓ^{max}	X				X	X

Table 6.7: The optimal set of variables defining the likelihood ratio for each ΔM region in the $jj\ell$ topology for the analyses of 2000 C1 and S1 data.

Topology	Variables	ΔM regions (GeV$/c^2$)					
		$3 \leq \Delta M < 5$	$5 \leq \Delta M < 10$	$10 \leq \Delta M < 25$	$25 \leq \Delta M < 35$	$35 \leq \Delta M < 50$	$50 \leq \Delta M$
radiative	Acoplanarity	X				X	
	E_{vis}	X				X	
	P^{max}_{track}	X				X	
	P^{2nd}_{track}	X				X	
	P$^{max}_{jet}$	X				X	
	E_t	X				X	
	E^{ch}_t	X				X	
	E^{max}_{γ}/E_{EM}	X				X	

Table 6.8: The optimal set of variables defining the likelihood ratio for each ΔM region in the *radiative* topology for the analyses of 2000 C1 and S1 data.

Topology	Variables	ΔM regions (GeV/c^2)					
		$3 \leq \Delta M < 5$	$5 \leq \Delta M < 10$	$10 \leq \Delta M < 25$	$25 \leq \Delta M < 35$	$35 \leq \Delta M < 50$	$50 \leq \Delta M$
	# Part			X	X	X	X
	# Tracks	X	X	X	X	X	
	# ℓ			X		X	X
	Acoplanarity	X	X	X	X	X	X
	$\not{P}_t$		X	X	X	X	X
	$\theta_{\not{p}}$	X	X	X	X	X	X
$\ell\ell$	% $E_{30^\circ}^{cone}$	X		X	X		
	M_{vis}		X			X	X
	P_{track}^{max}		X		X	X	X
	θ_{track}^{max}			X		X	X
	E_t^{ch}	X	X	X			
	$\tilde{P}^2$		X				X

Table 6.9: The optimal set of variables defining the likelihood ratio for each ΔM region in the $\ell\ell$ topology for the analyses of 2000 C1 and S1 data.

6.5 Data-Monte Carlo comparison

All data collected by DELPHI in year 2000 and the Monte Carlo background events were compared at four different levels in the selection chain: after the *common* selection, after the preselection, as function of the likelihood ratio cut and after the optimal likelihood ratio cut, the latter being discussed in chapter 7.

6.5.1 Comparison at the *common* selection level

Appendix E contains the distributions of the main variables used in the chargino analysis for the data collected in the year 2000 (dots) and SM background (histogram) events after the *common* selections. A good general agreement between the real data and SM background is observed in all distributions for both reprocessing C1 and S1 within each topology. The relative difference between the data and MC is ranging from 1% to 10%. The difference between the data and MC rates originates mainly from the cut on the $\not{P}_t$ variable where a shift between the data and MC distribution is observed before applying a $\not{P}_t$ cut (see Fig 6.16 and Table 6.3). The origin of this shift/discrepancy between the data and the MC distributions is not yet completely understood. Nevertheless the following effects seem to be the major sources of this problem:

- For low multiplicities, the TPC distortions (not taken into account in the simulation of the DELPHI detector), which produce track mis-recontructions, give rise to substantial $\not{P}_t$ in events with few tracks [106], hence generating a shift with respect to the SM simulation.
- Z^0 radiative returns have usually both jets in the same hemisphere which typically point to the forward part of DELPHI. $\not{P}_t$ arises due to a wrong reconstruction of one of the jets, as jets are energetic, small mis-reconstruction of one of them is enough to produce substantial $\not{P}_t$. This happens typically when one of the jets has a part going into a hole, for example between modules of the HPC or in the 40° region [107]. This effect will be illustrated by one of the candidates of the *radiative* topology at the end of the chapter 7.

The maximal differences are observed in the (ΔM,$jets$) windows where the cut on the visible mass increases the relative contribution of the Z^0 with radiative return events. It has to be emphasized that the same situation occurred for the data collected during year 1999.

6.5.2 Comparison at the preselection level

The distribution of one of the typical variables used in the chargino analysis for data (dots) and background events (histogram) are shown in appendix F for each (ΔM,topology) window for the data collected in the year 2000 with and without TPC sector 6 before(left plot) and after(right plot) the likelihood ratio cut. As at the *common* selection levels, a relative difference ranging from 1% to 10% is observed.

6.5.3 Comparison as a function of the likelihood ratio cut

A comparison between the data collected in year 2000 and the simulated SM background processes was made at the end of the preselection chain in each window of investigation. A typical variable distribution is shown for every window before(left plot) and after(right plot) the likelihood ratio cut in appendix F. The data and MC agreement in each window before applying the likelihood ratio cut is of about 1% to 10% depending of the investigated windows. After applying the corresponding preselection cuts depending on each ΔM region and topology, the evolution of the number of real data and background events as a function of the likelihood ratio cut was studied.

Using the optimal combination of discriminating variables in order to have the minimal expected σ^{95}_{excl}, a likelihood ratio function was built for each ΔM region and topology. The variation of the number of events passing a cut on this variable was plotted. Appendix G contains the distributions of the number of real data (dots) and background events (histogram) as a function of the likelihood ratio cut for the $jets$, $jj\ell$, $\ell\ell$ and *radiative* topologies for the data collected in year 2000 with and without TPC sector 6. Obviously, the number of data and background events decreases when the likelihood ratio cut increases. In general, the agreement between data and the Monte Carlo is quite good in all the topologies for any value of the likelihood ratio cut. Almost all the discrepancies observed at the preselection level disappear as soon as a cut on the corresponding likelihood ratio is performed. Nevertheless, in some windows, data-MC agreement is achieved after requiring stronger value of the likelihood function. At their optimal cut, (which was determined without studying the real data) all windows, but one, select real data in agreement with the SM expectations as illustrated in appendix G (right plots). In the case of the first leptonic window, an excess of MC with respect to the real data is observed when considering the data collected in year 2000 without TPC sector 6 (S1 reprocessing). First of all, at the level of the preselection which contains several cuts constraining the events to contain particles with a low momentum and low $\not{p}_t$ (due to the automatic procedure which generated the cuts to focus on the signal), there is already an excess of the SM expectation with respect to the real data of about 1.2 (1.3 with "unbiased" $\gamma\gamma$) standard deviation as illustrated in Fig. 6.13.a. In the same figure, one sees that the effect of the loss of the TPC sector 6 seen in the real data is well reproduced in the SM simulation. The problem seems in fact related to the distribution of the momentum of the charged particles, as illustrated in Fig. 6.13.b for the momentum of the most energetic track, where a shift between the real data and the simulation is observed. When considering data-MC agreement at the level of the final selection (Fig. 6.14.a and 6.14.b) one sees that the excess of the MC is located in the low values of the $\not{p}_t$ (Fig. 6.14.a) This is one of the reasons why this problem disappears when considering the other leptonic windows where the minimal value of the $\not{p}_t$ was set by hand to 4 GeV/c. The shift appears when considering the first leptonic window of the other centre-of-mass energies investigated in this thesis but gives a disagreement in terms of final numbers within one standard deviation (when considering all the centre-of-mass energies separately). Finally, Fig. 6.14.b shows that the excess of MC is not located in the TPC sector 6 region, hence making it hard to understand the reason why this effect is stronger when considering the data recorded in year 2000 without TPC sector 6. Nevertheless, this could be due only to a statistical fluctuation.

This effect was taken into account as a systematical effect and a procedure was defined to propagate it in the mass and cross-section limits. This will be discussed in chapter 7 and appendix I.

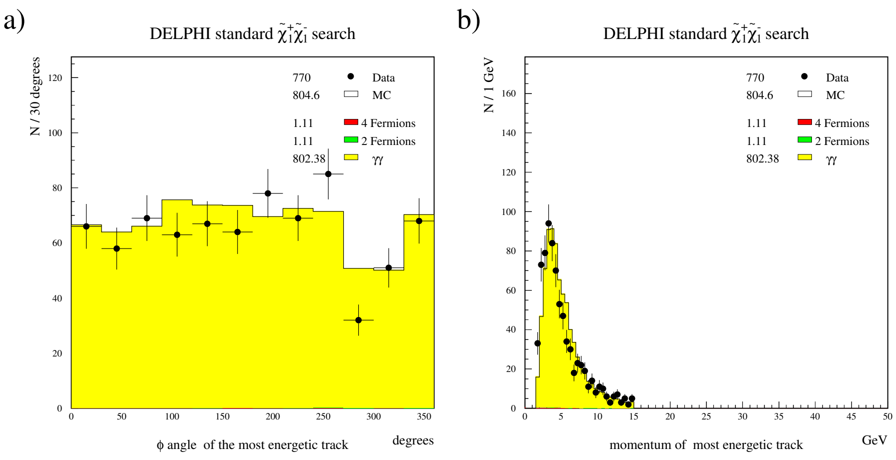

Figure 6.13: Comparison between the real data (2000 S1) and the SM expectation at the preselection level of the first leptonic topology.

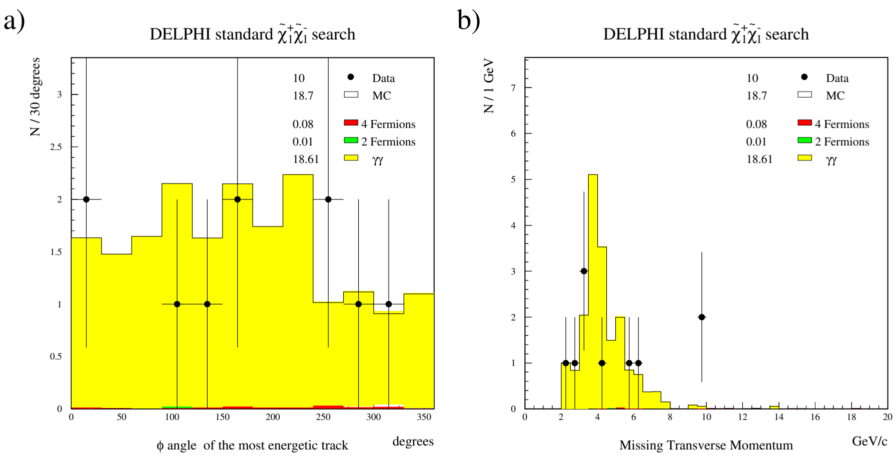

Figure 6.14: Comparison between the real data (2000 S1) and the SM expectation at the optimal likelihood ratio cut level of the first leptonic topology.

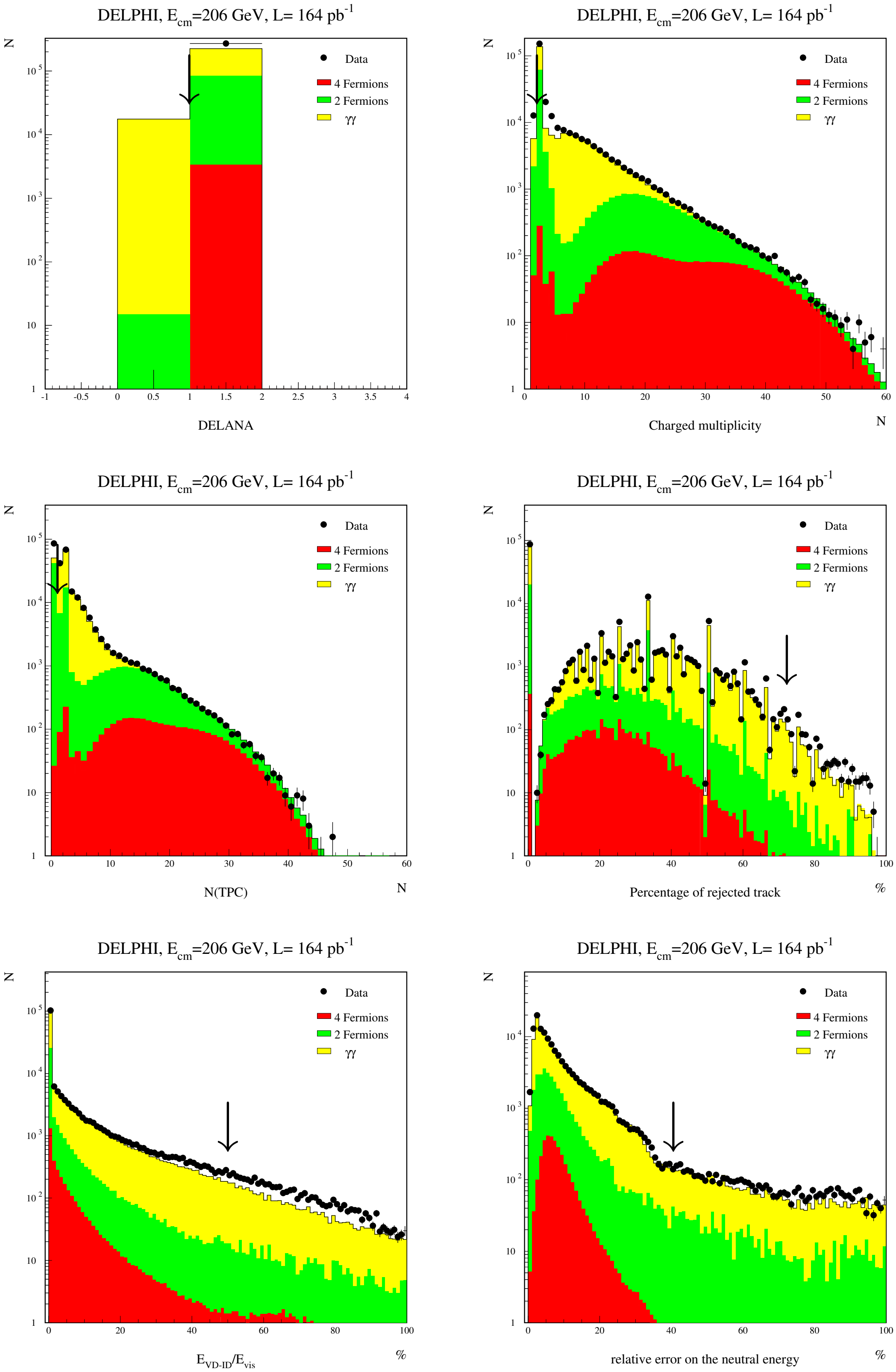

Figure 6.15: Comparison between the real data (2000 C1) and the SM expectation before each cut common to the 4 topologies.

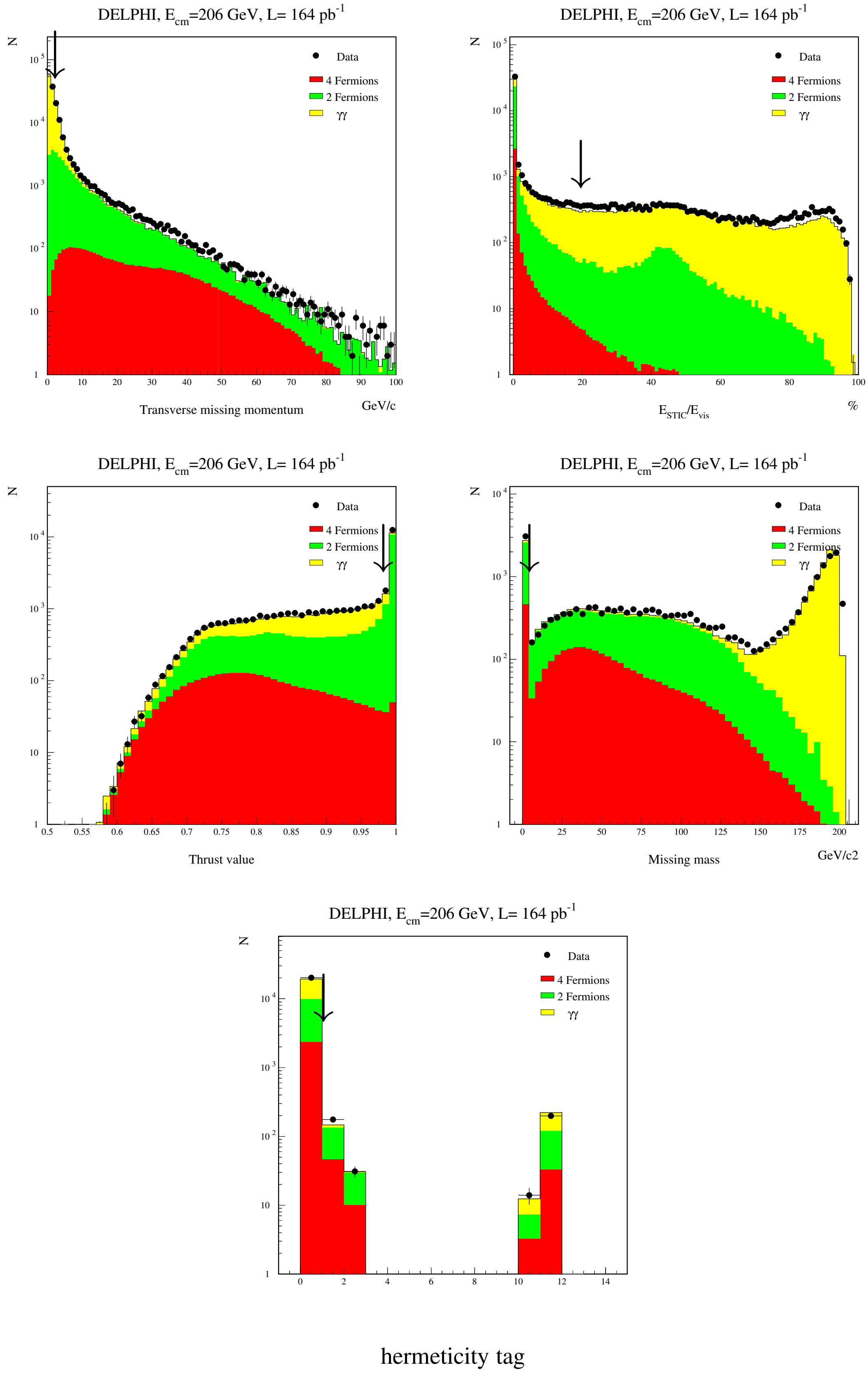

Figure 6.16: Comparison between the real data (2000 C1) and the SM expectation before each cut common to the 4 topologies.

Chapter 7

Results

7.1 Chargino detection efficiencies

The efficiencies of the chargino selection in the four topologies were computed separately for up to 132 (chargino,neutralino) simulated sets [1] using the $\mathcal{L}_R$ function and the $\mathcal{L}_{R_{CUT}}$ of the corresponding topology and ΔM region. To pass from the efficiencies of the chargino selection in the four topologies (i.e. $\ell\ell$, $jj\ell$, $jets$, *radiative*) to the efficiencies in the four decay channels defined in section 4.2 (i.e. $\ell\ell_c$, $jj\ell_c$, $jets_c$, *rad*$_c$), all the migration effects were computed for all the generated points of the signal simulation and the efficiency in the decay channel X was defined as (for a given centre-of-mass energy)

$$\varepsilon^{\mathrm{X}} = \frac{\mathrm{N\ in\ dec.\ chan.\ X}}{\mathrm{Number\ of\ events\ in\ dec.\ chan.\ X\ without\ any\ cut.}} \tag{7.1}$$

where N is the number of events selected by the 4 likelihood ratio functions of the corresponding ΔM region. When considering the rad_c decay channel (if open) ΔM is defined as $M_{\tilde{\chi}_1^\pm}$-$M_{\tilde{\chi}_2^0}$. Once the efficiencies for the allowed samples were calculated for all the decay channels, it was necessary to parametrize their behavior over all the MSSM space. The efficiency dependence on (μ, M_2, $\tan\beta$, m_0) can be more easily represented as a function of $M_{\tilde{\chi}^\pm}$ and $M_{\tilde{\chi}_1^0}$ ($M_{\tilde{\chi}_2^0}$ for the *radiative* decay). With this choice of axes, the efficiency parametrization in each decay channel was performed in the following way:

- For a given point in the ($M_{\tilde{\chi}^\pm}$, $M_{\tilde{\chi}_1^0}$) plane, for which the efficiency was unknown, the three nearest generated points in the ($M_{\tilde{\chi}^\pm}$,$M_{\tilde{\chi}_1^0}$) plane were searched for.

- If the triangle formed by these three points in the ($M_{\tilde{\chi}^\pm}$, $M_{\tilde{\chi}_1^0}$) plane was containing the investigated point, its efficiency was computed by an interpolation within the plane defined by these three generated points in the ($M_{\tilde{\chi}^\pm}$, $M_{\tilde{\chi}_1^0}$, efficiency) space.

- This parametrization was done in mass steps of 1 GeV/c^2 and in the ($M_{\tilde{\chi}^\pm}$,$M_{\tilde{\chi}_2^0}$) plane for the rad_c decay channel. In this first level of parametrization, the efficiencies were computed only for the points contained in the triangle defined by their corresponding three nearest generated points.

[1] This number depends on the number of allowed points for a given centre-of-mass energy. For instance a simulated (chargino,neutralino) set yielding a chargino mass of 103 GeV/c^2 was not used for the parametrization of the efficiency at 200 GeV.

- The second parametrization level investigated points not contained in the triangle defined by their three nearest generated points. In that case, the points got an efficiency equal to the nearest "known" point either from the parametrization or from the simulated samples.

These efficiencies as functions of $M_{\tilde{\chi}_1^{\pm}}$ and $M_{\tilde{\chi}_1^0}$ are shown in Fig. 7.1(7.2) for a mean centre-of-mass energy of 206(206.3) GeVwith(without) the TPC sector 6.

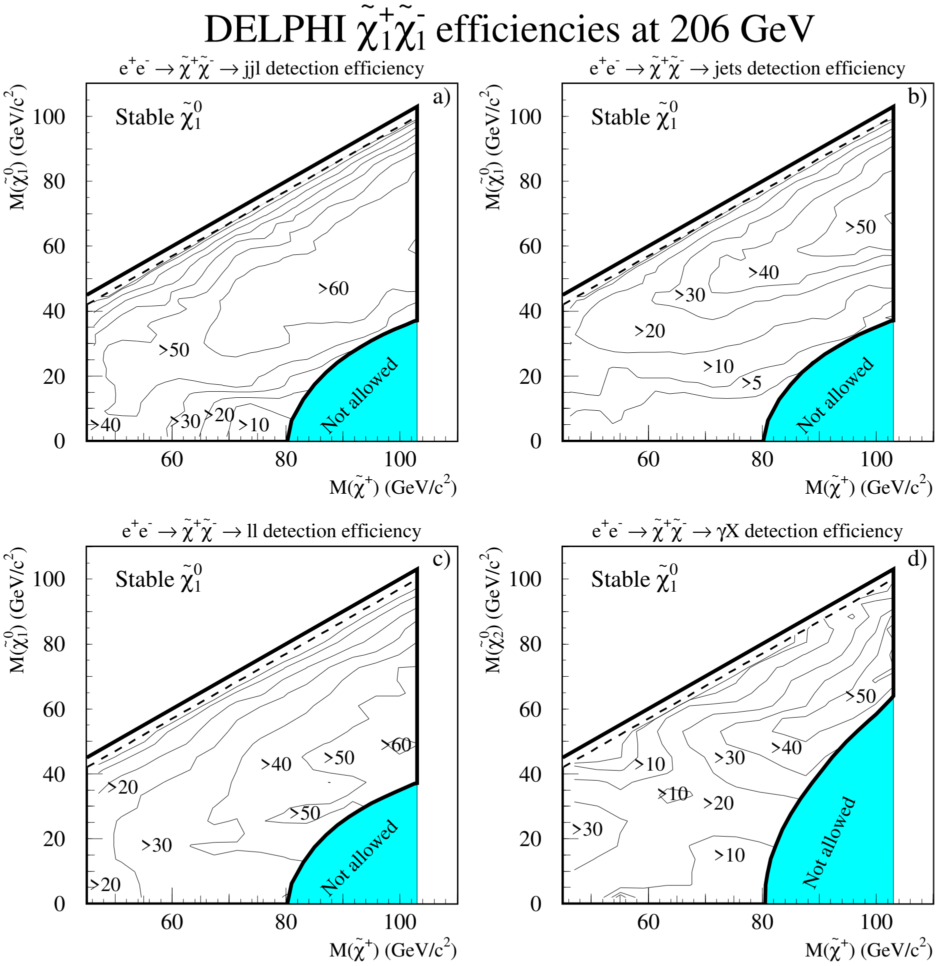

Figure 7.1: Chargino pair production detection efficiencies (%) for the four decay channels a) $jj\ell_c$, b) $jets_c$, c) $\ell\ell_c$ and d) rad_c, at 206 GeV in the $(M_{\tilde{\chi}^{\pm}}, M_{\tilde{\chi}^0})$ plane. TPC sector 6 ON and a stable $\tilde{\chi}_1^0$ were assumed. The shaded areas are disallowed in the MSSM scheme.

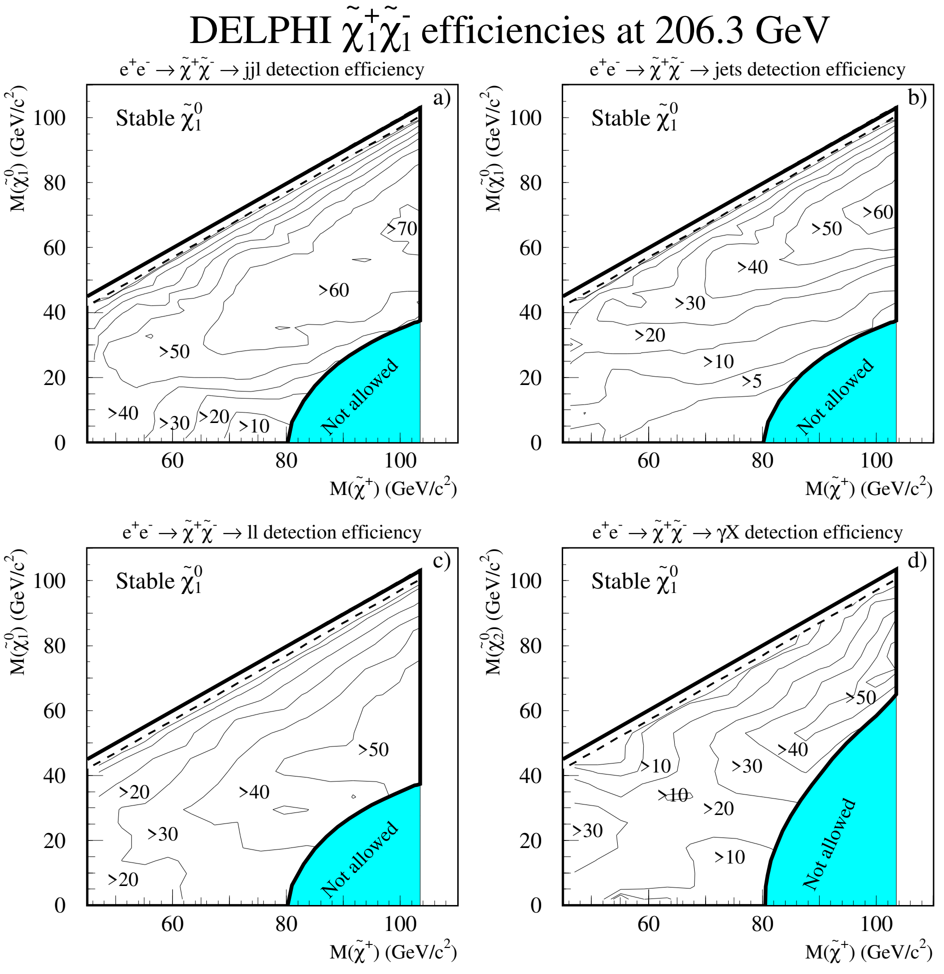

Figure 7.2: Chargino pair production detection efficiencies (%) for the four decay channels a) $jj\ell_c$, b) $jets_c$, c) $\ell\ell_c$ and d) rad_c, at 206.3 GeV in the $(M_{\tilde{\chi}^{\pm}}, M_{\tilde{\chi}^0})$ plane. TPC sector 6 OFF and a stable $\tilde{\chi}_1^0$ were assumed. The shaded areas are disallowed in the MSSM scheme.

At each $\sqrt{s}$ the total efficiency was then computed with the following formula:

$$\begin{aligned}
\varepsilon^{tot}\,(M_{\tilde{\chi}^{\pm}}, M_{\tilde{\chi}_1^0}, M_{\tilde{\chi}_2^0}, B_\ell, P_\gamma) = \quad & [B_\ell^2 \cdot \varepsilon^{\ell\ell_c}\,(M_{\tilde{\chi}^{\pm}}, M_{\tilde{\chi}_1^0}) + \\
& 2B_\ell\,(1-B_\ell) \cdot \varepsilon^{jj\ell_c}\,(M_{\tilde{\chi}^{\pm}}, M_{\tilde{\chi}_1^0}) + \\
& (1-B_\ell)^2 \cdot \varepsilon^{jets_c}\,(M_{\tilde{\chi}^{\pm}}, M_{\tilde{\chi}_1^0})\,] \cdot (1-P_\gamma)\ + \\
& \varepsilon^{rad_c}\,(M_{\tilde{\chi}^{\pm}}, M_{\tilde{\chi}_2^0})\ \cdot P_\gamma
\end{aligned} \tag{7.2}$$

where $\varepsilon^{\ell\ell_c}\,(M_{\tilde{\chi}^{\pm}}, M_{\tilde{\chi}_1^0})$, $\varepsilon^{jj\ell_c}\,(M_{\tilde{\chi}^{\pm}}, M_{\tilde{\chi}_1^0})$, $\varepsilon^{jets_c}\,(M_{\tilde{\chi}^{\pm}}, M_{\tilde{\chi}_1^0})$ and $\varepsilon^{rad_c}(M_{\tilde{\chi}^{\pm}}, M_{\tilde{\chi}_1^0}, M_{\tilde{\chi}_2^0})$ are the efficiencies for each decay channel coming from the parametrization, B_ℓ is the chargino leptonic branching ratio and P_γ is the probability to have at least one photon in the $\tilde{\chi}^+\tilde{\chi}^-$ final states (from $\tilde{\chi}_2^0 \to \tilde{\chi}_1^0\gamma$).

B_ℓ and P_γ have been computed with SUSYGEN [91] to interpolate between the simulated ($\tilde{\chi}_1^\pm$,$\tilde{\chi}_1^0$) sets.

Nevertheless, the decay channel efficiencies give only enough information to compute the number of expected event ($N_{\rm exp}$) from a given chargino signal. In order to compute the channel probabilities needed by the Bayesian algorithm (see appendix H), the knowledge of the efficiency within each topology is required (since the background and real data numbers are only known within the topologies). In order to do so, the efficiency for every chargino topological sample was computed for each decay channel, using only one likelihood ratio function at one time. This defined 16 (4 decay channels times 4 topologies) efficiency tables in ($M_{\tilde{\chi}_1^\pm}$,$M_{\tilde{\chi}_{1,2}^0}$) with which the efficiency in a given topology could be computed.

To study the systematics on the estimation of the detection efficiency both the "shaking" method and the "smearing" method were used (the two methods are described in appendix I). For the high multiplicity topologies ($jets$ & $jj\ell$) the "shaking" method was used. The difference between the efficiencies obtained with and without applying the algorithms related to the two methods are interpreted as a measure of the systematic uncertainties on the estimation of the detection efficiency.

For the first two ΔM regions the relative systematic uncertainty is between 4-13%. For the other ΔM regions the effect is less than 4%. The relative difference for these two topologies can be seen in table I.2. All the results from the "shaking" method for these topologies gave a higher efficiency indicating that the "unshaken" efficiencies can be regarded as conservative.

For the leptonic ($\ell\ell$) topology the "smearing" method was used. Relative uncertainties of about 2% for the whole ΔM range are measured.

In the case of the radiative topology which consists of both high and low multiplicity events both the "shaking" method and the "smearing" method were used to study the systematics. The two methods gave compatible results and the relative uncertainties are less than 2%.

It has to be emphasized that the determination of the systematics yields results for the topologies, not the decay channels. Since the computation showed that the efficiencies were underestimated in all the windows apart from the $\ell\ell$ and *radiative* topologies, where the maximum relative difference was of about 2%, a total negative relative uncertainty, due to systematics, of 2% was used in all the (ΔM,topology) windows. This conservative number is nevertheless extremely small and the uncertainties which have an impact on the limits are related to the background rate determination and the statistical uncertainty on the efficiency determined by the following formula

$$\frac{\sigma_\varepsilon}{\varepsilon} = \sqrt{\frac{(1-\varepsilon)}{\varepsilon}/N_{tot}} \tag{7.3}$$

where N_{tot} is the total number of events used to compute the efficiency (this expression comes from the binomial law). For instance, in the first ΔM region, near ΔM = 3 GeV$/c^2$, the efficiency is of about 3% and was computed with samples with $N_{tot} = 3000$, hence giving rise to a relative statistical uncertainty of about 10%.

Moreover, the robustness of the parametrization procedure was checked by masking, one by one, samples near the kinematic limit and measuring the difference between the parametrization estimation and the real efficiency measurement of the masked point. A maximum relative difference of 3% for the total efficiency was found and was propagated into the limits.

Finally, signal samples were split into two samples, one used to generate the pdf's and the other for the efficiency computation after the $\mathcal{L}_{R_{CUT}}$. Efficiency estimation with all statistics and with the split samples were found to be compatible.

As said in section 4.1, the year 2000 real data with TPC sector 6 (reprocessing C1) was split in 3 windows of investigation with mean centre-of-mass energies ranging from 204.8 GeV to 208.0

GeV but the (chargino,neutralino) samples were generated only up to a centre-of-mass energy of 207 GeV. In order to take into account this difference between the $\sqrt{s}$ of the generated chargino samples and the mean $\sqrt{s}$ of the real data, a proportional stretching was performed in the ($M_{\tilde{\chi}_1^\pm}$,$M_{\tilde{\chi}_1^0}$) plane (($M_{\tilde{\chi}_1^\pm}$,$M_{\tilde{\chi}_2^0}$) for the *radiative* case). For instance the efficiency of a chargino(neutralino) of 104.0(45.0) GeV/c^2 at $\sqrt{s}$ = 208.0 GeV is associated to the efficiency of a chargino of 103.5(45.0) GeV/c^2($\sqrt{s}$ = 207.0 GeV). Every time there was a difference between the available chargino samples generated $\sqrt{s}$ and the real data, this stretching was performed. The biggest difference between the real data set and the chargino sample generated $\sqrt{s}$ occurred for the real data sample with a mean centre-of-mass energy of 208.0 GeV where the chargino samples were generated at 207 GeV. The resulting change in efficiency is found to be negligible compared to the estimated systematic and statistical errors.

7.2 Background estimation and selected events

Table 7.1 gives the total number of events selected in data and expected from the SM simulation after the preselections and after the final selections for the different centre-of-mass energies collected during the years 1999 and 2000. The total number of background events expected in the different windows are shown in tables 7.2, 7.3 and 7.4 together with the number of events selected in the data collected in 1999 and 2000. The asymmetry of the statistical uncertainties is Poissonian.

$\sqrt{s}$	$\int \mathcal{L}$	Preselection		Final sel.	
(GeV)	(pb^{-1})	Data	MC	Data	MC
192	25.4	1966	2012 ± 11	21	$23.7^{+1.4}_{-0.8}$
196	76.2	5926	5818 ± 25	85	$71.6^{+3.8}_{-2.2}$
200	84.0	6433	6331 ± 22	60	$72.3^{+2.1}_{-1.5}$
202	40.4	3086	2994 ± 11	26	$35.0^{+1.0}_{-0.8}$
205	78.3	5796	5734 ± 21	56	$54.6^{+1.9}_{-1.1}$
207	78.8	5795	5770 ± 21	63	$54.9^{+1.9}_{-1.1}$
208	7.2	530	528 ± 2	3	$5.1^{+0.2}_{-0.1}$
206.3$^{(*)}$	60.0	4119	4356 ± 16	53	$58.7^{+2.2}_{-1.5}$
all		33651	33543 ± 50	367	$375.9^{+6.6}_{-4.0}$

Table 7.1: Numbers of events selected in data and expected from the SM simulation in the standard chargino search at the preselection and at the final selection level, for the different centre-of-mass energies collected during the years 1999 and 2000. The $(*)$ indicates the data collected with the TPC sector 6 off. Simulation uncertainties are statistical.

The systematics shown in tables 7.2, 7.3 and 7.4 were obtained with the "re-weighting" method described in section I.1.1. Almost all the selected events in the real data are compatible with the expectation from the background simulation with two exceptions. The problem related to the first $\ell\ell$ windows has already been discussed in the previous chapter and is taken into account by means of the propagation of the systematics. Another problem is located in the fourth $jj\ell$ region when summing all the data recorded in year 1999. This excess was studied, and led to the following conclusions

- 3 out of 6 events contain an electron in the forward part of the DELPHI detector which has been reconstructed by clustering several charged and neutral particles with the REMCLU package. Hence the problem could be related to the REMCLU package,

- the excess is not located in one centre-of-mass energy but is spread in the 4 samples and no excess is observed at higher energy where it should be the case if a new signal was present,
- the other topologies do not show any excess,
- since this excess seems more like a local effect not related to a possible chargino-like signal and that, as will be seen in the section dedicated to the limits, the final chargino mass limit in this region is set above the kinematic limit of the highest $\sqrt{s}$ achieved in year 1999, no further study was performed.

As no clear evidence for a signal was found, exclusion limits were set at 95 % confidence level using the multichannel Bayesian approach.

To illustrate the background composition at the final level of selection, tables 7.5, 7.7, 7.6 and 7.8 indicate the main sources of background for each selection, as well as their contribution in percentage to the total background for each ΔM region when considering the background samples related the the real data recorded in year 2000 with TPC sector 6 (C1 reprocessing).

The main background contamination in the $jj\ell$ topology comes from WW events in the non–degenerate ΔM regions, representing more than 60 % of the total background contribution, as can be seen in table 7.5. This was to be expected since the characteristics of these events are very similar to those of the chargino signal. $q\,\bar{q}\,(\gamma)$ events add a small contribution due to the presence of b quarks whose decay generates isolated and energetic leptons. The degenerate region is strongly dominated by the $\gamma\gamma$ with production of taus due to its high cross–section with 47 % of the total expected events. The contribution of the hadronic $\gamma\gamma$, corresponding to 3 events (0.37 after normalization) selected in the simulation are located at the end of the $\not{P}_t$ tail, and must been seen more like a statistical fluctuation than a real contribution.

Table 7.6 shows the background composition in the $\ell\ell$ topology. The contribution of $\gamma\gamma$ events dominates in the degenerate regions and decreases when ΔM increases. For high ΔM, the WW background constitutes $\sim$ 80 % of the number of expected events.

In the $jets$ topology (table 7.7) there are two main processes contributing to the non–degenerate regions: four–fermion events ($\sim$ 25 % in the 5th and 6th ΔM regions) and $We\,\nu_e \rightarrow q\,\bar{q}$ eν_e ($\sim$ 30 % from the 2th to 6th region). This last background is especially dangerous when the electron is very energetic and escapes at low angles and the neutrino is emitted at high angles generating missing mass and transverse momentum. Other important processes in these regions are $\nu\,\bar{\nu}q\,\bar{q}$ and $q\,\bar{q}\,(\gamma)$. In the degenerate regions, $\gamma\gamma$ events are 80 to 60 % of the total background contribution and decrease in importance as ΔM increases.

Finally, the most important backgrounds in the *radiative* topology are WW (γ), $q\,\bar{q}\,(\gamma)$ and $\tau^+\,\tau^-\,(\gamma)$ for the non–degenerate case due to the high rate of events with initial state radiation. In the degenerate case, the $\tau^+\,\tau^-\,(\gamma)$ and $WW(\gamma)$ events constitute almost 70 % of the total background. In particular, the $\tau^+\,\tau^-\,(\gamma)$ process can be an irreducible background if the photon is soft and the neutrinos carry most of the energy in the event.

Stable $\tilde{\chi}_1^0$ 1999 data, $\mathcal{L} = 227\ pb^{-1}$

Topology:	$jj\ell$	$\ell\ell$	$jets$	rad	Total
	$3 \leq \Delta M < 5$ GeV$/c^2$				
Obs. events:	4	39	3	7	53
Expect. events:	$2.3^{+1.2+1.2}_{-0.2-0.1}$	$49.2^{+3.2+2.6}_{-2.0-5.7}$	$5.3^{+1.4+0.0}_{-0.5-2.7}$	$5.3^{+1.2+0.9}_{-0.3-0.2}$	$62.1^{+4.0+3.0}_{-2.2-6.3}$
	$5 \leq \Delta M < 10$ GeV$/c^2$				
Obs. events:	4	13	1	7	25
Expect. events:	$2.3^{+1.2+1.2}_{-0.2-0.1}$	$11.9^{+1.9+0.5}_{-0.7-3.0}$	$2.5^{+1.2+0.5}_{-0.3-0.7}$	$5.3^{+1.2+0.9}_{-0.3-0.2}$	$22.0^{+2.9+1.6}_{-0.9-3.1}$
	$10 \leq \Delta M < 25$ GeV$/c^2$				
Obs. events:	4	14	17	7	42
Expect. events:	$2.3^{+1.2+1.2}_{-0.2-0.1}$	$14.3^{+1.6+1.7}_{-0.4-3.1}$	$15.8^{+1.9+2.1}_{-0.9-1.4}$	$5.3^{+1.2+0.9}_{-0.3-0.2}$	$37.6^{+3.0+3.1}_{-1.1-3.4}$
	$25 \leq \Delta M < 35$ GeV$/c^2$				
Obs. events:	6	21	10	7	44
Expect. events:	$2.2^{+0.4+0.7}_{-0.1-0.0}$	$25.1^{+1.6+4.2}_{-0.5-3.5}$	$8.3^{+0.4+0.8}_{-0.2-0.0}$	$5.3^{+1.2+0.9}_{-0.3-0.2}$	$40.6^{+2.2+4.4}_{-0.7-3.5}$
	$35 \leq \Delta M < 50$ GeV$/c^2$				
Obs. events:	2	40	28	14	84
Expect. events:	$2.3^{+0.3+0.7}_{-0.0-0.1}$	$45.1^{+1.8+3.1}_{-0.6-4.2}$	$23.6^{+0.5+3.4}_{-0.4-0.4}$	$12.9^{+1.2+1.7}_{-0.3-0.2}$	$84.1^{+2.2+4.9}_{-0.8-4.2}$
	$50 \leq \Delta M$				
Obs. events:	9	60	37	14	120
Expect. events:	$7.5^{+0.5+2.2}_{-0.2-0.3}$	$68.2^{+1.9+4.4}_{-0.8-6.9}$	$36.8^{+0.6+4.9}_{-0.4-0.4}$	$12.9^{+1.2+1.7}_{-0.3-0.2}$	$125.4^{+2.4+7.1}_{-1.0-6.9}$
	TOTAL (logical .OR. between different ΔM windows)				
Obs. events:	14	109	54	15	192
Expect. events:	$10.7^{+1.3}_{-0.3}$	$126.1^{+3.7}_{-2.4}$	$52.8^{+2.2}_{-1.3}$	$13.9^{+1.3}_{-0.4}$	$202.6^{+4.7}_{-2.8}$

Table 7.2: Number of events observed in data and the expected number of background events in the different chargino search channels under the hypothesis of a stable neutralino for all the data collected in 1999. The first uncertainties are statistical and the second ones are systematic. The "re-weighting" method used to compute the systematics is described in section I.1.

Stable $\tilde{\chi}^0_1$ $\quad$ $< E_{cm} >$ = 206 GeV, $\mathcal{L} = 164.4\ pb^{-1}$

Topology:	$jj\ell$	$\ell\ell$	$jets$	rad	Total
	$3 \leq \Delta M < 5$ GeV$/c^2$				
Obs. events:	0	20	5	3	28
Expect. events:	0.4 $^{+1.2+0.1}_{-0.1-0.0}$	20.6 $^{+2.6+0.3}_{-1.6-2.4}$	7.5 $^{+1.6+1.3}_{-0.8-0.6}$	2.5 $^{+1.4+1.1}_{-0.2-0.1}$	31.0 $^{+3.6+1.7}_{-1.8-2.5}$
	$5 \leq \Delta M < 10$ GeV$/c^2$				
Obs. events:	0	0	2	3	5
Expect. events:	0.4 $^{+1.2+0.1}_{-0.1-0.0}$	2.0 $^{+1.4+0.1}_{-0.4-0.5}$	1.4 $^{+1.3+0.5}_{-0.2-0.3}$	2.5 $^{+1.4+1.1}_{-0.2-0.1}$	6.4 $^{+2.6+1.2}_{-0.5-0.6}$
	$10 \leq \Delta M < 25$ GeV$/c^2$				
Obs. events:	0	8	4	3	15
Expect. events:	0.4 $^{+1.2+0.1}_{-0.1-0.0}$	7.7 $^{+1.7+0.9}_{-0.6-0.4}$	5.6 $^{+1.4+1.3}_{-0.5-0.5}$	2.5 $^{+1.4+1.1}_{-0.2-0.1}$	16.3 $^{+2.9+1.9}_{-0.8-0.6}$
	$25 \leq \Delta M < 35$ GeV$/c^2$				
Obs. events:	1	13	3	3	20
Expect. events:	0.4 $^{+1.2+0.0}_{-0.0-0.0}$	11.6 $^{+1.6+0.7}_{-0.5-2.1}$	4.0 $^{+1.3+1.0}_{-0.4-0.0}$	2.5 $^{+1.4+1.1}_{-0.2-0.1}$	18.5 $^{+2.8+1.6}_{-0.7-2.1}$
	$35 \leq \Delta M < 50$ GeV$/c^2$				
Obs. events:	2	23	10	11	46
Expect. events:	2.4 $^{+1.3+0.1}_{-0.2-0.1}$	26.8 $^{+1.7+1.2}_{-0.7-2.8}$	8.0 $^{+1.4+2.0}_{-0.4-0.0}$	10.3 $^{+1.3+1.6}_{-0.5-0.5}$	47.5 $^{+2.9+2.8}_{-0.9-2.8}$
	50 GeV$/c^2 \leq \Delta M$				
Obs. events:	3	40	22	11	76
Expect. events:	3.8 $^{+1.3+0.4}_{-0.2-0.3}$	38.9 $^{+1.7+4.3}_{-0.7-1.1}$	18.7 $^{+1.4+4.2}_{-0.6-0.0}$	10.3 $^{+1.3+1.6}_{-0.5-0.5}$	71.7 $^{+2.9+6.2}_{-1.0-1.2}$
	TOTAL (logical .OR. between different ΔM windows)				
Obs. events:	4	76	31	11	122
Expect. events:	5.0 $^{+1.4}_{-0.3}$	69.7 $^{+3.1}_{-2.1}$	29.0 $^{+1.9}_{-1.1}$	10.9 $^{+1.4}_{-0.5}$	114.6 $^{+4.1}_{-2.4}$

Table 7.3: The number of events observed in data and the expected number of background events in the different chargino search channels under the hypothesis of a stable neutralino for all the events recorded in 2000 with the TPC sector 6 ($< E_{cm} >$ = 206 GeV, reprocessing C1). The first uncertainties are statistical and the second ones are systematic. The "re-weighting" method used to compute the systematics is described in section I.1.

Stable $\tilde{\chi}^0_1$ E_{cm} = 206.3 GeV, $\mathcal{L}$ = 60.0 pb^{-1}

Topology:	$jj\ell$	$\ell\ell$	$jets$	rad	Total
	$3 \leq \Delta M < 5$ GeV$/c^2$				
Obs. events:	0	10	2	2	14
Expect. events:	$0.2\,^{+0.5+0.1}_{-0.0-0.0}$	$18.8\,^{+1.5+0.0}_{-1.1-4.0}$	$2.1\,^{+0.8+0.9}_{-0.4-0.0}$	$1.3\,^{+0.5+1.0}_{-0.1-0.0}$	$22.5\,^{+1.8+1.3}_{-1.2-4.0}$
	$5 \leq \Delta M < 10$ GeV$/c^2$				
Obs. events:	0	4	4	2	10
Expect. events:	$0.2\,^{+0.5+0.1}_{-0.0-0.0}$	$3.6\,^{+0.8+0.0}_{-0.4-0.5}$	$3.9\,^{+1.0+2.3}_{-0.6-0.1}$	$1.3\,^{+0.5+1.0}_{-0.1-0.0}$	$9.1\,^{+1.4+2.5}_{-0.7-0.5}$
	$10 \leq \Delta M < 25$ GeV$/c^2$				
Obs. events:	0	3	7	2	12
Expect. events:	$0.20\,^{+0.5+0.1}_{-0.0-0.0}$	$2.31\,^{+0.6+0.0}_{-0.2-0.4}$	$5.4\,^{+1.0+2.7}_{-0.6-0.0}$	$1.3\,^{+0.5+1.0}_{-0.1-0.0}$	$9.3\,^{+1.3+2.9}_{-0.7-0.4}$
	$25 \leq \Delta M < 35$ GeV$/c^2$				
Obs. events:	0	3	4	2	9
Expect. events:	$0.4\,^{+0.5+0.1}_{-0.0-0.1}$	$5.3\,^{+0.6+0.0}_{-0.2-2.2}$	$3.2\,^{+0.7+1.2}_{-0.3-0.0}$	$1.3\,^{+0.5+1.0}_{-0.1-0.0}$	$10.3\,^{+1.1+1.6}_{-0.4-2.2}$
	$35 \leq \Delta M < 50$ GeV$/c^2$				
Obs. events:	0	10	6	5	21
Expect. events:	$0.7\,^{+0.4+0.0}_{-0.0-0.1}$	$11.7\,^{+0.7+0.0}_{-0.3-5.2}$	$5.0\,^{+0.6+2.1}_{-0.3-0.0}$	$4.3\,^{+0.5+1.3}_{-0.2-0.0}$	$21.6\,^{+1.1+2.5}_{-0.4-5.2}$
	50 GeV$/c^2 \leq \Delta M$				
Obs. events:	1	16	9	5	31
Expect. events:	$2.0\,^{+0.5+0.0}_{-0.1-0.6}$	$14.2\,^{+0.6+4.1}_{-0.3-1.1}$	$6.3\,^{+0.6+2.4}_{-0.2-0.0}$	$4.3\,^{+0.5+1.3}_{-0.2-0.0}$	$26.8\,^{+1.1+4.9}_{-0.4-1.3}$
	TOTAL (logical .OR. between different ΔM windows)				
Obs. events:	1	31	16	5	53
Expect. events:	$2.3\,^{+0.5}_{-0.1}$	$38.8\,^{+1.7}_{-1.2}$	$13.1\,^{+1.2}_{-0.8}$	$4.5\,^{+0.5}_{-0.2}$	$58.7\,^{+2.2}_{-1.5}$

Table 7.4: The number of events observed in data and the expected number of background events in the different chargino search channels under the hypothesis of a stable neutralino for all the events recorded in 2000 without the TPC sector 6 ($< E_{cm} >$ = 206.3 GeV, S1 reprocessing). The first uncertainties are statistical and the second ones are systematic. The "re-weighting" method used to compute the systematics is described in section I.1.

<table>
<tr><th rowspan="2">$jj\ell$ topology</th><th colspan="6">ΔM regions</th></tr>
<tr><th>1</th><th>2</th><th>3</th><th>4</th><th>5</th><th>6</th></tr>
<tr><th>BACKGROUND</th><th colspan="6">% of the total backg per ΔM</th></tr>
<tr><td>$e^+e^- \to q\,\bar{q}\,(\gamma)$</td><td colspan="3">3</td><td>8</td><td>5</td><td>5</td></tr>
<tr><td>$e^+e^- \to \tau^+\tau^-(\gamma)$</td><td colspan="3">–</td><td>16</td><td>3</td><td>3</td></tr>
<tr><td>$e^+e^- \to W^+W^-\,(\gamma)$ –like</td><td colspan="3">45</td><td>65</td><td>69</td><td>75</td></tr>
<tr><td>$e^+e^- \to W e\,\nu_e \to q\,\bar{q}\,e\nu_e$</td><td colspan="3">–</td><td>3</td><td>3</td><td>4</td></tr>
<tr><td>$e^+e^- \to \tau^+\tau^- q\,\bar{q}$</td><td colspan="3">–</td><td>3</td><td>2</td><td>1</td></tr>
<tr><td>$e^+e^- \to \nu\,\bar{\nu} q\,\bar{q}$</td><td colspan="3">5</td><td>5</td><td>3</td><td>2</td></tr>
<tr><td>$e^+e^- \to e^+e^-\,\tau^+\tau^-\,(\gamma\gamma)$</td><td colspan="3">47</td><td>–</td><td>–</td><td>–</td></tr>
<tr><td>$e^+e^- \to e^+e^- q\,\bar{q}\,(\gamma\gamma)$</td><td colspan="3">–</td><td>–</td><td>15</td><td>10</td></tr>
</table>

Table 7.5: Relative weight of the main background processes for each ΔM region in the $jj\ell$ topology.

$\ell\ell$ topology	ΔM regions					
	1	2	3	4	5	6
BACKGROUND	% of the total backg per ΔM					
$e^+e^- \to \tau^+\,\tau^-\,(\gamma)$	–	–	4	3	3	3
$e^+e^- \to W^+W^-\,(\gamma)$ –like	–	2	42	74	84	91
$e^+e^- \to e^+e^- q\,\bar{q}\,(\gamma\gamma)$	43	40	14	–	–	–
$e^+e^- \to e^+e^-e^+e^-\,(\gamma\gamma)$	17	5	4	3	2	–
$e^+e^- \to e^+e^-\mu^+\mu^-\,(\gamma\gamma)$	3	13	14	12	7	4
$e^+e^- \to e^+e^-\tau^+\tau^-\,(\gamma\gamma)$	35	40	18	8	4	2

Table 7.6: Relative weight of the main background processes for each ΔM region in the $\ell\ell$ topology.

7.2.1 Candidates

This section shows as an example the graphical scan of three representative candidates selected at the end of the event selection chain for different topologies and ΔM regions at E_{cm} = 196 and 206 GeV(C1 reprocessing).

Fig. 7.3 shows an event selected as candidate of the $\ell\ell$ topology in the regions with $\Delta M > 50$ GeV$/c^2$. This is an event with two tracks, in the barrel region, identified as a μ^+ and a e^-. The values of the direction and momentum of the tracks (θ, ϕ, p) are respectively (72°, 79°, 32.8 GeV$/c$) and (50°, 139°, 49.6 GeV$/c$). The acoplanarity of the event is 120°. The missing transverse momentum

jets topology	ΔM regions					
	1	2	3	4	5	6
BACKGROUND	% of the total backg per ΔM					
$\mathrm{e}^+\mathrm{e}^- \rightarrow q\,\bar{q}\,(\gamma)$	1	1	2	10	10	8
$\mathrm{e}^+\mathrm{e}^- \rightarrow W^+W^-\,(\gamma)$ –like	3	3	6	12	23	28
$\mathrm{e}^+\mathrm{e}^- \rightarrow W e\,\nu_e \rightarrow q\,\bar{q}\,\mathrm{e}\nu_e$	4	28	25	28	34	34
$\mathrm{e}^+\mathrm{e}^- \rightarrow\ \nu\,\bar{\nu} q\,\bar{q}$	1	9	9	10	13	17
$\mathrm{e}^+\mathrm{e}^- \rightarrow e^+e^- q\,\bar{q}\,(\gamma\gamma)$	82	59	58	40	20	13
$\mathrm{e}^+\mathrm{e}^- \rightarrow e^+e^-\tau^+\tau^-\,(\gamma\gamma)$	9	–	–	–	–	–

Table 7.7: Relative weight of the main background processes for each ΔM region in the *jets* topology.

radiative topology	ΔM regions					
	1	2	3	4	5	6
BACKGROUND	% of the total backg per ΔM					
$\mathrm{e}^+\mathrm{e}^- \rightarrow q\,\bar{q}\,(\gamma)$	8				24	
$\mathrm{e}^+\mathrm{e}^- \rightarrow \tau^+\,\tau^-\,(\gamma)$	39				26	
$\mathrm{e}^+\mathrm{e}^- \rightarrow W^+W^-\,(\gamma)$ –like	27				45	
$\mathrm{e}^+\mathrm{e}^- \rightarrow W e\,\nu_e \rightarrow q\,\bar{q}\,\mathrm{e}\nu_e$	4				2	
$\mathrm{e}^+\mathrm{e}^- \rightarrow\ \nu\,\bar{\nu} q\,\bar{q}$	3				3	
$\mathrm{e}^+\mathrm{e}^- \rightarrow e^+e^- XX\,(\gamma\gamma)$	19				–	

Table 7.8: Relative weight of the main background processes for each ΔM region in the *radiative* topology.

is 60 GeV/c and it points to the polar direction θ = 120°and the visible energy is 82 GeV. The μ^+ is identified by the the Muon Barrel Chambers while the identified electron is measured by the TPC $\frac{dE}{dx}$ and the HPC. The high missing transverse momentum, the lepton flavors and the high momenta of the tracks are compatible with a WW process with one of the W^+ boson decaying into a μ^+ and a neutrino and the W^- boson decaying into a e^- and a neutrino.

Fig. 7.4 shows a candidate selected by the $jj\ell$ topology in the non–degenerate regions with ΔM $>$ 35 GeV/c^2. An isolated μ^+ with a momentum of 23.4 GeV/c and a polar angle of 64 ° is observed. Excluding the isolated μ^+, two jets are reconstructed with an invariant mass of 40GeV/c^2. The values of the θ direction and momentum of the jets (θ, p) are respectively (55°, 40 GeV/c) and (140°, 10 GeV/c). Hence, one jet points to the 140°region of DELPHI where hermeticity taggers have been fired. This could explain why the energy of the jet is so small with respect to the other one (since it has been mis-reconstructed) and why the event remains until the end of the selection stream. The missing momentum points to ($\theta \sim 118^\circ$) and $\not{P}_t$ = 45.6 GeV$/c$. The total visible energy is 75 GeV and the acoplanarity is 99°. This candidate is compatible with the hypothesis of WW with the W^+ boson decaying into an μ^+ (τ^+) and neutrino(s) and the W^- boson decaying into $q\,\bar{q}$ with a badly reconstructed jet in the 140°region.

In Fig. 7.5, a candidate selected by the *radiative* topology in the non–degenerate region can be seen. An isolated photon of 25.5 GeV in the HPC and two jets are observed. The direction of the photon is (θ = 52°, ϕ = 81°). Excluding the isolated photon, the momentum and the direction of the two reconstructed jets (p, θ, ϕ) are (38 GeV$/c$, 38°, 0°) and (43 GeV$/c$, 81°, 209°), respectively. The first jet seems not well reconstructed since it points to the 40° region where taggers have been fired. The invariant mass of the two jet system is 73.2 GeV$/c^2$ which is close to the Z^0 mass. The missing transverse momentum of the events is 9.6 GeV$/c$ and the missing momentum is pointing close to the beam-pipe direction. The missing transverse momentum of the event can be due to the bad reconstruction of one jet. This event is compatible with the production of a Z^0 boson decaying into $q\,\bar{q}$ with two ISR photons, one in the beam-pipe and one in the DELPHI detector.

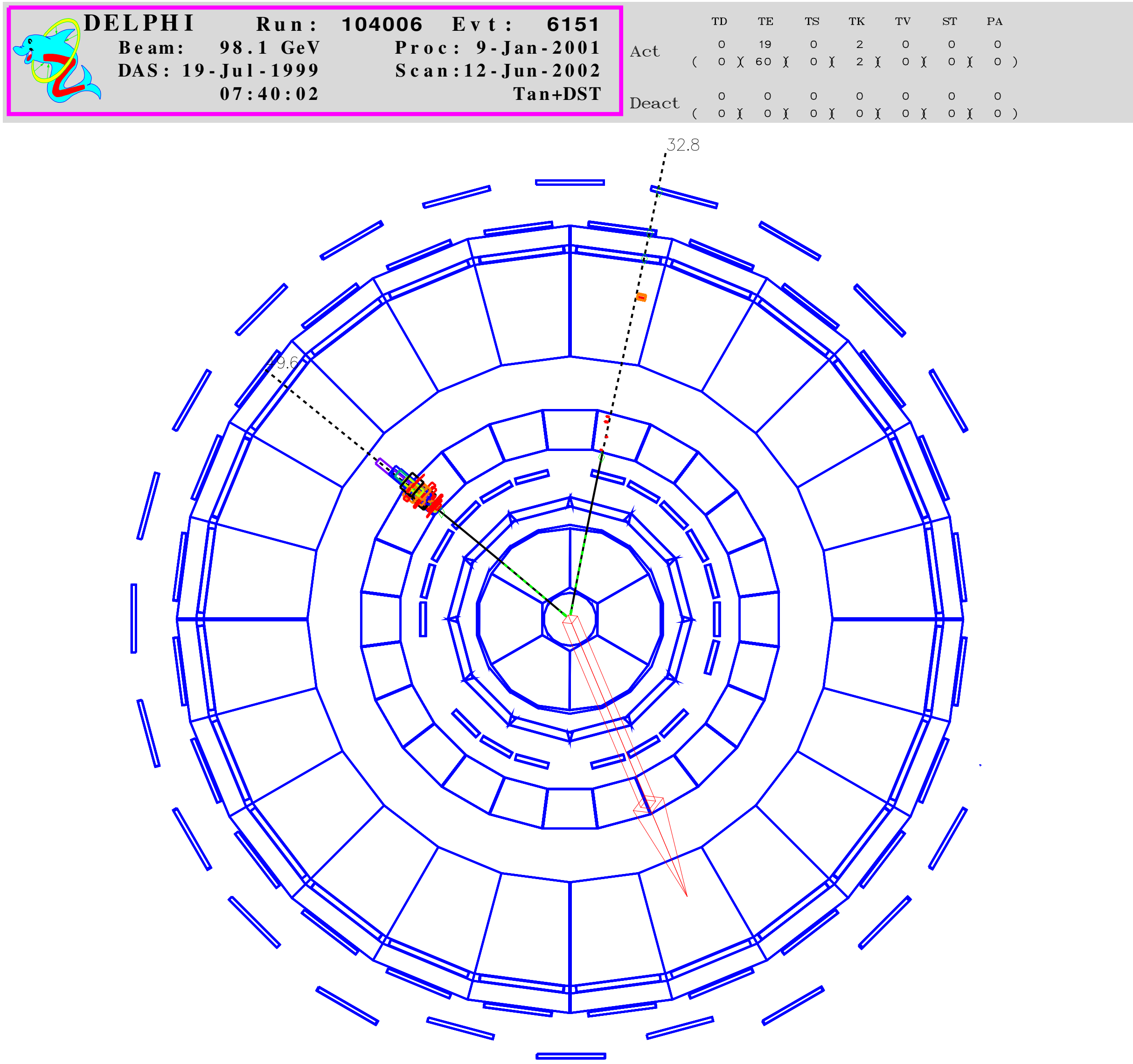

Figure 7.3: Candidate selected in the $\ell\ell$ topology in the non–degenerate regions at E_{cm} = 196 GeV.

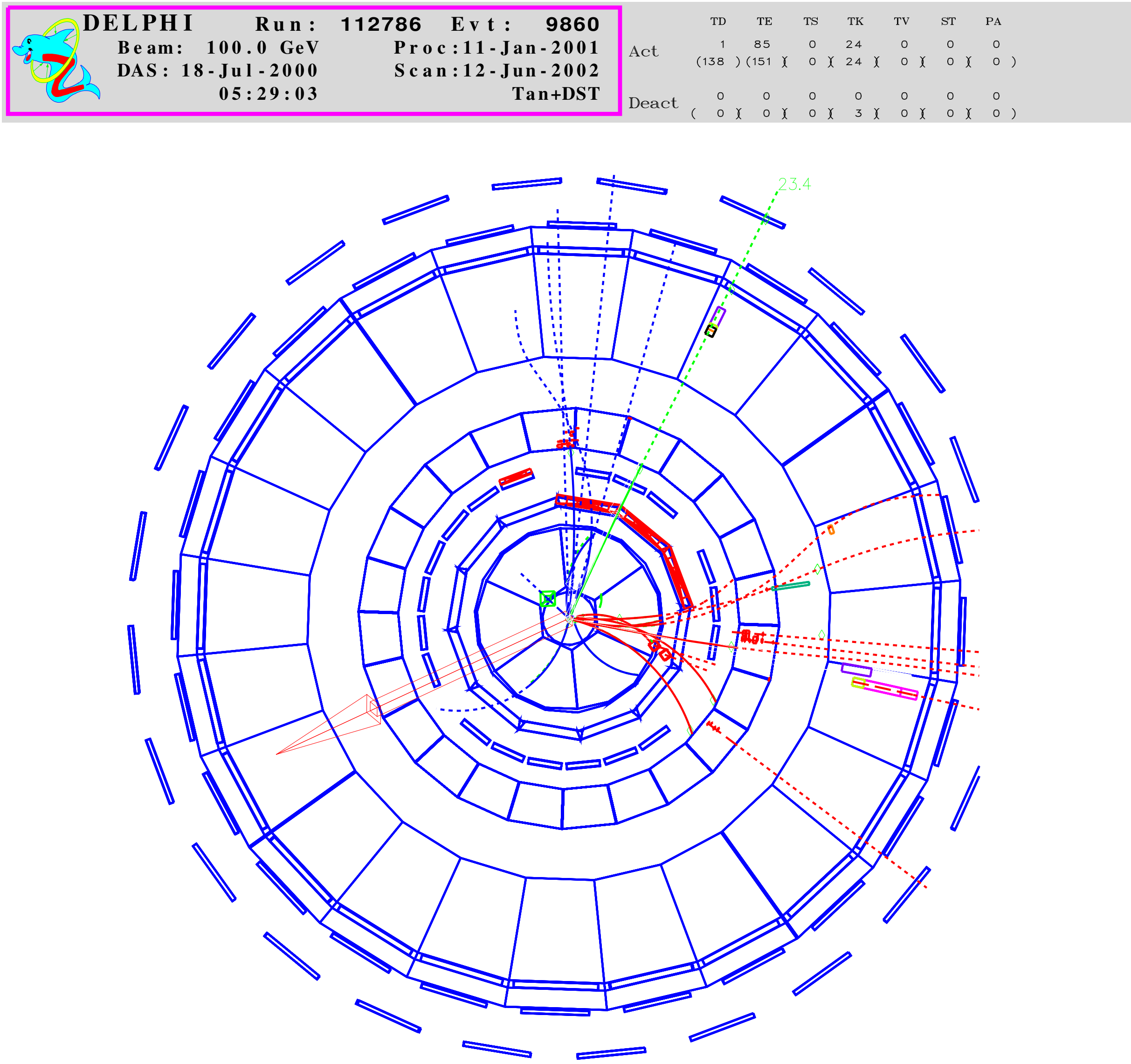

Figure 7.4: Candidate selected in the $jj\ell$ topology in the non–degenerate regions at E$_{cm}$ = 206 GeV.

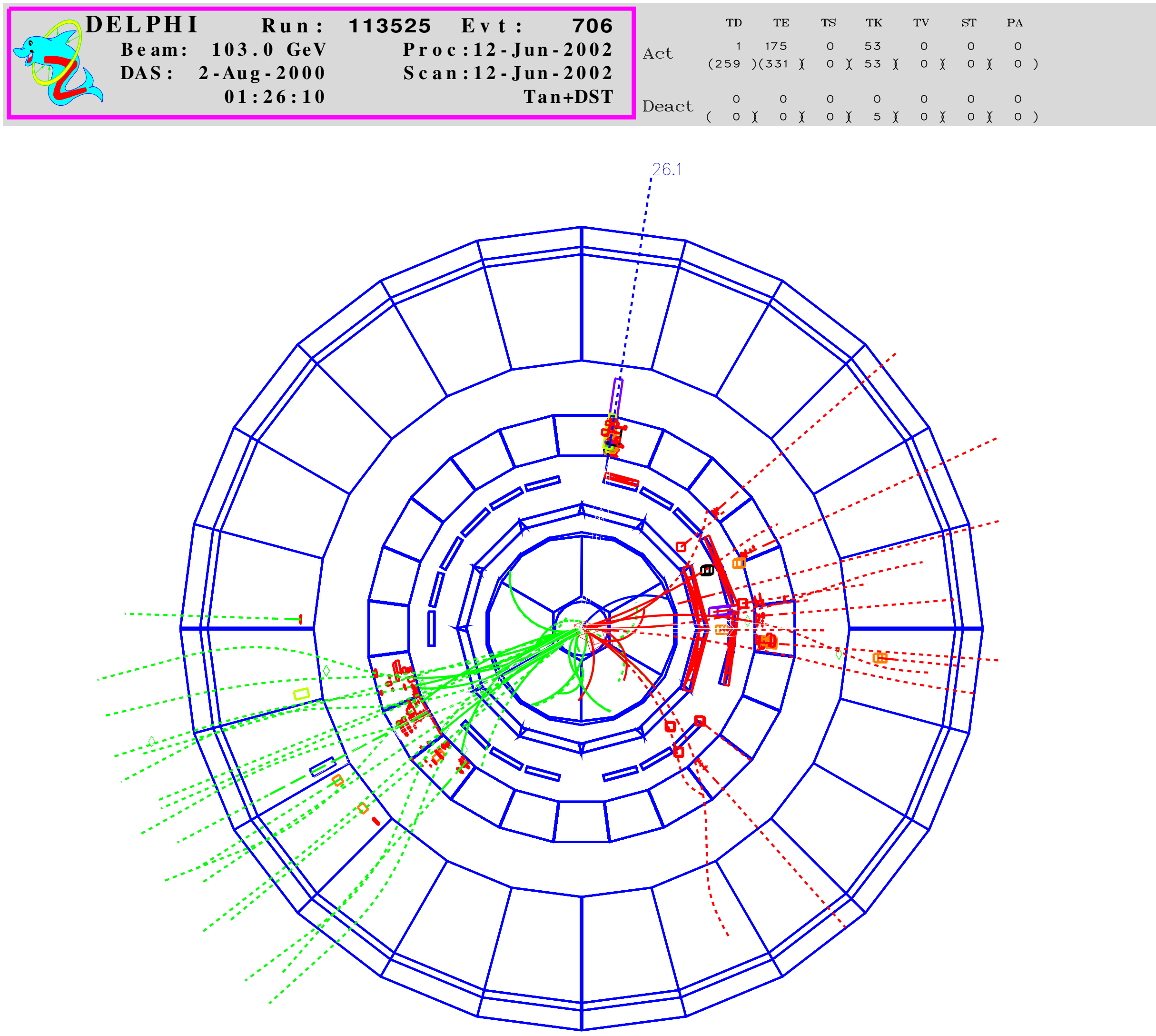

Figure 7.5: Candidate selected in the *radiative* topology in the non–degenerate regions at E_{cm} = 206 GeV.

Chapter 8

Exclusion Limits

Unfortunately, the comparison between the number of events observed in the data collected in the years 1999 and 2000 and the corresponding expected number of background events showed that no clear evidence for a chargino signal was found. Hence, in the SUGRA scheme, exclusion limits were set at 95 % confidence level on the chargino mass versus $\Delta M$and $M_{\tilde{\chi}_1^0}$ and on the chargino pair production cross–section while in the GMSB scheme exclusion limits were set at 95 % of confidence level on the chargino mass versus the lightest stau mass.

8.1 Limits in the SUGRA scheme

Results on efficiency, expected number of background events and observed events in the data recorded at centre-of-mass energies ranging from 196 to 208 GeV were used to compute the present limits. The multi–channel Bayesian formula/approach, described in appendix H, which takes into account the branching ratio and the efficiency of each chargino decay channel was used.

The method used to obtain exclusion limits consists basically (when the uncertainties are not propagated) of comparing the expected number of signal events ($N_{\rm exp}$) to the upper limit on the number of signal events ($N_{\rm up}^{95\%}$) at 95 % of confidence level computed after applying the window final selection cuts. Points in the MSSM parameter space with $N_{\rm exp} > N_{\rm up}^{95\%}$ were excluded. As mentioned before, 4 different topologies were defined in order to adapt the analysis to the particular characteristics of the various chargino signals. A chargino signal can thus be observed simultaneously at several centre-of-mass energies and in several topologies. The informations from all these different channels were taken into account to compute the final limits.

8.1.1 Limits computation

To compute the exclusion limits, several millions of (μ,M_2,$\tan\beta$) sets were investigated. The scan was done randomly in the ranges $0 < M_2 < 3000$ GeV/c^2, $-200 < \mu < 200$ GeV/c^2 for 3 fixed values of $\tan\beta$ namely 1,1.5 and 35 and in the hypothesis of high scalar masses. All the exclusion limits have been calculated assuming the gaugino mass unification relation, $M_1 = \frac{5}{3}\tan^2\theta_W M_2 \approx 0.5M_2$ at the EW scale.
For each set the following exclusion procedure was adopted:

- the production cross-section [1] (for each allowed centre-of-mass energy), the chargino and neutralino masses, the ΔM value (as the corresponding ΔM region), the various decay channel

[1] When the $\tilde{\chi}_1^\pm$ and $\tilde{\chi}_2^\pm$ were degenerated in masses, their 2 pair production cross-sections were summed (see section 4.2). Only the decay characteristics of the $\tilde{\chi}_1^\pm$ were taken into account.

branching ratios and the probability to have a photon from a $\tilde{\chi}_2^0$ decay (if the $\tilde{\chi}_2^0$ was kinematically allowed) were determined using SUSYGEN [91],

- then, the corresponding total efficiency at each allowed centre-of-mass energy was deduced and $N_{\rm exp}$ could be calculated as

$$N_{\rm exp} = \sum_{\sqrt{s}=196}^{208} \epsilon_{tot}\left(M_{\tilde{\chi}_1^\pm}, M_{\tilde{\chi}_1^0}, M_{\tilde{\chi}_2^0}, B_\ell, P_\gamma, \sqrt{s}\right) \cdot \mathcal{L}\left(\sqrt{s}\right) \cdot \sigma\left(M_{\tilde{\chi}_1^\pm}, \sqrt{s}\right) \tag{8.1}$$

where ϵ_{tot} is the total efficiency defined in Eq. 7.2, $\mathcal{L}$ is the integrated luminosity collected at each energy and σ is the corresponding chargino production cross–section,

- to compute $N_{\rm up}^{95\%}$, a total of 8 (often reduced to 4) "independent" channels for each centre-of-mass energy were considered for each investigated MSSM parameter set. The 4 corresponding (topology,ΔM region) windows and the 4 corresponding (topology,ΔM_{rad} region) windows [2], with $\Delta M_{rad} = M_{\tilde{\chi}_1^\pm} - M_{\tilde{\chi}_2^0}$. The first 4 channel probabilities were computed using the following formula

$$\begin{aligned} \mathrm{P}_\alpha = \; & \varepsilon_\alpha^{jets_c}(M_{\tilde{\chi}_1^\pm}, M_{\tilde{\chi}_1^0}) \cdot BR_{jets_c} + \varepsilon_\alpha^{jj\ell_c}(M_{\tilde{\chi}_1^\pm}, M_{\tilde{\chi}_1^0}) \cdot BR_{jj\ell_c} + \\ & \varepsilon_\alpha^{\ell\ell_c}(M_{\tilde{\chi}_1^\pm}, M_{\tilde{\chi}_1^0}) \cdot BR_{\ell\ell_c} \end{aligned} \tag{8.2}$$

where ε_α^X is the efficiency of the α-topological selection ($\alpha = \ell\ell, jj\ell, jets, radiative$) for the decay channel X and BR_X is the branching ratio of the signal in the X decay channel (computed with SUSYGEN). This is identical to the signal efficiency in the topology α (times the topological branching ratio) when one takes into account only non-radiative events. The 4 last channel probabilities were computed using the following formula

$$\mathrm{P}_\alpha = \varepsilon_\alpha^{rad_c}(M_{\tilde{\chi}_1^\pm}, M_{\tilde{\chi}_2^0}) \cdot BR_{rad_c} \tag{8.3}$$

which is identical to the signal efficiency in the topology α (times the topological branching ratio) when one takes into account only radiative events. From the point of view of the channel probability definition, the 8 channels are independent since the signal events, used for the parametrization, were belonging to only one channel. 8 channels were considered, only when the ΔM and the ΔM_{rad} values related to the investigated MSSM set were belonging to different ΔM regions (in that case, the SM background and real data are usually different in 2 ΔM regions). The fact that there could be SM background and/or real data overlaps in a given topology between different ΔM regions ensured the computation to be conservative (i.e., in that case, the value $N_{\rm up}^{95\%}$ is overestimated), even if this effect was not desired. When ΔM and ΔM_{rad} were belonging to the same ΔM region or when the probability to have a photon ($P_\gamma \equiv BR_{rad_c}$ and $B_\ell \equiv BR_{ll_c}$) was zero, the 8 channels were reduced to 4 and the channel probabilities were computed using the following formula

$$\begin{aligned} \mathrm{P}_\alpha = \; & \varepsilon_\alpha^{jets_c}(M_{\tilde{\chi}_1^\pm}, M_{\tilde{\chi}_1^0}) \cdot BR_{jets_c} + \varepsilon_\alpha^{jj\ell_c}(M_{\tilde{\chi}_1^\pm}, M_{\tilde{\chi}_1^0}) \cdot BR_{jj\ell_c} + \\ & \varepsilon_\alpha^{\ell\ell_c}(M_{\tilde{\chi}_1^\pm}, M_{\tilde{\chi}_1^0}) \cdot BR_{\ell\ell_c} + \varepsilon_\alpha^{rad_c}(M_{\tilde{\chi}_1^\pm}, M_{\tilde{\chi}_2^0}) \cdot BR_{rad_c} \end{aligned} \tag{8.4}$$

[2]The ΔM_{rad} regions are identical to the ΔM regions (see section 6.3).

where ε_α^X is the efficiency of the α-topological selection criteria for the decay channel X and BR_X is the branching ratio of the signal in the X decay channel (computed with SUSYGEN). Then, each P_α was weighted by $\mathcal{L}(\sqrt{s}) \cdot \sigma\left(M_{\tilde{\chi}_1^\pm}, \sqrt{s}\right)$, where $\mathcal{L}$ is the integrated luminosity collected at the channel probability centre-of-mass energy and σ is the corresponding chargino production cross–section. Finally all the channel probabilities were divided by $N_{\rm exp}$. Adding up the seven energies, a maximum of 56 different channels were considered in order to compute the limits. This procedure permitted to compute the pdf distribution of the number of signal events compatible with the observed data ($N_{\rm sig}$) [3], from which $N_{\rm up}^{95\%}$ may be obtained by integration,

- in order to account for the systematical and statistical uncertainties, the difference $N_{\rm exp}$-$N_{\rm sig}$ was computed up to 50.000 times while varying randomly the different sources of the uncertainties. In the present thesis, the positive(negative) statistical and sytematic uncertainties related to the background estimation were summed quadratically before being propagated assuming a positive(negative) Gaussian contribution. Finally, the MSSM parameter set was excluded if the lower limit of $N_{\rm exp}$-$N_{\rm sig}$ at 95 % CL was greater than 0.

8.1.2 Release of the sneutrino mass constraint

The present searches considered the hypothesis of high scalar masses (obtained by assuming $m_0 = 1\mathrm{TeV}/c^2$). This prevents the chargino two-body decays and the chargino production cross-section to be dependent of the sneutrino mass. Nevertheless, in the higgsino region ($M_2 > |\mu|$) the cross-section and decay type of the chargino are independent of the sneutrino mass value ($m_{\tilde{\nu}}$) if $m_{\tilde{\nu}} > M_{\tilde{\chi}_1^\pm}$. Hence, the scalar masses unification at GUT scale with $m_0 = 1$ TeV was released for the sneutrino and two different hypothesis were considered in the computation of the limits [4]

- *Any sneutrino:* For low ΔM values ($\Delta M \leq 5$ GeV$/c^2$), the chargino is essentially higgsino (high M_2) and there is no coupling to the sneutrino. Therefore, the dependence of the cross–section on $m_{\tilde{\nu}}$ vanishes and the limits are valid for $m_{\tilde{\nu}} > M_{\tilde{\chi}_1^\pm}$.

- *Heavy sneutrino:* in this case, limits are computed for $m_{\tilde{\nu}} > 1000$ GeV$/c^2$. The t–channel is very suppressed and the dependence of the cross–section on $m_{\tilde{\nu}}$ is weak. This hypothesis was considered for $\Delta M > 5$ GeV$/c^2$.

8.1.3 Limits on chargino mass

The lightest chargino mass limit [in a given parameter range] was determined as the minimal chargino mass [in this given parameter range] of the non–excluded MSSM points. The cross–section limits were computed at the highest center–of–mass energy, namely 208.0 GeV.

The chargino mass limit versus ΔM and M_2 [5] assuming a heavy sneutrino are shown in Fig. 8.1 and 8.2. The behavior of the curve in Fig. 8.1 depends very weakly on the relation between M_1 and M_2. Note that in Fig. 8.2, for a fixed high value of M_2, the chargino mass limit is lower for positive μ than for negative μ. This is due to higher degeneracy for positive μ than for a negative μ, for a fixed value of M_2. Fig. 8.1 contains the obtained and expected [6] mass limits. Both curves are close to each

[3] The method used to compute $N_{\rm sig}$ from Eq.(H.18) is described in [108].

[4] This corresponds to consider the sneutrino mass as an additional free parameter of the theory.

[5] The matching between the chargino mass and the M_2 parameter was computed at the tree-level.

[6] The expected limits are computed assuming that the number of observed events is equal to the number of expected background events.

other except near ΔM = 3 GeV$/c^2$ due the excess of SM background with respect to the real data observed in the $\ell\ell$ topology (as already discussed previously).

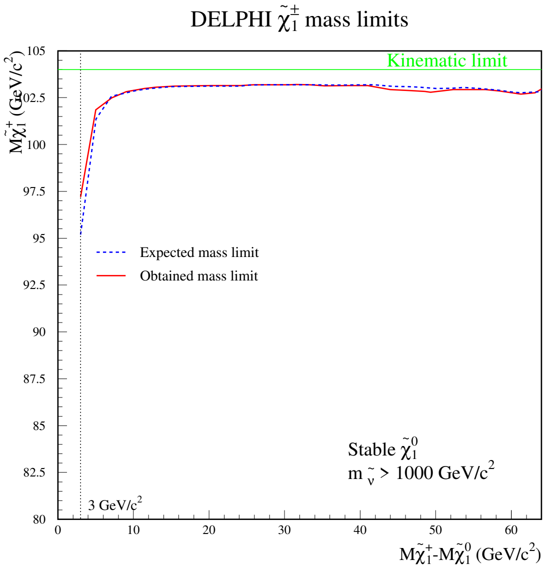

Figure 8.1: The chargino mass limit as function of the ΔM value under the assumption of a heavy sneutrino. The limit applies to the case of a stable $\tilde{\chi}_1^0$. The straight horizontal line shows the kinematic limit.

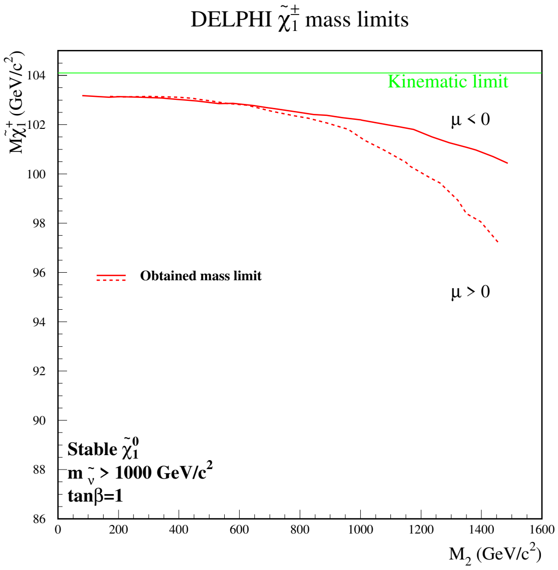

Figure 8.2: Chargino mass limit as a function of the M_2 value for $\tan\beta$ = 1 in the case of a heavy sneutrino and a stable $\tilde{\chi}_1^0$. The straight horizontal line shows the kinematic limit.

The chargino mass limit at 95 % confidence level for the non–degenerate case ($\Delta M > 10$ GeV$/c^2$) and a heavy sneutrino depends on the chargino mixing parameters and are ranging from 102.7 GeV$/c^2$ for a mostly higgsino–like chargino to 103.3 GeV$/c^2$ for a mostly wino–like chargino. In the degenerate cases (ΔM = 5 GeV$/c^2$ and ΔM = 3 GeV$/c^2$), the cross–sections do not depend significantly on the sneutrino mass, since the chargino is higgsino–like under the assumption of gaugino mass unification. The chargino mass limits, valid for $m_{\tilde{\nu}} > M_{\tilde{\chi}_1^{\pm}}$, are 101.7 GeV$/c^2$ and 97.1 GeV$/c^2$ for ΔM = 5 GeV$/c^2$ and ΔM = 3 GeV$/c^2$ respectively. These mass limits are valid even for $|\mu|$ values outside the [-200,200] range. In these 2 ($|\mu| > 200$GeV$/c^2$) regions, the allowed ΔM values are above 10 GeV$/c^2$ and the charginos are gaugino-like and thus, have a high cross-section with respect to the higgsino case where a limit of 102.7 GeV$/c^2$ was set [7].

8.1.4 Limits on chargino cross-section

The computation of the limits on the cross-section used the mass limit for ΔM = 3 GeV$/c^2$ and $\Delta M > 10$ GeV$/c^2$ to find the minimal allowed chargino production cross–section corresponding to $M_{\tilde{\chi}_1^{\pm}}$ below the corresponding obtained mass limit. The obtained excluded cross–sections at $\sqrt{s}$ = 208.0 GeV are shown in Fig. 8.3 for the non–degenerate ($\Delta M > 10$ GeV$/c^2$) and degenerate (ΔM = 3 GeV$/c^2$) cases. Points, corresponding to (chargino,neutralino) sets in the corresponding ΔM validity range, were generated varying the MSSM parameters as mentioned at the beginning of this section. A heavy sneutrino was considered in the non–degenerate case and $m_{\tilde{\nu}} > M_{\tilde{\chi}_1^{\pm}}$ in the

[7]Tests were performed, by scanning random parameter sets, and gave mass limits greater than 103 GeV$/c^2$ in both regions.

degenerate case. Limits on the chargino mass and the corresponding production cross–section are shown by the continuous lines. In the upper plot, it can be seen that the theoretical value of the cross–section depends on the chargino mass and also on the chargino field composition which induces a spread in the value for a given mass. For a given chargino mass value, the cross–section ranges from a lower value for a chargino mostly higgsino to a higher value where the chargino composition is purely gaugino. The cross–section is independent of the sneutrino mass for $m_{\tilde{\nu}} > 1000$ GeV$/c^2$. In the degenerate case with ΔM = 3 GeV$/c^2$ (lower plot), $M_2 >> \mu$ and the chargino is essentially higgsino. Thus, the dispersion of the σ value is weak. The upper limit on the chargino production cross–section at 95 % CL is, for a heavy sneutrino and $\Delta M > 10$ GeV$/c^2$, 0.39 pb. In the degenerate case with ΔM = 3 GeV$/c^2$, the cross–section limit is 1.17 pb.

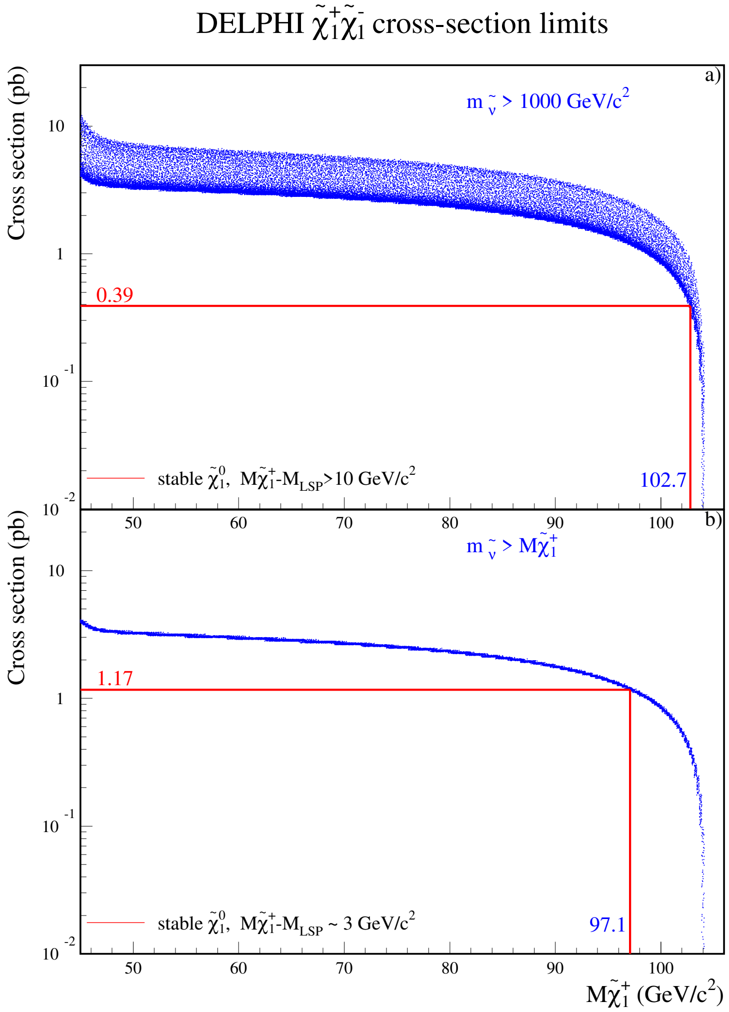

Figure 8.3: Cross-sections in pb at 208.0 GeV (dots) versus the chargino mass in a) for $\Delta M >$ 10 GeV$/c^2$ and b) for $\Delta M \sim$ 3 GeV$/c^2$. The spread in the dots originates from the random scan over the parameters μ and M_2. A heavy sneutrino ($m_{\tilde{\nu}} >$ 1000 GeV$/c^2$) has been assumed in a) and $m_{\tilde{\nu}} > M_{\tilde{\chi}_1^{\pm}}$ in b).The upper limit at 95 % CL on the cross-section are indicated by the horizontal lines.

8.1.5 Limits in the MSSM parameter space

The behavior of the chargino mass limit in the MSSM parameter space can be seen in Fig. 8.4. The regions in the (μ,M_2) plane excluded at 95 % confidence level by the chargino search are shown for different values of $\tan\beta$, assuming a heavy sneutrino (m_0 = 1 TeV/c^2). The lightly shaded (yellow) areas are those excluded at lower energy by LEP1[89][90], corresponding to an excluded chargino mass up to 45 GeV/c^2. The dark shaded (blue) areas show the regions excluded by this search. The matching between the chargino(neutralino) masses and the MSSM theoretical parameters have been computed using tree-level relations. These limits improve the previous limit at lower energies[88].

Fig. 8.5 shows the region in the ($M_{\tilde{\chi}_1^\pm}$,$M_{\tilde{\chi}_1^0}$) excluded by the present searches. The continuous thin lines corresponds to the kinematic limit at $\sqrt{s}$ = 208.0 GeV. The dotted line (partly hidden under the real exclusion limit) shows the expected exclusion limit. The lightly shaded region in the bottom right corner (for $M_{\tilde{\chi}_1^\pm} > 80$ GeV/c^2 and $M_{\tilde{\chi}_1^0} < 30$ GeV/c^2) is not allowed in the cMSSM due to the gaugino running mass relation (see Fig. C.1 and Fig. C.3). For $\Delta M > 10$ GeV/c^2, the chargino mass limit ranges from 102.7 GeV/c^2 to 103.3 GeV/c^2. The region $0 < \Delta M < 3$ GeV/c^2 is not excluded because it was not considered in this analysis. The expected excluded region in this plane is seen to match nearly the obtained limit. A mass limit on the lightest neutralino was derived. The obtained value is indicated by the horizontal dashed line in Fig. 8.5.

8.1.6 Limits on the LSP mass for high m_0

The results can be translated into a limit on the mass of the lightest neutralino as shown in the ($M_{\tilde{\chi}_1^\pm}$,$M_{\tilde{\chi}_1^0}$) plane in Fig. 8.5. A lower limit of 38.2 GeV/c^2 on the lightest neutralino mass is obtained, valid for $\tan\beta \geq 1$ and a heavy sneutrino. This limit is reached for $\tan\beta$ = 1, $\mu = -65.1$ GeV/c^2, M_2 = 65.0 GeV/c^2. The obtained excluded region depends strongly on the the assumed GUT relation between M_1 and M_2.

If one takes into account the excluded region in the (μ, M_2) plane obtained from the search for neutralino production described in [72], this limit improves by ~ 1 GeV/c^2. Thus from chargino and neutralino searches the LSP mass can be constrained to be $M_{\tilde{\chi}_1^0} > 39.2$ GeV/c^2 and the limit occurs at $\tan\beta$= 1.0. Figure 8.6 shows the region in the (μ,M_2) plane for $\tan\beta$=1 excluded by the chargino and neutralino searches, relevant for the LSP mass limit at $m_0 = 1000$ GeV/c^2. The lowest value of $M_{\tilde{\chi}_1^0}$ not excluded by chargino and neutralino searches occurs for $\tan\beta$=1, $\mu = -76.5$ GeV/c^2 and M_2 = 67.0 GeV/c^2. For these parameters, $\tilde{\chi}_4^0\tilde{\chi}_2^0$ production and chargino pair production are important.

8.1.7 Stability of the limits

In order to check the stability and validity of the obtained mass limits, additional studies were performed consisting mainly of measuring the mass limit variation when modifying parameters entering the exclusion chain.

- The propagation of the statistical and systematical uncertainties, described in chapter 7, leads to a decrease of the mass limits of about 1 GeV/c^2 for ΔM = 3 GeV/c^2 and of about 100 MeV for $\Delta M \geq 10$ GeV/c^2. This is reflected in the mass limits given previously.

- A decrease of 300 MeV/c^2 on the $\tilde{\chi}_1^0$ mass limit and of 200 MeV/c^2 on the corresponding $\tilde{\chi}_1^\pm$ mass limit is observed if the $\tilde{\chi}_2^\pm$ pair production is not considered in the computation of N_{exp}.

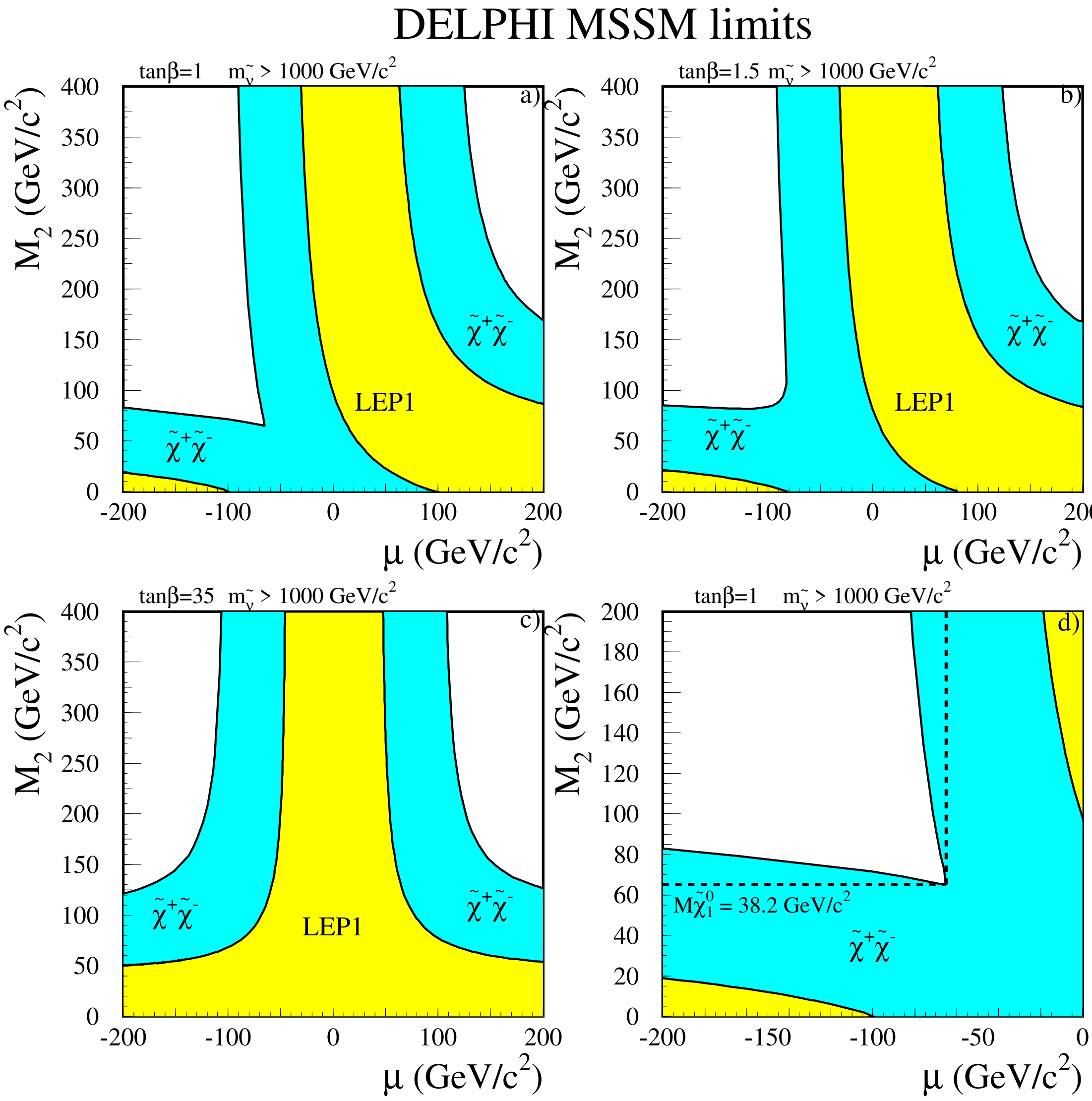

Figure 8.4: a), b), and c), regions excluded at 95 % confidence level in the (μ, M_2) plane under the assumption of a heavy sneutrino for $\tan\beta$ = 1, 1.5 and 35. The dark shading shows the region excluded by the chargino search and the light shaded region is the one excluded by LEP1. The constant mass curve for the LSP mass limit is shown in d) by the dashed line, for $\tan\beta$ = 1.

- Using the modified frequentist approach [109], instead of the Bayesian approach, leads to an improvement of the limits of about 100 MeV/c^2.
- The dependence of the mass limits to the leptonic branching ratio (B_ℓ) and the probability to have a photon (P_γ) was also studied. It has to be emphasized that the study on B_ℓ was not performed to compute limits considering light scalar masses. Such analysis requires to find the minimum of the cross-section as function of the sneutrino mass in all the allowed MSSM parameter ranges and to generate chargino decays with scalar production to parametrize correctly

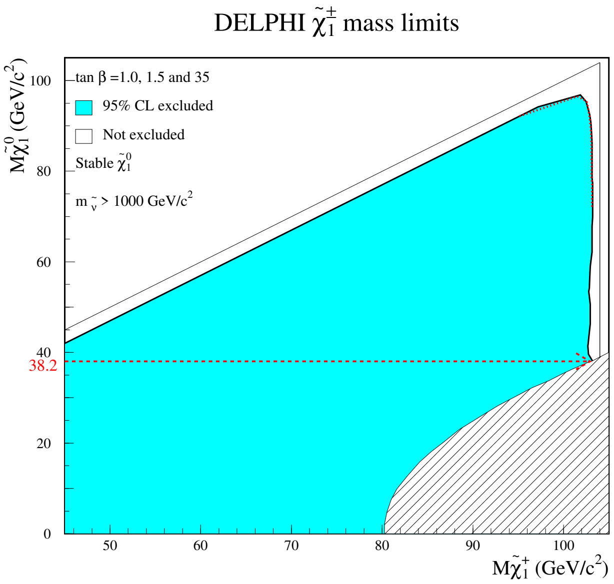

Figure 8.5: Region excluded at 95% confidence level in the plane of the mass of the lightest neutralino versus that of the lightest chargino under the assumption of a heavy sneutrino, for $\tan\beta$ = 1.0, 1.5 and 35. The thin lines show the kinematic limits in the production and the decay. The dotted line (partly hidden by the shading) shows the expected exclusion limit. The dashed region is not allowed in the MSSM. The limit applies in the case of a stable $\tilde{\chi}_1^0$. The mass limit on the lightest neutralino is indicated by the horizontal dashed line.

the efficiencies. In fact, both studies permitted to check the stability of the obtained limits when considering small deviations of those parameters around their theoretical prediction (given by SUSYGEN). Moreover, since they enter the definition of the Bayesian channel probabilities, this gives a measurement of another systematical effect on the mass limits. The results are summarized in Fig. 8.7 and Fig. 8.8 where both variable ranges were extended to [0%,100%] for didactical purposes.

Fig. 8.7 shows the chargino mass limit as function B_ℓ (expressed in %) for three different ΔM values. The vertical dotted line shows the leptonic branching ratio expected by the theory with the assumption of high scalar masses (at the EW scale). The behavior of the three curves can be straightly deduced from the efficiency plots given in Fig. 7.1. When considering small deviations ($\pm 10\%$) from the corresponding theoretical value, the obtained mass shifts is, at maximum, of about 100 MeV/c^2.

Fig. 8.8 shows the chargino mass limit as function of the P_γ (expressed in %) for three different ΔM values. The dot on each curve is the theoretical probability computed using the theoretical parameter set where the limit was set. When considering small deviations ($\pm 10\%$) from the corresponding theoretical value, the obtained mass shifts are, like when varying B_ℓ, less than 100 MeV/c^2.

- The last effects which can be taken into account are the one-loop radiative corrections in the chargino-neutralino sector. These effects are discussed in appendix D and do not affect the chargino mass limits. On the other hand, the indirect $\tilde{\chi}_1^0$ mass limit, was found to be slightly

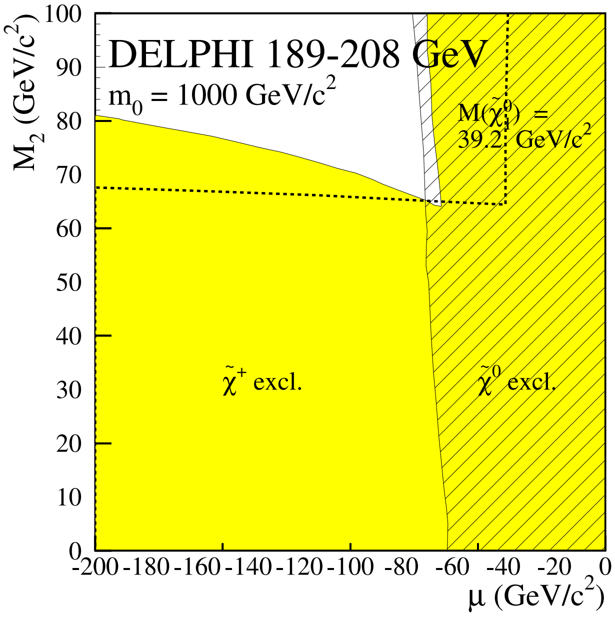

Figure 8.6: Excluded regions in the (μ,M_2) plane for $\tan\beta\ = 1$ for m_0 = 1000 GeV/c^2. The shaded areas show regions excluded by searches for charginos and the hatched areas show regions excluded by searches for neutralinos. The thick dashed curve shows the isomass contour for $M_{\tilde{\chi}^0_1}\ = 39.2\ \mathrm{GeV}/c^2$, the lower limit on the LSP mass obtained at $\tan\beta$=1. The chargino exclusion is close to the isomass contour for $M_{\tilde{\chi}^\pm_1}$ at the kinematic limit. From chargino searches alone the lower limit on $M_{\tilde{\chi}^0_1}$ is $M_{\tilde{\chi}^0_1}\ = 38.2\ \mathrm{GeV}/c^2$.

sensitive to the radiative corrections. Lowering it by 500 MeV/c^2 permits to conservatively account for these effects.

From all these additional studies, one sees that an uncertainty of the order of 1 GeV/c^2 may be considered as a conservative estimate of the uncertainties on the $\tilde{\chi}^\pm_1$ and $\tilde{\chi}^0_1$ mass limits.

8.1.8 Summary

The chargino mass and cross-section limits are summarized in Table 8.1. The table gives also the upper limit on the number of signal events ($N^{95\%}_{\mathrm{up}}$) where the limits were set for the corresponding ΔM ranges. The uncertainties on the mass limits are of the order of 1 GeV/c^2.

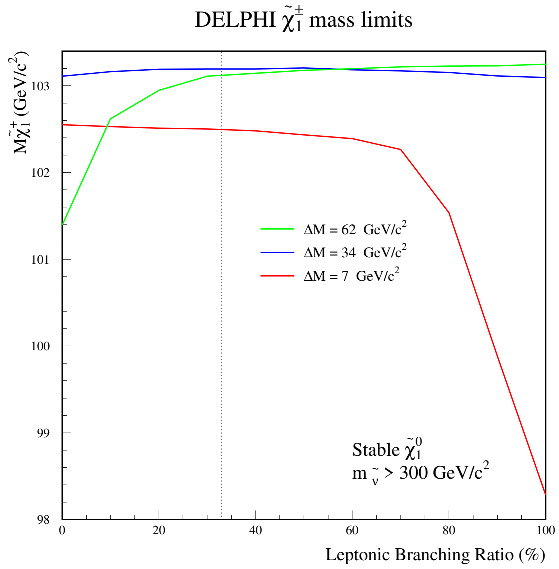

Figure 8.7: Chargino mass limit as function of the leptonic branching ratio for three different ΔM values. The vertical dotted line shows the leptonic branching ratio expected by the theory with the assumption of high scalar masses.

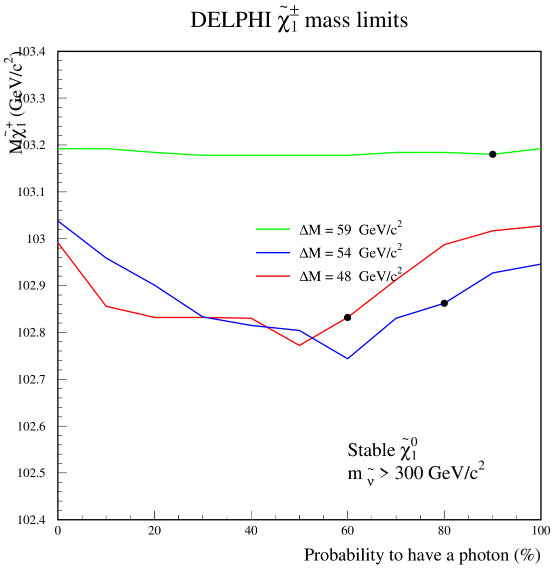

Figure 8.8: Chargino mass limit as function of the probability to have a photon for three different ΔM values. The dot on each curve is the theoretical probability computed using the theoretical parameter set where the limit was set.

Case	$m_{\tilde{\nu}}$ (GeV/c^2)	$M^{min}_{\chi^\pm}$ (GeV/c^2)	σ^{max} (pb)	$N^{95\%}_{\mathrm{up}}$
Stable $\tilde{\chi}_1^0$ $< E_{cm} >$ = 195.6-208.0 GeV				
$\Delta M > 10$ GeV$/c^2$	> 1000	102.7	0.39	13.8
$\Delta M = 5$ GeV$/c^2$	$> M_{\tilde{\chi}_1^\pm}$	101.7	0.57	7.3
$\Delta M = 3$ GeV$/c^2$	$> M_{\tilde{\chi}_1^\pm}$	97.1	1.17	18.1

Table 8.1: 95% confidence level lower limits for the chargino mass, the corresponding pair production cross-sections at 208.0 GeV and the 95% confidence level upper limit on number of signal events.

8.2 Limits in the GMSB scheme

Since in the hypothesis of low gravitino masses, the GMSB signatures are equivalent to the SUGRA ones assuming a massless neutralino. The GMSB analysis was set using the $\ell\ell$ likelihood ratio functions of the 6^{th} ΔM region at each centre-of-mass energy. In order to take into account decays only through $\tilde{\tau}_1$ emission, the efficiencies were recomputed and interpolated using GMSB simulated chargino samples covering all the allowed ($M_{\tilde{\chi}_1^\pm}$, $M_{\tilde{\tau}_1}$) plane and assuming a gravitino mass of 1 eV$/c^2$.

8.2.1 efficiencies and selected events

The efficiency in the ($M_{\tilde{\chi}_1^\pm}$, $m_{\tilde{\tau}_1}$) plane, assuming a gravitino mass of $1 \text{ eV}/c^2$, typically ranges in each $\sqrt{s}$ from a minimum value of 30% to a maximum value of 50 % and is proportional to the $\tilde{\tau}_1$ mass.

The selected background and real data events are extracted from tables 7.2, 7.3 and 7.4. Assuming only the $\ell\ell$ selections of 6^{th} ΔM region. The numbers are summarized in table 8.2

$\ell\ell$ topology - 6^{th} ΔM region - $\tilde{G}$ LSP				
Samples	1999	2000(C1)	2000(S1)	Total
Obs. events:	60	40	16	116
Expect. events:	$68.2^{+1.9+4.4}_{-0.4-6.9}$	$38.9\,^{+1.7+4.3}_{-0.7-1.1}$	$14.2\,^{+0.6+4.1}_{-0.3-1.1}$	$121.3^{+2.6+7.3}_{-0.9-7.1}$

Table 8.2: The number of events observed in data and the expected number of background events in the $\ell\ell$ topology by the 6^{th} ΔM region selections.The first errors are statistical and the second ones are systematic. The "re-weighting" method used to compute the systematics is described in section I.1.

8.2.2 Limits in the ($M_{\tilde{\chi}_1^\pm}$,$M_{\tilde{\tau}_1}$) plane

In order to set limits in the ($M_{\tilde{\chi}_1^\pm}$,$M_{\tilde{\tau}_1}$) plane, several analyses dependent of the gravitino mass or, equivalently, of the mean decay length of the $\tilde{\tau}_1$ (Eq.(1.64)), were merged together. When the $\tilde{\tau}_1$ decays at the vertex, the combination of the present analysis and the search for acoplanar taus in the SUGRA scheme [72] were exploited. For intermediate mean decay lengths of the $\tilde{\tau}_1$, the topology is large impact parameter tracks or kinks, therefore two dedicated analyses were used. Finally, if the stau decays outside the tracking devices the signature corresponds to stable heavy τ's and the search for heavy stable charged particles was exploited. The selections developed for these searches were thus applied to simulated data samples with different gravitino masses, and the results are presented in terms of 95% confidence level (CL) excluded regions in the plane. These three analyses and the technique used to compute the excluded region in the ($M_{\tilde{\chi}_1^\pm}$,$M_{\tilde{\tau}_1}$) plane are described in [110].

Limits on the production cross-section for chargino pairs were derived for each ($m_{\tilde{G}}$, $M_{\tilde{\tau}_1}$, $M_{\tilde{\chi}_1^+}$) combination. Figure 8.9 shows the regions excluded at 95% CL in the ($M_{\tilde{\chi}_1^+}$,$M_{\tilde{\tau}_1}$) plane. The positive-slope area is excluded for $m_{\tilde{G}} > 1 \text{ eV}/c^2$. This limit is also valid for smaller masses of the gravitino because they lead to the same final state topologies. The negative-slope area is only excluded for $m_{\tilde{G}} > 100 \text{ eV}/c^2$. The area below $M_{\tilde{\tau}_1}$= 82.5 GeV/c^2 is excluded by the direct search for stau pair production in SUGRA models [72]. In Figure 8.9 the exclusion region given by the search for charginos in GMSB scenarios start at this value. The area of $\Delta M \leq 0.3 \text{ GeV}/c^2$ is not excluded because in this region the charginos do not decay mainly to $\tilde{\tau}_1$ and ν_τ, but to a W and a $\tilde{G}$. Thus, if $\Delta M \geq 0.3 \text{ GeV}/c^2$, the chargino mass limits are 100 GeV/c^2 for all $m_{\tilde{G}}$, and 102 GeV/c^2 for $m_{\tilde{G}} > 100 \text{ eV}/c^2$. The chargino mass limit decreases with decreasing $M_{\tilde{\tau}_1}$ because in scenarios with gravitino LSP, small stau masses correspond to small sneutrino masses (both are proportional to Λ) and hence to smaller production cross-sections due to the destructive interference between the s- and t-channels.

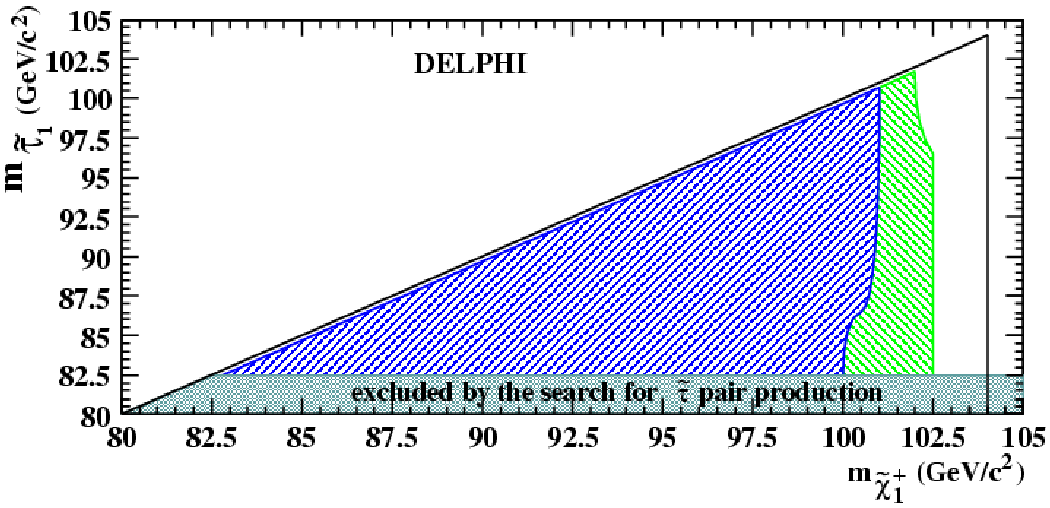

Figure 8.9: Areas excluded at 95% CL in the ($M_{\tilde{\chi}_1^+}$,$M_{\tilde{\tau}_1}$) plane. The positive-slope hatched area is excluded for all gravitino masses. The negative-slope hatched area is only excluded for $m_{\tilde{G}} > 100\mathrm{eV}/c^2$. The Grey area is excluded by the search for stau pair production in gravity mediated supersymmetry breaking models. The plot has been obtained using all DELPHI data up to 208 GeV [110].

Conclusions and future prospects

The analyses made and the results obtained in the search for charginos carried out with the data taken by the DELPHI detector during the years 1999 and 2000 at energies up to $\sqrt{s}$ = 209 GeV have been presented in this thesis. A total integrated luminosity of 451 pb^{-1} was analyzed.

The search has been performed in the framework of the Minimal Supersymmetric extension of the Standard Model (MSSM) assuming R–parity conservation and mass universality at high energy scale. The relation between the gaugino masses at the EW scale, $M_1 = \frac{5}{3}tan^2\theta_W M_2 \sim \frac{1}{2}M_2$, was assumed to be satisfied. The SUGRA scheme, where the lightest supersymmetric particle (LSP) is the lightest neutralino, and the GMSB scheme, where the LSP is the gravitino, have been assumed.

In order to estimate the chargino detection efficiency, several generated chargino points have been chosen to represent different regions of the SUSY parameter space from a wide range of the chargino mass and the mass difference between the chargino and the lightest neutralino (ΔM).

At LEP2 centre-of-mass energies, the $\tilde{\chi}^0_2$ can be lighter than the $\tilde{\chi}^\pm_1$. Therefore, the cascade decays giving rise to complex topologies with the possible presence of energetic isolated photons, multi–jets and multi–leptons have been searched for. In order to account for the various decay types of the produced charginos, four topologies have been defined. Moreover, the characteristics of the chargino final states are affected by the variation of ΔM, hence specific analyses have been set to optimize the selection for six different ranges of ΔM within each topology.

The likelihood ratio (LR) method has been developed and used to optimize the search for charginos. The LR method combines different variables into a single discriminating function. The probability density functions of a set of discriminating variables corresponding to the signal and background events have been used to build the likelihood ratio functions. Events have been selected as chargino candidates with one single cut on this variable. The variable combination and the likelihood ratio value have been chosen for each (ΔM,topology) window in order to have the minimal expected excluded cross–section at 95 % C.L.

After the analysis of all the statistics collected by DELPHI in the years 1999 and 2000, no significant excess of events have been observed. In both SUSY breaking scenarios, the number of events passing the selection criteria is compatible with the background estimation. The agreement between data and Monte Carlo events was also studied at any level of the analysis and is found to be satisfactory.

Hence, new more constraining limits on masses and cross–sections have been set for charginos within the SUGRA and GMSB models.

In the SUGRA scheme, the Bayesian multi–channel approach, assuming a flat prior, has been applied to combine the results from all the different channels considered for each (ΔM topology) window and to compute the final limits. Moreover, a detailed study of possible systematics source was performed. The statistical and investigated systematic uncertainties have been propagated into the mass and cross-section limits. The obtained results show a slight dependence on those uncertainties with a maximum effect of lowering by 1 GeV$/c^2$ the chargino mass limit valid for ΔM = 3 GeV$/c^2$. Taking into account other possible sources, a total uncertainty of 1 GeV$/c^2$ on the present mass limits may be regarded as a conservative estimate. The results are the following:

- Assuming high scalar masses, a difference in mass between the chargino and the neutralino greater than 10 GeV/c^2 and a sneutrino heavier than 1000 GeV/c^2, the existence of a chargino lighter than 102.7 GeV/c^2 has been excluded. If a gaugino–dominated chargino is assumed in addition, the kinematic limit is reached. For ΔM = 5 GeV/c^2 and ΔM = 3 GeV/c^2, the mass limit becomes 101.7 GeV/c^2 and 97.1 GeV/c^2 respectively, valid for a sneutrino heavier than the lightest chargino. The exclusion limits at 95 % C.L. obtained combining the results at the different energies are summarized in the following table

Case	$m_{\tilde{\nu}}$ (GeV/c^2)	$M^{min}_{\chi^\pm}$ (GeV/c^2)	σ^{max} (pb)	$N^{95\%}_{\mathrm{up}}$
Stable $\tilde{\chi}^0_1$ $< E_{cm} >$ = 195.6-208.0 GeV				
$\Delta M > 10\ \mathrm{GeV}/c^2$	$>$ 1000	102.7	0.39	13.8
$\Delta M = 5\ \mathrm{GeV}/c^2$	$>M_{\tilde{\chi}^\pm_1}$	101.7	0.57	7.3
$\Delta M = 3\ \mathrm{GeV}/c^2$	$>M_{\tilde{\chi}^\pm_1}$	97.1	1.17	18.1

- These experimental results have been translated into exclusion regions in the MSSM parameter space. An indirect lower limit on the mass of the first neutralino has been set. This limit is $M_{\tilde{\chi}^0_1}$ $>$ 38.2 GeV/c^2 at $\tan\beta$ = 1 and assuming a heavy sneutrino. This limit reaches 39.2 GeV/c^2 when taking into account neutralino searches at LEP2 [72].

In the GMSB scheme, the chargino mass limits were computed using several different searches. The SUGRA results of the present thesis were reinterpreted and combined with other searches including the SUGRA direct stau search and analyses dedicated to the peculiar signatures of the GMSB models. If $\Delta M \geq 0.3\ \mathrm{GeV}/c^2$, the chargino mass limits are 100 GeV/c^2 for all $m_{\tilde{G}}$, and 102 GeV/c^2 for $m_{\tilde{G}}$ $>$ 100 eV/c^2 at 95 % CL.

It has to be emphasized that the results given in this thesis are compatible with the ones obtained by the other three LEP collaborations [111].

In the SUGRA scheme, the 4 LEP collaboration chargino analyses were combined by the LEP2 SUSY working group [112]. The results from these channels were combined under the assumption that the charginos decay to the lightest neutralino with a W emission. To illustrate this combination Fig. 8.10 shows the excluded production cross-section at 95% CL in the ($M_{\tilde{\chi}^\pm_1}$,$M_{\tilde{\chi}^0_1}$) plane considering the last energy bin of the year 2000 data taking. Fig. 8.11 shows the obtained mass limit as function of the $m_{\tilde{\nu}}$ considering MSSM theoretical parameter sets with $\mu =$ -200 GeV/c^2 and $\tan\beta$= 2 (corresponding to a ΔM value greater 20 GeV/c^2). The combination yields a chargino mass limit of 103.5 GeV/c^2 (with an expected mass limit of 103.3 GeV/c^2) valid for $m_{\tilde{\nu}} > 300\ \mathrm{GeV}/c^2$.

Future prospects

No new signal related to the supersymmetry has been discovered during the eleven years of LEP operation. New hadron colliders, namely TeVatron and LHC, or the next linear $\mathrm{e^+e^-}$ colliders (e.g. TESLA), may be the future SUSY discovery machines. The TeVatron has been recently upgraded with respect to its first years of data taking and is in operation since year 2001. This $p^+\bar{p}^-$ collider operates at a centre-of-mass energy of 2 TeV and was designed to collect and integrated luminosity

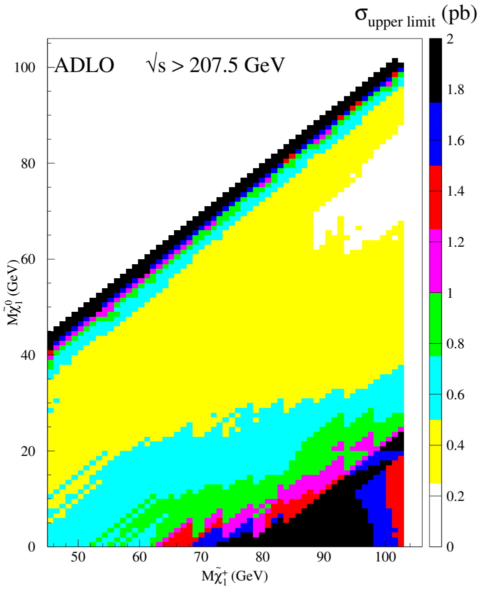

Figure 8.10: Excluded cross-section at 95 % CL in the ($M_{\tilde{\chi}_1^\pm}$,$M_{\tilde{\chi}_1^0}$) plane considering the last energy bin of the year 2000 data taking [112].

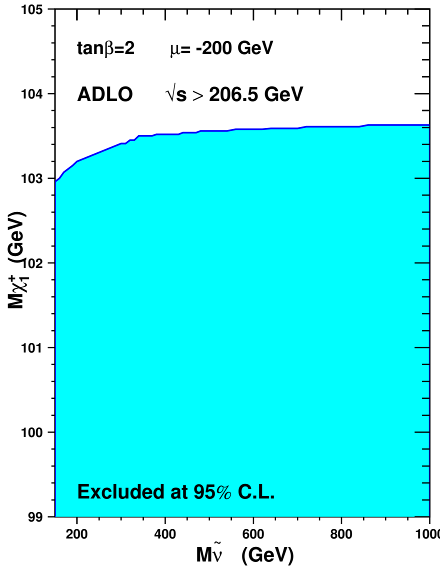

Figure 8.11: Obtained mass limit as function of the $m_{\tilde{\nu}}$ considering MSSM theoretical parameter sets with $\mu =$ -200 $\mathrm{GeV}/c^2$and $\tan\beta$= 2 [112].

of about 10 fb^{-1}. The LHC, the future CERN p^+p^+ collider, is designed to reach a centre-of-mass energy of 14 TeV with an expected integrated luminosity of 100 fb^{-1}. At hadron colliders, mSUGRA chargino events which can be easily extracted from the high hadronic background are events characterized by 3 charged leptons, no jet and high missing transverse energy [113][114]. This signature arises from the $\tilde{\chi}_2^0\tilde{\chi}_1^\pm$ production with both sparticles decaying in leptons. For instance, in CMS (one of the LHC collaborations), a discovery potential of a chargino with mass up to 250 GeV/c^2(all m_0) and 400 GeV/c^2($m_0 \leq 120$ GeV/c^2) is expected for high ΔM values [114]. A strong dependence on the m_0 value is found since it enters the definition of the leptonic branching fraction of both chargino and neutralino. On the other hand, the not-yet-accepted TESLA project is a collider using enhanced LEP acceleration techniques. The machine is designed to handle polarized beams (possible since it is a linear collider) to centre-of-mass energies ranging from the Z^0 pole to 0.8 TeV with an expected integrated luminosity of 500 fb^{-1}. The chargino signatures are identical to those described in the present thesis and a similar event selection could be performed in order to extract from the real data a possible chargino signal. A discovery potential of a chargino with mass up to about 0.90 $\sqrt{s}$/2 is expected (the 0.9 factor accounts for beamstrahlung and a 5-σ discovery) for high ΔM and high m_0 values [115].

Part IV

Appendices

Appendix A

Notations and Conventions

A.1 Space-time metric convention

In the present work, the space-time metric $\eta_{\mu\nu}(= \text{diag}(-1, 1, 1, 1))$ was used even if usually particle physicists use the "Bjorken and Drell" Minkowski space-time metric ($\eta_{\mu\nu} = \text{diag}(1, -1, -1, -1)$). This choice was motivated by the fact that almost all the chapter dedicated to the supersymmetric theories was derived from the primer of S. Martin [42] which was based on this metric definition (often used by people involved in general relativity).

A.2 Dirac, Weyl and Majorana fermions

A four-component Dirac fermion Ψ_D with mass M is described by the Lagrangian

$$\mathcal{L}_{\text{Dirac}} = -i\overline{\Psi}_D\gamma^\mu\partial_\mu\Psi_D - M\overline{\Psi}_D\Psi_D \,. \tag{A.1}$$

with the γ^μ satisfying the anti-commutation rule $\{\gamma^\mu\gamma^\nu\} = -2\eta^{\mu\nu}$. It is easy to verify that the tensors $\Sigma^{\mu\nu} \equiv \frac{i}{4}[\gamma^\mu\gamma^\nu]$ verify the Lorentz algebra, and in fact on the Dirac spinor, the Poincaré generators are given by

$$\left\{\begin{array}{ccc} P^\lambda & = & i\partial^\lambda \\ M^{\mu\nu} & = & x^\mu P^\nu - x^\nu P^\mu + \frac{1}{2}\Sigma^{\mu\nu} \end{array}\right. \tag{A.2}$$

For our purposes it is convenient to use the specific representation of the 4×4 gamma matrices given in 2×2 blocks by

$$\gamma_\mu = \begin{pmatrix} 0 & \sigma_\mu \\ \overline{\sigma}_\mu & 0 \end{pmatrix}; \qquad \gamma_5 \equiv i\gamma^0\gamma^1\gamma^2\gamma^3 = \begin{pmatrix} 1 & 0 \\ 0 & -1 \end{pmatrix}, \tag{A.3}$$

where

$$\sigma_0 = \overline{\sigma}_0 = \begin{pmatrix} 1 & 0 \\ 0 & 1 \end{pmatrix}; \qquad \sigma_1 = -\overline{\sigma}_1 = \begin{pmatrix} 0 & 1 \\ 1 & 0 \end{pmatrix};$$
$$\sigma_2 = -\overline{\sigma}_2 = \begin{pmatrix} 0 & -i \\ i & 0 \end{pmatrix}; \qquad \sigma_3 = -\overline{\sigma}_3 = \begin{pmatrix} 1 & 0 \\ 0 & -1 \end{pmatrix}. \tag{A.4}$$

We see that in this representation the upper two components of the Dirac spinor have left chirality while the bottom two components have right chirality, this comes from the relation valid in the extreme relativistic limit (i.e. m = 0) where

$$\left\{ \begin{array}{lcl} \Psi_L & = & \frac{(1+\gamma_5)}{2}\Psi_D \\ \Psi_R & = & \frac{(1-\gamma_5)}{2}\Psi_D \end{array} \right. \tag{A.5}$$

In this basis, called the Weyl basis, a four component Dirac spinor is written in terms of 2 two-component, complex, anticommuting objects $(\xi)_\alpha$ with $\alpha = 1, 2$ and $(\chi^\dagger)^{\dot\alpha}$ with $\dot\alpha = 1, 2$, where the † does not denote (yet) any kind of conjugation but just "tells" the presence of a dotted index

$$\Psi_D = \begin{pmatrix} \xi_\alpha \\ \chi^{\dagger\dot\alpha} \end{pmatrix} \tag{A.6}$$

The undotted (dotted) indices are used for the first (last) two components of a Dirac spinor. The right and left part do not have same indices since the two type of spinor transform differently under Lorentz boost

$$\frac{1}{2}\Sigma^{0i} = \begin{pmatrix} -i\sigma^i & 0 \\ 0 & i\sigma^i \end{pmatrix} \tag{A.7}$$

These two spinors $(\xi)_\alpha$ and $(\chi^\dagger)^{\dot\alpha}$ are called Weyl spinors. Thus we write in the Weyl representation

$$\Psi_L = \begin{pmatrix} \xi_\alpha \\ 0 \end{pmatrix} ; \Psi_R = \begin{pmatrix} 0 \\ \chi^{\dagger\dot\alpha} \end{pmatrix} \tag{A.8}$$

Now suppose that the Dirac spinor has a charge, i.e. satisfies

$$-(i\partial_\mu + eA_\mu)\gamma^\mu\Psi_D - M\Psi_D = 0 \tag{A.9}$$

The charge conjugation $\Psi_D \to \Psi_D^C$ transforms the Dirac equation by changing the charge sign, i.e.

$$-(i\partial_\mu - eA_\mu)\gamma^\mu\Psi_D^C - M\Psi_D^C = 0 \tag{A.10}$$

The charge conjugation operation is interpreted as converting a particle into its anti-particle (even a neutral one) and vice versa. In our basis Ψ_D^C is expressed as

$$\Psi_D^C = \begin{pmatrix} i\sigma^2(\chi^{\dagger\dot\alpha})^* \\ -i\sigma^2(\xi_\alpha)^* \end{pmatrix} \tag{A.11}$$

We see that $i\sigma^2(\chi^{\dagger\dot\alpha})^*$ transforms like a left-handed fermion (χ_α) and $-i\sigma^2(\xi_\alpha)^*$ like a right-handed fermion $(\xi^{\dagger\dot\alpha})$. If we define

$$\left\{ \begin{array}{lcl} (\chi^{\dagger\dot\alpha})^* & \equiv & \chi^\alpha \\ (\xi_\alpha)^* & \equiv & \xi^\dagger_{\dot\alpha} \end{array} \right. \tag{A.12}$$

and $\epsilon_{\alpha\beta}$, $\epsilon^{\alpha\beta}$, $\epsilon_{\dot{\alpha}\dot{\beta}}$, $\epsilon^{\dot{\alpha}\dot{\beta}}$ with $\epsilon^{12} = -\epsilon^{21} = \epsilon_{21} = -\epsilon_{12} = 1$; $\epsilon_{11} = \epsilon_{22} = \epsilon^{11} = \epsilon^{22} = 0$ we obtain a rule to raise and lower indices as

$$\xi_\alpha = \epsilon_{\alpha\beta}\xi^\beta; \qquad \xi^\alpha = \epsilon^{\alpha\beta}\xi_\beta; \qquad \chi^\dagger_{\dot{\alpha}} = \epsilon_{\dot{\alpha}\dot{\beta}}\chi^{\dagger\dot{\beta}}; \qquad \chi^{\dagger\dot{\alpha}} = \epsilon^{\dot{\alpha}\dot{\beta}}\chi^\dagger_{\dot{\beta}}\,. \tag{A.13}$$

Using those definitions we obtain the following expression for Ψ^C_D and $\overline{\Psi}_D$ ($\Psi^\dagger_D\gamma^0$)

$$\Psi^C_D = \begin{pmatrix} \chi_\alpha \\ \xi^{\dagger\dot{\alpha}} \end{pmatrix} \qquad\qquad \overline{\Psi}_D = (\,\chi^\alpha \quad \xi^\dagger_{\dot{\alpha}}\,)\ . \tag{A.14}$$

So, using Eq.(A.12) we see that the hermitian conjugate of a left-handed Weyl spinor is a right-handed Weyl spinor $(\psi_\alpha)^\dagger = (\psi_\alpha)^* = (\psi^\dagger)_{\dot{\alpha}}$ and vice versa $(\psi^{\dagger\dot{\alpha}})^\dagger = (\psi^{\dagger\dot{\alpha}})^* = \psi^\alpha$. Therefore any particular fermionic degrees of freedom can be described equally well using a Weyl spinor which is left-handed (with an undotted index) or by one which is right-handed (with a dotted index). The heights of these indices are important; for example, comparing Eqs. (A.1)-(A.6), we observe that the matrices $(\sigma^\mu)_{\alpha\dot{\alpha}}$ and $(\overline{\sigma}^\mu)^{\dot{\alpha}\alpha}$ defined by Eq.(A.4) carry indices with the heights as indicated. In this basis $\overline{\sigma}^\mu$ and σ^μ a related together by

$$\begin{cases} (\sigma^\mu)_{\alpha\dot{\alpha}} & = \quad \epsilon_{\alpha\beta}\epsilon_{\dot{\alpha}\dot{\beta}}(\overline{\sigma}^\mu)^{\dot{\beta}\beta} \\ (\overline{\sigma}^\mu)^{\dot{\alpha}\alpha} & \quad\quad\ \epsilon^{\dot{\alpha}\dot{\beta}}\epsilon^{\alpha\beta}(\sigma^\mu)_{\beta\dot{\beta}} \end{cases} \tag{A.15}$$

It is useful to abbreviate expressions with two spinor fields by suppressing undotted indices contracted like ${}^\alpha{}_\alpha$ and dotted indices contracted like ${}_{\dot{\alpha}}{}^{\dot{\alpha}}$. In particular,

$$\xi\chi \equiv \xi^\alpha\chi_\alpha = \xi^\alpha\epsilon_{\alpha\beta}\chi^\beta = -\chi^\beta\epsilon_{\alpha\beta}\xi^\alpha = \chi^\beta\epsilon_{\beta\alpha}\xi^\alpha = \chi^\beta\xi_\beta \equiv \chi\xi \tag{A.16}$$

with, conveniently, no minus sign in the end. Likewise, $\xi^\dagger\chi^\dagger$ and $\chi^\dagger\xi^\dagger$ are equivalent abbreviations for $\chi^\dagger_{\dot{\alpha}}\xi^{\dagger\dot{\alpha}} = (\xi\chi)^*$, the complex conjugate of $\xi\chi$. In a similar way,

$$\xi^\dagger\overline{\sigma}^\mu\chi = -\chi\sigma^\mu\xi^\dagger = (\chi^\dagger\overline{\sigma}^\mu\xi)^* = -(\xi\sigma^\mu\chi^\dagger)^* \tag{A.17}$$

stands for $\xi^\dagger_{\dot{\alpha}}(\overline{\sigma}^\mu)^{\dot{\alpha}\alpha}\chi_\alpha$, etc. With these conventions, the Dirac Lagrangian Eq.(A.1) can now be rewritten:

$$\mathcal{L}_{\text{Dirac}} = -i\overline{\Psi}_D\gamma^\mu\partial_\mu\Psi_D - M\overline{\Psi}_D\Psi_D = -i\xi^\dagger\overline{\sigma}^\mu\partial_\mu\xi - i\chi^\dagger\overline{\sigma}^\mu\partial_\mu\chi - M(\xi\chi + \xi^\dagger\chi^\dagger) \tag{A.18}$$

where we have dropped a total derivative piece $i\partial_\mu(\chi^\dagger\overline{\sigma}^\mu\chi)$ which does not affect the action.

A four-component Majorana spinor is a Dirac spinor which is identical to its charge conjugate spinor, i.e. its own anti-particle.

$$\Psi^C_M = \Psi_M \tag{A.19}$$

So, a Majorana spinor has no charge and in the Weyl representation we see that a Majorana spinor can be obtained from the Dirac spinor of Eq.(A.6) by imposing the constraint $\chi = \xi$, so that

$$\Psi_{\text{M}} = \begin{pmatrix} \xi_\alpha \\ \xi^{\dagger\dot{\alpha}} \end{pmatrix}; \qquad\qquad \overline{\Psi}_{\text{M}} = (\,\xi^\alpha \quad \xi^\dagger_{\dot{\alpha}}\,)\,. \tag{A.20}$$

Clearly a Weyl spinor cannot be a Majorana spinor and vice versa. However, given a Weyl spinor ψ_α we can always construct a Majorana spinor from it by the relation defined in Eq.(A.20). A general Dirac spinor Ψ_D and its charge conjugate can always be rewritten in terms of two Majorana spinors

$$\begin{cases} \Psi_D &= \Psi_{M1} + i\Psi_{M2} \\ \Psi_D^C &= \Psi_{M1} - i\Psi_{M2} \end{cases} \tag{A.21}$$

The Lagrangian for a Majorana fermion with mass M

$$\mathcal{L}_{\text{Majorana}} = -\frac{i}{2}\overline{\Psi}_{\text{M}}\gamma^\mu\partial_\mu\Psi_{\text{M}} - \frac{1}{2}M\overline{\Psi}_{\text{M}}\Psi_{\text{M}} \tag{A.22}$$

in the four-component Majorana spinor form can therefore be rewritten

$$\mathcal{L}_{\text{Majorana}} = -i\xi^\dagger\overline{\sigma}^\mu\partial_\mu\xi - \frac{1}{2}M(\xi\xi + \xi^\dagger\xi^\dagger) \tag{A.23}$$

in the more economical two-component Weyl spinor representation.

More generally, any theory involving spin-1/2 fermions can *always* be written down in terms of a collection of left-handed Weyl spinors ψ_i with

$$\mathcal{L} = -i\psi^{\dagger i}\overline{\sigma}^\mu\partial_\mu\psi_i + \ldots \tag{A.24}$$

where the ellipses represent possible mass terms, gauge interactions, and Yukawa interactions with scalar fields. Here the index i runs over the appropriate gauge and flavor indices of the fermion. There is a different ψ_i for the left-handed piece and for the hermitian conjugate of the right-handed piece of a Dirac fermion. If one has any expression involving bilinears in four-component spinors

$$\Psi_1 = \begin{pmatrix} \xi_1 \\ \chi_1^\dagger \end{pmatrix} \qquad \text{and} \qquad \Psi_2 = \begin{pmatrix} \xi_2 \\ \chi_2^\dagger \end{pmatrix}, \tag{A.25}$$

then one can translate into two-component Weyl spinor language (or vice versa) using the dictionary:

$$\overline{\Psi}_1 P_L \Psi_2 = \chi_1\xi_2; \qquad \overline{\Psi}_1 P_R \Psi_2 = \xi_1^\dagger\chi_2^\dagger; \tag{A.26}$$

$$\overline{\Psi}_1\gamma^\mu P_L \Psi_2 = \xi_1^\dagger\overline{\sigma}^\mu\xi_2; \qquad \overline{\Psi}_1\gamma^\mu P_R \Psi_2 = \chi_1\sigma^\mu\chi_2^\dagger \tag{A.27}$$

A.3 SM fermionic free Lagrangian density

Let us now see how the Standard Model quarks and leptons are described in this notation. The complete list of left-handed Weyl spinors can be given names corresponding to the chiral supermultiplets in Table 1.2:

$$Q_i = (u\,d),\ (c\,s),\ (t\,b) \tag{A.28}$$

$$\overline{u}_i = \overline{u},\, \overline{c},\, \overline{t} \qquad \overline{d}_i = \overline{d},\, \overline{s},\, \overline{b} \tag{A.29}$$

$$L_i = (\nu_e\,e),\ (\nu_\mu\,\mu),\ (\nu_\tau\,\tau) \tag{A.30}$$

$$\overline{e}_i = \overline{e},\, \overline{\mu},\, \overline{\tau}. \tag{A.31}$$

Here $i = 1, 2, 3$ is a family index. The bars on these fields are part of the names of the fields, and do *not* denote any kind of conjugation. Rather, the unbarred fields are the left-handed pieces of a

Dirac spinor, while the barred fields are the names given to the conjugates of the right-handed piece of a Dirac spinor. For example, e is the same thing as e_L in Table 1, and $\overline{e}$ is the same as $e_R^\dagger$ ($(e_R^{\dot\alpha})^\dagger$= $(e_R^\dagger)^\alpha$), and so run on an undotted index). Together they form a Dirac spinor:

$$\begin{pmatrix} e \\ \overline{e}^\dagger \end{pmatrix} \equiv \begin{pmatrix} e_L \\ e_R \end{pmatrix} \tag{A.32}$$

with similar equations for all of the other quark and charged lepton Dirac spinors. (The neutrinos of the Standard Model are not part of a Dirac spinor.) The fields Q_i and L_i are weak isodoublets which always go together when one is constructing interactions invariant under the full Standard Model gauge group $SU(3)_C \times SU(2)_L \times U(1)_Y$. Suppressing all color and weak isospin indices, the purely kinetic part of the Standard Model fermion Lagrangian density is then

$$\mathcal{L} = -iQ^{\dagger i}\overline{\sigma}^\mu \partial_\mu Q_i - i\overline{u}^{\dagger i}\overline{\sigma}^\mu \partial_\mu \overline{u}_i - i\overline{d}^{\dagger i}\overline{\sigma}^\mu \partial_\mu \overline{d}_i - iL^{\dagger i}\overline{\sigma}^\mu \partial_\mu L_i - i\overline{e}^{\dagger i}\overline{\sigma}^\mu \partial_\mu \overline{e}_i \tag{A.33}$$

with the family index $i = 1, 2, 3$ summed over.

Appendix B

The supersymmetric Higgs sector

B.1 Where is the SUSY Higgs potential ?

In the MSSM, the description of electroweak symmetry breaking is complicated slightly by the fact that there are two complex Higgs doublets $H_u = (H_u^+,\ H_u^0)$ and $H_d = (H_d^0,\ H_d^-)$ rather than just one in the Standard Model. The classical scalar potential for the Higgs scalar fields in the MSSM is given by

$$\begin{aligned} V &= (|\mu|^2 + m_{H_u}^2)(|H_u^0|^2 + |H_u^+|^2) + (|\mu|^2 + m_{H_d}^2)(|H_d^0|^2 + |H_d^-|^2) \\ &\quad + B_0\,(H_u^+ H_d^- - H_u^0 H_d^0) + \text{c.c.} \\ &\quad + \frac{1}{8}(g^2 + g'^2)(|H_u^0|^2 + |H_u^+|^2 - |H_d^0|^2 - |H_d^-|^2)^2 \\ &\quad + \frac{1}{2} g^2 |H_u^+ H_d^{0*} + H_u^0 H_d^{-*}|^2. \end{aligned} \tag{B.1}$$

The terms proportional to $|\mu|^2$ come from F-terms. The terms proportional to $m_{H_u}^2$, $m_{H_d}^2$ and B_0 are nothing but a rewriting of the Higgs mass terms present in $\mathcal{L}_{soft}$. Finally, the terms proportional to g^2 and g'^2 are the D-term contributions which may be derived from the scalar potential (after some rearranging).

B.2 The supersymmetric Brout-Englert-Higgs mechanism

The supersymmetric Higgs potential, considering only neutral Higgses, is

$$V(H_d^0, H_u^0) = \frac{1}{8}(g^2 + g'^2)(|H_d^0|^2 - |H_u^0|^2)^2 + \mu_1^2 |H_d^0|^2 + \mu_2^2 |H_u^0|^2 - \mu_3^2 (H_u^0 H_d^0 + \text{c.c.}) \tag{B.2}$$

where the scale dependent mass coefficient are $\mu_1^2 \equiv m_{H_d^0}^2 + \mu^2$, $\mu_2^2 \equiv m_{H_u^0}^2 + \mu^2$, $\mu_3^2 \equiv B_0$ with $m_{H_u^0}^2 = m_{H_d^0}^2 = m_0^2$ at the GUT scale. A suitable redefinition of the Higgs fields phases permits to yield a real positive value μ_3. To obtain a minimum of the potential for non-vanishing values of Higgs fields, the potential should decrease in the vicinity of the origin. This requirement is expressed by the following constraint

$$\mu_1^2 \mu_2^2 < \mu_3^4 \tag{B.3}$$

If this inequality is not satisfied, then $< H_u^0 >_0 = < H_d^0 >_0 = 0$ will be a stable minimum of the potential, and electroweak symmetry breaking will not occur. When running down $m^2_{H_u^0}$ and $m^2_{H_d^0}$ with the RGEs, their value gets a positive contribution from the gauge couplings and a negative contribution from the Yukawa couplings. As the top mass is large and its Yukawa is also typically large, the Yukawa contribution will dominate the running of $m^2_{H_u^0}$, driving $m^2_{H_u^0}$ to negative values before the EW scale and hence prevent the potential to admit $< H_u^0 >_0 = < H_d^0 >_0 = 0$ as a stable minimum. It has to be emphasized that a negative value of $m^2_{H_u^0}$ is not necessary to ensure $\mu_1^2\mu_2^2 < \mu_3^4$. Furthermore, even if $m^2_{H_u^0} < 0$, there may be no electroweak symmetry breaking if $|\mu|$ is too large or if B_0 is too small [42]. Nevertheless, it is an important factor in explaining why the electroweak symmetry breaking can *naturally* be broken in SUSY models. Since if the breaking is obtained, it is due only to quantum effects, this mechanism is usually called *radiative electroweak symmetry breaking*.

Moreover, the minimization of the potential determines the vevs $v_{d,u} = < H^0_{d,u} >_0$ values.

$$\frac{\partial V}{\partial H_d^0} = +\frac{1}{2}(g^2 + g'^2)(v_d^2 - v_u^2)v_d + 2\mu_1^2 v_d - 2\mu_3^2 v_u = 0 \tag{B.4}$$

$$\frac{\partial V}{\partial H_u^0} = -\frac{1}{2}(g^2 + g'^2)(v_d^2 - v_u^2)v_u + 2\mu_2^2 v_u - 2\mu_3^2 v_d = 0 \tag{B.5}$$

One sees that both vevs have to be non-zero else the equations yield the solution $v_u = v_d = 0$ preventing the breaking. By taking the combination $v_u \frac{\partial V}{\partial H_d^0} + v_d \frac{\partial V}{\partial H_u^0}$ and defining $\tan\beta \equiv v_u/v_d$, one obtains

$$\mu_3^2 = \frac{\mu_1^2 + \mu_2^2}{1 + \tan^2\beta}\tan\beta \tag{B.6}$$

which permits to relate the low energy scale parameter $\tan\beta$ to the parameter B_0. The other combination $v_d \frac{\partial V}{\partial H_d^0} - v_u \frac{\partial V}{\partial H_u^0}$ determines $\eta^2 \equiv v_u^2 + v_d^2$

$$\eta^2 = 4\frac{\mu_1^2 - \mu_2^2\tan^2\beta}{(g^2 + g'^2)(\tan^2\beta - 1)} \tag{B.7}$$

For the electroweak symmetry to be correctly broken, the vev η should reproduce the Z^0 mass, which yields $\eta \simeq 246\ \ GeV$. This induces a constraint among the scale parameters (at the EW scale) which is used to determine $|\mu|$ as a function of the remaining parameters

$$\mu^2 = \frac{m^2_{H_d} - m^2_{H_u}\tan^2\beta}{\tan^2\beta - 1} - M^2_{Z^0} \tag{B.8}$$

B.3 Higgses physical states

Starting from the 8 degrees of freedom contained in the two complex MSSM Higgs doublets, when the electroweak symmetry is broken, three of them are the would-be Nambu-Goldstone bosons which become the longitudinal modes of the Z^0 and $W^{\pm}$ massive vector bosons. The remaining five Higgs scalar mass eigenstates consist of one CP–odd neutral scalar A^0, a charge +1 scalar H^+ and its conjugate charge -1 scalar H^- and two CP-even neutral scalars h^0 and H^0 with tree-level masses [42]:

$$m_{A^0}^2 = 2B_0/\sin 2\beta \tag{B.9}$$
$$m_{H^\pm}^2 = m_{A^0}^2 + m_W^2 \tag{B.10}$$
$$m_{h^0,H^0}^2 = \frac{1}{2}\Big(m_{A^0}^2 + m_Z^2 \mp \sqrt{(m_{A^0}^2 + m_Z^2)^2 - 4m_Z^2 m_{A^0}^2 \cos^2 2\beta}\Big) \tag{B.11}$$

The Feynman rules for couplings of the mass eigenstate Higgs scalars to the Standard Model quarks and leptons and the electroweak vector bosons, as well as to the various sparticles, have been worked out in detail in [116][117] The masses of A^0, H^0 and $H^\pm$ can, in principle, be arbitrarily large since they all grow with $B_0/\sin 2\beta$. In contrast, the mass of h^0 is bounded from above. One can show from Eq.(B.11) that

$$m_{h^0} < |\cos 2\beta| m_Z \tag{B.12}$$

However, the tree-level mass formulas given above for the Higgs mass eigenstates are subject to quite significant quantum corrections which are especially important to take into account in the case of h^0. The largest such contributions typically come from top-stop loop corrections to the terms in the scalar potential. In the limit of stop squark masses $m_{\tilde{t}_1}$ and $m_{\tilde{t}_2}$ much greater than the top quark mass m_t, one finds a one-loop radiative correction to Eq.(B.11):

$$\Delta(m_{h^0}^2) = \frac{3}{4\pi^2}\eta^2 y_t^4 \sin^4\beta \, \ln\left(\frac{m_{\tilde{t}_1} m_{\tilde{t}_2}}{m_t^2}\right). \tag{B.13}$$

Including this and other corrections, [118], one can obtain only a considerably weaker, but still very interesting, bound

$$m_{h^0} \lesssim 130 \text{ GeV} \tag{B.14}$$

So, if we are embedded in a supersymmetric reality, it is likely that TeVatron or LHC will at least discover one Higgs.

Appendix C

Diagrams in the SUSY parameter space

In Figures C.1 to C.7 we show the contour distributions in the (μ, M_2) plane of the most relevant variables used in the analysis: chargino and neutralino masses, ΔM, chargino production cross–section and the branching fraction of the radiative channel ($\tilde{\chi}_2^0 \rightarrow \tilde{\chi}_1^0\gamma$). Each variable has been plotted at the **tree-level** for three values of $\tan\beta$ (1, 1.5 and 35) and assuming heavy sfermions ($m_0 = 1$ TeV/c^2). Regions excluded by the chargino search at LEP 1 ($M_{\tilde{\chi}_1^\pm} > 45$ GeV/c^2) are also marked in the diagrams.

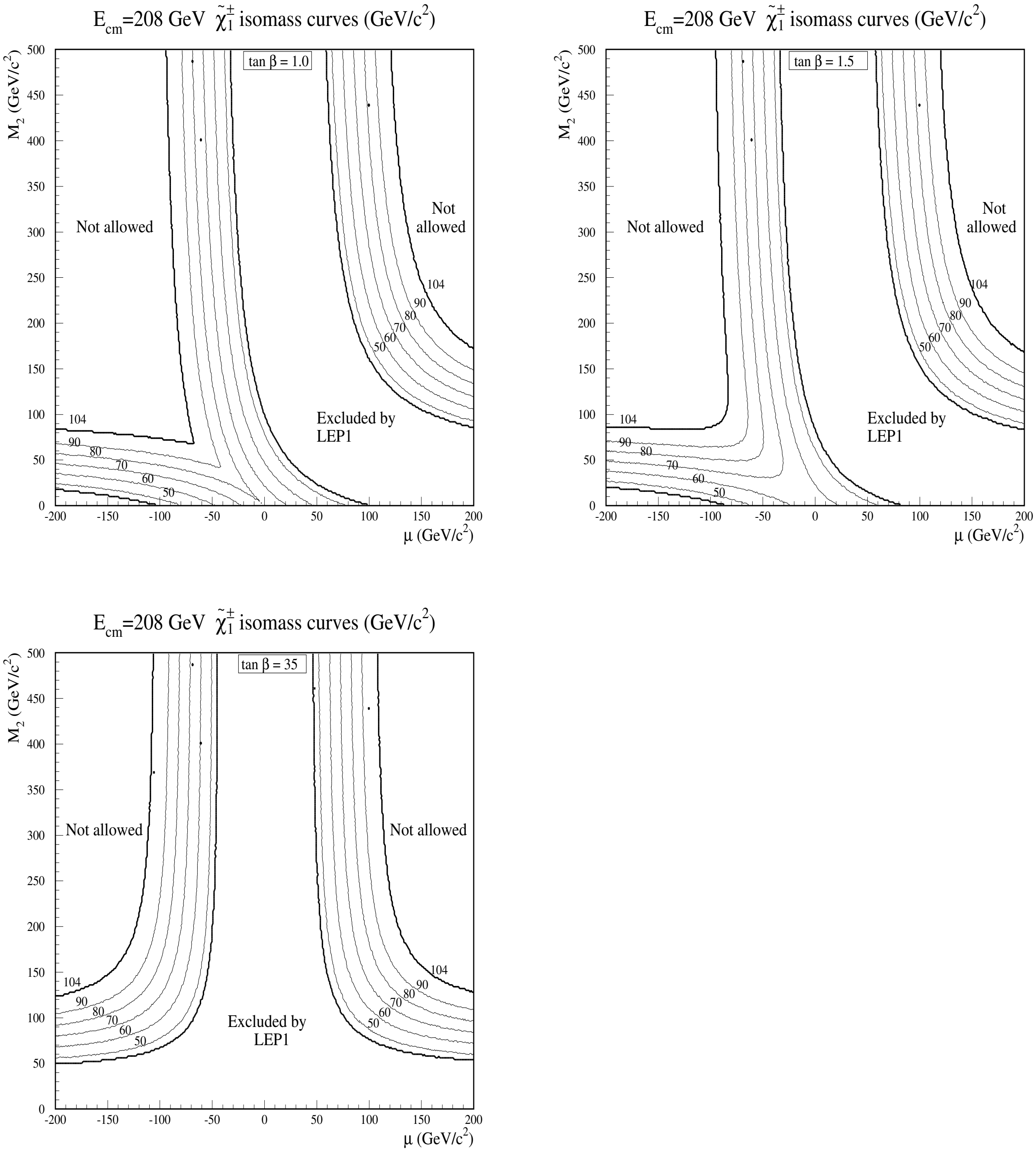

Figure C.1: Contours of constant $M_{\tilde{\chi}_1^{\pm}}$ in the (μ, M_2) plane for three values of $\tan\beta$ (1, 1.5 and 35). The numbers written in the plot indicate the mass values in GeV/c^2.

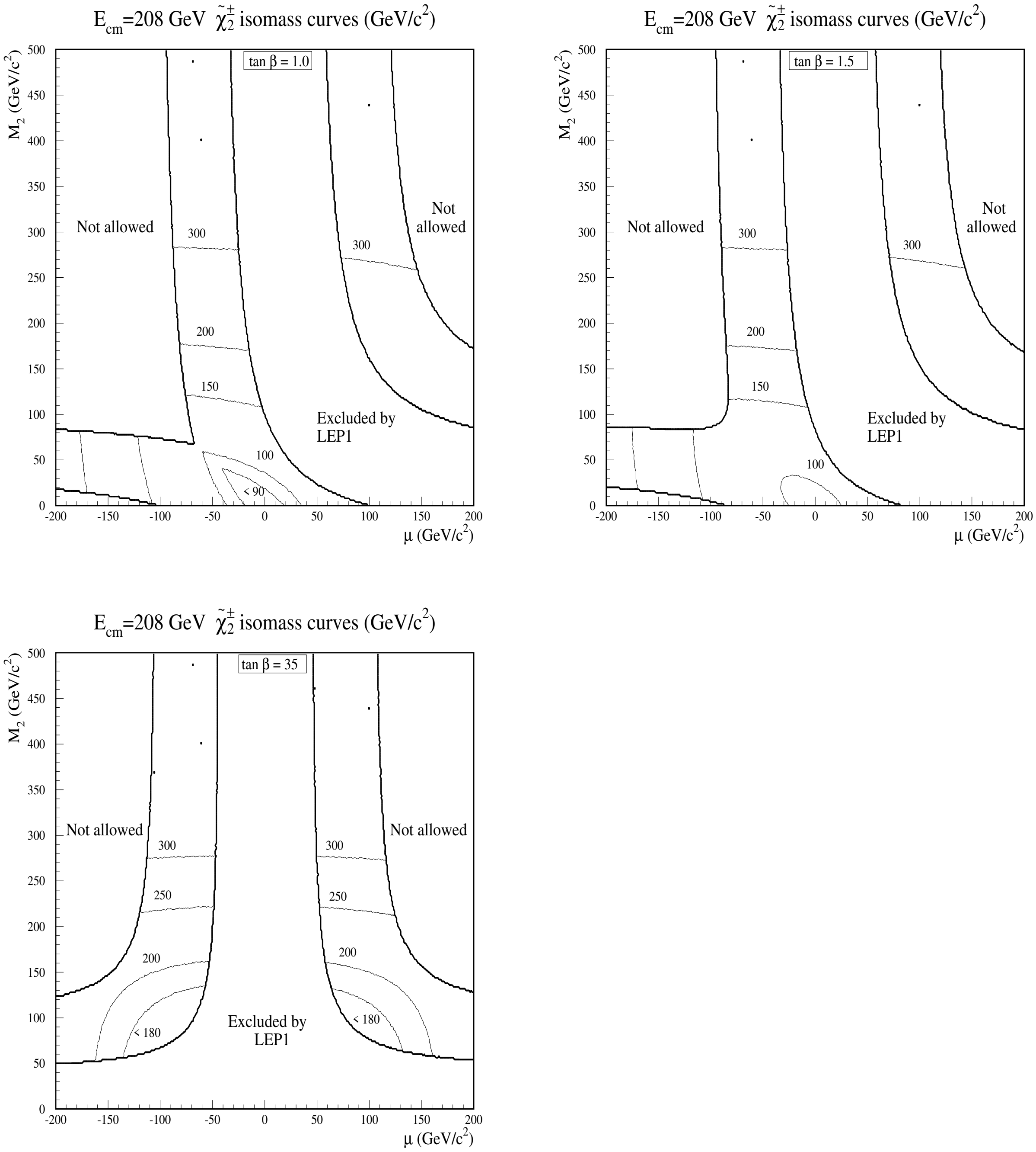

Figure C.2: Contours of constant $M_{\tilde{\chi}_2^{\pm}}$ in the (μ, M_2) plane for three values of $\tan\beta$ (1, 1.5 and 35). The numbers written in the plot indicate the mass values in GeV/c^2.

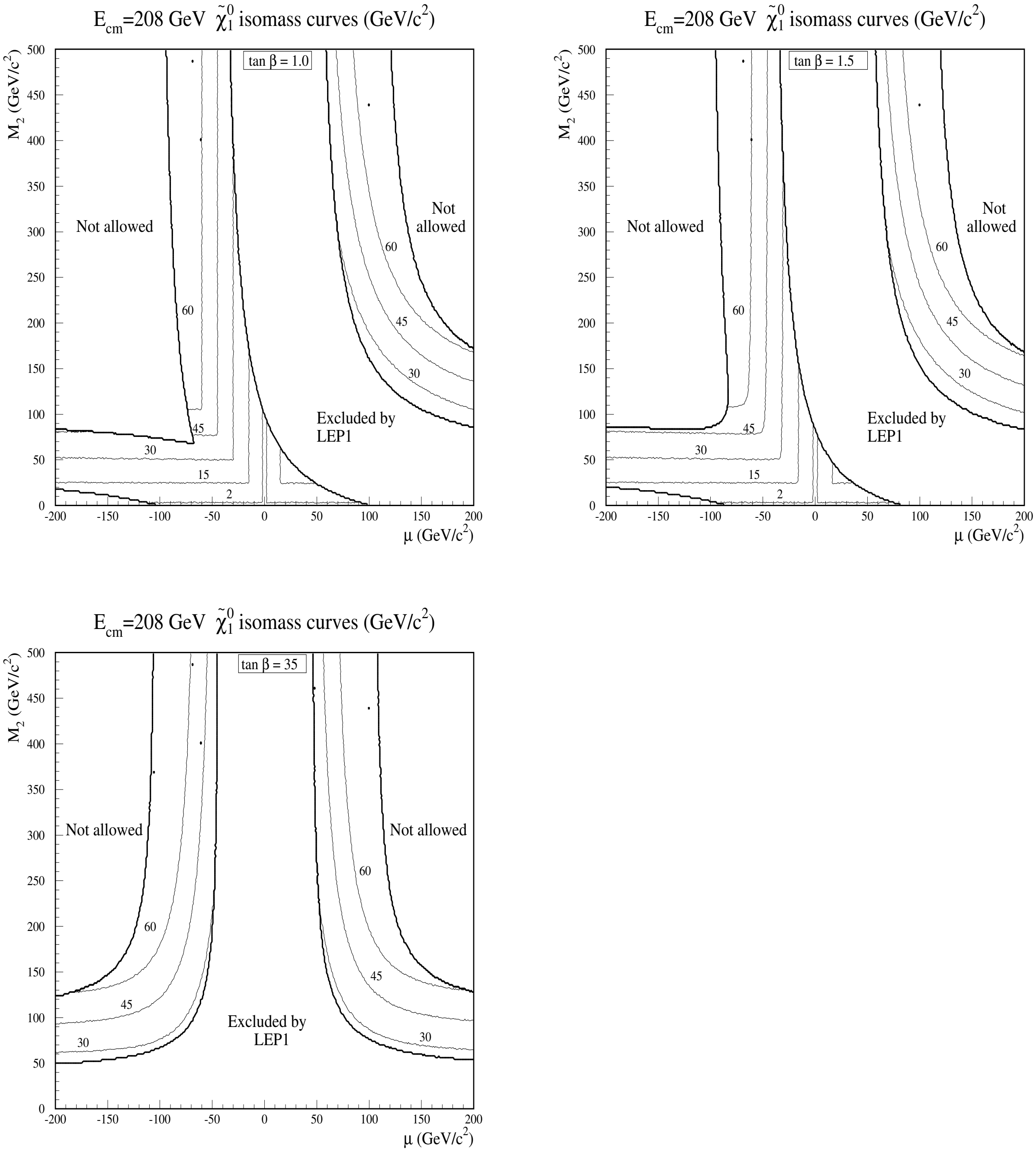

Figure C.3: Contours of constant $M_{\tilde{\chi}_1^0}$ in the (μ, M_2) plane for three values of $\tan\beta$ (1, 1.5 and 35). The numbers written in the plot indicate the mass values in GeV/c^2.

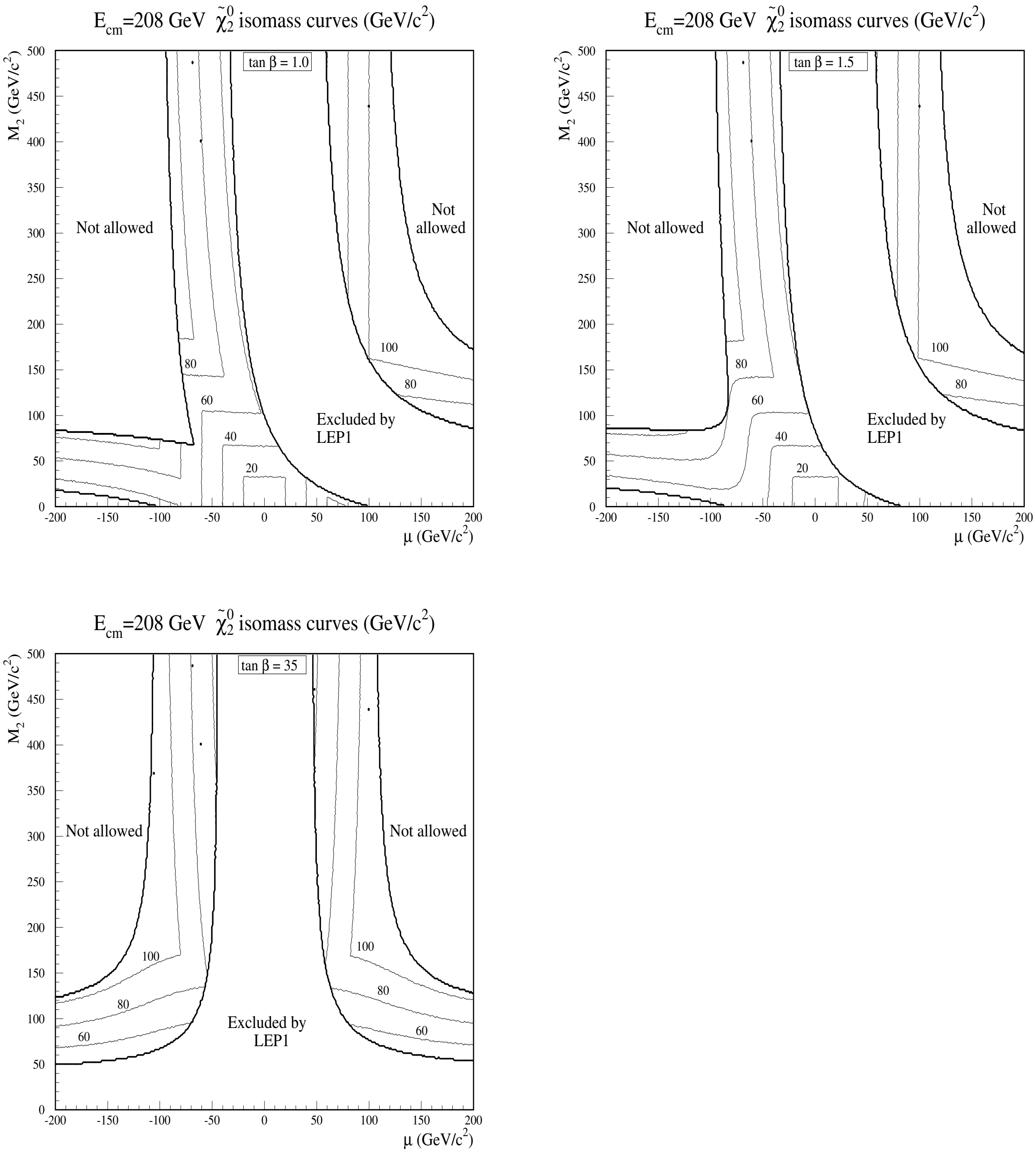

Figure C.4: Contours of constant $M_{\tilde{\chi}_2^0}$ in the (μ, M_2) plane for three values of $\tan\beta$ (1, 1.5 and 35). The numbers written in the plot indicate the mass values in GeV/c^2.

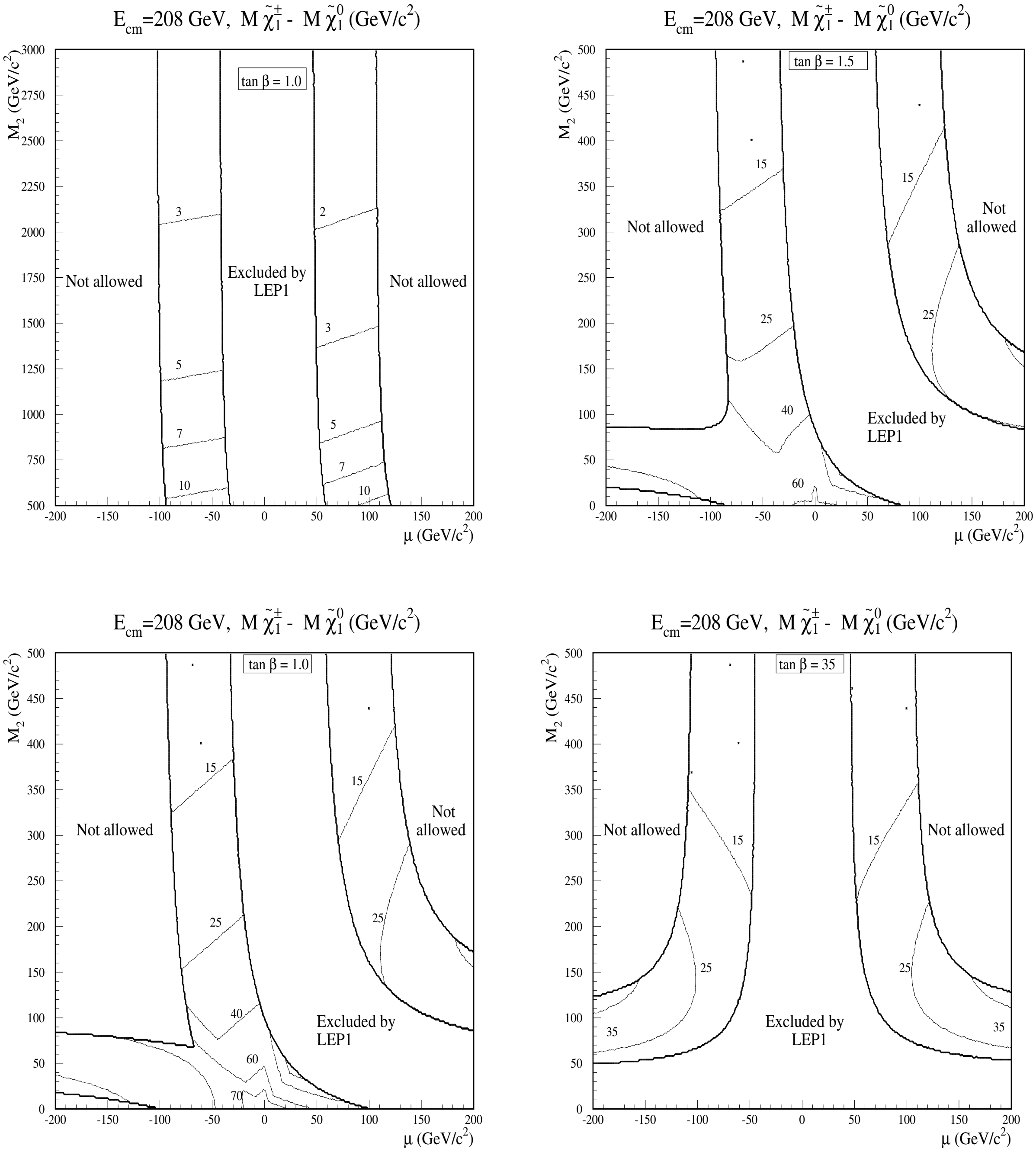

Figure C.5: Contours of constant $\Delta M = M_{\tilde{\chi}_1^\pm} - M_{\tilde{\chi}_1^0}$ in the (μ, M_2) plane for three values of $\tan\beta$ (1, 1.5 and 35). The numbers written in the plot indicate the mass values in GeV/c^2.

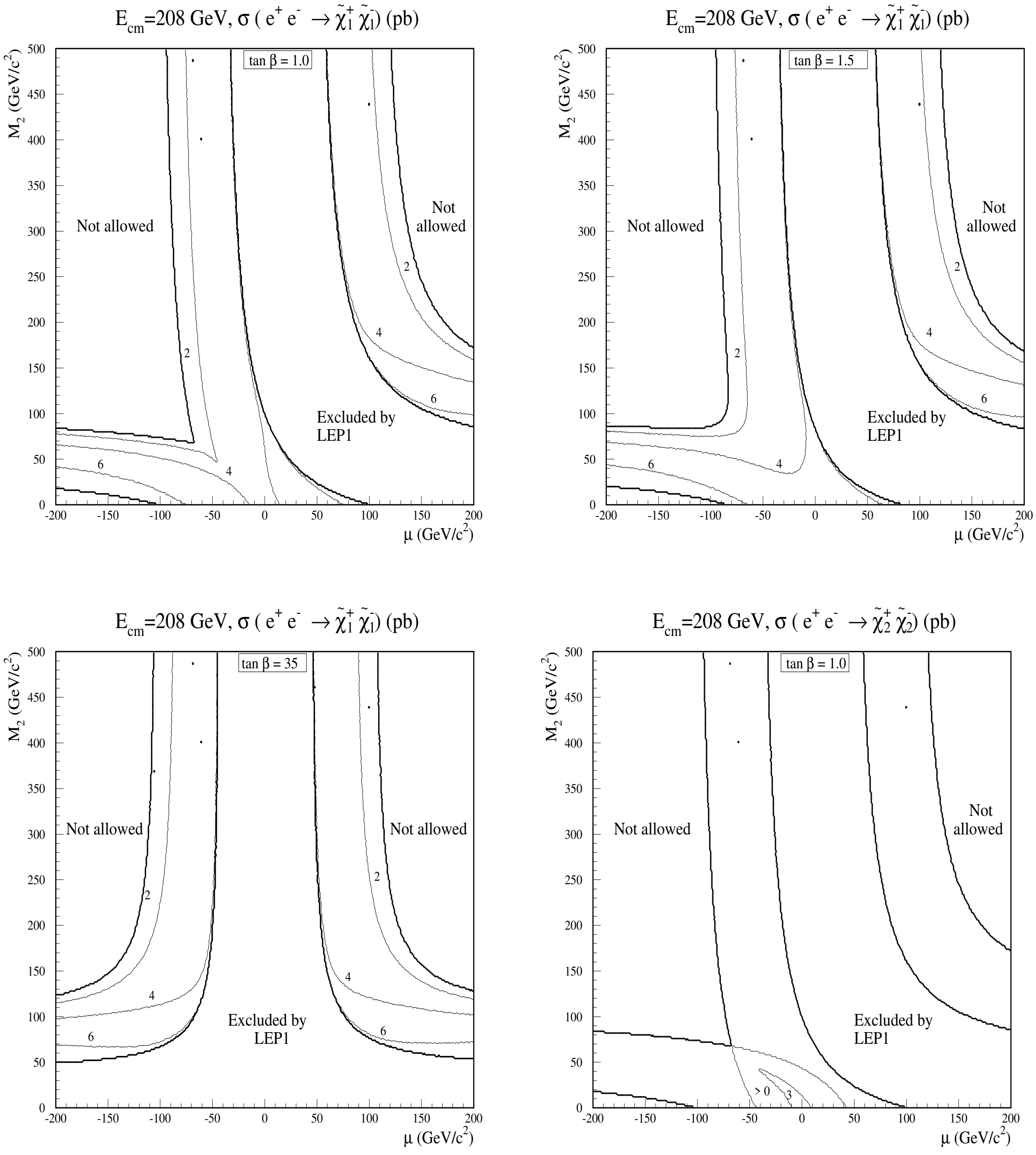

Figure C.6: Contours of constant σ_{tot} in the (μ, M_2) plane for three values of $\tan\beta$ (1, 1.5 and 35). The numbers written in the three first plots indicate the values of the $\tilde{\chi}^{\pm}_{1}$ pair production cross section in pb. The last plot (lower-right) shows the $\tilde{\chi}^{\pm}_{2}$ pair production cross-section for $\tan\beta = 1$ ($\tilde{\chi}^{\pm}_{2}$ pair production in LEP2 energy range is only possible for $\tan\beta \simeq 1$).

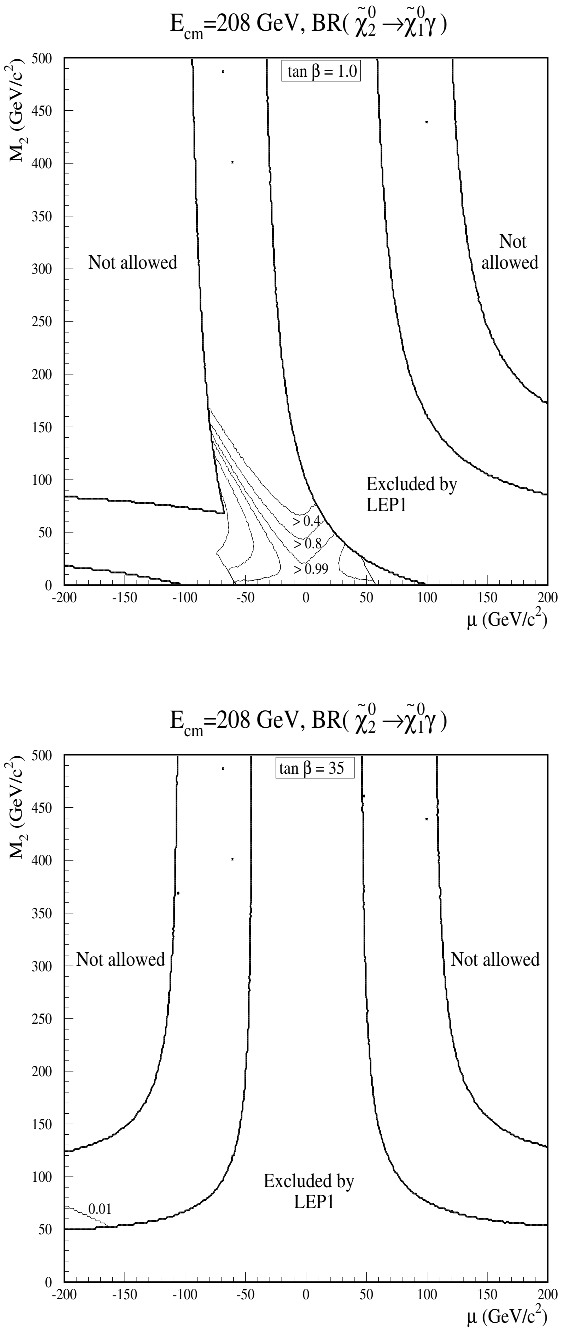

Figure C.7: Contours of constant value of the *radiative branching fraction* ($\tilde\chi^0_2 \to \tilde\chi^0_1\gamma$), assuming a $\tilde\chi^0_2$ lighter than the $\tilde\chi^\pm_1$, in the (μ, M_2) plane for three values of $\tan\beta$ (1, 1.5 and 35).

Appendix D

Radiative corrections in the $\tilde{\chi}_i$ sector

We have seen (Eq.(B.12)) that without radiative corrections (quantum effects) the MSSM would be ruled out by the negative Higgs boson searches at LEP2. It is interesting to see how such effects affect the chargino and neutralino sector. In the present work, those quantum effects will be considered only as a source of uncertainties on the $\tilde{\chi}_1^{\pm}$ and $\tilde{\chi}_1^0$ mass limits and only relevant informations from the experimentalist point of view will be given.

Given a set of theoretical parameters, those quantum corrections are a source of uncertainties on :

- the chargino/neutralino mass determination,
- the chargino pair production cross-section determination.

As we will see, for e^+e^- initial states within LEP2 energy range, the quantum corrections to the chargino pair production cross-section are positive and so using tree-level(Born) cross-sections gives conservative results since $N_{exp}(=\sigma\epsilon\mathcal{L})$ is underestimated. From the mass point of view, it has to be emphasized that those corrections only modify the matching between theoretical parameters (μ,M_2,$\tan\beta$) and physical masses and hence do not affect the chargino mass limits given in chapter 8, but are a cause of uncertainty to the indirect mass limit on the neutralino mass. This is due to the fact that this mass limit is set by finding the $\tilde{\chi}_1^0$ isomass curve which is fully contained in the (μ,M_2) regions excluded by the direct chargino search. This procedure is only possible because of the relation between the running gaugino masses set by the GUT assumptions ($M_2(m_Z^2) \simeq 2M_1(m_Z^2)$).

Corrections to the chargino and neutralino masses

Since the top one-loop correction (Fig D.1.a) on m_H^2 is of the order of 60% (Eq.(B.13)), one can ask if a such strong effect will be seen in the higgsino sector and how this will affect the physical chargino and neutralino masses. Pierce and Papadopoulos [119] showed that the stop/top(sbottom/top) one-loop corrections on the neutral(charged) higgsinos, depicted in Fig D.1.b for the neutral higgsino case, yield the correction

$$\frac{\Delta m_{\tilde{h}}}{m_{\tilde{h}}} \simeq 3\frac{\lambda_t^2}{16\pi^2} ln(\frac{m_{\tilde{t}}^2}{m_t^2}) \simeq 5\% \quad (m_{\tilde{h}} = 90 \text{ GeV}/c^2) \tag{D.1}$$

which are of the same order of the one-loop corrections to the gaugino masses. Hence, due to their fermionic nature, higgsino mass corrections are mild compared to the Higgs boson mass corrections [119].

Figure D.1: (a) Top quark contribution to the Higgs boson mass. (b) Top/stop contribution to the higgsino mass [119].

The complete lepton/slepton and gauge/Higgs/gaugino/higgsino one-loop corrections to the chargino and neutralino masses can be found in [120]. The computation takes into account one-loop corrections on all the parameters entering the chargino/neutralino mass matrices (which consists namely on the determination of $\mu(\mu^2)$, $M_1(M_1^2)$, $M_2(M_2^2)$ and $\tan\beta(m_Z^2)$) and assumed mass universality in the gaugino sector and high sfermion masses, $m_{\tilde{f}} \simeq 1\ \ \mathrm{TeV}/c^2$. It has to be emphasized that this choice matches perfectly our theoretical assumptions and parameter constraints and so the results can be translated into an estimate of the uncertainty on our $\tilde{\chi}_1^0$ mass limit.

To illustrate those corrections, Fig. D.2a-b shows contours of the $\tilde{\chi}$ masses at the tree level (dashed lines) and sfermions/fermions one-loop level (solid lines) in the (μ,M_2) plane with $\tan\beta$ = 2 for the $\tilde{\chi}_1^{\pm}$,$\tilde{\chi}_2^{\pm}$,$\tilde{\chi}_1^0$ and $\tilde{\chi}_2^0$. For the lightest chargino and neutralino, we see that both isomass curve shifts occur in the same way and that the percentage change in the mass in the (μ,M_2) plane along the upper right contour $M_{\tilde{\chi}_1^{\pm}}$ = 45 GeV/c^2 typically increases by 10-20% (8-10%) for $\tan\beta \simeq 1$ ($\tan\beta \geq 4$) [119] but remains practically unchanged in the region where the indirect $\tilde{\chi}_1^0$ mass limit is set, i.e. $\mu \simeq -M_2$. If one includes the gauge/Higgs/gaugino/higgsino one-loops [120] which account for typically a 1% mass correction, the worst case, i.e. high squark masses and low $\tan\beta$, leads to a maximum difference between $\Delta\tilde{\chi}_1^{\pm}/\tilde{\chi}_1^{\pm}$ and $\Delta\tilde{\chi}_1^0/\tilde{\chi}_1^0$ of 1% in the region where the LSP limit is set [120]. This difference is mainly due to the fact that M_1 and M_2 are not evaluated at the same energy scale anymore. Hence, the indirect $\tilde{\chi}_1^0$ mass limit given in section 8, is almost not sensitive to the one-loop radiative corrections and it has been decided to lower it by 500 MeV/c^2 to conservatively account for the effects of radiative corrections.

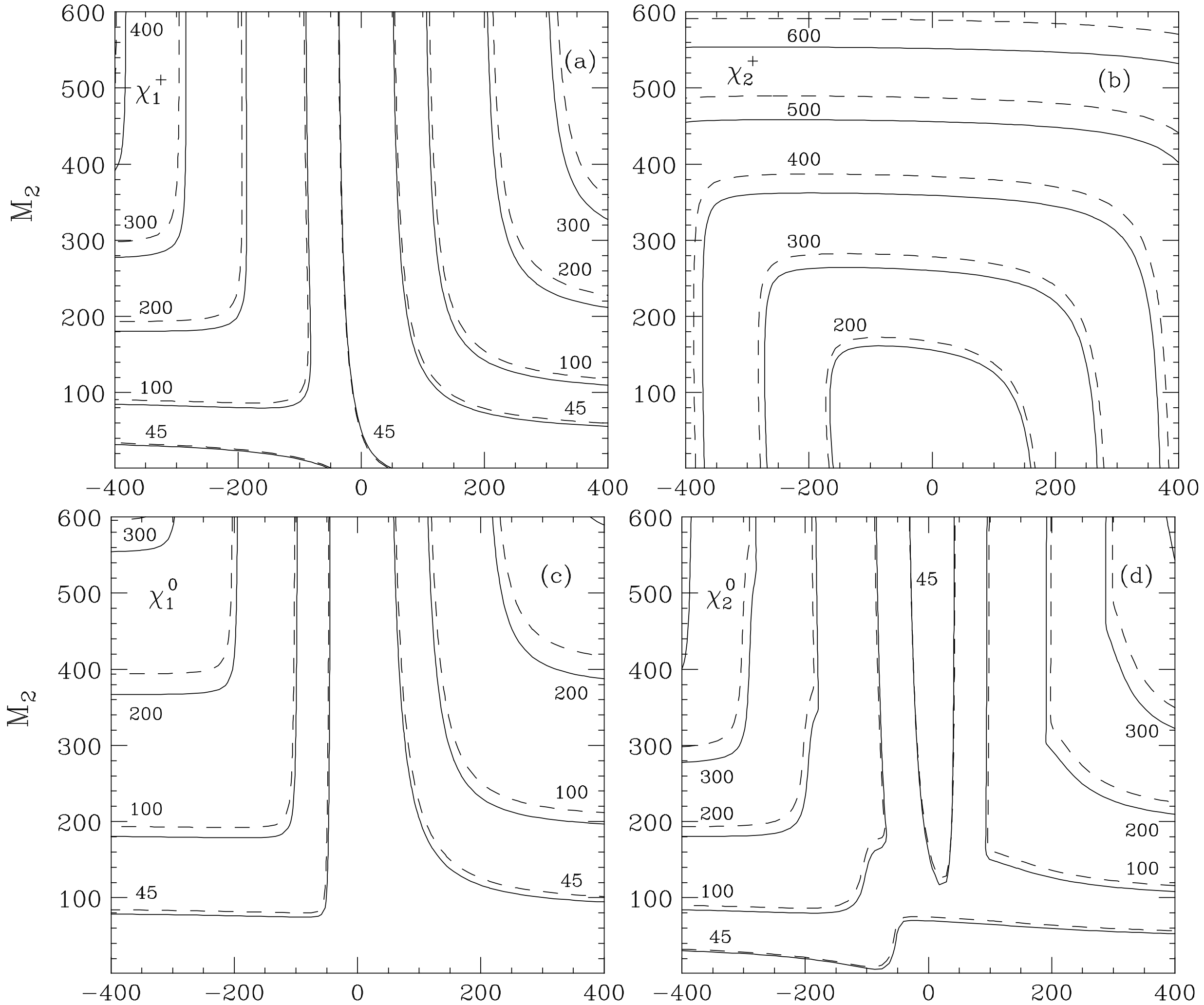

Figure D.2: Contours of first 2 chargino and neutralino masses in the μ, M_2 plane at tree-level (dashed lines) and sfermions/fermions one-loop (solid) level with $\tan\beta = 2$. The axes and contours are labelled in GeV/c^2 units [119].

Corrections to the chargino pair production cross-section

In all new phenomena searches, it is important to have a precise theoretical determination of the new signal production cross-section. Even if the first aim of a scientist is to discover the signal and not to exclude it, in the case of no discovery, the informations that will be deduced [1] from the non signal measurement is highly sensitive to the theoretical production cross-section. This is because, all the exclusion chain is related to the expected number of signal events $N_{exp}(signal)$ which linearly depends on σ_{signal}. If this number is overestimated and no discovery has been made, the excluded regions (in term of the masses or whatever variable linked to the new phenomenon) will be overestimated. This can be dangerous since the design of future experiments may rely on those excluded areas (e.g. the energy range).

Although the chargino pair production process does not contain any coloured particles, and so is

[1] Statistical methods which permit to draw such informations are discussed in appendix H.

immune to QCD corrections, there are other radiative corrections coming from loops of top and bottom quarks and squarks which are important due to the large Yukawa couplings of these heavy quarks and squarks. Diaz, King and Ross [121] have computed those corrections for $\mathrm{e}^+\mathrm{e}^-$ initial states in the LEP2 energy range, namely $\sqrt{s}$ = 192 GeV. Those corrections involve several contributions divided into two categories:

- the quark/squark loop contributions to the unrenormalized Z and γ self-energies, $Z-\gamma$ mixing, charginos self energy and charginos mixing as shown in Fig. D.3,
- the unrenormalized (s)quarks irreductible triangular diagrams contributing to the $Z\tilde{\chi}^+\tilde{\chi}^-$ and $\gamma\tilde{\chi}^+\tilde{\chi}^-$ vertices as shown in Fig. D.4.

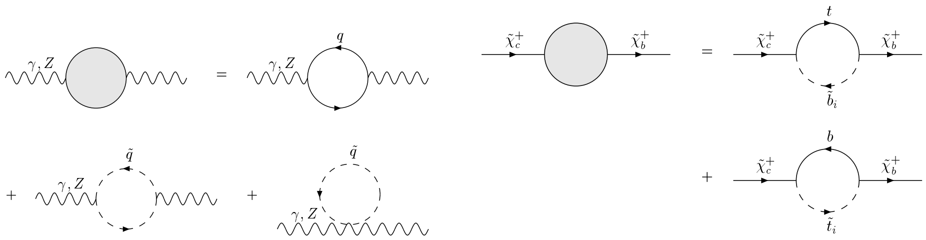

Figure D.3: (left) Top and bottom quark and squark contributions to the unrenormalized Z and γ self-energies and to the $Z-\gamma$ mixing. (right) Feynman diagrams contributing to the unrenormalized chargino two–point functions (self–energies and mixing). [121]

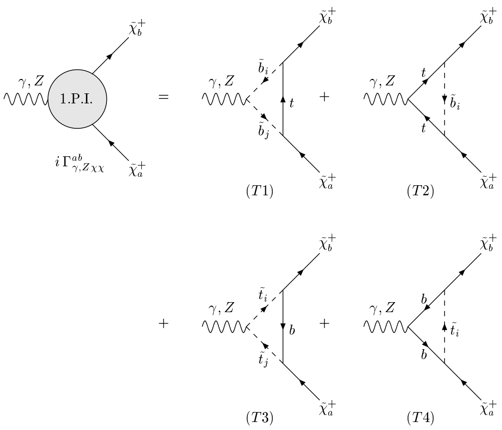

Figure D.4: Unrenormalized one–particle irreducible triangular diagrams contributing to renormalization of the $Z\tilde{\chi}^+\tilde{\chi}^-$ and $\gamma\tilde{\chi}^+\tilde{\chi}^-$ vertices. [121]

It has to be emphasized that squarks/quarks contributions to the $e^-\tilde{\nu}_e\tilde{\chi}^+$ vertex consist only of charginos self–energies and mixing terms (Fig. D.3(right)) and are hence weak compared to those related to the $Z\tilde{\chi}^+\tilde{\chi}^-$ and $\gamma\tilde{\chi}^+\tilde{\chi}^-$ vertices.

The corrections were parametrized by the squark soft masses which were taken degenerated $M_Q = M_U = M_D$, and by the trilinear soft mass parameters $A \equiv A_U = A_D$ also taken degenerate. This choice was done at the weak scale and was made for simplicity and similar results are expected when releasing the degeneracies. This computation shows that for centre–of–mass energies relevant for LEP2, the radiative corrections to the production cross-section of a pair of $\tilde{\chi}_1^{\pm}$ grow logarithmically with the squarks soft mass. To illustrate this effect, Fig. D.5 show the one-loop and tree-level chargino production cross-section as a function of the $\tilde{\chi}_1^{\pm}$ mass and $\tan\beta$ for $\sqrt{s}$ = 192 GeV assuming a negative μ value. From Fig. D.5(left) we observe that the quantum corrections on

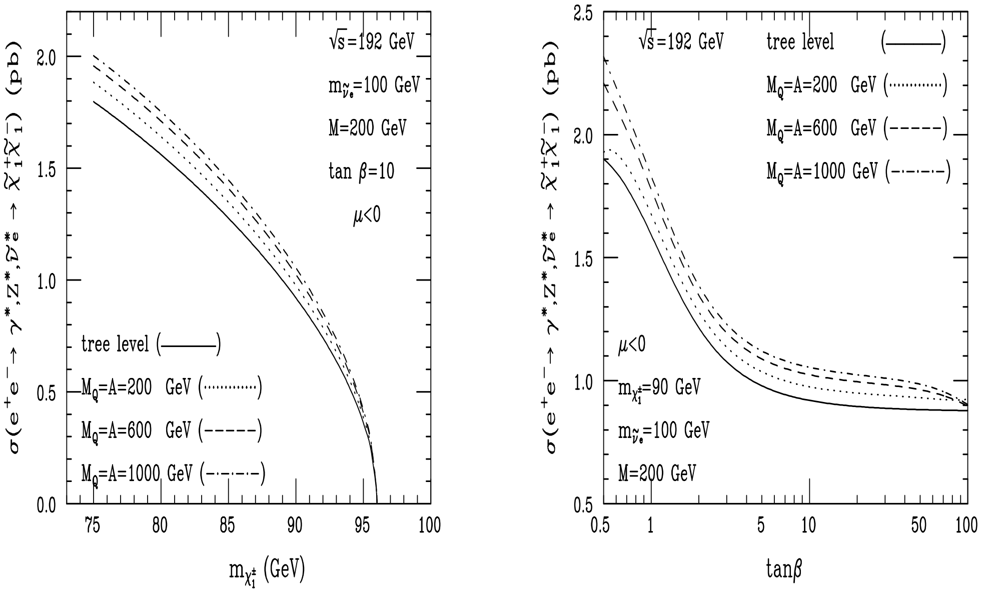

Figure D.5: One–loop and tree-level chargino production cross section as a function of the $\tilde{\chi}_1^{\pm}$ mass (left) and $\tan\beta$ (right), for $\sqrt{s}$ = 192 GeV. [121]

the cross-section grow with the chargino mass from 11% for $M_{\tilde{\chi}_1^{\pm}}$ = 75 GeV$/c^2$ to 15% for $M_{\tilde{\chi}_1^{\pm}}$ = 95 GeV$/c^2$ when $M_Q = A = 1\ TeV$ and that the corrections decrease with a smaller squark mass parameter. Fig. D.5(right) shows the logarithmic growth of the quantum corrections in almost all the $\tan\beta$ range expect if $\tan\beta < 1$ and $\tan\beta > 30$ where there is not a single scale for the squark masses due to the non diagonal terms in the third squark family mass matrix. In both plots, the value of μ is not constant along the curves because it is fixed to achieve the required chargino mass.

From the experimentalist point of view, since in all the cases, the contributions are positive, using tree-level cross-sections in all the exclusion procedures will yield conservative results. This choice was made in the present work.

Appendix E

Data–MC comparison after the common selections

In this appendix, the distributions of the main variables used in the chargino analysis for the data collected in the year 2000 (dots) and background (histogram) events are shown. This appendix contains the distributions for each topology after the *common* selections, used for all the different ΔM regions.

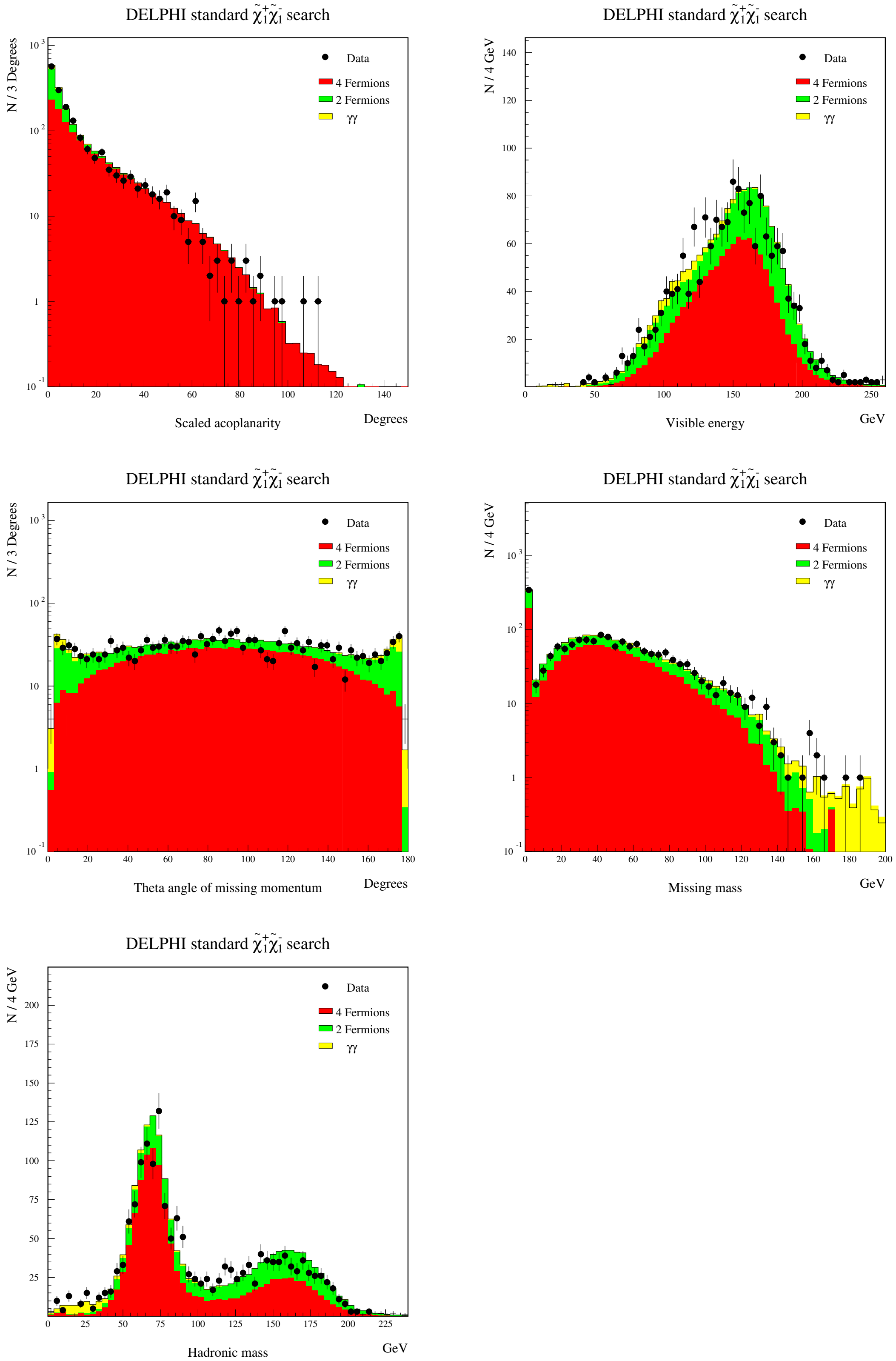

Figure E.1: Data–MC comparison at the *common* selection level for the $jj\ell$ topology is shown for the data sample of year 2000 with the TPC sector 6.

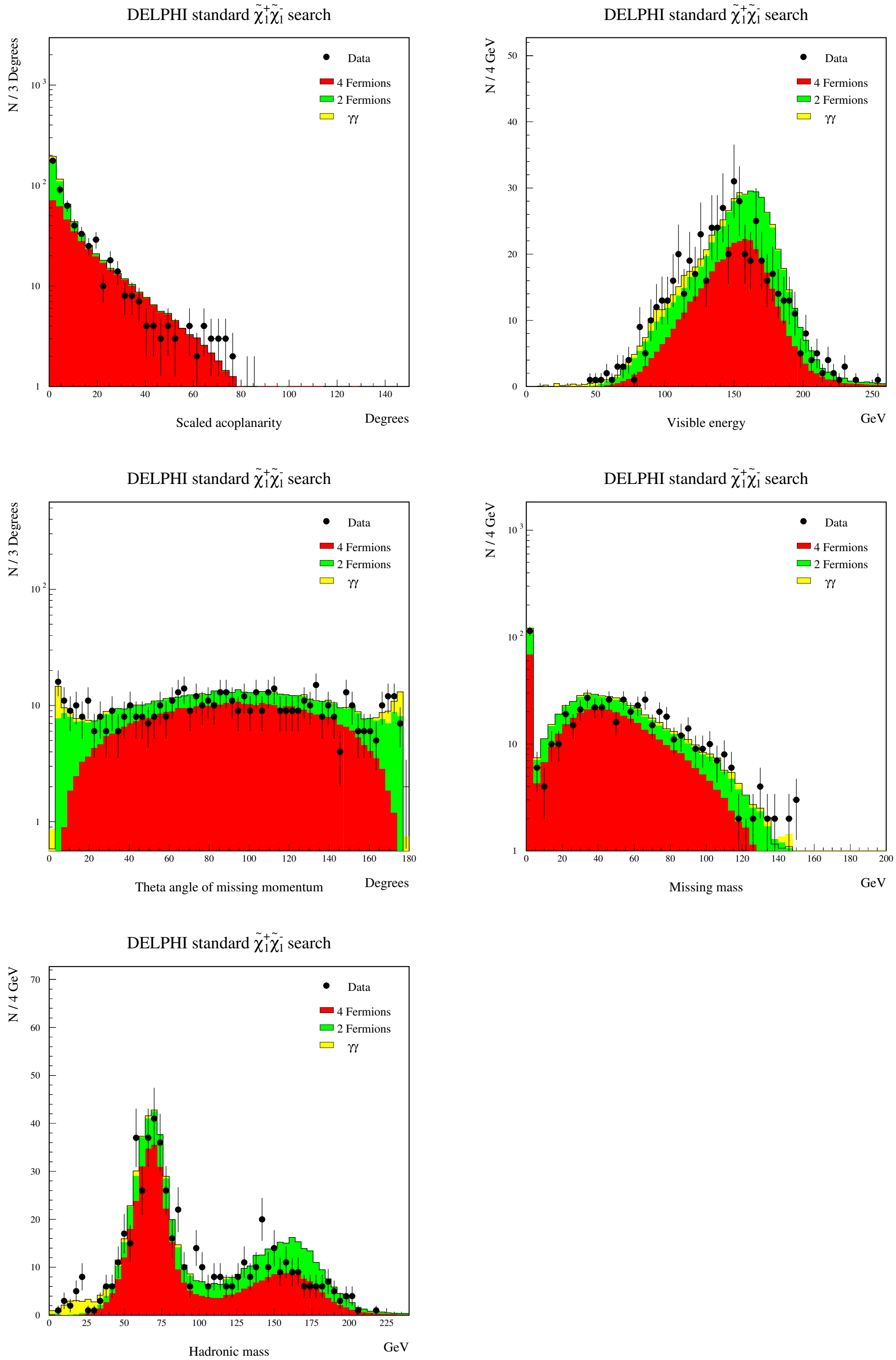

Figure E.2: Data–MC comparison at the *common* selection level for the $jj\ell$ topology is shown for the data sample of year 2000 without the TPC sector 6.

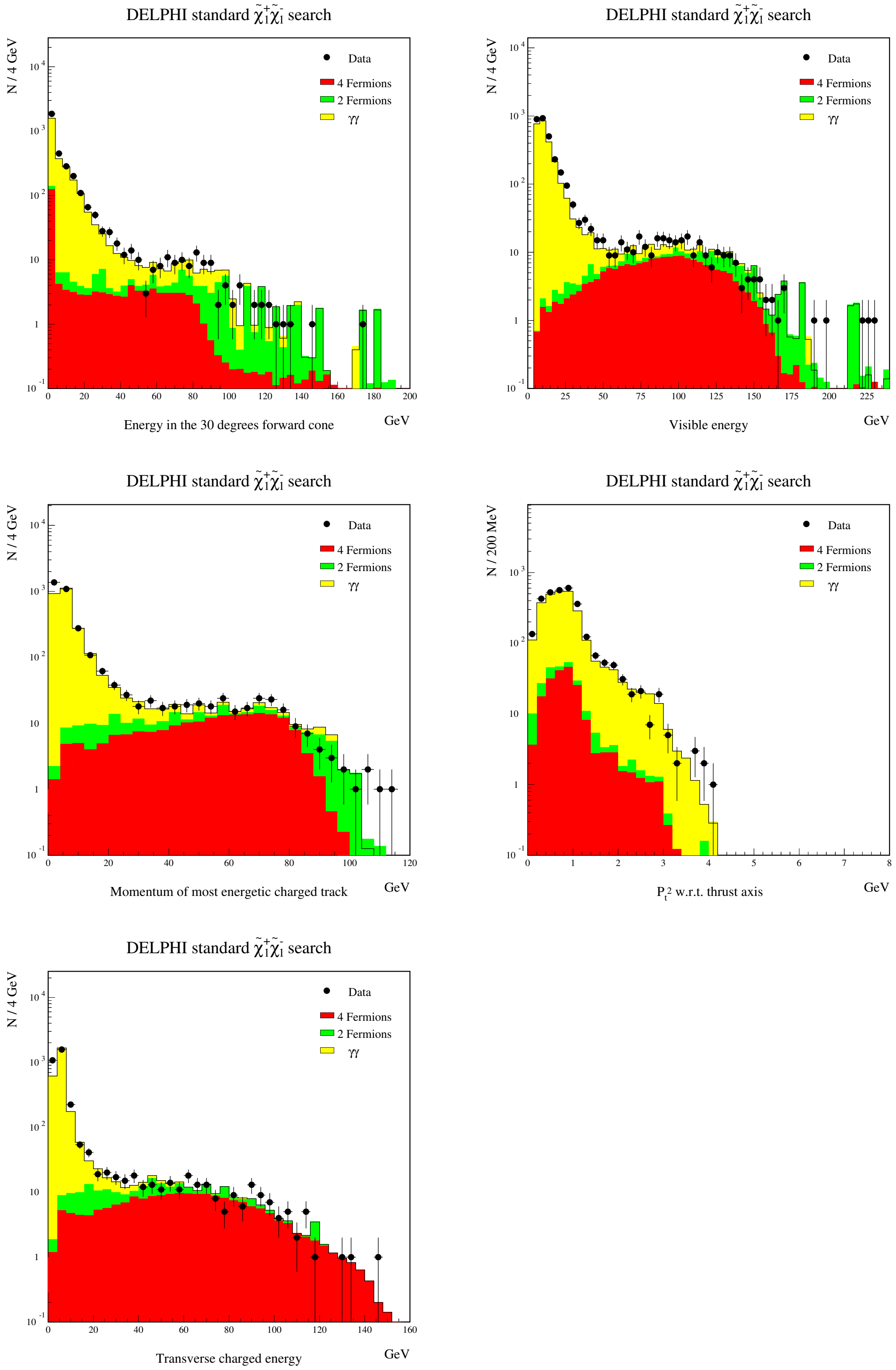

Figure E.3: Data–MC comparison at the *common* selection level for the $\ell\ell$ topology is shown for the data sample of year 2000 with the TPC sector 6.

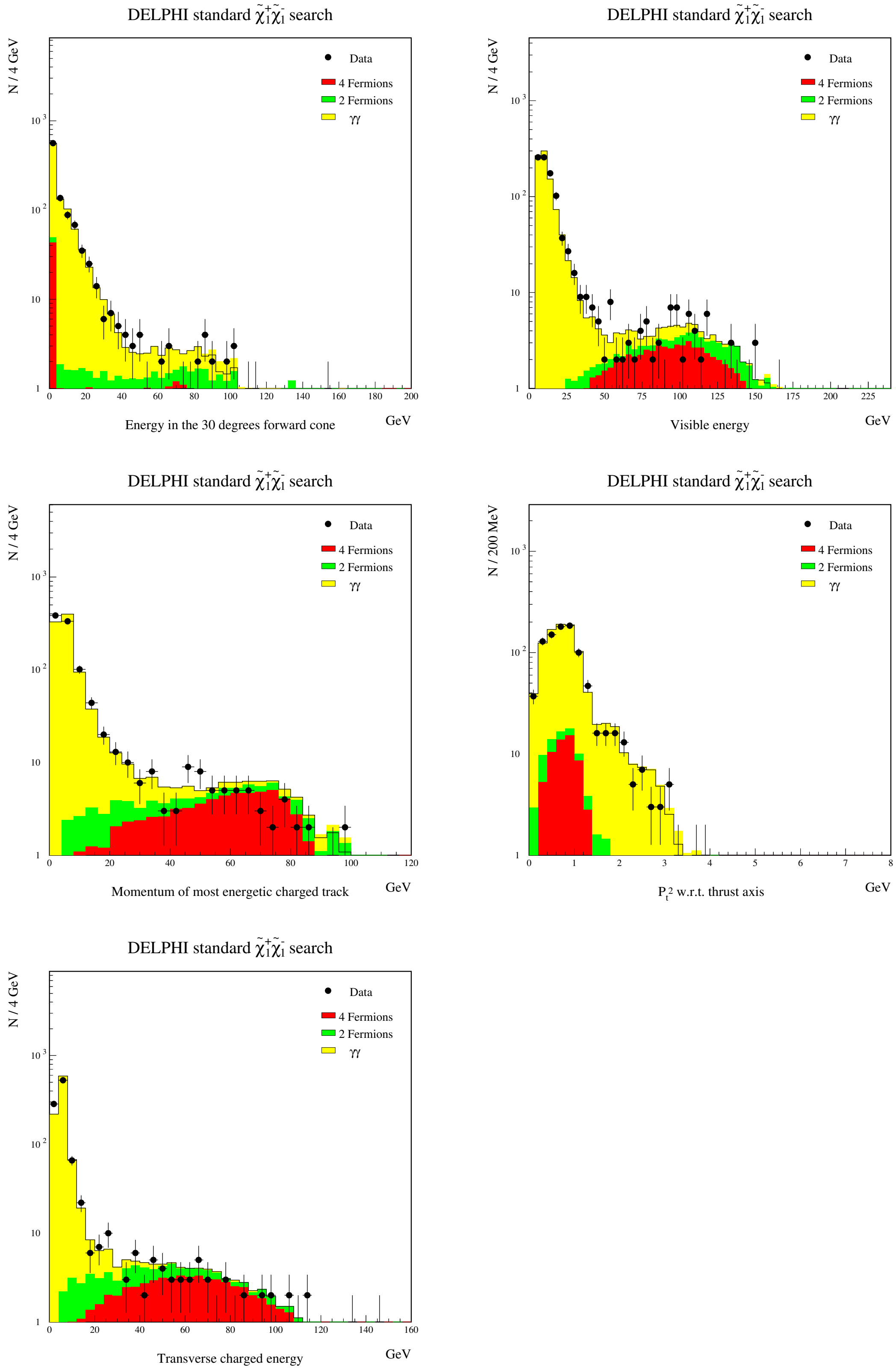

Figure E.4: Data–MC comparison at the *common* selection level for the $\ell\ell$ topology is shown for the data sample of year 2000 without the TPC sector 6.

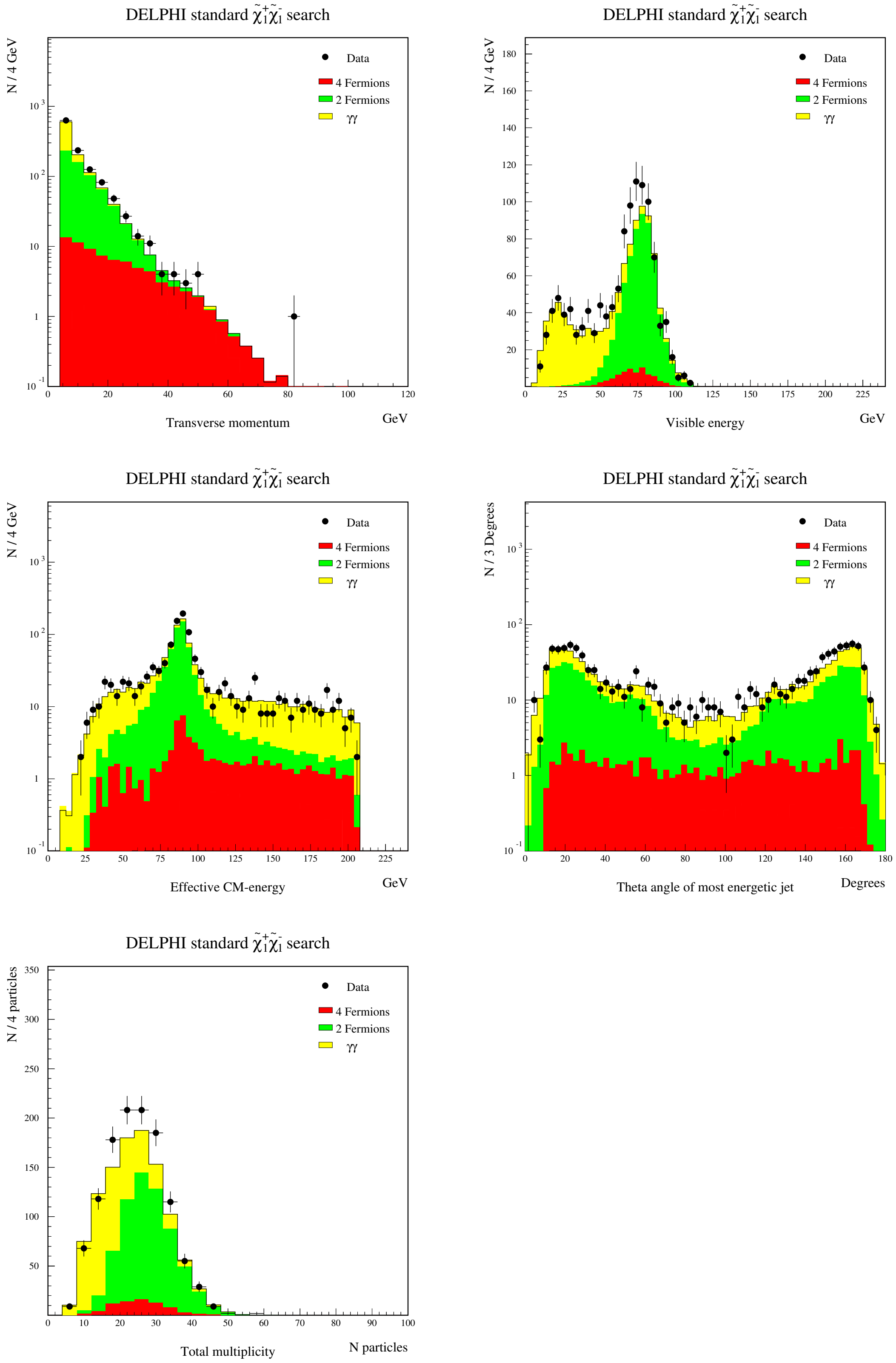

Figure E.5: Data–MC comparison at the *common* selection level for the *jets* topology is shown for the data sample of year 2000 with the TPC sector 6.

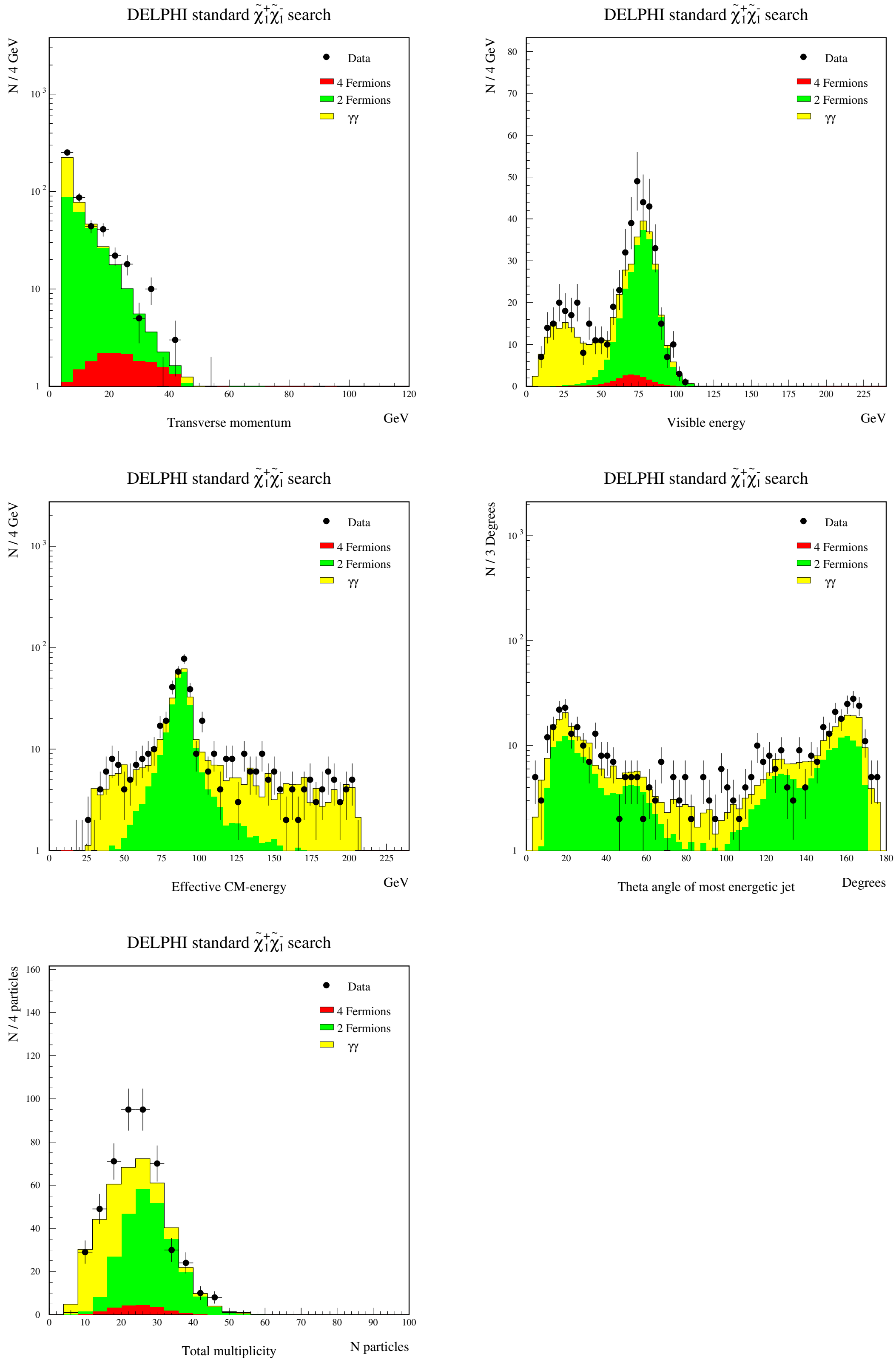

Figure E.6: Data–MC comparison at the *common* selection level for the *jets* topology is shown for the data sample of year 2000 without the TPC sector 6.

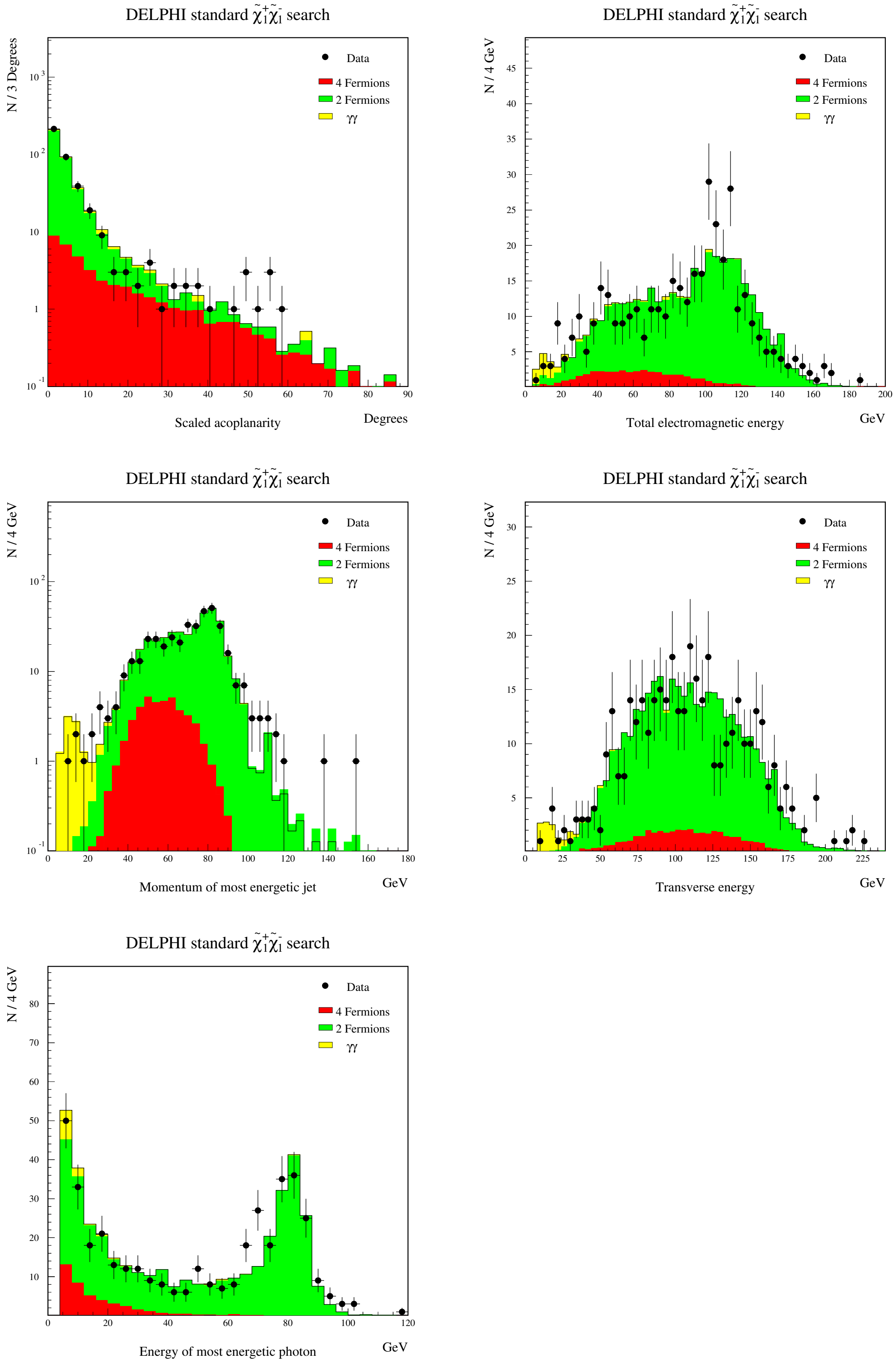

Figure E.7: Data–MC comparison at the *common* selection level for the *radiative* topology is shown for the data sample of year 2000 with the TPC sector 6.

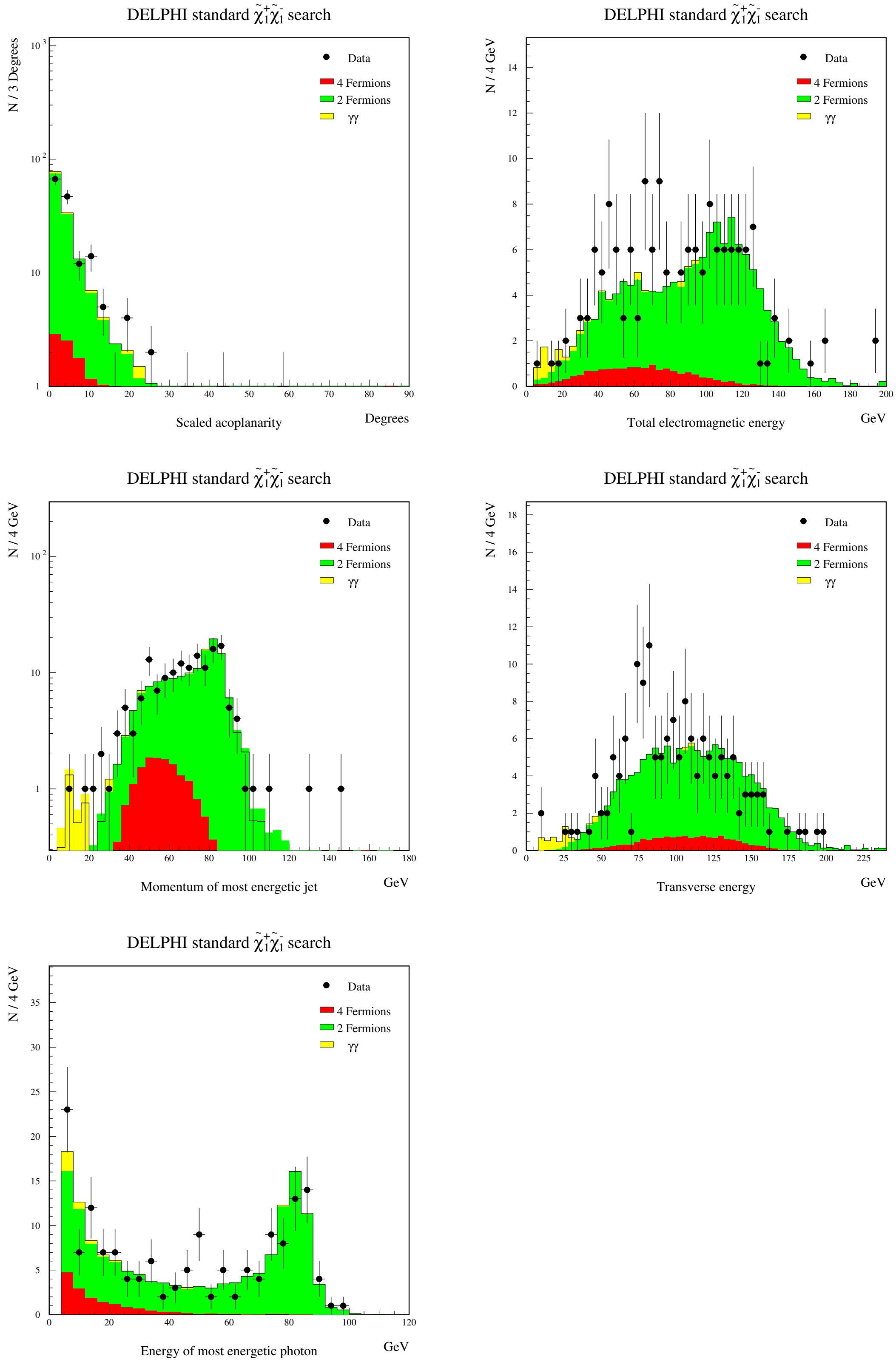

Figure E.8: Data–MC comparison at the *common* selection level for the *radiative* topology is shown for the data sample of year 2000 without the TPC sector 6.

Appendix F

Data–MC comparison at pre- and final selection levels

In this appendix, the distributions of the main variables used in the chargino analysis for the data collected in the year 2000 (dots) and background (histogram) events are shown. This appendix contains the distributions from each ΔM region and topology after applying the respective pre-selection and final-selection criteria.

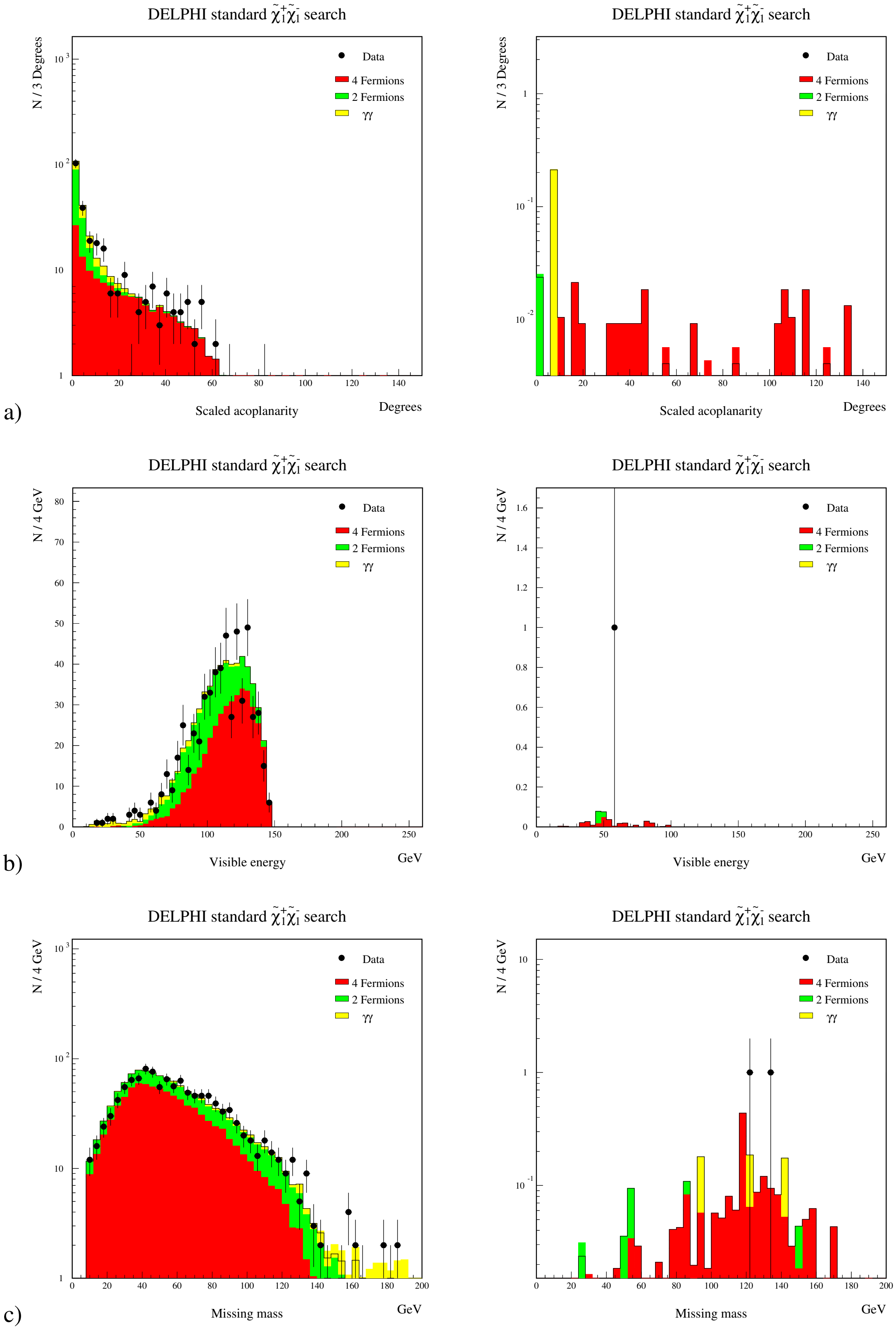

Figure F.1: Data–MC comparison at the preselection and final level for the $jj\ell$ topology. The three cases correspond to the ΔM regions, a) $3 \le \Delta M < 25$ GeV/c^2, b) $25 \le \Delta M < 35$ GeV/c^2, c) $35 \le \Delta M < 50$ GeV/c^2, with the data from year 2000 with TPC sector 6.

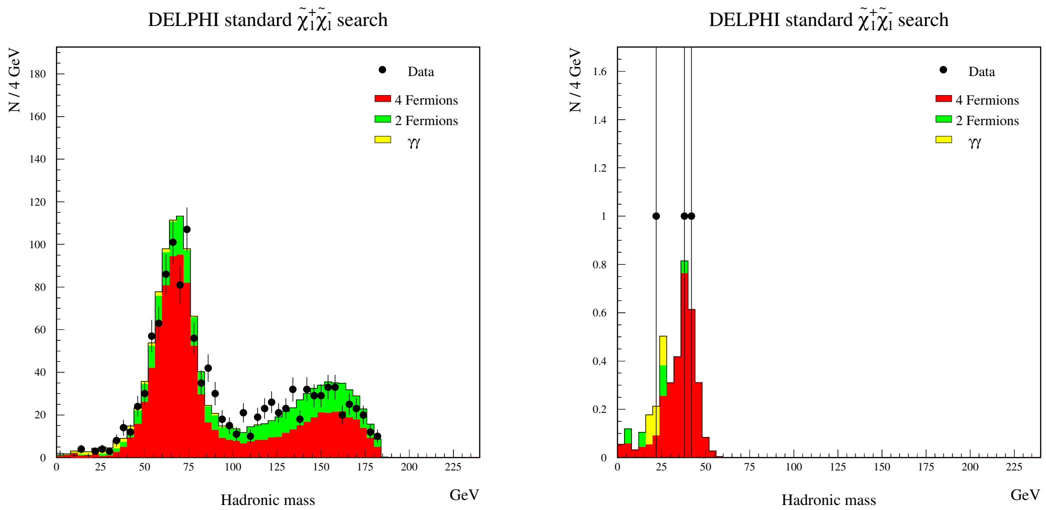

d)

Figure F.2: Data–MC comparison at the preselection level for the $jj\ell$ topology. The data from year 2000 with TPC sector 6 is shown from the region, d) 50 $\mathrm{GeV}/c^2 \leq \Delta M$

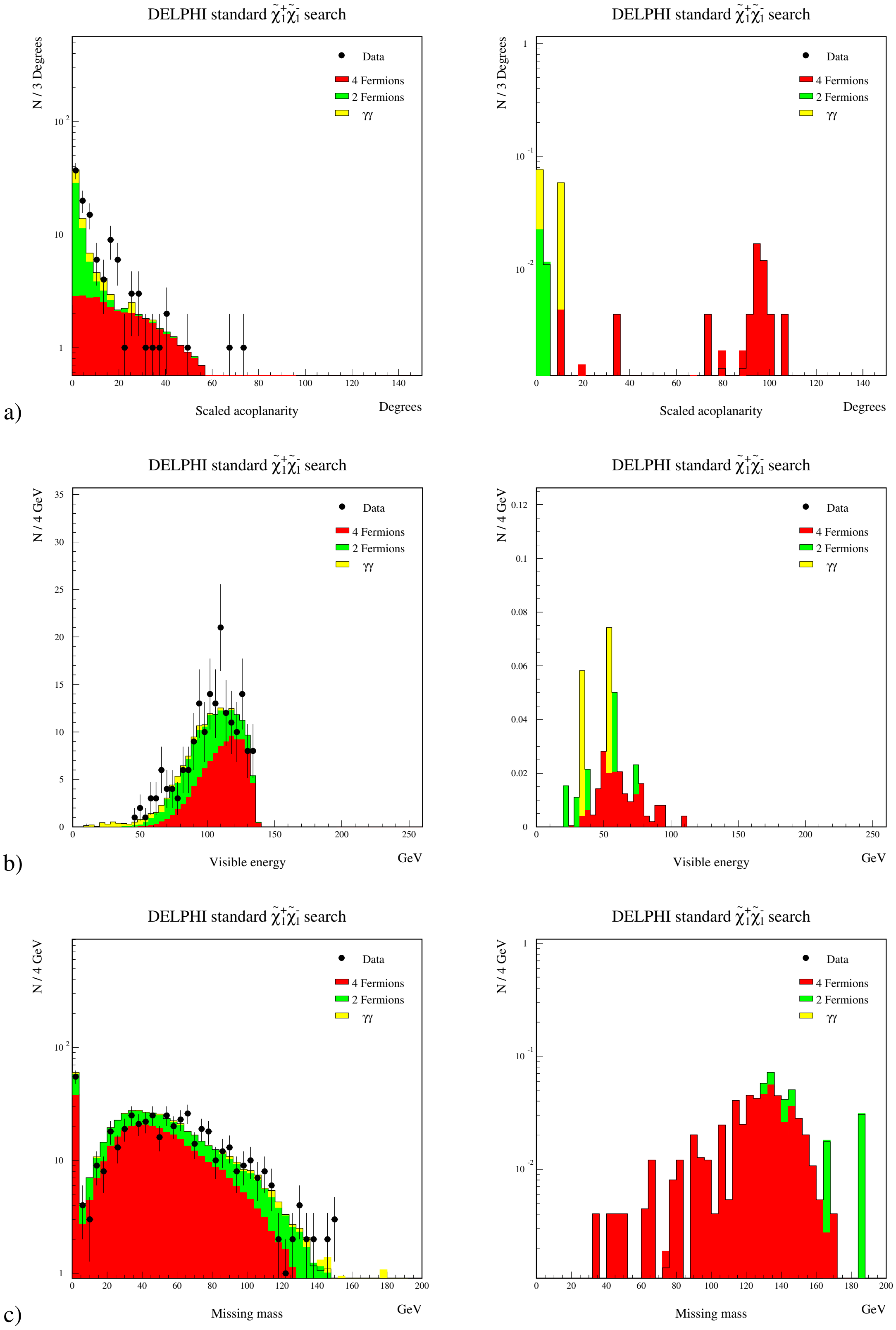

Figure F.3: Data–MC comparison at the preselection level for the $jj\ell$ topology. The three cases correspond to the ΔM regions, a) $3 \leq \Delta M < 25$ GeV$/c^2$, b) $25 \leq \Delta M < 35$ GeV$/c^2$, c) $35 \leq \Delta M < 50$ GeV$/c^2$, with the data from year 2000 without TPC sector 6.

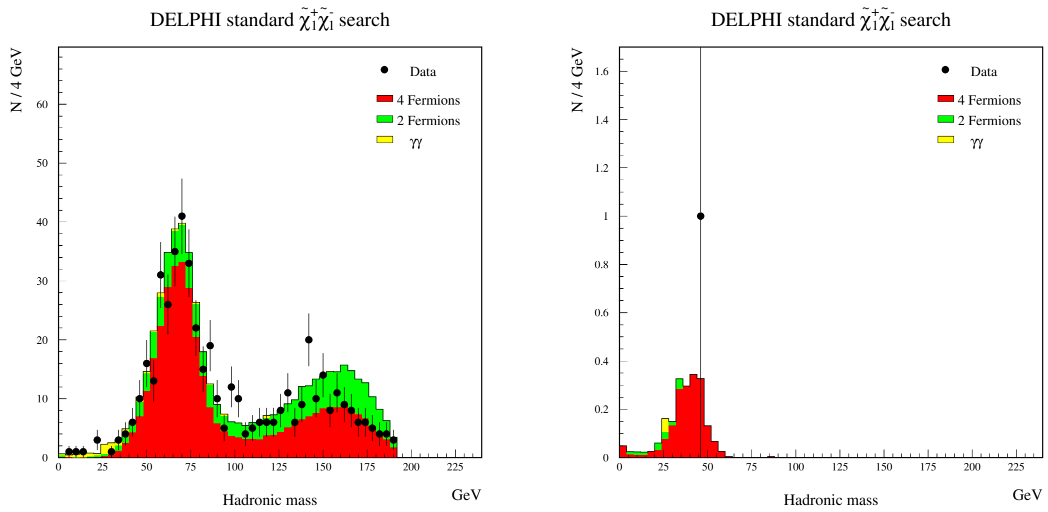

d)

Figure F.4: Data–MC comparison at the preselection level for the $jj\ell$ topology. The data from year 2000 without TPC sector 6 is shown from the region, d) 50 $\mathrm{GeV}/c^2 \leq \Delta M$

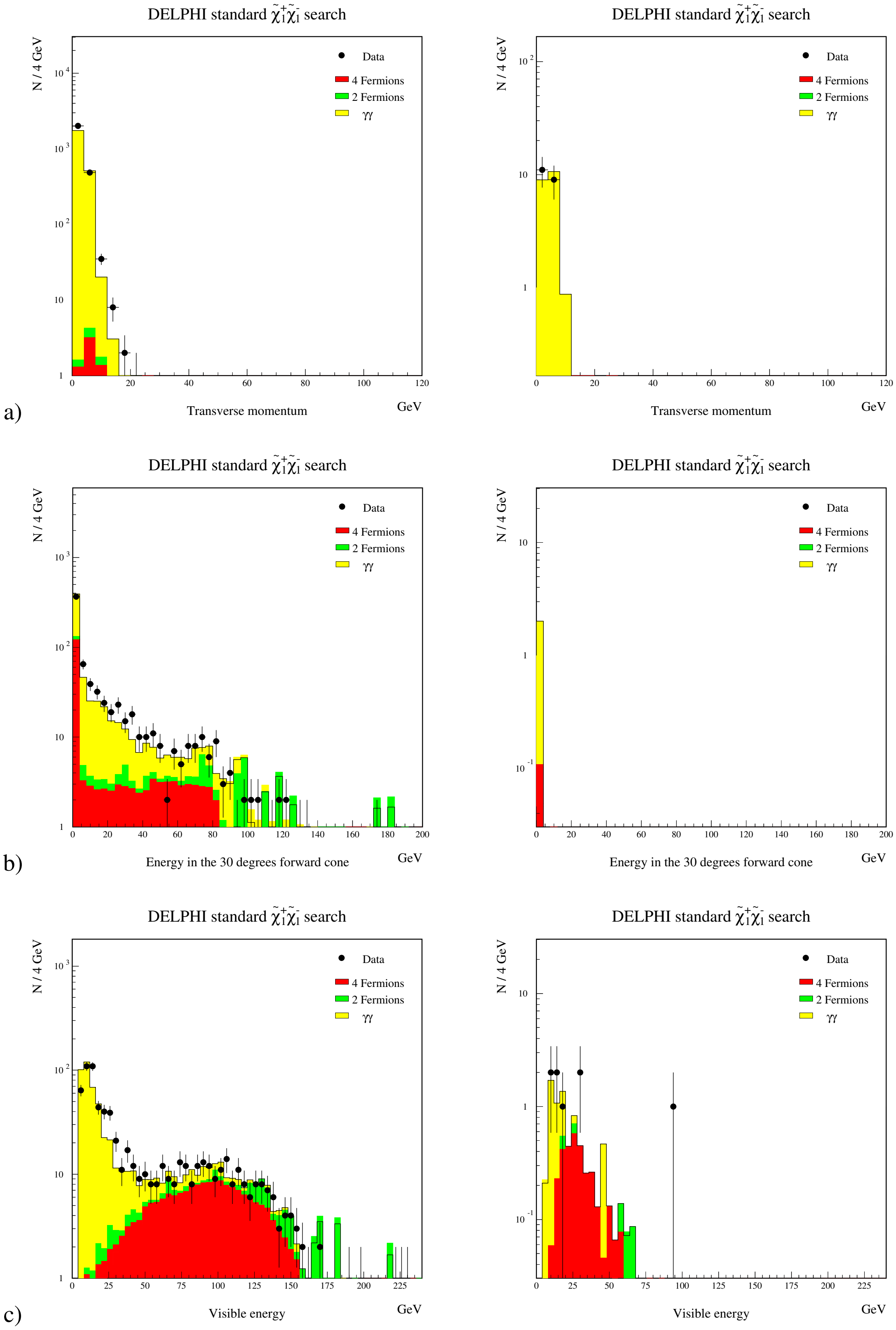

Figure F.5: Data–MC comparison at the preselection level for the $\ell\ell$ topology. The three cases correspond to the ΔM regions, a) $3 \leq \Delta M < 5$ GeV$/c^2$, b) $5 \leq \Delta M < 10$ GeV$/c^2$, c) $10 \leq \Delta M < 25$ GeV$/c^2$, with the data from year 2000 with TPC sector 6.

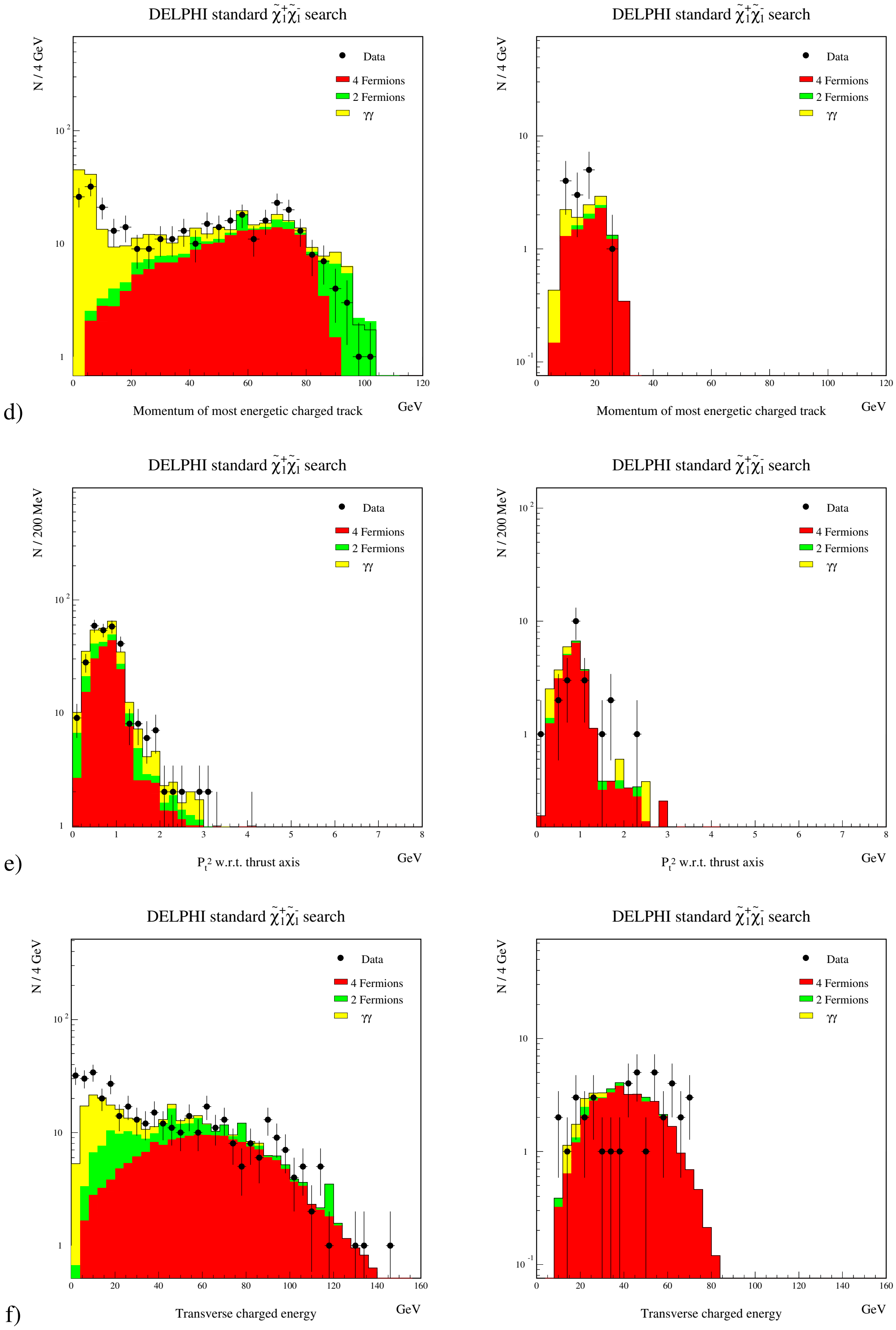

Figure F.6: Data–MC comparison at the preselection level for the $\ell\ell$ topology. The three cases correspond to the ΔM regions, d) $25 \leq \Delta M < 35$ GeV$/c^2$, e) $35 \leq \Delta M < 50$ GeV$/c^2$, f) 50 GeV$/c^2 \leq \Delta M$ with the data from year 2000 with TPC sector 6.

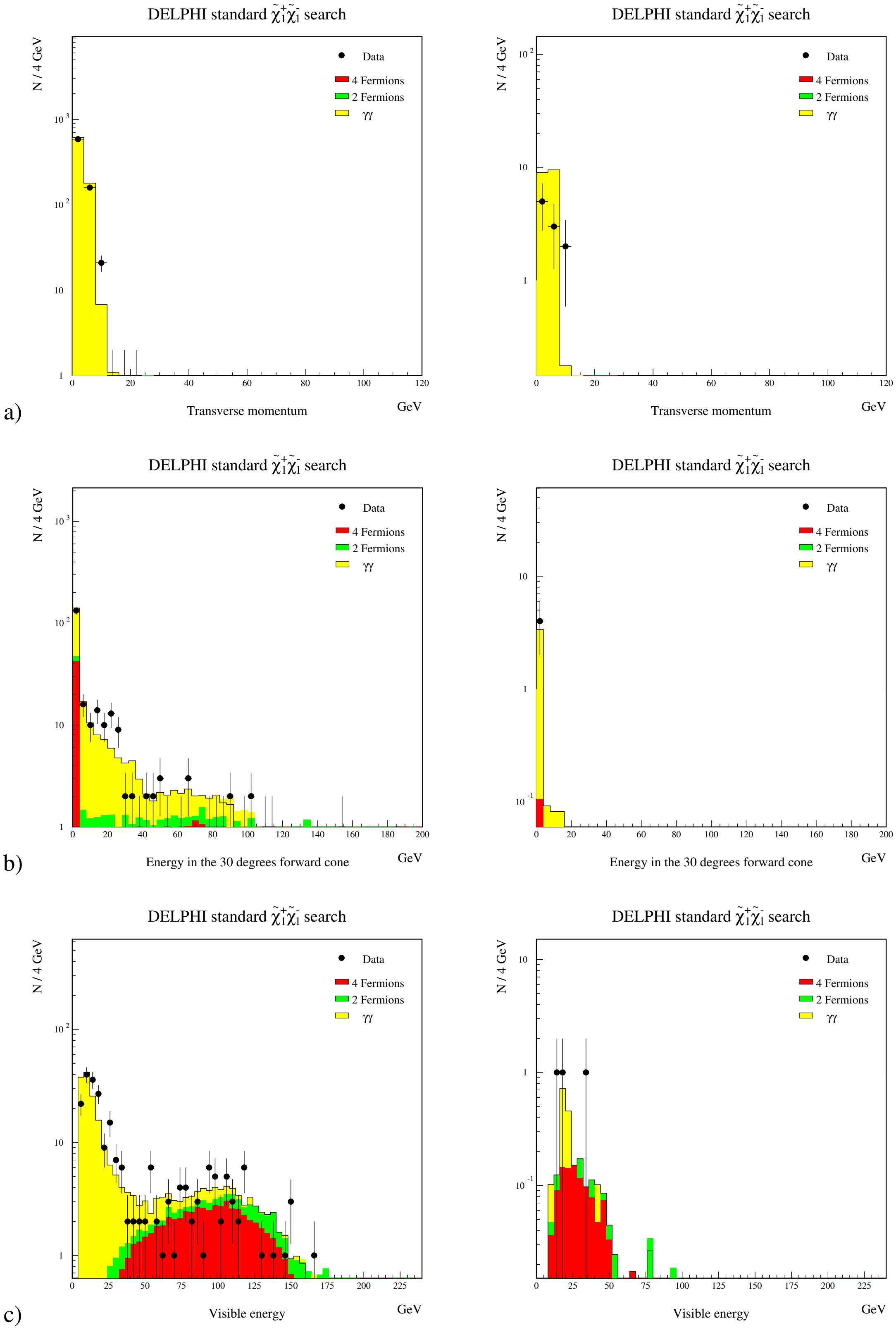

Figure F.7: Data–MC comparison at the preselection level for the $\ell\ell$ topology. The three cases correspond to the ΔM regions, a) $3 \leq \Delta M < 5$ GeV$/c^2$, b) $5 \leq \Delta M < 10$ GeV$/c^2$, c) $10 \leq \Delta M < 25$ GeV$/c^2$, with the data from year 2000 without TPC sector 6.

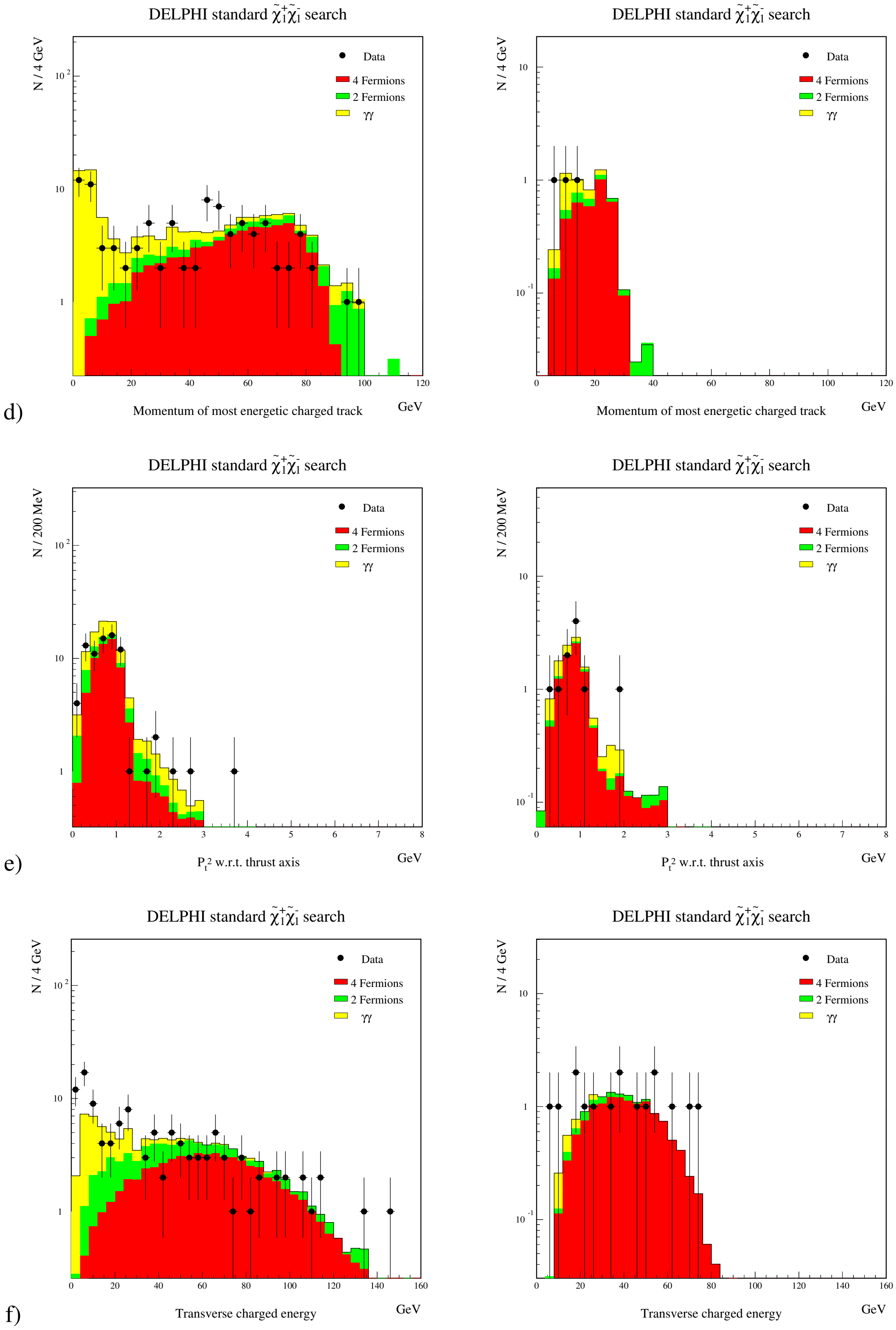

Figure F.8: Data–MC comparison at the preselection level for the $\ell\ell$ topology. The three cases correspond to the ΔM regions, d) $25 \leq \Delta M < 35$ GeV$/c^2$, e) $35 \leq \Delta M < 50$ GeV$/c^2$, f) 50 GeV$/c^2 \leq \Delta M$ with the data from year 2000 without TPC sector 6.

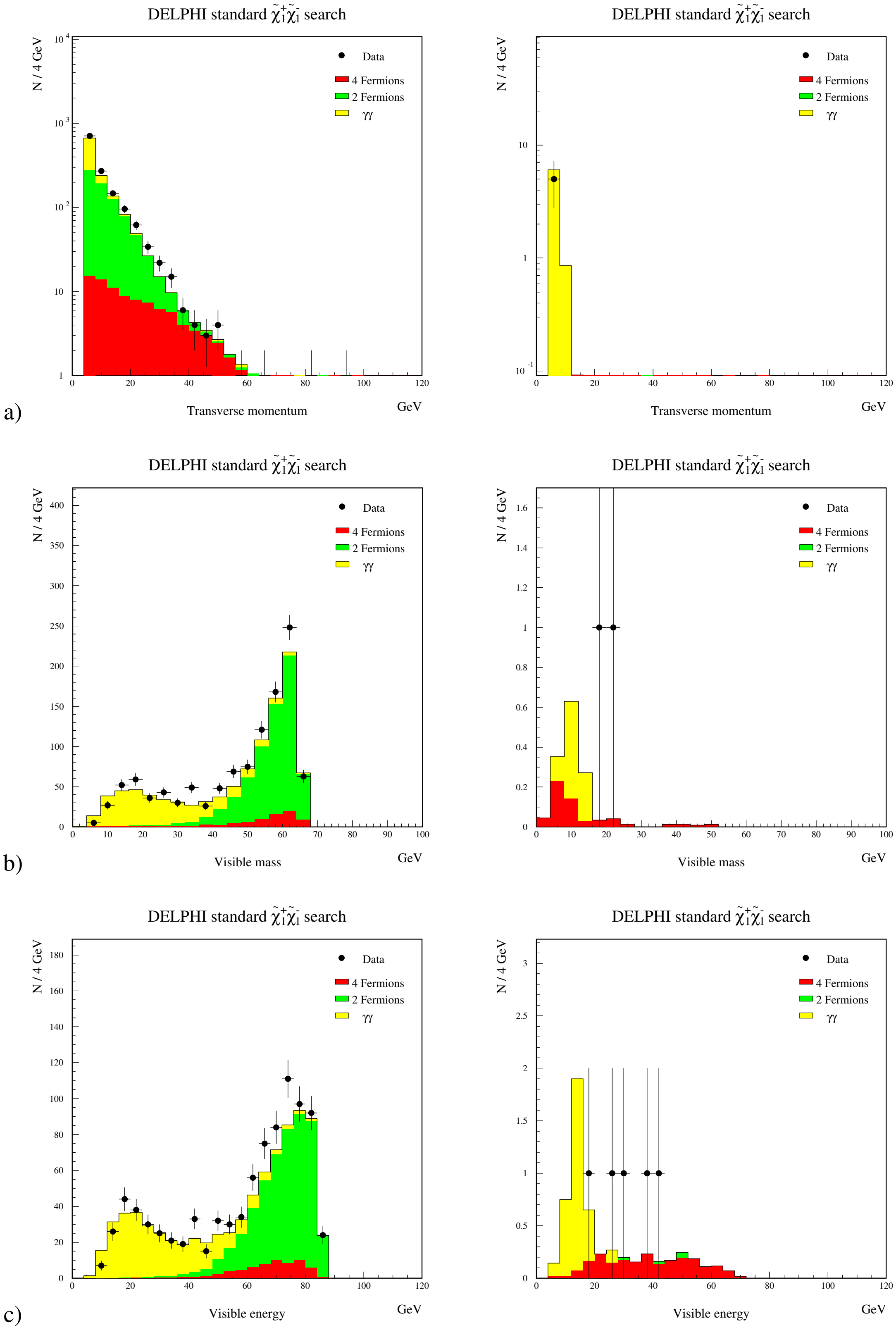

Figure F.9: Data–MC comparison at the preselection level for the *jets* topology. The three cases correspond to the ΔM regions, a) $3 \leq \Delta M < 5$ GeV$/c^2$, b) $5 \leq \Delta M < 10$ GeV$/c^2$, c) $10 \leq \Delta M < 25$ GeV$/c^2$, with the data from year 2000 with TPC sector 6.

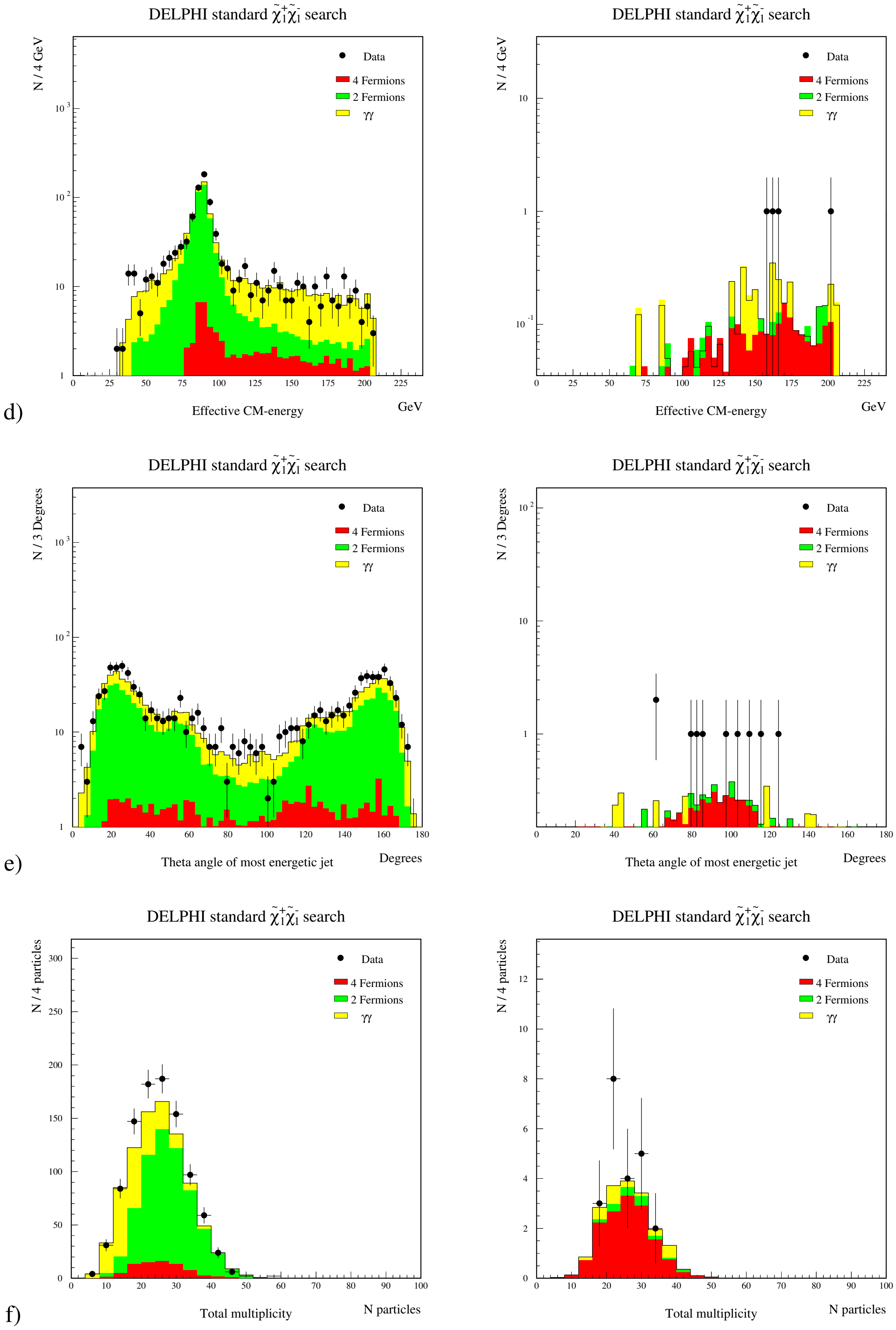

Figure F.10: Data–MC comparison at the preselection level for the *jets* topology. The three cases correspond to the ΔM regions, a d) $25 \leq \Delta M < 35$ GeV$/c^2$, e) $35 \leq \Delta M < 50$ GeV$/c^2$, f) 50 GeV$/c^2 \leq \Delta M$ with the data from year 2000 with TPC sector 6.

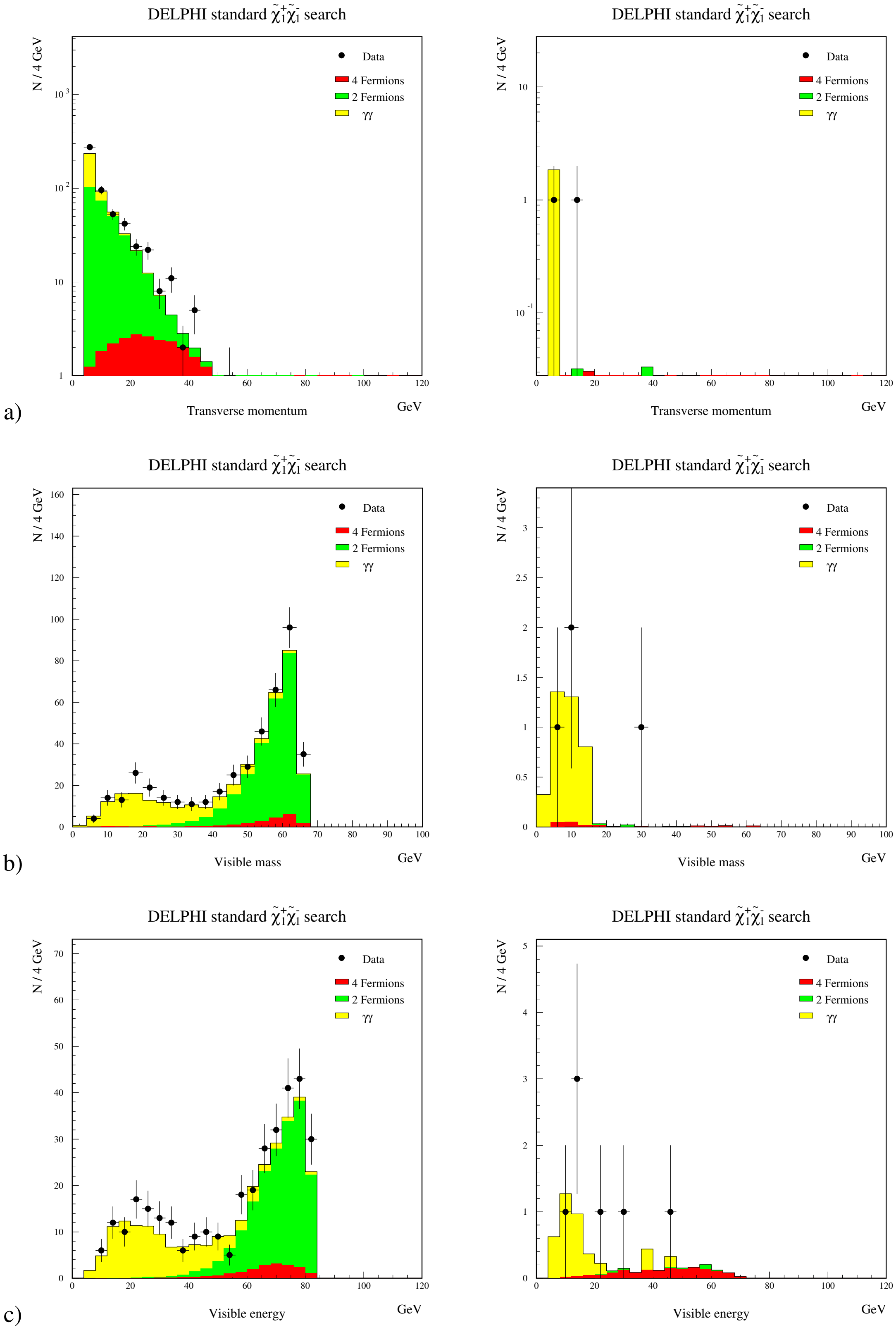

Figure F.11: Data–MC comparison at the preselection level for the *jets* topology. The three cases correspond to the ΔM regions, a) $3 \leq \Delta M < 5$ GeV$/c^2$, b) $5 \leq \Delta M < 10$ GeV$/c^2$, c) $10 \leq \Delta M < 25$ GeV$/c^2$, with the data from year 2000 without TPC sector 6.

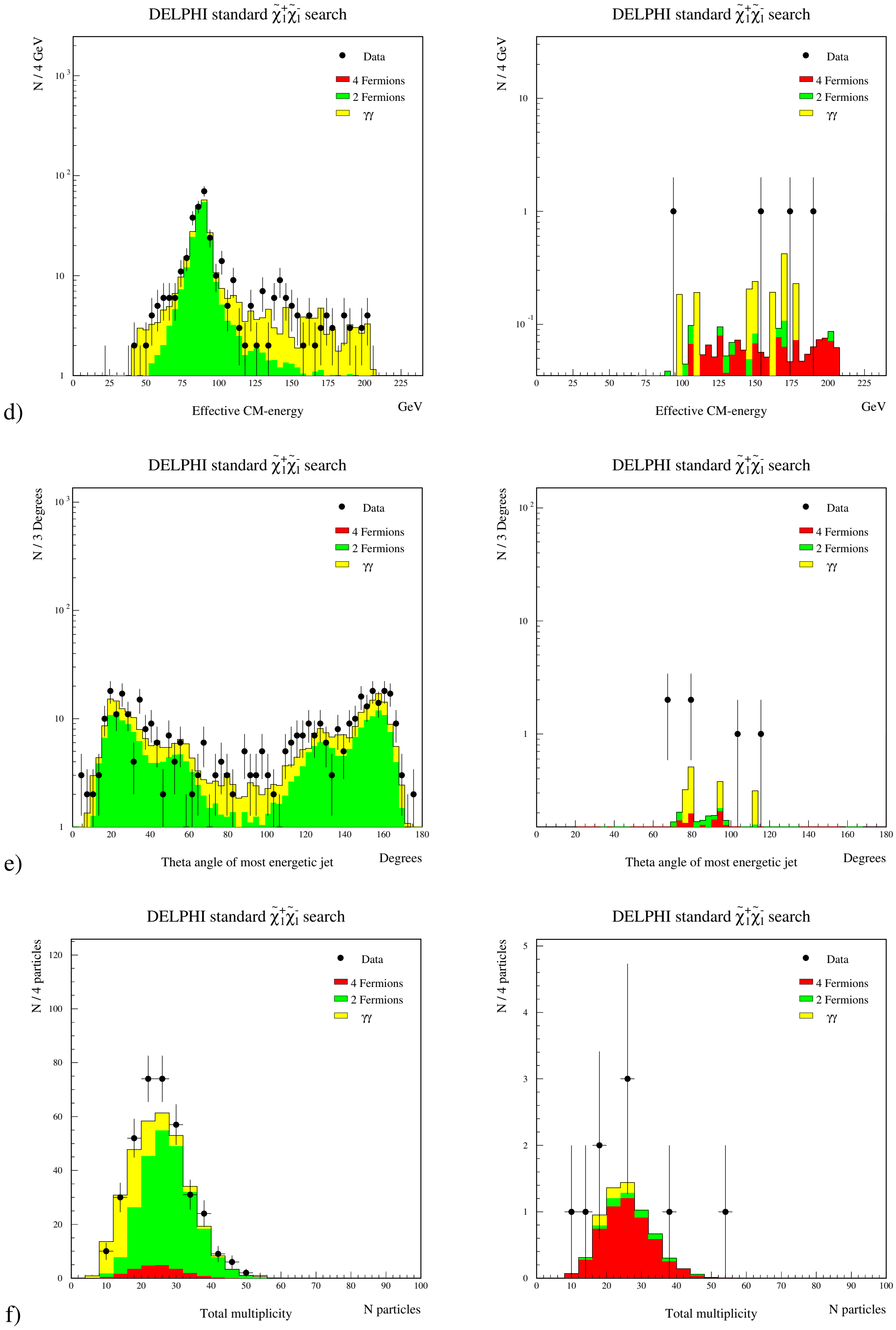

Figure F.12: Data–MC comparison at the preselection level for the *jets* topology. The three cases correspond to the ΔM regions, d) $25 \leq \Delta M < 35$ GeV$/c^2$, e) $35 \leq \Delta M < 50$ GeV$/c^2$, f) 50 GeV$/c^2 \leq \Delta M$ with the data from year 2000 without TPC sector 6.

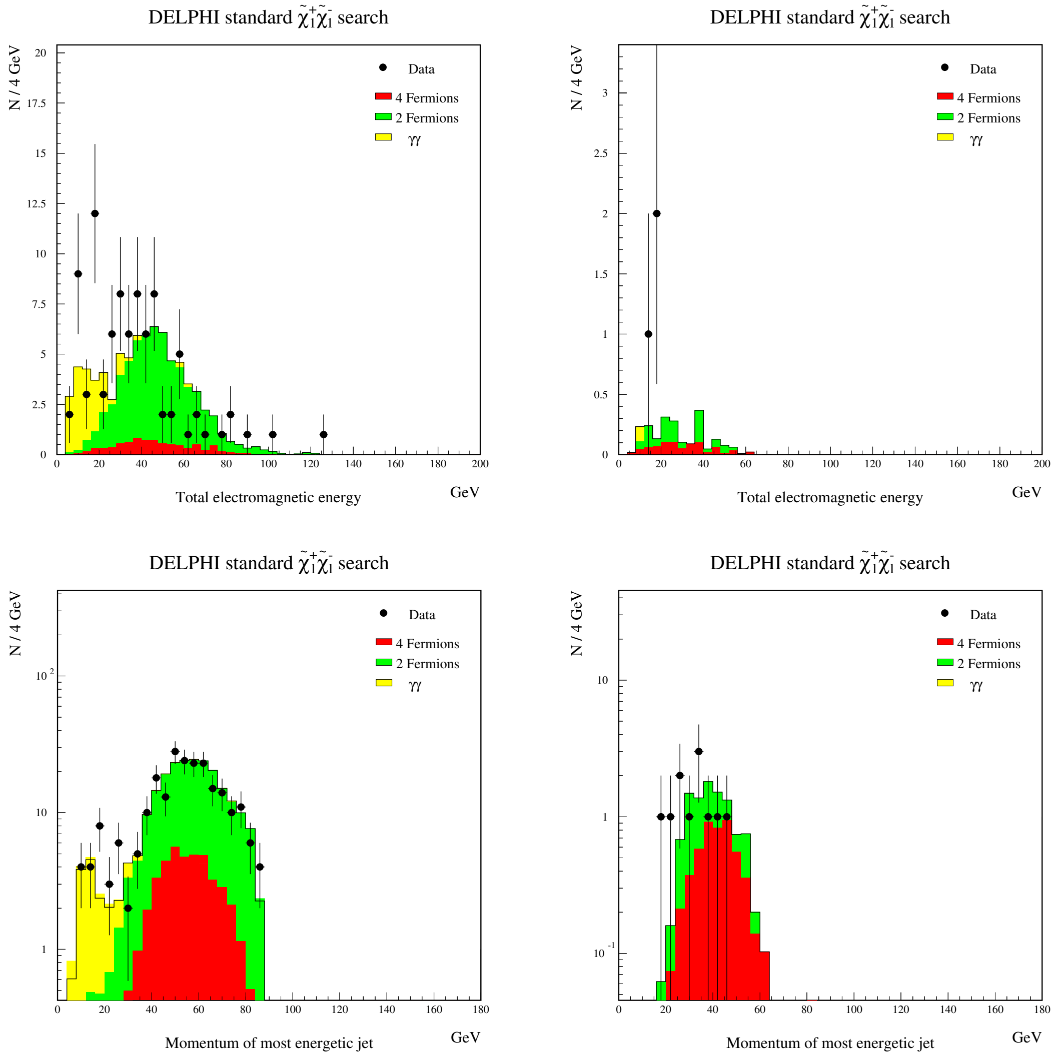

a)

b)

Figure F.13: Data–MC comparison at the preselection level for the radiative topology. The two cases correspond to the ΔM regions, a) $3 \leq \Delta M < 35$ GeV$/c^2$, b) 35 GeV$/c^2 \leq \Delta M$ with the data from year 2000 with TPC sector 6.

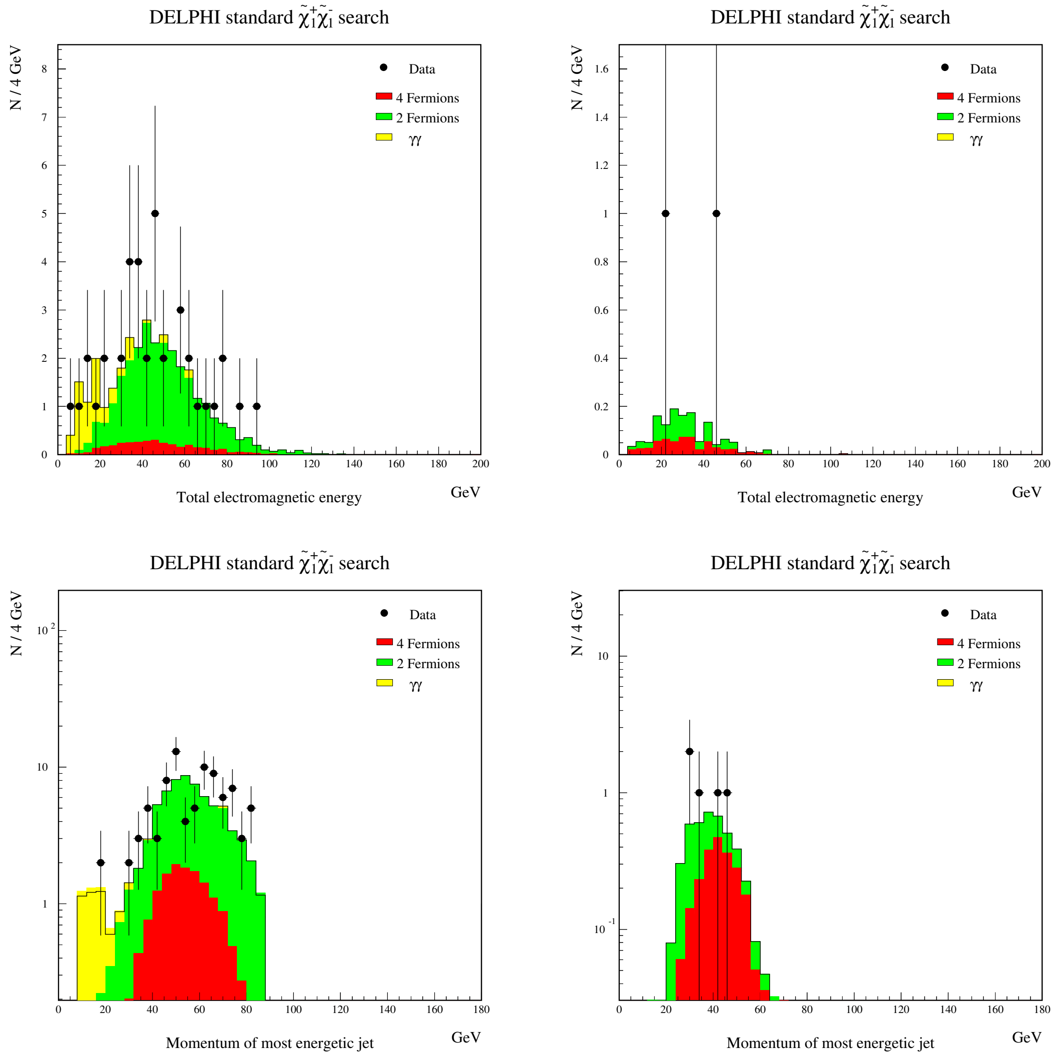

a)

b)

Figure F.14: Data–MC comparison at the preselection level for the radiative topology. The two cases correspond to the ΔM regions, a) $3 \leq \Delta M < 35$ GeV$/c^2$, b) 35 GeV$/c^2 \leq \Delta M$ with the data from year 2000 without TPC sector 6.

Appendix G

Data–MC comparison at the level of the Likelihood ratio cut

In this appendix, the distribution of the number of real data and background events that pass the likelihood ratio cut as a function of this likelihood ratio cut is shown for each ΔM region and topology. The errors in the bins are the square root of the corresponding number of events.

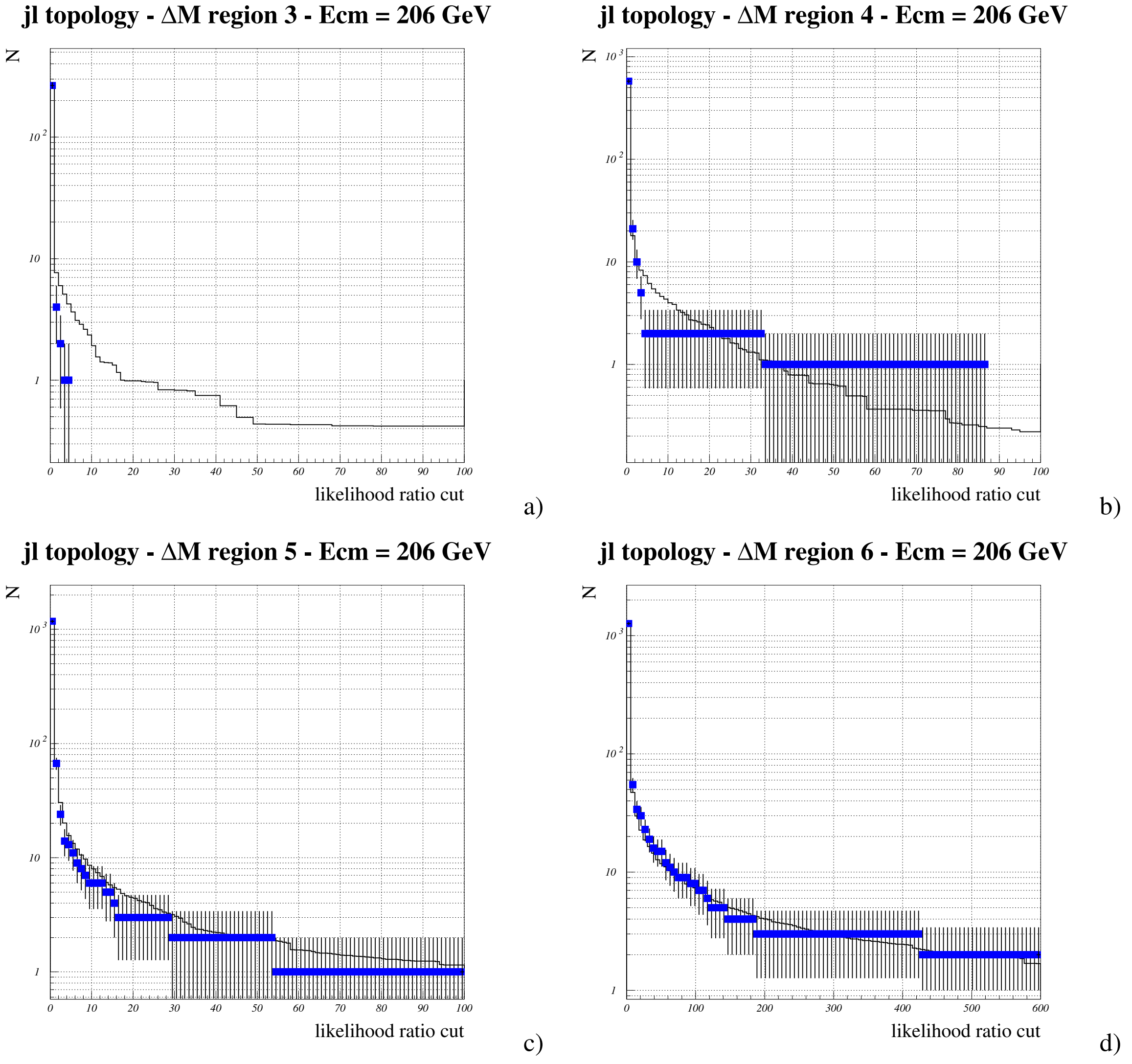

Figure G.1: Distributions of the number of real data (dots) and background events (histogram) as a function of the Likelihood Ratio cut for the $jj\ell$ topology: a) $3 \leq \Delta M < 25$ GeV$/c^2$, b) $25 \leq \Delta M < 35$ GeV$/c^2$, c) $35 \leq \Delta M < 50$ GeV$/c^2$, d) 50 GeV$/c^2 \leq \Delta M$. All plots show the data from year 2000 with TPC sector 6.

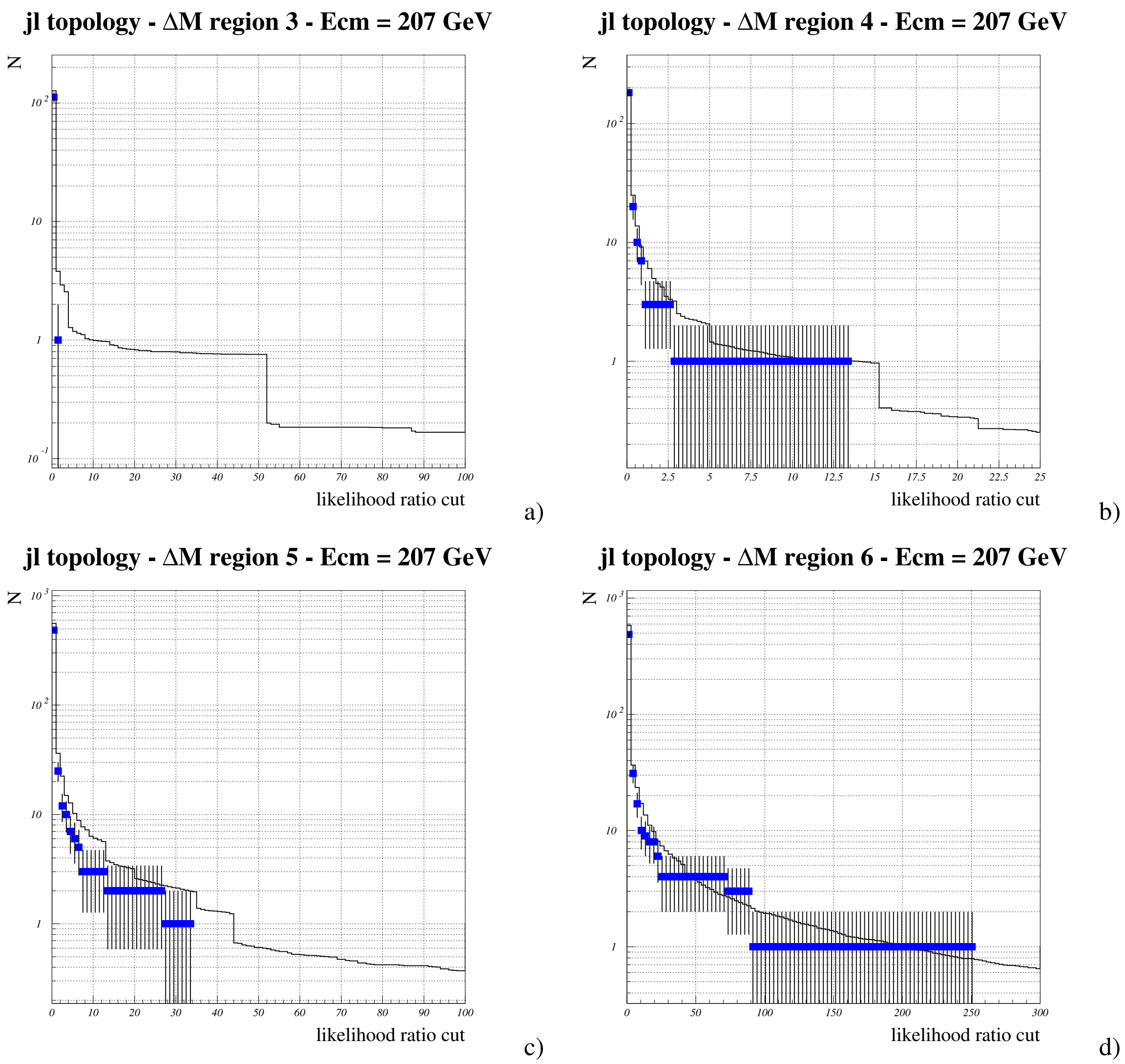

Figure G.2: Distributions of the number of real data (dots) and background events (histogram) as a function of the Likelihood Ratio cut for the $jj\ell$ topology: a) 3 $\leq \Delta M <$ 25 GeV/c^2, b) 25 $\leq \Delta M <$ 35 GeV/c^2, c) 35 $\leq \Delta M <$ 50 GeV/c^2, d) 50 $\mathrm{GeV}/c^2 \leq \Delta M$. All plots show the data from year 2000 without TPC sector 6.

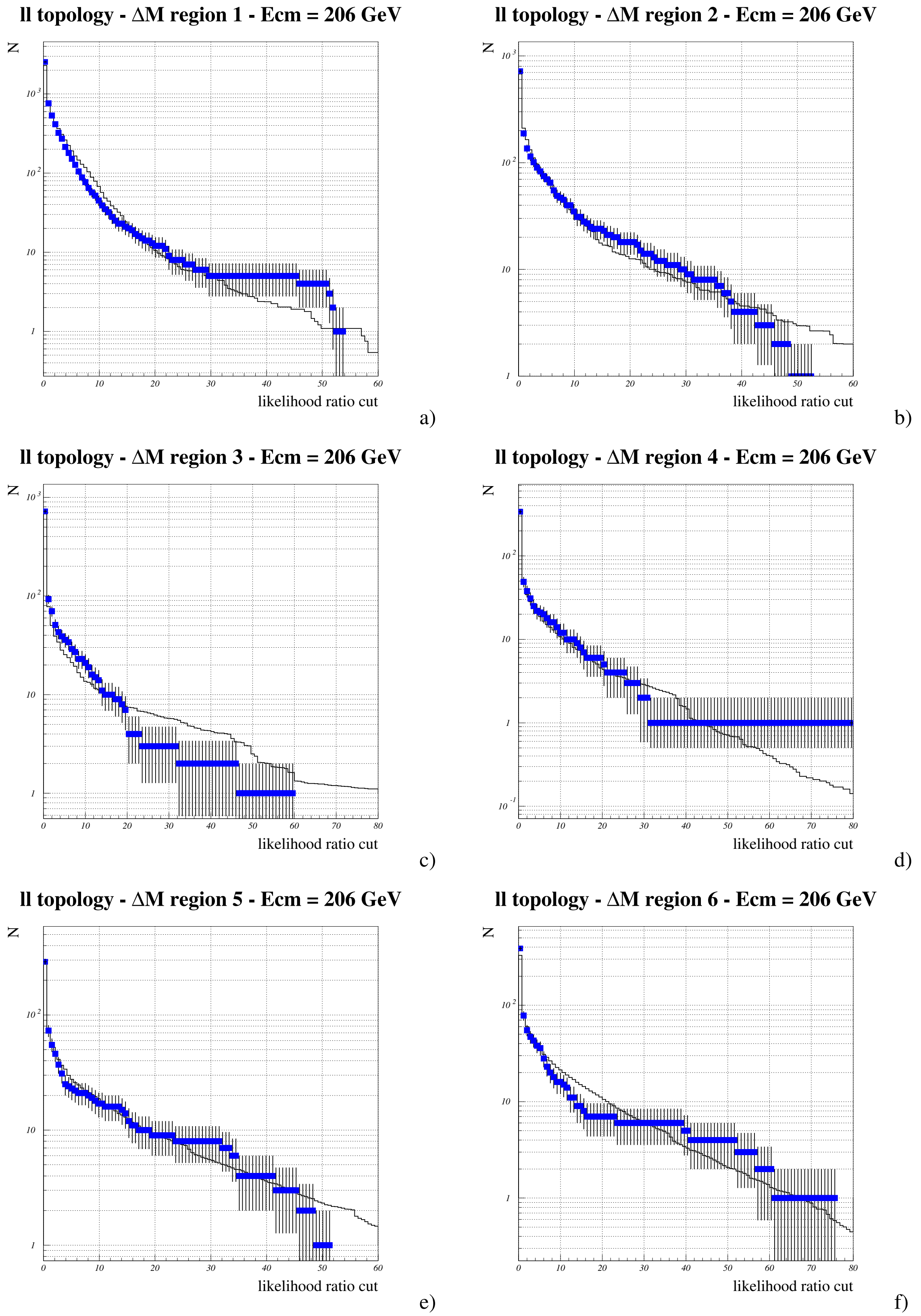

Figure G.3: Expected excluded cross section as a function of the Likelihood Ratio cut for the $\ell\ell$ topology: a) $3 \leq \Delta M < 5$ GeV$/c^2$, b) $5 \leq \Delta M < 10$ GeV$/c^2$, c) $15 \leq \Delta M < 25$ GeV$/c^2$, d) $25 \leq \Delta M < 35$ GeV$/c^2$, e) $35 \leq \Delta M < 50$ GeV$/c^2$, f) 50 GeV$/c^2 \leq \Delta M$. All plots show the data from year 2000 with TPC sector 6.

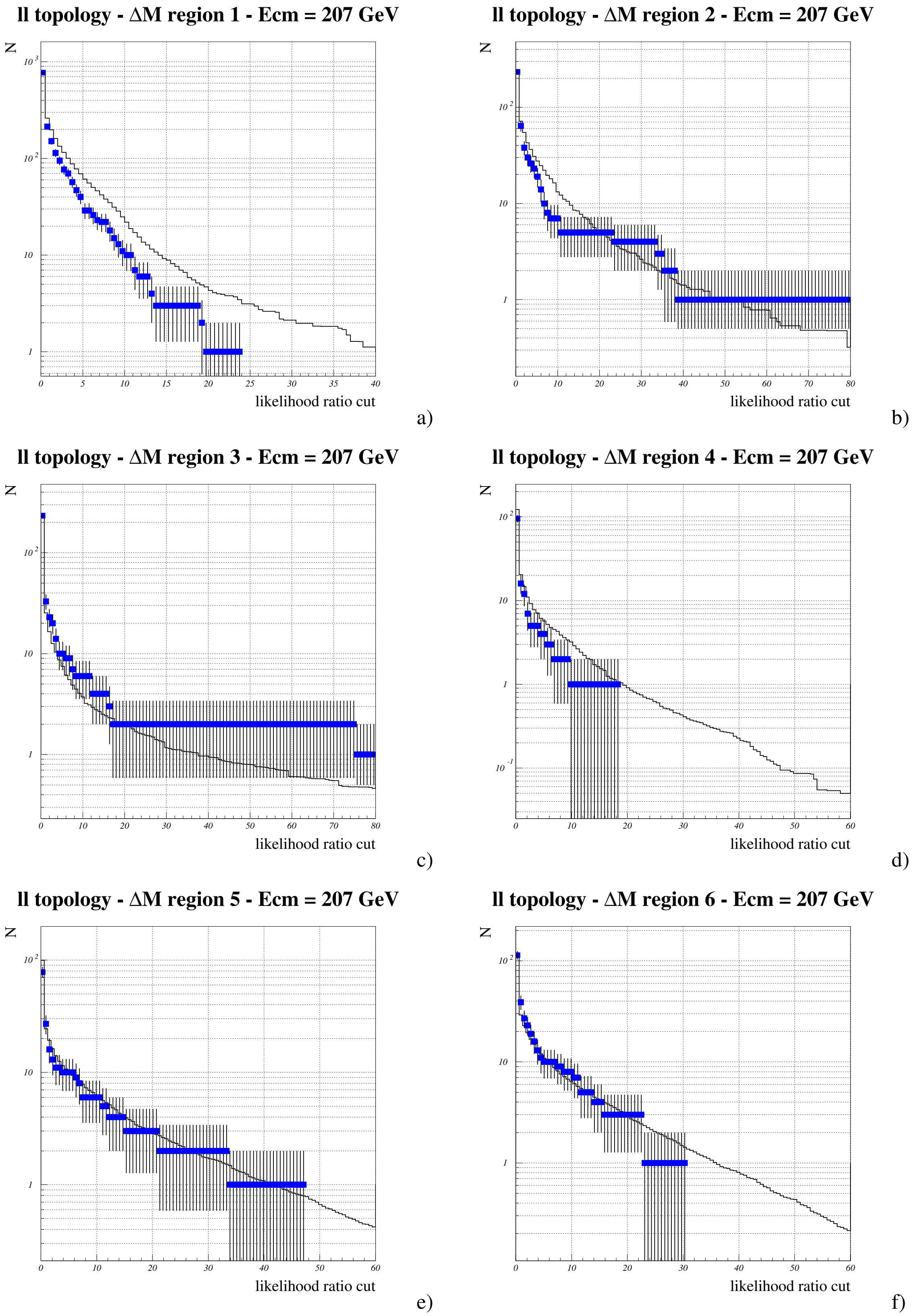

Figure G.4: Expected excluded cross section as a function of the Likelihood Ratio cut for the $\ell\ell$ topology: a) $3 \leq \Delta M < 5$ GeV$/c^2$, b) $5 \leq \Delta M < 10$ GeV$/c^2$, c) $15 \leq \Delta M < 25$ GeV$/c^2$, d) $25 \leq \Delta M < 35$ GeV$/c^2$, e) $35 \leq \Delta M < 50$ GeV$/c^2$, f) 50 GeV$/c^2 \leq \Delta M$. All plots show the data from year 2000 without TPC sector 6.

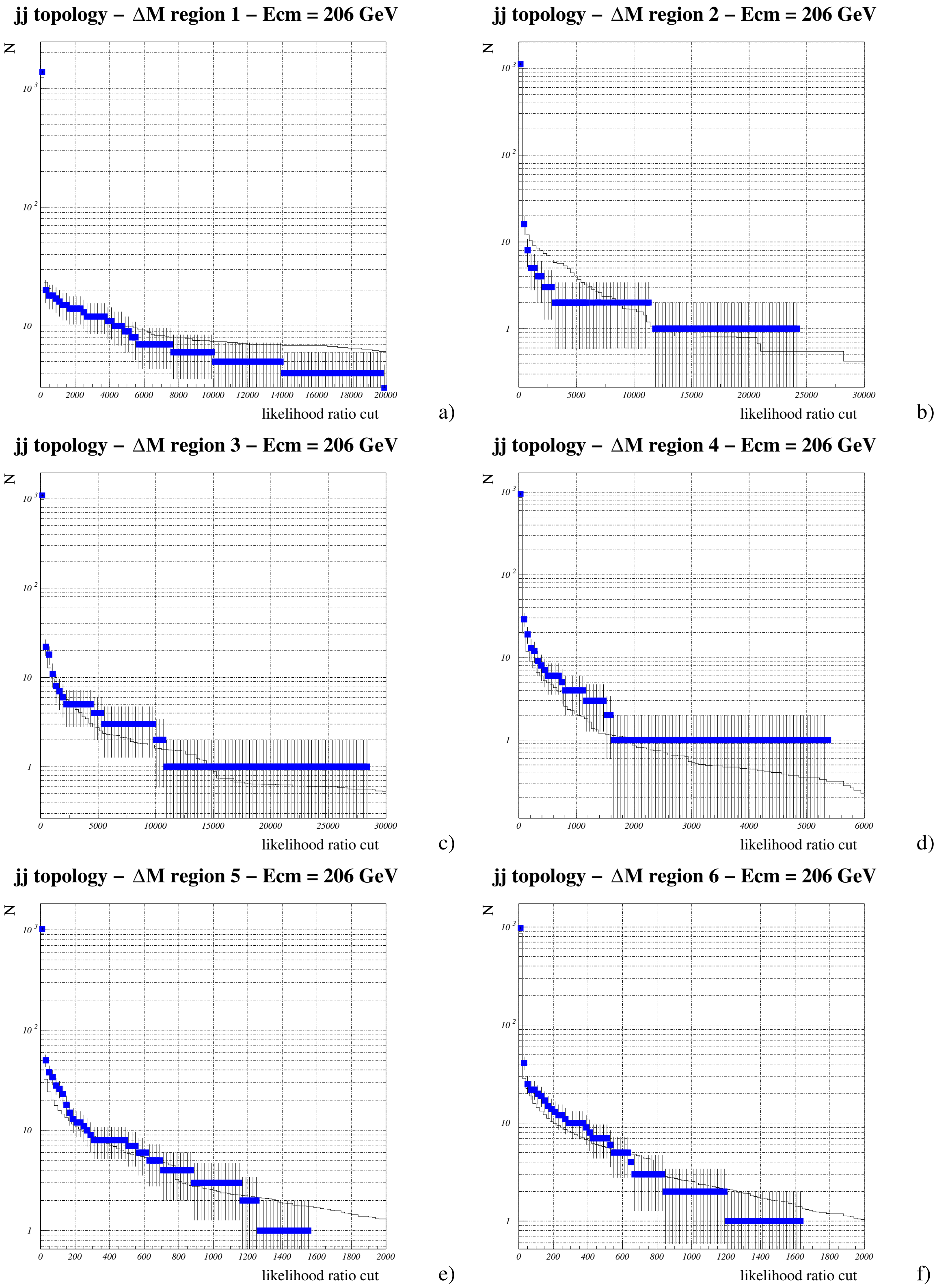

Figure G.5: Expected excluded cross section as a function of the Likelihood Ratio cut for the *jets* topology: a) $3 \leq \Delta M < 5$ GeV$/c^2$, b) $5 \leq \Delta M < 10$ GeV$/c^2$, c) $15 \leq \Delta M < 25$ GeV$/c^2$, d) $25 \leq \Delta M < 35$ GeV$/c^2$, e) $35 \leq \Delta M < 50$ GeV$/c^2$, f) 50 GeV$/c^2 \leq \Delta M$. All plots show the data from year 2000 with TPC sector 6.

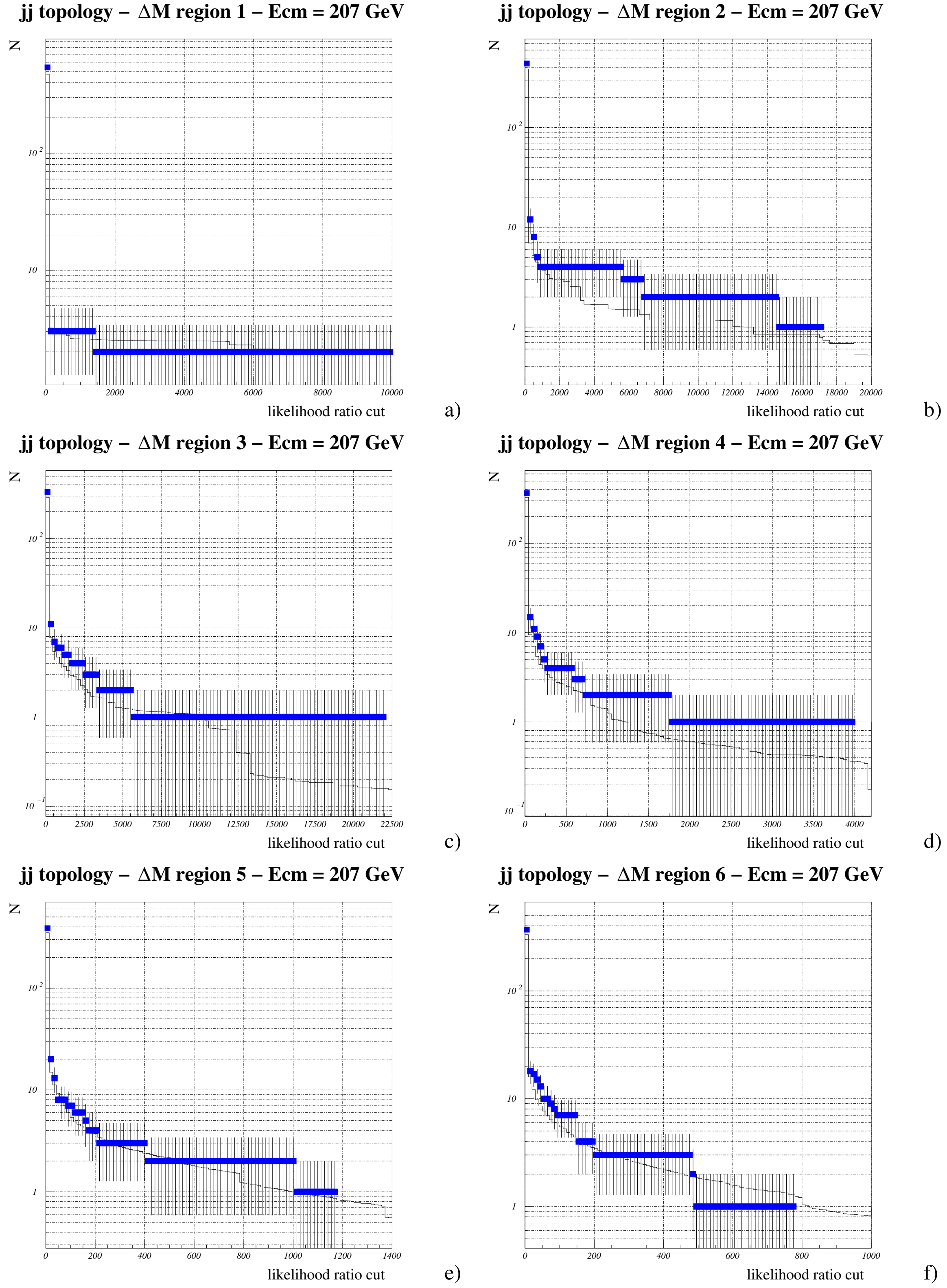

Figure G.6: Expected excluded cross section as a function of the Likelihood Ratio cut for the $jets$ topology: a) $3 \leq \Delta M < 5$ GeV$/c^2$, b) $5 \leq \Delta M < 10$ GeV$/c^2$, c) $15 \leq \Delta M < 25$ GeV$/c^2$, d) $25 \leq \Delta M < 35$ GeV$/c^2$, e) $35 \leq \Delta M < 50$ GeV$/c^2$, f) 50 GeV$/c^2 \leq \Delta M$. All plots show the data from year 2000 without TPC sector 6.

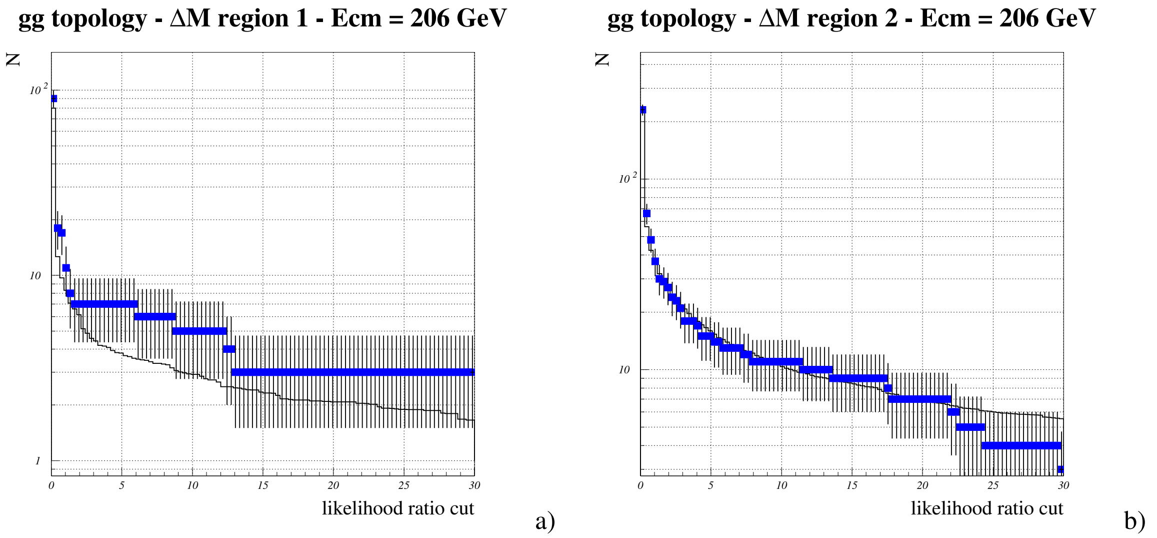

Figure G.7: Distributions of the number of real data (dots) and background events (histogram) as a function of the Likelihood Ratio cut for the radiative topology: a) $3 \leq \Delta M < 35$ GeV$/c^2$, b) 35 GeV$/c^2 \leq \Delta M$. All plots show the data from year 2000 with TPC sector 6.

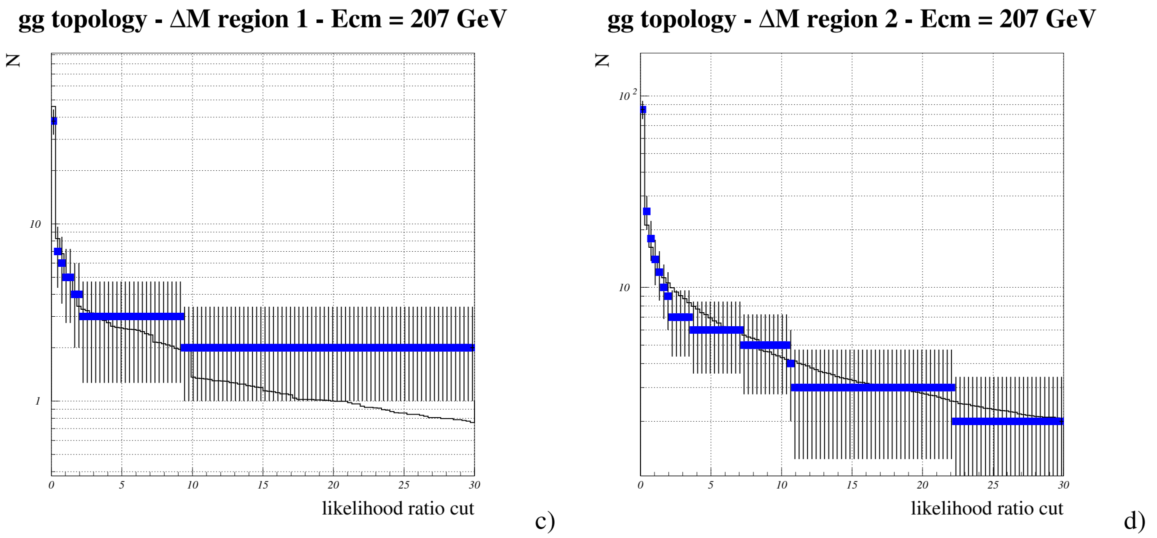

Figure G.8: Distributions of the number of real data (dots) and background events (histogram) as a function of the Likelihood Ratio cut for the radiative topology: c) $3 \leq \Delta M < 35$ GeV$/c^2$, d) 35 GeV$/c^2 \leq \Delta M$. All plots show the data from year 2000 without TPC sector 6.

Appendix H

Upper limits computation

H.1 Probability definitions

H.1.1 Mathematical definition (Kolmogorov)

If Ω is the set of all possible outcomes of a given experiment and $\emptyset$ is the null set (the impossible event), the probability $P(E)$ of a given outcome/event E is defined as an application from Ω to $\mathbb{R}$, fulfilling the following axioms

- $P(\Omega) = 1$ (the experiment must have an outcome),
- $0 \leq P(E)$ for all $E \in \Omega$,
- $P(\cup E_i) = \sum P(E_i)$, for any set of disjoint[1] E_i, $E_i \in \Omega$,

it is straightforward to derive the following theorems

1. $P(E) = 1 - P(E^c)$, where $\Omega = E \cup E^c$ and E and E^c are disjoint,
2. $P(E) \leq 1$,
3. $P(\emptyset) = 0$,
4. if $E_1, E_2 \in \Omega$ and are not necessarily disjoint, then $P(E_1 \cup E_2) = P(E_1) + P(E_2) - P(E_1 \cap E_2)$
5. $P(A|B)P(B) = P(B|A)P(A)$, where $P(A|B)$ is the conditional probability[2].
   (Bayes' theorem)

In this approach we began with three axioms, from which we can derive everything. We can calculate the probability of any complicated event for which we know the a *priori* probabilities of its components. But this is simply mathematics. To draw meaning from probability, one requires a connection to the real world.

[1] $E_i and E_j$ are disjoint if $E_i \cap E_j = \emptyset$ for $i \neq j$.
[2] $P(A|B) \equiv P(A \cap B)/P(B)$.

H.1.2 Empirical Frequency definition (Von Mises)

In this approach, largely due to von Mises, probability is viewed as the limits of the frequency of a result of an experiment or observation when the number of **identical** experiments is very large. The probability of an outcome x_i is defined as

$$P(x_i) = \lim_{N\to\infty} \frac{N_i}{N} \tag{H.1}$$

where N_i is the number of experiments yielding the outcome x_i and N is the total number of **identical** experiments.

There are two shortcomings to this approach

- $P(x_i)$ is not just a property of the experiment. It also depends on the "collection" or "ensemble", i.e., on the N repetitions of the experiment. For example, if one takes a resistor out of a box of resistors, the probability that one measures the resistance as 1 ohm depends not only on how the resistor was made, but also on how all the other resistors in the box were made,

- the experiment must be repeatable, under identical conditions, but with different possible outcomes. This is a great restriction on the number of situations in which one can use the concept of probability. For example, what is the probability that it will rain tomorrow ? Such question is meaningless for the frequentists, since the experiment cannot be repeated.

H.1.3 Subjective (Bayesian) probability

This approach attempts to extend the notion of probability to the areas where the experiment of the frequentist cannot be repeated. Here, probability is a subjective "degree of belief" which can be modified by observations. This was in fact, the interpretations of such pioneers in probability as Bayes and Laplace.

This approach takes the Bayes' theorem $P(A|B)P(B) = P(B|A)P(A)$ and interprets A as a theory or hypothesis and B as a result or observation. $P(A)$ is then the probability that A is true, or, in other words, our "belief" in the theory. Then Bayes' theorem becomes

$$P(\text{theory}|\text{result}) = \frac{P(\text{result}|\text{theory})}{P(\text{result})} P(\text{theory}) \tag{H.2}$$

here, $P(\text{theory})$ is our "belief" in the theory before doing the experiments, $P(\text{results}|\text{theory})$ is the probability of getting the result if the theory was true, $P(\text{result})$ is the probability of getting the result irrespectively of whether the theory is true or not, and $P(\text{theory}|\text{result})$ is our belief in the theory after the result has been obtained. We see that if the theory predicts the result with high probability, i.e., $P(\text{result}|\text{theory})$ is big, then $P(\text{theory}|\text{result})$, i.e., your belief in the theory after the result, will be higher than it was before, $P(\text{theory})$, and vice versa. However, if the result is likely even if the theory is not true, then your belief in the theory will not increase by very much since $\frac{P(\text{result}|\text{theory})}{P(\text{result})}$ is not much greater than 1. If we are interested in determining a parameter of the nature, λ, by doing an experiment which as an outcome z. And supposing we know the conditional pdf to get z given λ : $f(z|\lambda)$. Our prior, i.e., before we do the experiment, belief about λ is given by $P_{prior}(\lambda)$. The probability of z, $P(z)$, is just the marginal pdf $f_1(z) = \sum_{\lambda'} f(z|\lambda')P_{prior}(\lambda')$. Bayes' theorem yields

$$P_{posterior}(\lambda|z) = \frac{f(z|\lambda)}{f_1(z)} P_{prior}(\lambda) \tag{H.3}$$

This works if $P_{prior}(\lambda)$ is given. The problem here is: what is $P_{prior}(\lambda)$? By its nature this is not known. Guessing the prior probability is clearly subjective and unscientific. The usual prescription is the **Bayes' postulate**

If completely ignorant about $P_{prior}(\lambda)$, take all values of λ as equiprobable.

There are objections to this postulate

- If we are completely ignorant about $P(\lambda)$, how do we know $P_{prior}(\lambda)$ is a constant ?
- A different choice of $P_{prior}(\lambda)$ would give a different $P_{posterior}$.
- If we are ignorant about $P(\lambda)$, we are also ignorant about $P(\lambda^2)$ or $P(\sqrt{\lambda})$. Taking any of these as constant would imply a different $P_{prior}(\lambda)$, giving a different posterior probability.

These objections are usually answered by the assertion (supported by the experience) that $P_{posterior}$ usually converges to about the same value after several experiments irrespective of the initial choice of P_{prior}. Nevertheless, in the particular case of this work, this assertion is false since the experiment was done once. Hence, if we want to work in the Bayesian approach of the probability, the results will be dependent on our subjective choice of P_{prior}.

H.2 Are we frequentist or Bayesian ?

The answer of this question is clearly dependent of the type of experiment we have to deal with and the conclusions that we want to draw from the measurement(s). Usually, whenever the frequentist approach is possible and gives rise to physical results, this is the approach to choose. This provides a way to report objectively the outcome of the experiment without the need to incorporate prior beliefs. The Bayesian inference, on the other hand, is better suited, when one knows about the prior (which is an additional information). For instance, for the direct W mass measurement, we know that $P_{prior}(m_{W^\pm})$ is a Breit-Wigner. It has to be emphasized, that for many inference problems, the frequentist and Bayesian, with Bayes' postulate, approaches give the same numerical answers, even though they are based on fundamentally different definitions of probability. For small data samples, however, and for measurements of a parameter near a physical boundary, the different approaches may yield different results. In some cases, the frequentist approach leads to unphysical results (e.g., a negative upper limit on the new signal cross-section), so we are forced to make a choice. Finally, when inferring on a signal which may be observed in several independent channels, the classical (frequentist) approach [3] may give rise to situation where adding a channel contribution lowers the expected exclusion power. This can be understood, since it ignores the relation between the amount of expected background and the observed candidates in the individual channels, and, hence it looses information. These problems can be avoided only by means of including subjectivity in the inferring approaches [109], either by using a "modified" frequentist or a Bayesian approach. For a discussion of Bayesian vs. non-Bayesian methods, see References written by a statistician [122], by a physicist [123], or the more detailed comparison in [109]

H.3 Upper limit computation

It is possible to use the known expected background and the observed number of events to estimate an upper limit on the signal at a given confidence level. This limit is usually referred to as the "exclusion limit".

[3] Set by summing all the channel contributions.

H.3.1 Classical (frequentist) definition of the upper limit

If an experiment yields n observed events, the upper limit μ_{up} at α confidence level (CL) responsible of the observation, is the parameter of the Poisson law [4], such that a random repeat of the experiment, assuming the Poisson parameter μ_{up}, will yield a number of events greater than n in a α fraction of the experiments. Hence, in the frequentist approach, the upper limit at α CL is found

$$1 - \alpha = \sum_{k=0}^{n} \frac{e^{-\mu}\mu^k}{k!} \tag{H.4}$$

by solving this equation for μ given the number of observed events n. Moreover, using the Neyman's construction [109], Eq.(H.4) implies the following statement about the upper limit μ_{up}.

$$P(\mu_{true} < \mu_{up}(n)) = \alpha \tag{H.5}$$

in this probability statement, $\mu_{up}(n)$ is the random variable and μ_{true} is an unknown constant. If the experiment were to be repeated a large number of times, $\mu_{up}(n)$ would vary and would be greater than the fixed value μ_{true} in a fraction α of the experiments.

If one considers an experiment where a background contributes (with a Poisson parameter b) to the observation and assuming independent background and signal processes, the joint probability distribution of the the number of events is obtained from two independent Poisson distributions, one for the signal and one for the background

$$P(n_s, n_b|s, b) = \frac{e^{-s}s^{n_s}}{n_s!}\frac{e^{-b}b^{n_b}}{n_b!} \tag{H.6}$$

where the number of signal and background events are respectively n_s and n_b. In "counting experiments", the background is indistinguishable from the signal events and the number which is really observed by an experiment is the total number of events n = n_s + n_b. The corresponding probability distribution is computed by summing over all values of n_s and n_b giving a fixed total number n

$$P(n|s, b) = \frac{e^{-(s+b)}(s+b)^n}{n!} \tag{H.7}$$

In this case, the frequentist upper limit, s_{up}, at α CL given n and a background with (usually computed by MC) parameter b is

$$s_{up}(n) = \mu_{up}(n) - b \tag{H.8}$$

If b is high and n is low (even if it is not likely), this may lead to a negative value on the upper limit which is unphysical. The only way to avoid such situations is to consider either the "modified" frequentist or the Bayesian approach.

H.4 Choice of the approach

In this work the Bayesian approach (described later) was chosen assuming Bayes' postulate. The reasons motivating this choice were

- The Bayesian approach is well suited for multi-channel analyses.

[4] In counting experiments (e.g., LEP), the measurement of a given process follows a Poisson law. Nevertheless the following discussion applies for any pdf's.

- Both, multi-channel suited, approaches rely on a subjective [5] choice.
- The Bayesian approach permits to propagate easily the systematic and statistical uncertainties.
- Considering Bayes' postulate, the Bayesian approach yields conservative results with respect to the ("modified") frequentist approaches, i.e., $\mu_{up}^{Bayes} \geq \mu_{up}^{modified} \geq \mu_{up}^{Freq}$ at a given CL.
- Technically, the Bayesian algorithm is 100 times faster than the "modified" frequentist algorithm.

H.5 Bayesian definition of the upper limit

In the Bayesian approach, by the cost of introducing subjectivity, the probability statement will consider μ_{true} as a random variable and μ_{up} as a constant. Using the Bayes' theorem, the upper limit μ_{up} at α CL is expressed as

$$\alpha = \int_0^{\mu} P(s|n)ds = \frac{\int_0^{\mu} P(n|s)P(s)ds}{\int_0^{\infty} P(n|s)P(s)ds} \tag{H.9}$$

Considering Bayes' postulate and a processes following a Poisson distribution, this reduces to

$$1 - \alpha = \int_{\mu}^{\infty} \frac{e^{-x}x^n}{n!}dx \tag{H.10}$$

Using the property of the cumulative Poisson distribution, the upper limit at α CL is obtained

$$1 - \alpha = \sum_{k=0}^{n} \frac{e^{-\mu}\mu^k}{k!} \tag{H.11}$$

by solving this equation for μ, given the observed number of events n. One sees that both approaches lead to the same numerical results.

When considering a background contribution, the Bayes formula leads to the relation

$$1 - \alpha = \sum_{k=0}^{n} \frac{e^{-(\mu+b)}(\mu+b)^k}{k!} / \sum_{k=0}^{n} \frac{e^{-b}b^k}{k!} \tag{H.12}$$

The upper limit is obtained by solving this equation for μ, with a given number of observed events n and of background parameter b. An important issue is the presence of the denominator, which follows naturally in the Bayesian approach and prevents the signal upper limit from being forced into the non-physical region.

H.5.1 Multichannel without background

The probability to observe n_i events in channel i with a Poisson parameter s_i is given by the Poisson law. If the probability distributions of the different channels can be considered as independent, the joint distribution is

$$P(n_1, \cdots, n_k | s_1, \cdots, s_k) = \frac{e^{-s_1}s^{n_1}}{n_1!} \cdots \frac{e^{-s_k}s^{n_k}}{n_k!} \tag{H.13}$$

[5]The definition of the statistic Q in the "modified" frequentist approach.

where the n_i are independent random variables giving rise to the total number of events observed, $n = n_1 + \cdots + n_k$, and the total average, $s = s_1 + \cdots + s_k$.

The channels can be written in terms of known branching probabilities, p_i, as $s_i = sp_i$ with the normalization condition $p_1 + \cdots + p_k = 1$. Expression H.13 becomes

$$P(n, n_1, \cdots, n_k | s, p_1, \cdots, p_k) = \frac{e^{-s} s^n}{n!} \left[\frac{n!}{n_1! \cdots n_k!} p_1^{n_1} \cdots p_k^{n_k} \right] \tag{H.14}$$

showing that the product of Poisson distributions can be viewed as a single Poissonian for the total number of events with a multinomial branching into the sub-channels, conditional upon $\sum n_i = n$. The branching probabilities p_i take into account the efficiencies and the branching ratios of the different channels. They are normalized to 1. This multinomial factor is a distinctive feature of "distinguishable channels".

In expression H.14, the only free parameter is the total signal s. Applying the Bayes formula, the α CL will be

$$1 - \alpha = \int_\mu^\infty \frac{e^{-s} s^n}{n!} ds \Big/ \int_0^\infty \frac{e^{-s} s^n}{n!} ds \tag{H.15}$$

of the same form as for the single Poisson distribution without background and formula H.11 applies. The result is the same as if the channels were indistinguishable.

H.5.2 Multichannel with background

The total probability distribution in the case of sub channels with background can be written in terms of the branching probabilities p_i and of a "renormalized" background β_i defined as $\beta_i = b_i/p_i$

$$P(n, n_1, \cdots, n_k | s, b, p_1, b_1, \cdots, p_k, b_k) =$$

$$e^{-(s+b)} \tfrac{(s+\beta_1)^{n_1} \cdots (s+\beta_k)^{n_k}}{n!} \left[\tfrac{n!}{n_1! \cdots n_k!} p_1^{n_1} \cdots p_k^{n_k} \right] \tag{H.16}$$

Then, $s_i + b_i = p_i(s + \beta_i)$ where the quantities p_i and β_i are known for each channel and s is the sum of the Poisson parameters in the observed channels.

Unlike the single channel case, its dependence on the signal plus background cannot be reduced to a Poisson distribution of parameter $(s + b)$, unless all renormalized backgrounds b_i/p_i are equal. This situation occurs when the backgrounds in the channels are distributed in the same proportions, p_i, as the signal events.

The factor in square brackets in the probability distribution H.16 is independent of s and will cancel in the ratio entering the Bayes formula. It is left out in the following calculation of the integral

$$F(\mu, n_1, \cdots, n_k) = \int_\mu^\infty e^{-(s+b)} (s + \beta_1)^{n_1} \cdots (s + \beta_k)^{n_k} ds \tag{H.17}$$

The resolution of this integral can be found in reference [124] and the α CL is

$$1 - \alpha = \frac{e^{-(\mu+b)} \sum_{j=0}^{n} (n-j)! \sum_{\nu_1 + \cdots + \nu_k = j} C_{\nu_1}^{n_1} \cdots C_{\nu_k}^{n_k} (\mu + \beta_1)^{\nu_1} \cdots (\mu + \beta_k)^{\nu_k}}{e^{-b} \sum_{j=0}^{n} (n-j)! \sum_{\nu_1 + \cdots + \nu_k = j} C_{\nu_1}^{n_1} \cdots C_{\nu_k}^{n_k} \beta_1^{\nu_1} \cdots \beta_k^{\nu_k}} \tag{H.18}$$

with $\nu_i \leq n_i$ and the $C_{\nu_k}^{n_k}$ are the binomial coefficients.

For a single channel this formula takes the same form as the single channel formula H.12. When the renormalized backgrounds of some channels are equal, their contributions are summed as if they were a single channel.

Appendix I

Systematics computation and propagation

The excluded cross-sections and masses can be affected by the systematic uncertainties related to the SM background rate and signal efficiency determinations. These are mainly due to imperfections in

- the description of the differential cross-sections,
- the modeling of the fragmentation and hard gluon radiation,
- the modeling of the detector response.

Inaccuracy of the description of the differential cross-sections of various SM processes was studied extensively in the context of their measurements at LEP and is typically small, except for the hadronic $\gamma\gamma$ background. On the other hand, in the present thesis, uncertainties in the SUSY modeling, which are usually computed with a comparison between existing SUSY generators, were not taken into account since they are expected to be extremely small when considering chargino production and decays in the scenarios with high scalar quarks. Modeling of fragmentation and hard gluon radiation was not studied either, since in the MSSM model it mainly affects searches for the stop quark, due to the uncertainties on the modeling of the stop fragmentation. The largest contribution to the systematics on both background rate and efficiency determination arises from the modeling of the detector response. This was addressed in several ways, depending on the type of the final state searched for. Below, a review of all of these systematic effects is given, together with the methods used to address them. Then, each of the methods used to estimate the systematics is discussed in more detail. Finally, the method used to propagate those uncertainties in the limit computation is briefly presented.

I.1 Review of the main systematic sources

Description of the differential cross-sections

The uncertainty on the differential cross-section of the most important SM processes is [125][126] less than 1% for WW production, around 0.5% for $Z\gamma$, 2% for $Z^0 Z^0$ and about 5% for $We\nu_e$ and $Z^0 e^+ e^-$. The uncertainty of the description of the $Z\gamma^*$ process is typically 5%, reaching 20% in the region of very small masses of γ^*. While the uncertainties are small for two-photon interactions giving leptons (less than 5%), the description of the hadronic $\gamma\gamma$ processes is subject to large uncertainties in some regions of the parameter space. The effect was studied comparing various two-photon generators [104] leading to an estimate of the systematic uncertainty of 15% on the hadronic $\gamma\gamma$ differential cross-section. Nevertheless, in the present work those uncertainties have not been used since the technique developed to estimate the detector response systematics included an estimation of the uncertainty on the differential cross-sections.

Modeling of the detector response

The modeling of the detector response is the main source of systematics in the searches for new particles. The next section gives a review of the methods which were developed to address primarily the influence of this uncertainty on the SM background rate and efficiency determinations in the case of chargino search.

I.1.1 Methods to evaluate detector response systematics

The "re-weighting" method

This method estimates the systematic uncertainty on the number of selected background events from imperfect simulation of the detector response, as well as from possible large uncertainties in the modeling of the differential cross-section from SM processes. It propagates the difference between the data and the simulated background at preselection level to the final selection level for the variables relevant for the analysis. The propagation was performed as follows: for each discriminating variable, used in the event selection, a 25 bin histogram was built from the data and the simulated background at both preselection and final level.

From the **preselection** histograms a re-weight factor was calculated for each bin, N_{Data}/N_{Back}, if the bin contained at least 1 % of the total number of background events and the number of data events was not equal to zero, which got the background in perfect agreement with the data.

The background histograms at the **final** selection level were then re-weighted with the factors from the corresponding bins at preselection level and the systematic uncertainty for each variable was then determined by subtracting the total number of selected background events from the total number of re-weighted background events. Figure I.1 shows the difference between the number of selected background events with and without re-weighting for different variables.

The total positive and negative systematic uncertainties were then computed by a quadratic sum over the uncertainties from the different variables with a positive or a negative contribution:

$$\epsilon^{+} = \sqrt{\sum (N_{Back}^{RW}(i) - N_{Back})^2}\ , \ \ if\ N_{Back}^{RW}(i) > N_{Back}.$$

$$\epsilon^{-} = \sqrt{\sum (N_{Back}^{RW}(i) - N_{Back})^2}\ , \ \ if\ N_{Back}^{RW}(i) < N_{Back}.$$

Where $N_{Back}^{RW}(i)$ is the total number of re-weighted background events from variable i and N_{Back} is the number of selected background events without re-weighting.

Then a Kolmogorov test was made, which is the probability that the data and background histograms at preselection level come from the same distribution. This test was used to study how the compatibility between the data and background histograms of a variable change when it is re-weighted with respect to all the other variables. Table I.1 gives an example of how the probability

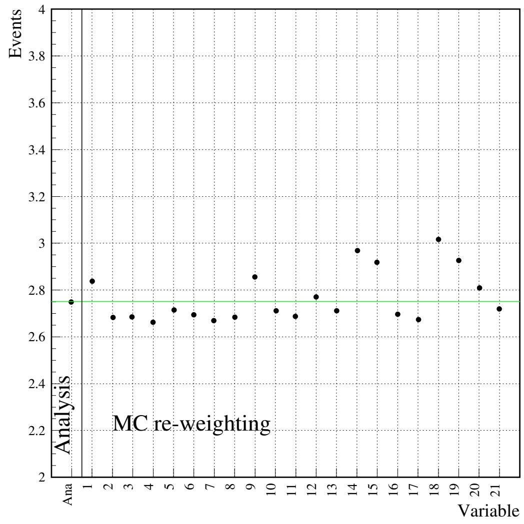

Figure I.1: A comparison between the number of selected background events before and after re-weighting with respect to the different variables used in the analysis. The plot is an example from the $jj\ell$ topology.

from the Kolmogorov test change when the background histograms for 6 different variables are re-weighted with respect to each other and one can see that when the background distribution for one variable is corrected also the agreement for most of the other variables are improved.

	Acop	$\not{P}_t$	$\theta_{\not{p}}$	$M_{\ell\nu}$	M_{jj}	P_ℓ
pre	0.957	0.834	0.174	0.924	1.000	0.869
Acop	1.000	0.995	0.244	(0.878)	1.000	0.922
$\not{P}_t$	0.991	1.000	0.241	(0.913)	1.000	0.922
$\theta_{\not{p}}$	0.9997	0.995	1.000	(0.911)	1.000	(0.834)
$M_{\ell\nu}$	0.991	0.940	0.241	1.000	1.000	0.939
M_{jj}	(0.928)	(0.789)	0.177	0.926	1.000	0.872
P_ℓ	0.991	0.904	(0.145)	0.955	1.000	1.000

Table I.1: Results from the Kolmogorov test of five different variables. The row "Pre." shows the results for the different variables distributions at preselection level without re-weighting and the rows contain the results when the background variable distributions are re-weighted. This table is an example from a Kolmogorov test performed in the third $jj\ell$ window.

The correlation between the variables was not studied with this method, but since the total systematic uncertainties are computed as the sum of the separately obtained uncertainties from the different variables the total uncertainties are overestimated. This is implied by the Kolmogorov test since it shows that the contributions from the different variables partly contain the same error. The systematic uncertainties from this method are additionally overestimated since the statistical uncertainty for each bin is included in the re-weight factor and they also grow with the number of variables used in the analysis. The effect of this is that the overestimation of the uncertainties increase with the number of variables, but as long as the uncertainties have an negligible effect on the final results (in this case the exclusion limits) they can be used in a conservative manner. Nevertheless this method is only valid for studying systematic uncertainties from the detector response on the background, since it works with the individual variable histograms where the signal usually has a very different shape compared to the background. The main advantages of this method is the simplicity and conservative uncertainty estimation. This method was used to compute the systematics on SM expectations in all the windows of investigation for all the data collected in years 1999 and 2000.

The "shaking" method

The "shaking" method was used to estimate systematic uncertainties from MC simulated events by modifying the multiplicity of the events and hence also "shake" the other variables. It has been found out, by the DELPHI measurement teams, that the most critical variable with respect to data-MC agreement is the multiplicity [127]. This is the reason why only the multiplicity was chosen to be the adjusting variable, since when the multiplicity distribution of the MC events is set to a good agreement with the data all the other variables agree much better with the data as well. However this method is only suited for high multiplicity events, since adding or subtracting tracks in a low multiplicity topology, e.g. pure leptonic, might give unphysical effects. The "shaking" method can still be used in high multiplicity topologies with isolated leptons or photons. In these topologies the method gives an estimation of the systematic uncertainty which includes both the effect from "shaking" the variables as well as the effect of additional tracks that violate the isolation criteria for the isolated lepton or photon. The improving effect from correcting the multiplicity is seen also in the tails of the distributions [127], which implies that this method is perfectly valid also for high multiplicity topologies with missing energy, typical of SUSY searches.

Since the charged and neutral multiplicity are differently well simulated, due to detector limitations, these were studied separately. Also the phase space was divided into 10 different regions,

- Track angle: $\cos\theta < 0.7$ (barrel), $\cos\theta > 0.7$ (forward)
- Track momentum: $|\vec{p}|$ within [0.,0.5] [0.5,1.] [1.,2.] [2.,5.] [5.,∞] GeV

since the hadronic multiplicity is a function of phase space.

For each region a correction coefficient was determined by the mean multiplicity from the data and the MC simulation,

$$P = \frac{< N_{Data} > - < N_{MC} >}{< N_{MC} >}.$$

The mean multiplicity was determined by fitting a Poisson function to the multiplicity distribution and these coefficients were then used as the probability to add or remove a track in the corresponding region. The multiplicities in the different regions were then modified according to the probabilities from the P-coefficients in a way that did not violate the constrains from the specific event topology [127]. The P-coefficients were obtained using LEP1 data, due to its high statistics. This is possible because the multiplicity varies very little with $\sqrt{s}$ and this also ensures that a possible signal, in the LEP2 data, did not affect the P-coefficients.

The results from the analysis were then compared with the results from the same analysis using the "shaken" MC samples and the difference was then interpreted as a measure of the systematic uncertainty from the MC simulation.

This method was tested in the study of systematics of the ZZ cross-section measurement [128] and in the search for the invisibly decaying Higgs boson [129]. The multiplicity adjustment is of the order of 1%-2%. It led to a better agreement between the data taken at energies above Z^0 peak and the Standard Model background, typically predicting slightly higher observed missing energy and momentum.

This method was used to study the systematic uncertainty on the detection efficiency in $jets$, $jj\ell$ and *radiative* (with high charged multiplicity) topologies. The values in table I.2 correspond to the $jets$ and $jj\ell$ windows and were averaged over several chargino points with model parameters corresponding to the specific ΔM region.

ΔM	1	2	3	4	5	6
$jets$	+6.8 %	+8.8 %	+3.1 %	+0.5 %	+1.0 %	+3.4 %
$jj\ell$	+12.9 %	+4.1 %	+0.5 %	+0.4 %	+0.0 %	+0.9 %

Table I.2: The relative difference in the chargino detection efficiency obtained with and without "shaking" in the year 2000 simulation with the DELPHI detector fully operational. The values shown correspond to the different ΔM regions of the $jets$and $jj\ell$ topologies.

Except for the lowest ΔM regions where systematic uncertainties due to tracking and neutral energy reconstruction have the biggest effect, the variation in the detection efficiency is very small. The efficiencies for the "shaken" signal are typically larger than for the "unshaken" signal.

Methods dedicated to the topologies with low charged multiplicities ("smearing" technique)

Uncertainty on the track momentum reconstruction arising from the modeling of the detector response was studied by smearing the momentum distribution of all the charged tracks present in the event using the algorithm described in [130]. A small effect was found on the determination of efficiency in the $\ell\ell$ and *radiative* (with low charged multiplicity) topologies. The estimated systematic uncertainty on the efficiency is of the order of 1-2%.

I.2 Propagation of the uncertainties into the limits [108]

A probability distribution function (pdf) was assumed for the efficiency and the background in any single channel, the estimate of their mean value and standard deviation are given in sections 7.1 and 7.2. A channel corresponds to a single $\sqrt{s}$ and to a single topology (see section 8.1.1). The pdf's were either assumed Gaussian or constant, depending on the method used to evaluate the uncertainty of the parameter (statistics of the simulation or estimated systematic uncertainties). Then, they were convoluted in the formula giving the overall number N_{exp} of the expected number of signal events

$$N_{\mathrm{exp}} = \sum_{\mathrm{i}=1}^{\#_{ecm}} \sum_{\mathrm{j}=1}^{\#_{decay}} \sigma_{\mathrm{i}}\, \mathcal{L}_{\mathrm{i}}\, \varepsilon_{\mathrm{i,j}}\, BR_{\mathrm{i,j}} \tag{I.1}$$

and in the pdf of the number of signal events (N_{sig}) compatible with the observation (using the number of candidates in each channel) from which one can compute by integration, N_{up} at the CL wanted (the formula used is the one described in appendix H).

Usually one compares $N_{\rm exp}$ (which is a constant if there are no uncertainties associated to the factors that compose it) with $N_{\rm up}$ (by performing the integration of $N_{\rm sig}$ to obtain the desired CL). If $N_{\rm up}$, computed at a given CL, remains below $N_{\rm exp}$, the MSSM point can be excluded at the same CL. However, here, $N_{\rm exp}$ itself is not constant, because the terms that define it have a pdf with non zero width. Both the quantities $N_{\rm exp}$ and $N_{\rm sig}$ (hence $N_{\rm up}$ at a given CL) that must be compared are varying. The best way to account for the correlations between the two terms is to consider the difference $N_{\rm exp} - N_{\rm sig}$. A MSSM point is discarded (i.e. incompatible with the experimental outcomes) at a given CL if the lower limit at the same CL on

$$N_{\rm exp} - N_{\rm sig} \tag{I.2}$$

is positive. In the present analysis, the difference in Eq.(I.2) was computed through a MC integration which took into account all the pdf's of the variables entering in the calculation.

To conclude, it has to be emphasized that the worsening of the limit as obtained with the exact calculation is much less relevant than the unnecessary over-conservative approach that would lead to reduce all efficiencies and all backgrounds by one standard deviation, and then computing the limit as if there was no uncertainty on the modified parameters.

Bibliography

[1] S. Weinberg, *The quantum theory of fields. Vol.1: Foundations*, Cambridge, UK: Univ.Press, 1995;
S. Weinberg, *The quantum theory of fields. Vol.2: Modern applications*, Cambridge, UK: Univ.Press, 1995.

[2] C. Yang and R. Mills, Phys. Rev. **D96**(1954) 191.

[3] J. Schwinger, Ann. of Phys.**2**(1957) 407.

[4] S.L. Glashow, Nucl. Phys. **B22**(1961) 579.

[5] M. Veltman, *About the genesis of the Standard Model*, in the Proceedings of the international conference "Neutral Currents: twenty years later", World Scientific 1993.

[6] T.D. Lee and C.N. Yang, Phys. Rev.**119**(1960) 1410.

[7] M. Gell-Mann, Phys. Lett.**8**(1964) 214.

[8] G. Zweig, CERN-TH 8419/TH.412 (1964)

[9] M. Gell-Mann, *Physics* **1**(1964) 63.

[10] Y. Hara, Phys. Rev.**134**(1964) B701.

[11] B. J. Bjorken and S. L. Glashow, Phys. Lett.**11**(1964) 255.

[12] O. W. Greenberg, Phys. Rev. Lett.**13**(1964) 598.

[13] M. Y. Han and Y. Nambu, Phys. Rev.**139**(1965) B1006.

[14] M. Breindenbach *et al.*, Phys. Rev. Lett.**23**(1969) 935.

[15] A.Salam and J.C. Ward, Phys. Lett.**13**(1964) 168.

[16] S. Weinberg, Phys. Rev. Lett.**19**(1967) 1264.

[17] T. W. Kibble, Phys. Rev.**155**(1967) 1554.

[18] R. Brout and F. Englert, Phys. Rev. Lett.**13**(1964) 321;
P.W. Higgs, Phys. Rev. Lett.**12**(1964) 132, Phys. Rev. Lett.**13**(1964) 508.

[19] S.L. Glashow, J. Iliopoulos and L. Maiani, Phys. Rev.**2**(1970) 1285.

[20] G. 't Hooft, Nucl. Phys. **B33**(1971) 173.

[21] C. Bouchiat, J. Iliopoulos and Ph. Meyer, Phys. Lett. **B38**(1972) 519.

[22] F.J. Hasert *et al.*, Phys. Lett. **B46**(1973) 138.

[23] J. E. Augustin *et al.*, Phys. Rev. Lett.**33**(1974) 1406;
Aubert *et al.*, Phys. Rev. Lett.**33**(1974) 1404.

[24] D.J. Gross, F. Wilczek, Phys. Rev. Lett.**30**(1973) 1343;
H.D. Politzer, Phys. Rev. Lett.**30**(1973) 1346.

[25] P. *et al.*, Nucl. Phys. **B142**(1978) 1;
J. G. H. de Groot *et al.*, Phys. Lett. **B82**(1979) 292.

[26] M. Perl *et al.*, Phys. Rev. Lett.**35**(1975) 1489.

[27] S. W. Herb *et al.*, Phys. Rev. Lett.**39**(1977) 252.

[28] CDF Collaboration, Phys. Rev. Lett.**74**(1995) 2626;
D0 Collaboration, Phys. Rev. Lett.**74**(1995) 2632.

[29] G. Arnison *et al.*, Phys. Lett. **B122**(1983) 103;
M. Banner *et al.*, Phys. Lett. **B122**(1983) 476.

[30] D. Treille, *The Standard Model and LEP Physics.*, Les Houches, Session $LXVIII$,1997 and references therin.

[31] D. E. Groom *et al.*, Review of Particle Physics, Eur. Phys. J. **C15**(2000) 1

[32] LEP EWWG, *A combination of the preliminary measurements and constraints on the Standard Model*, hep-ex/0112021

[33] A.D. Martin, J. Outhwaite and M.G. Ryskin, Phys. Lett. **B492**(2000) 69

[34] P. Fayet, Nucl.Phys.Proc.Suppl.101,81(2001) (hep-ph/010722)

[35] Y. A. Gol'fand and E. P. Likhtman, *JETP Letters* **13**(1971) 452;
D. V. Volkov and V. P. Akulov, *JETP Letters* **16**(1972) 621;
J. Wess and B. Zumino, Phys. Lett. **B49**(1974) 52

[36] P. Fayet and S. Ferrara, Phys. Rev.**32**(1977) 249.

[37] H. E. Haber and G. L. Kane, Phys. Rev.**117**(1985) 75.

[38] J.Wess and J. Bagger, *Supersymmetry and Supergravity*, Princeton Univ. Press, 1983.

[39] P. West, *Introduction to Supersymmetry and Supergravity*, World Scientific, 1986.

[40] S. Weinberg, *The quantum theory of fields. Vol.3: Supersymmetry*, Cambridge, UK: Univ.Press, 2000.

[41] D. Bailin and A. Love, *Supersymmetric Gauge Field Theory and String Theory*, IOP Publishing, 1994.

[42] S.P. Martin, *A Supersymmetry Primer*, hep-ph/9709356.

[43] P. Fayet, Phys. Lett. **B64**(1976) 159;
P. Fayet, Phys. Lett. **B69**(1977) 489;
P. Fayet, Phys. Lett. **B84**(1979) 416.

[44] E. Gildener and S. Weinberg, Phys. Rev. **D13**(1976) 3333 ;
E. Gildener, Phys. Rev. **D14**(1976) 1667;
L. Susskind, Phys. Rev. **D20**(1979) 2619.

[45] M. Drees, *An Introduction to Supersymmetry*, hep-ph/9611409.

[46] E. Witten, *Nucl. Phys.***B188**(1981) 513;
N. Sakai, Z. Phys. **C11**(1981) 153;
S. Dimopoulos and H. Georgi, *Nucl. Phys.***B193**(1981) 150;
R.K. Kaul and P. Majumdar, *Nucl. Phys.***B199**(1982) 36.

[47] G.G. Ross, *Grand Unified Theories*, Benjamin & Cummings, 1985.

[48] S. Bethke; hep-ex/0004021.

[49] U. Amaldi, W. de Boer and H. Fürstenau, Phys. Lett. **B260**(1991) 447.

[50] J. Ellis, S. Kelley and D. V. Nanopoulos, *Constraints From Gauge Coupling Unification On The Scale Of Supersymmetry Breaking*, CERN-TH 6481/92.

[51] W. de Boer, *Search for SUSY and Higgs Particles*, talk given at XVIII Phys. in Coll., Frascatti 1998.

[52] S. Coleman and J. Mandula Phys. Rev.**159**(1967) 1251.

[53] P. Nath and R. Arnowitt, Phys. Lett. **B32**(1977) 249;
D. Z. Freedman, P. van Nieuwenhuizen and S. Ferrara, Phys. Rev. **D13**(1976) 3214;
S. Deser and B. Zumino, Phys. Lett. **B62**(1976) 335.

[54] L. Pape, *Search for New Particles in the context of SUSY*,
Proceedings of the X Jorge A. Swieca summerschool, World Scientific, 1999.

[55] P. Fayet and J. Iliopoulos Phys. Lett. **B51**(1974) 461.

[56] A. Salam and J. Stradhee, Nucl. Phys. **B87**(1975) 85;
P. Fayet, Nucl. Phys. **B90**(1975) 104.

[57] L. Girardello and M.T. Grisaru, *Nucl. Phys.***B194**(1982) 65.

[58] P. Fayet, Phys. Lett. **B70**(1977) 461.

[59] F. Fayet, Phys. Lett. **B78**(1978) 417.

[60] M. Dine and W. Fischler, Phys. Lett. **B110**(1982) 227; C.R. Nappi and B.A. Ovrut, Phys. Lett. **B113**(1982) 175; L. Alvarez-Gaumé, M. Claudson, and M. B. Wise, *Nucl. Phys.***B207**(1982) 96.

[61] M. Dine, A. E. Nelson, Phys. Rev. **D48**(1993) 1277; M. Dine, A.E. Nelson, Y. Shirman, Phys. Rev. **D51**(1995) 1362; M. Dine, A.E. Nelson, Y. Nir, Y. Shirman, Phys. Rev. **D53**(1996) 2658.

[62] G. F. Giudice, R. Rattazzi, Phys. Rev.**322**(1999) 419, CERN-TH/97-380, hep-ph/9801271.

[63] R. Arnowitt, A. Chamseddine and P. Nath, *N=1 Supergravity*, World Scientific, Singapore, 1984.

[64] G.F. Giudice, M. Luty, H.Murayama, R.Rattazzi, JHEP **98** (1998) 12.

[65] T. Alderweireld *et al.*, *Search for AMSB with the DELPHI data*, DELPHI note 2002-040 CONF 574, (2002).

[66] A. Bartl, H. Fraas, W. Majoretto and B. Mösslacher, Z. Phys. **C55**(1992) 257.

[67] A. Bartl, H. Fraas, W. Majoretto and N. Oshimo, Phys. Rev. **D40**(1989) 1594.

[68] A. Bartl, H. Fraas, W. Majoretto and N. Oshimo, Z. Phys. **C30**(1986) 441;
Z. Phys. **C41**(1988) 475.

[69] J.L. Feng and M.J. Strassler, Phys. Rev. **D51**(1995) 4661.

[70] Dr. Pierpaolo Rebecchi, private communication.

[71] K. Cheung, D. A. Dicus, B. Dutta and S. Nandi, Phys. Rev. **D58**(1998) 015008

[72] J. Abdallah *et al.*, *Searches for supersymmetric particles in e+e- collisions up to 208 GeV, and interpretation of the results within the MSSM*, DELPHI note 2002-027-CONF-561, (2002).

[73] DELPHI Collaboration, Phys. Lett. **B485**(2000) 65;
DELPHI Collaboration, Eur. Phys. J. **C11**(1999) 1.

[74] LEP Energy Working Group, Evaluation of the LEP centre-of-mass energy above the W pair production threshold, Eur. Phys. J. **C11**(1999) 573;
LEP Energy Working Group, Evaluation of the LEP centre-of-mass energy for data taken in 1998, LEP Energy working group note 99/01;
LEP Energy Working Group, Evaluation of the LEP centre-of-mass energy for data taken in 1999, LEP Energy working group note 00/01;
LEP Energy Working Group, Evaluation of the LEP centre-of-mass energy for data taken in 2000, LEP Energy working group note 01/01

[75] The LEP collaborations, Combination procedure for the precise determination of Z boson parameters from results of the LEP experiments, CERN-EP/2000-153 (2000)

[76] L. Arnaudon et al., The effects of terrestrial tides on the LEP beam energy,
Nucl. Instrum. Methods **A357**(1995) 249

[77] A.A. Sokolov and I.M. Ternov. On polarization and spin effects in the theory of synchrotron radiation. In *Sov. Dokl. 8* page 1203 (1964)

[78] DELPHI Collaboration, Luminosity measurement in 1994 with the STIC detector., DELPHI 97-08 PHYS 667 (1997)

[79] Pr. Marco Paganoni, private communication

[80] DELPHI Collaboration, The DELPHI Detector at LEP,
Nucl. Instrum. Methods **A303**(1991) 233;
DELPHI Collaboration, Performance of the DELPHI Detector,
Nucl. Instrum. Methods **A378**(1996) 57

[81] DELPHI Collaboration, DELPHI Data Analysis Program (DELANA) User's Guide, DELPHI 89-44 PROG 137 (1989)

[82] V. Perevozchikov and N. Smirnov, PHDST Package Description V.3 VZD — Viewer of Zebra Data for DELPHI User's Manual, DELPHI 92-118 PROG 189

[83] Tz. Spassov and N. Smirnov, SKELANA — Skeleton Analysis Program, 1995;
F. Cossutti et al., Improvements to SKELANA for Version 2.0, DELPHI 99-175 PROG 239

[84] DELPHI Collaboration, DELPHI event generation and detector simulation - User Guide, DELPHI 89-67 PROG 142 (1989)

[85] F. Cossutti, A. Tonazzo, F. Mazzucato, REMCLU : a package for the Reconstruction of Electromagnetic CLUsters at LEP200, DELPHI 2000-164 PROG 242

[86] S. Catani *et al.*, Phys. Lett. **B269**(432) 1991.

[87] T. Sjöstrand, Comput. Phys. Commun.**39**(347) 86;
T. Sjöstrand, `PYTHIA 5.6` *and* `JETSET 7.3`, CERN-TH/6488-92.

[88] DELPHI Collaboration, Phys. Lett. **B479**(2000) 118;
T. Alderweireld, I. Gil, P. Rebecchi, *Review of the chargino search in DELPHI. Latest results at* E_{cm} *= 189 GeV*, CERN-OPEN-2002-031;
DELPHI Collaboration, Phys. Lett. **B446**(1999) 75.

[89] K. Mönig, *Model independent limit of the Z-decay Width into Unknown particles*, CERN-OPEN-97-040. (1997)

[90] Particle Data Group, R.M. Barnett *et al.*, Phys. Rev. **D54**(1996) .

[91] S.Katsanevas and P.Morawitz, Comput. Phys. Commun.**112**(1998) 227.

[92] DELPHI Collaboration, Z. Phys. **C73**(1996) 11.

[93] T. Sjöstrand *et al.*, LU-TP/00-30, hep-ph/0010017.

[94] S. Jadach, B.F.L. Ward, Z. Was, Comput. Phys. Commun.**124**(1995) 233.

[95] J.E. Campagne and R. Zitoun, Z. Phys. **C43** (1989) 469.

[96] S. Jadach, W. Placzek, B.F.L. Ward, Phys. Lett. **B390**(1997) 198.

[97] F.A. Berends, R. Pittau, R. Kleiss, Comput. Phys. Commun.**85**(1995) 437.

[98] Y. Kurihara and others, KEK CP-035, KEK 95-126, 1995.

[99] Minami-Tateya Coll., "GRACE Manual ver. 1.0", KEK Report 92-19, 1993; Minami-Tateya Coll., "Brief Manual of GRACE system ver. 2.0/β", 1995.

[100] J. Fujimoto *et al.*, Comput. Phys. Commun.**100**(1997) 128.

[101] F.A. Berends, P.H. Daverveldt, R. Kleiss, Comput. Phys. Commun.**40**(1986) 271.

[102] S. Nova, A. Olshevski, and T. Todorov, note DELPHI 90-35 PROG 152.

[103] http://www.thep.lu.se/ torbjorn/Pythia.html

[104] T. Alderweireld, S. Todorova et P. Verdier, *Study of the hadronic $\gamma\gamma$ interactions at* $\sqrt{s}$ *= 200 GeV*, CERN-OPEN-2002-032;
T. Alderweireld *et al.*, *Event generators for $\gamma\gamma$ physics*, in *Reports of the Working Groups on Precision Calculations for LEP2 Physics*, CERN Yellow Report 2000-009;
P. Verdier, *Recherche des squakrs et des gluinos dans l'experience DELPHI au LEP*, Thèse Université Claude Bernard Lyon 1, 2001;
Christer Friberg, hep-ph/9907299;
Christer Friberg et Torbjörn Sjöstrand, hep-ph/0009003.

[105] http://delphiwww.cern.ch/ offline/delwww/mad/mad_dafne/datamc98/gghard/Welcome.html.

[106] http://lipniack.home.cern.ch/lipniack/mad/electrons/electrmom.html;
DELPHI Collaboration, Eur. Phys. J. **CC19**(2001) 201.

[107] http://lipniack.home.cern.ch/lipniack/mad/evis/evis.html.

[108] A. Perrotta, *Confidence limits with multiple channels and arbitrary probability distributions for sensitivity and expected background*, accepted by Int. J. Mod. Phys **C**.

[109] *1st Workshop on Confidence Limits*, CERN Yellow report CERN 2000-005, (2000).

[110] DELPHI Collaboration, Phys. Lett. **B494**(2000) 203;
DELPHI Collaboration, Phys. Lett. **B503**(2001) 34;
T. Alderweireld *et al.*, *Update of the search for supersymmetric particles in light gravitino*, DELPHI note 2002-024-CONF-558, (2002).

[111] ALEPH Collaboration, SUGRA results, ALEPH note 2002-028 (2002);
ALEPH Collaboration, GMSB results, CERN-EP/2002-021 (2002);
L3 Collaboration, L3 note L2731 (2002);
OPAL Collaboration, SUGRA results, Opal note PN503 (2002);
OPAL Collaboration, GMSB results, Opal note PN504 (2002).

[112] LEP2 SUSY Working group, http://lepsusy.web.cern.ch/lepsusy/www/inos_moriond01/charginos_pub.html.

[113] S. Abel *et al.*, *Report of SUGRA Working Group for RUN II of the Tevatron*, hep-ph/0003154 (2000).

[114] CMS Collaboration, CMS note 1997/007 (1997).

[115] R.-D. Heuer *et al.*, *TESLA Technical Design Report Part III: Physics at an e+e- Linear Collider*, hep-ph/0106315 (2001).

[116] J.F. Gunion and H.E. Haber, *Nucl. Phys.***B272**(1986) 1; *Nucl. Phys.***B278**(1986) 449; *Nucl. Phys.***B307**(1988) 445.

[117] J.F. Gunion, H.E. Haber, G.L. Kane and S. Dawson, *The Higgs Hunter's Guide* Addison-Wesley 1991, errata: hep-ph/9302272.

[118] H.E. Haber and R. Hempfling, Phys. Rev. Lett.**66**(1991) 1815; J. Ellis, G. Ridolfi and F. Zwirner, Phys. Lett. **B257**(1991) 83, Phys. Lett. **B262**(1991) 477.

[119] D. Pierce and A. Papadopoulos, Phys. Rev. **D50**(1994) 565.

[120] D. Pierce and A. Papadopoulos, Nucl. Phys. **B430**(1994) 278.

[121] M. A. Díaz, S. F. King and D. A. Ross, *Radiatively corrected chargino pair production at LEP2*, hep-ex/9801373 (LEP2 energy range);
M. A. Díaz, S. F. King and D. A. Ross,
Radiatively corrections to chargino production in electron-positron collisions,
hep-ex/9801373 (complete calculation and until $\sqrt{s}$ = 2 TeV).

[122] B. Efron, Am. Stat. **40**, 11 (1996).

[123] R.D. Cousins, Am. J. Phys. **63**, 398 (1995).

[124] V.F. Obraztsov, Nucl. Instrum. Methods **A316**(1992) 388;
V.F. Obraztsov, Nucl. Instrum. Methods **A399**(1997) 500.

[125] G. Altarelli *et al.*, *"Physics at LEP2"*, Yellow Report CERN 96-01, vol. 2. (1996)

[126] S. Jadach *et al.*, *LEP2 Monte Carlo Workshop : Report of the Working Groups on Precision Calculations for LEP2 Physics*, Yellow Report CERN 2000-009, (September 2000).

[127] P. Rehn, private communicaton;
P. Rehn *et al.*, *A technique to evaluate and propagate uncertainties in the Monte Carlo modeling of the event reconstruction*, publication in preparation.

[128] G. Borisov *et al.*, *Update of the ZZ cross-section measurement in e^+e^- interactions using data collected in 2000*, Note DELPHI 2001-105 CONF 533.

[129] M. Stanitzki *et al.*, *Searches for invisibly decaying Higgs bosons*, Note DELPHI 2001-79 CONF 507.

[130] A. Behrmann, P.J. Holt, *Muon Momentum and Muon Chamber Efficiency Corrections for LEP II*, note DELPHI 2002-017 PHYS 918.